UNIVERSITY OF SOUTHAMPTON

Electrochemical Investigations of Acoustically Driven Gas Bubbles

By

Yvonne Watson

A thesis submitted for the degree of

DOCTOR OF PHILOSOPHY

Electrochemistry Group,
Chemistry Department;
And
Fluid Dynamics and Acoustics Group,
Institute of Sound and Vibration Research.

Faculty of Engineering and Applied Science.

February 2003

UNIVERSITY OF SOUTHAMPTON

ABSTRACT

Faculty of Engineering and Applied Science
Chemistry Department
Institute of Sound and Vibration Research

Doctor of Philosophy

ELECTROCHEMICAL INVESTIGATIONS OF ACOUSTICALLY DRIVEN GAS BUBBLES

By Yvonne Watson

Electrochemical sensors are employed to study the motion of large gas bubbles in liquids driven into oscillation by an acoustic field. Investigations into potential applications of this study are also undertaken.

The electrochemistry close to the gas bubble/liquid interface is characterised prior to sound irradiation. A Scanning Electrochemical Microscopy (SECM) technique enables the bubble wall-microelectrode distance to be controlled. This is achieved by monitoring the current recorded at the microelectrode as the bubble wall is approached. This is followed by an extensive investigation into the interaction of sound with a bubble and its affect on the electrochemistry at a nearby microelectrode.

A bubble driven to oscillate by a sound field can be detected electrochemically via mass transfer enhancement of species to electrode surface compared to that recorded in the bulk solution in the absence of sound irradiation. Two of the main oscillatory modes of an oscillating bubble (*i.e.* fundamental and subharmonic motion) are detected using a novel electrochemical technique for the first time. Subharmonic motion is found to occur for a certain range of frequencies and pressures, and a threshold pressure amplitude exists at which this motion is detected. It is found that the onset of Faraday waves is responsible for subharmonic motion and an acoustic model is derived to confirm this. However, fundamental oscillatory motion of the bubble can also be detected over a wider frequency range using the electrochemical methodology presented. It is shown that the extent of mass transfer enhancement is smaller when compared to Faraday wave excitation of the bubble wall.

The effect of surfactants on the threshold pressure amplitude for the onset of Faraday waves and the mode number of an oscillating bubble is explored, and the results obtained are compared to the developed model. Prior to achieving steady state surface wave motion there is a ring-up period. Understanding of this ring-up behaviour is at a very early stage. This thesis introduces an electrochemical study of this phenomenon.

Electrochemical detection of both the fundamental and Faraday wave motion of an oscillating bubble is shown to have several useful applications. One such application would be in the detection and sizing bubbles in a population. Electrochemical detection of individual bubbles in a rising stream and Faraday wave motion of an oscillating rising bubble is explored extensively. Another application would in the area of bubble growth by a process known as rectified diffusion. Bubble growth rates are determined and these are compared to a theoretical model.

Finally, electrochemical detection of Faraday wave motion is employed in the detection of trace species in solution. In this sequence of experiments a novel approach to hydrodynamic voltammetry is introduced.

Contents

Acknowledgements

I would like to thank Dr Peter Birkin, my supervisor, for his constant help, interest, supervision and friendship developed during the course of this PhD. I would also like to sincerely thank him for his invaluable proof reading and patience while writing this thesis.

I would like to sincerely thank Prof. Tim Leighton, my supervisor, for his helpful insights and guidance while writing this thesis and also his invaluable supervision over the last three years.

I would like to thank the following people:

Dr Guy Denuault who kindly allowed me to use the SECM and also his assistance in obtaining data.

Jonathan Fleming an undergraduate student. The data obtained in chapter 8 was done in collaboration with this student.

Becky who has been a great friend over the past three years and for those memorable Friday nights in the staff club and wherever else we ended up (Kaos, Lennons, Frog.....).

All the lads on the 7th floor (Yannick, Doug, Matt, Richard, Tim) for their friendship and for all those unforgettable Friday nights in the staff club and their encouragement when I wanted to play pool!!!.

My family for their encouragement and support over the three years.

John for his patience, companionship and love over the past three years and for making the trip to Southampton worthwhile.

List of Symbols

a	Radius of electrode (m)
a_1	A function defined by equation 1.15
A	A function defined by equation 1.21
A_1	Area of electrode (m^2)
B	A function defined by equation 1.22
c	Concentration of electroactive material (mol dm^{-3})
c_i	Speed of sound (m s^{-1})
C_i	Bulk concentration of dissolved gas in a liquid (mol dm^{-3})
C_{sn}	Concentration of dissolved gas at the bubble wall at equilibrium (mol dm^{-3})
C_0	Saturation concentration of dissolved gas in a liquid (mol dm^{-3})
C_t	Normalised wall displacement amplitude threshold
C_{t0}	C_t at resonance circular frequency
C_p	Heat capacity at constant pressure (J kg^{-1} K^{-1})
d	Electrode/bubble wall distance (m)
d_1	Bubble diameter (m)
d_2	Distance in the x direction (m)
d_3	Distance from the microelectrode in a radial direction (m)
d_4,d_5,d_6	Various bubble wall microelectrode distances (m)
$d_{min},d_{max},d_{1/2}$	Displacement between bubble wall and microelectrode (see chapter 5) (m)
d_{th}	Thermal damping coefficient
d_{tot}	Total non dimensional damping coefficient
D	Diffusion coefficient (cm^2 s^{-1})
D_g	Thermal Diffusivity (m^2 s^{-1})
e	Electrons
F	Faradays constant (C mol^{-1})
g	Acceleration due to gravity (m s^{-2})
G_1,G_2	Gradients (see chapter 7)
i	Current (A)
i_{inf}	Current recorded in the bulk under SECM conditions (A)
i_l	Limiting current recorded at a rotating disk electrode (A)
i_{MTL}	Mass transfer limited current recorded by a microelectrode (A)
i_{tip}	Current recorded at the microelectrode tip under SECM conditions (A)
I_N	Normalised current (i/i_{MTL})
j	Flux (mol m^{-2} s^{-1})
k_m	Mass transfer coefficient (cm s^{-1})
k_1, k_2, k_3, k_4	Constants which depend on R_{glass}
K_g	Thermal conductivity of a gas (J m^{-1} s^{-1} K^{-1})

l	Diffusion length (m)
L	Electrode-substrate distance divided by electrode radius
n	Mode number
n_e	Number of electrons
n_g	Number of moles of gas
p	A function defined by equation 1.16
p_g	Instantaneous gas pressure inside a bubble (Pa)
$p_{g,e}$	Equilibrium gas pressure inside a bubble (Pa)
p_v	Vapour pressure (Pa)
p_0	Hydrostatic pressure (Pa)
P_A	Amplitude of acoustic pressure (Pa)
P_T	Acoustic pressure amplitude threshold for the onset of surface waves on the bubble of order of one half the driving frequency (Pa)
q	A function defined by equation 1.17
r	Radial distance in liquid from the centre of a bubble (m)
r_s	Radial distance from the centre of a bubble to its surface (m)
R	Instantaneous bubble radius (m)
Re	Reynolds number
R_g	Universal gas constant (J K^{-1} mol^{-1})
R_{glass}	Ratio of the insulating glass sheath radius to that of the electroactive disk
R_r	Linear resonance radius (m)
R_0	Equilibrium radius of a spherical bubble (m)
R_ε	Displacement of radius from equilibrium, such that $R(t)=R_\varepsilon(t)+R_0$ (m)
$R_{\varepsilon 0}$	Maximum radial displacement amplitude of the wall of a spherical bubble (m)
s	Power spectral density (A^2 Hz^{-1})
t	Time (s)
t_{ss}	Time to steady state (s)
T	Temperature (K)
T_1,T_2	Ring-up time (see chapter 7) (s)
T_b	Period of pulsating bubble (s)
U	Streaming velocity (m s^{-1})
U_θ	Streaming velocity with angular dependence (m s^{-1})
v	Rising velocity (m s^{-1})
V_A	Voltage amplitude (V)
V_u	Voltage/out setting on the hydrophone (V)
V_0	Acoustic velocity of a material (m s^{-1})
x	Distance (m)

Greek Letters

δ	Diffusion layer thickness (for a rotating disk electrode) (m)

γ	Ratio of specific heat at constant pressure to that at constant volume (adiabatic constant)
κ	Polytropic index
μ	Dynamic viscosity (kg m^{-1} s^{-1})
π	Pi ~ 3.141592654
ρ	Density of the fluid medium (kg m^{-3})
ρ'	Density of gas (kg m^{-3})
σ	Surface tension (N m^{-1})
υ	Kinematic viscosity (m^2 s^{-1})
υ_0	Linear frequency of bubble pulsations (Hz)
ω	Driving frequency (rad s^{-1})
ω_i	Frequency of imaging sound field (rad s^{-1})
ω_n	Mode frequency (rad s^{-1})
ω_0	Resonant frequency of a bubble (rad s^{-1})
ω_M	Minnaert resonant frequency (rad s^{-1})
ω_{RD}	Rotation rate of a rotating disk electrode (rad s^{-1})

Abbreviations

AC	Alternating Current
AcV	Acoustic Voltammetry
Ag	Silver
CMC	Critical Micelle Concentration
CV	Cyclic Voltammogram
DC	Direct Current
$Fe(CN)_6^{3-}$	Ferricyanide ion
$Fe(CN)_6^{4-}$	Ferrocyanide ion
FFT	Fast Fourier Transform
fps	Frames per second
ITIES	Interface between Two Immiscible Electrolyte Solutions
KCl	Potassium Chloride
Li	Lithium
Na	Sodium
PMMA	Polymethyl methacrylate
Pt	Platinum
PTFE	Polytetrafluoroethlylene
SECM	Scanning Electrochemical Microscopy
$Sr(NO_3)_2$	Strontium Nitrate

Introduction
Chapter 1

1.0 Introduction

Bubbles play an important role in many industrial, medical and environmental processes.[1-11] They are used in industry for a variety of purposes. These range from the mixing of solution through the disturbance of natural diffusion patterns to the exchange of materials between the gas and liquid phases. For example air sparging is used to purify ground water by volatilising contaminants and enhancing biodegradation.[12-14] In other large scale industrial process (*e.g.* the chlor-alkali industry) the generation and motion of bubbles has been recognised as being important in the overall efficiency of the process.[5,15]

Existing ways of monitoring how bubbles affect concentration gradients in solution are extensive. As an example the effect of bubbles on the mass transfer of material in a system has been investigated using a variety of electrochemical techniques.[16-18] However, it is well known that bubbles in liquids are extremely acoustically active and have been studied in relation to their passive acoustic emission and their interaction with a varying pressure field. Consequently, acoustic studies have been used to estimate bubble size distributions[19-23] within the oceans where they are thought to play a key role in the transfer of gases between the atmosphere and the water phase. This is an important parameter when considering the climatic influence of certain gases which readily exchange with the ocean.[24] Considering that bubbles interact strongly with sound it would be beneficial to study the influence of acoustics on the mass transfer of material to the solid/liquid interface of an electrode using a combined technique employing both electrochemistry and acoustic technology. This study could indicate whether acoustic irradiation of a bubbly liquid will have a strong influence on the concentration profiles within a solution. This could be significant, as it would demonstrate that acoustics could be used to not only measure bubble populations, but also to influence bulk solution characteristics. The solution characteristics in turn could be monitored using electrochemistry. The combination of acoustics and electrochemistry has led to the new field of 'acoustoelectrochemistry'.[25] Clearly considering the size distribution of bubbles within liquids it is necessary to employ an electrochemical technique with high

spatial resolution. In this thesis microelectrodes are used to monitor perturbations in concentration gradients caused by the motion of acoustically excited bubbles.

In addition to the study of the influence of sound on bubbles it is also vital to understand the effect of the gas/liquid interface on the electrochemical processes occurring at a microelectrode. The first part of this chapter reports on the phenomenon of mass transfer of materials in an electrochemical cell and how the presence of a gas/liquid boundary (bubble wall) can block the diffusion of species to the microelectrode surface or act as a source for species that are being depleted by a microelectrode. However, bubble motion will alter the experimental observations by providing a mechanism for forced convection of material to the electrode interface. This perturbation could be achieved through translation, pulsation and surface wave motion of a bubble. Pulsation and surface waves can be excited acoustically on the bubble. Both modes of the bubble wall are discussed, as electrochemical detection of both phenomena is the central topic of this thesis. Other fundamental phenomena associated with bubble motion such as bubble growth by rectified diffusion and non steady state oscillations are also discussed. Finally a summary is given of the work presented in each chapter of this thesis. Measurement of changes in mass transfer is employed as an analytical tool throughout the course of this thesis. This topic will now be discussed in depth.

1.1 Mass Transfer

Mass transfer is an important phenomenon when studying the nature of the gas/liquid interface and bubble motion. It can be regarded as the physical movement of material in solution from one place to another. There are three modes of mass transfer: diffusion, convection and migration.[16] Diffusion is the random motion of material within a phase. Diffusion causes the movement of material due to a concentration gradient (*e.g.* from areas of high concentration to areas of low concentration). Fick's first law of diffusion (equation 1.1) shows that the movement of a substance (the flux (j)) is proportional to the concentration (c) gradient with respect to distance (x) and the diffusion coefficient (D) of the species in question:[16]

$$j = -D\frac{dc}{dx} \qquad (1.1).$$

The movement of the bulk solution is termed convection. This can be a result of mechanical agitation, pressure, density gradients, temperature gradients or other mechanical forces such as those provided by the motion of a bubble.[16] It must be also noted that convection only brings about mass transfer when there is a concentration gradient present. Finally migration is the movement of charged particles due to an electrical potential gradient. However, this effect is normally suppressed by adding a large concentration of inert background electrolyte[16-18] and hence will be ignored from this point on.

Mass transfer can be monitored using electrochemical techniques.[16-18] Electrochemistry can be described as the driving of chemical processes through the transfer of electrons across an electrode/electrolyte interface. Normally two electrodes are placed in an appropriate solution. The conduction of the electrical current between the electrodes relies on ionic conduction in solution. If we consider a reaction where a species in solution (A) is oxidised at an electrode, it is possible to represent the process as:

$$A - n_e e \rightarrow B \qquad (1.2)$$

where 'n_e' represents the removal of n_e electrons e from the chemical species A, which produces species B. In order to maintain a charge balance, a reduction process (gain of electrons) has to occur at the other electrode. The reaction is monitored by recording the current flowing out of (oxidation) or into (reduction) one of the electrodes (termed the working electrode).

In the work presented here, the working electrodes employed are microelectrodes.[26,27] Microelectrodes are usually defined as electrodes with a critical dimension below 50 μm. These electrodes can be classed as wire, microband, microring or microdisk. Microdisk electrodes (an inlaid conductor, normally a disk surrounded by an insulating medium usually glass) are employed in the majority of experiments represented here. Hence we will discuss the properties of these electrodes in more detail.

Microelectrodes have several unique properties, which are beneficial to the study of bubble dynamics. In particular they are small and hence can approach the gas/liquid interface of a gas bubble. They can reach a steady state (response time is ms) and can monitor local changes in concentration. Many of their properties are dictated by the unusual mass transfer characteristics, which in turn are related to their small size. As an example figure 1.1 shows the concentration profile[28] developed under mass transfer steady state conditions (no convection, the electrode held at a potential sufficient to oxidise/reduce all

target material reaching the microelectrode surface). Under these conditions, the concentration of the chemical species (on which the reaction at that electrode is based) becomes depleted at the electrode surface resulting in a hemispherical diffusion pattern developing in front of the microelectrode.[29]

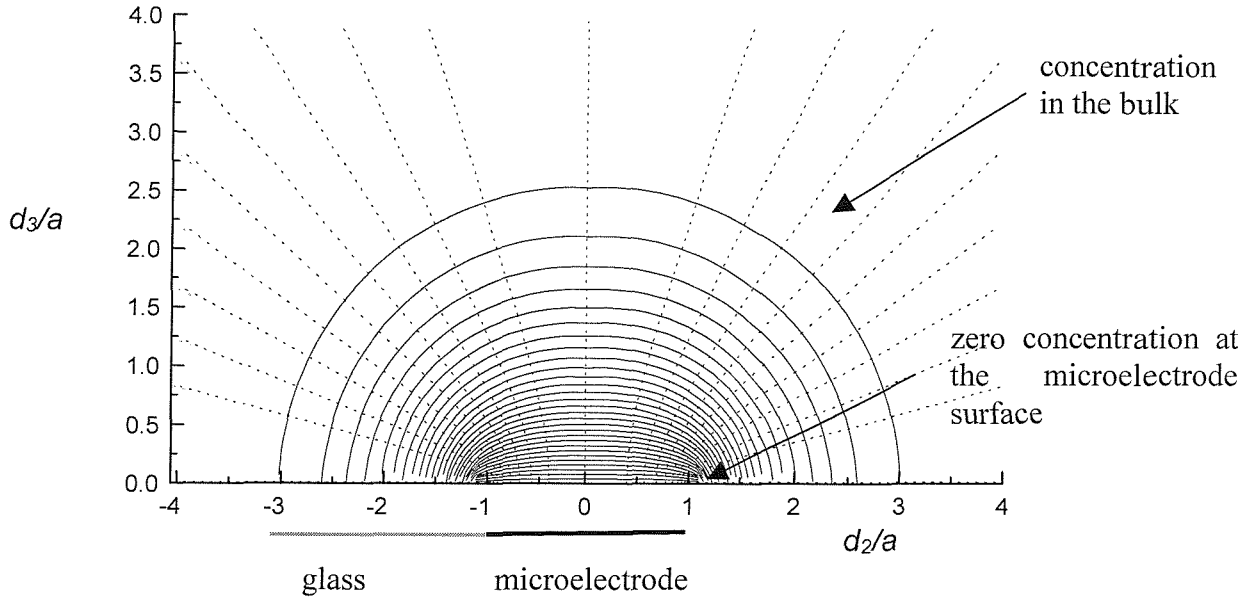

Figure 1.1 Diagram showing the diffusion hemisphere of a microelectrode. d_2/a is normalised distance where d_2 is distance in the x direction and a is the electrode radius. d_3/a is normalised distance in a radial direction from the microelectrode surface where d_3 is distance in a radial direction from the microelectrode and a is the microelectrode radius.

The steady state mass transfer limiting current[26,27] (i_{MTL}) recorded at the microelectrode under these conditions is given by equation 1.3:

$$i_{MTL} = 4n_e aFDc \qquad (1.3)$$

where F is Faraday's constant, a is the radius of the electrode, D is the diffusion coefficient and c is the bulk concentration of the particular electro-active species.

However, if the diffusion hemisphere surrounding the microelectrode is disturbed by, for example, forced convection (*i.e.* the stirring of the solution or motion of a bubble) the depleted layer around the microelectrode becomes refreshed. This enhances the transfer of material to the electrode surface, and hence augments the current recorded at the microelectrode. The mass transfer coefficient (k_m) under these conditions can be calculated

from equation 1.4 which is valid when the electrode potential is set to a value sufficient to oxidise or reduce a target species as it reaches the electrode surface:[16-18]

$$i = n_e F A_1 k_m c \qquad (1.4)$$

where A_1 is the area of the electrode. This equation is also valid in the absence of forced convection. The mass transfer coefficient can be related to the diffusion coefficient of a particular redox species by combining equations 1.3 and 1.4 to give equation 1.5:

$$k_m = (\frac{4D}{\pi a}) I_N \qquad (1.5)$$

where I_N is equal to i/i_{MTL}, i is the current recorded at the microelectrode and i_{MTL} is the mass transfer limited steady state current in the absence of convection. A typical value of k_m is 0.023 cm s^{-1} for a 10 μm diameter Pt microelectrode in 5 mmol dm^{-3} $Ru(NH_3)_6^{3+}$ in stagnant solution. This value will increase in the presence of convection due to bubble motion.[30]

In this thesis the majority of experiments will be performed with the microelectrode held at the mass transfer limiting potential close to the gas/liquid boundary of a bubble. Consequently, it is important to understand how the presence of a gas bubble may affect mass transfer to a microelectrode surface prior to irradiating the bubble with sound. Much work has been performed in relation to mass transfer at interfaces (*e.g.* solid/liquid and liquid/liquid).[31-46] Electrochemical techniques have been used extensively to examine interfaces. This is because electrochemistry is a powerful technique for investigating the nature of the physical and chemical processes at these boundaries.[34,35] One technique, Scanning Electrochemical Microscopy (SECM) has yielded some interesting results with regard to the nature of the phase transition between liquid/solid, liquid/liquid and liquid/gas interfaces.[35-46] A low resolution equivalent of this technique is employed throughout this thesis (*e.g.* see chapter 3) to study the gas bubble/liquid interface in the absence and presence of insonification. Hence, the subsequent section discusses this technique in more detail.

1.2 Interfaces

SECM is a technique mainly used to investigate reactivity at surfaces immersed in electrolyte solutions on the micrometer scale. Bard *et al.*[35,42] reported some of the earliest work involving SECM although the earliest report was by Engstrom *et al.* in 1986.[47] Bard *et al.*[35,42] examined the effect of microelectrode tip geometry (specifically the ratio of the electrode radius to the radius of the insulating sheath) on the current recorded at the microelectrode on approaching an insulating or conducting substrate. They showed that the ratio of the insulating glass sheath radius to that of the electroactive disk (R_{glass}) had a strong influence on the current recorded at the microelectrode when the microelectrode tip was moving in the vicinity of an inert substrate. The insulating medium disrupted the diffusion layer at the microelectrode tip when the tip was within a distance of *ca.* 10 times the microelectrode radius from the substrate. The presence of the substrate essentially hinders the diffusion of species from the bulk to the electrode tip and consequently reduces the tip current. This phenomenon is termed 'negative feedback' or hindered diffusion (see figure 1.2).

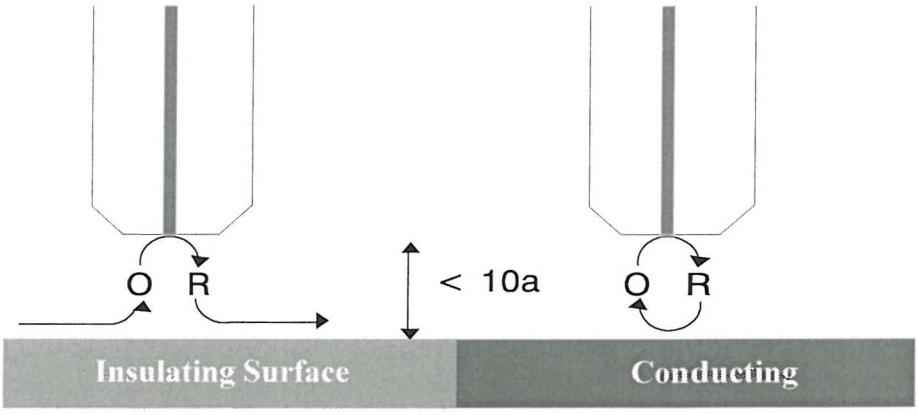

Figure 1.2 Schematic illustrating the motion of chemical species as a microelectrode approaches both an insulating and conducting surface operating under SECM conditions.

They also predicted that the tip current would not be affected by the thickness of the insulating sheath surrounding the electroactive disk when approaching a conducting material. If the microelectrode tip is brought close to a conducting substrate, at which the electroactive species can be regenerated, then the flux of these species detected by the

microelectrode tip is enhanced. The regeneration effect adds to the normal diffusion of species from the bulk. Therefore as the microelectrode tip gets closer to a conducting substrate, the measured tip current will increase considerably and becomes much greater than the current recorded in the bulk (see figure 1.2). Experimentally such an increase in tip current can often reach 10 times the value normally obtained in the bulk.[43] This regeneration effect is called 'positive feedback'.

Moving the tip close to the substrate while recording the tip current produces an approach curve. Two extremes of approach curve can be obtained, one with the microelectrode approaching a conductor, which leads to the positive feedback mechanism and the other with microelectrode approaching an insulator, which eventually leads to the negative feedback mechanism. In between these two cases a whole family of approach curves exist that depend on the reactivity of the substrate.

Most SECM investigations have explored interfaces that were macroscopic in nature (*e.g.* the planar interface between two liquids or the solid/liquid boundary). However, inclusions within another phase (*e.g.* gas bubbles) have not been investigated to the same extent. This will be dealt with in the following section.

1.2a Interface between a Gas Bubble and Liquid.

Investigations into the variation in mass transfer to a microelectrode as it approaches an air/liquid interface have been studied by Unwin *et al.*.[40,41,48] According to these authors the reduction of oxygen at a microelectrode creates a depleted region adjacent to the interface between a gas (in this case air) and liquid.[40] This provides a thermodynamic driving force for the transfer of oxygen across from the gas phase to the aqueous phase, and thus an enhancement in mass transfer to the microelectrode was observed. Although this type of response shows many similarities with systems operating under positive feedback conditions[49] it cannot be classified in this category. This is because the mechanism resulting in enhancement in current in the positive feedback case is different from the mechanism resulting in enhancement in current brought about by gas transfer across the interface. This will be discussed in detail in section 3.1b of this thesis.

In the same investigation the authors also reported on the effect of a monolayer (accumulated at an air/water interface) on oxygen transfer rates across an air/water interface.[40] The technique was illustrated through measurements of oxygen transfer across a monolayer of 1-octadecanol as a function of compression of the monolayer. The

experimental approach used an inverted microelectrode, positioned in the water phase in a Langmuir trough close to the air/water interface (see figure 1.3).

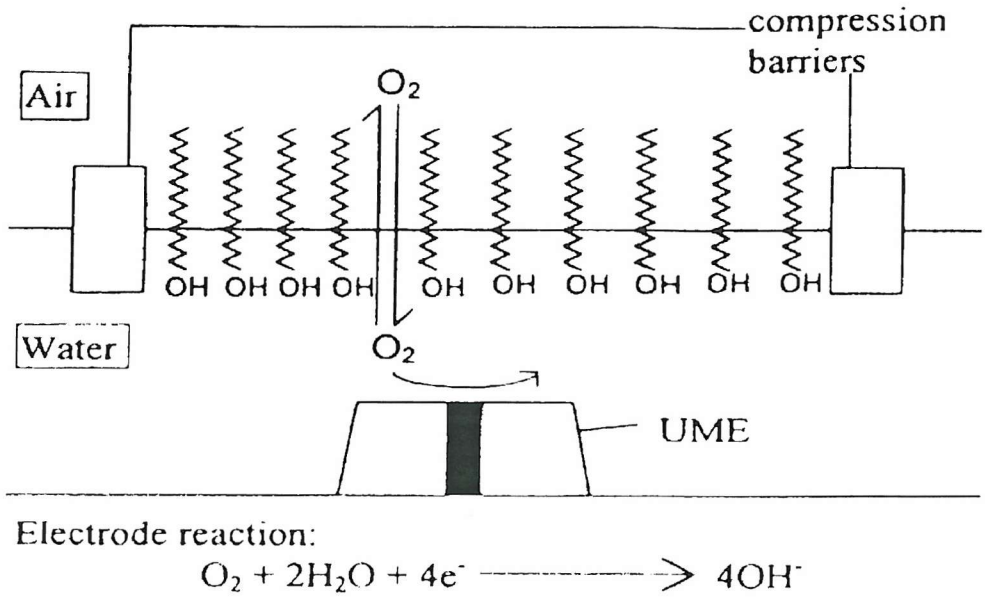

Figure 1.3 Schematic illustration of the equilibrium perturbation method for measuring oxygen transfer across a 1-octadecanol monolayer at the air/water interface using an inverted microelectrode. Reproduced from Unwin *et al.*.[40]

The steady state current, measured as a function of the microelectrode–interface distance at various monolayer compressions, demonstrated that the rate of oxygen transfer was governed primarily by the accessible free area of the interface. Clearly the interface between the gas phase and liquid phase of an air bubble can be considered in a similar manner to the Langmuir[50] trough experiment described by Unwin *et al.*.[40] However, no such investigations have been reported in the literature. This topic will be discussed in depth in section 3.1b of this thesis.

A gas bubble could also be considered as an inert substrate when monitoring the reduction of a non-volatile solution phase species at potentials insufficient to oxidise or reduce any gas phase material (*e.g.* $Fe(CN)_6^{3-}$). The presence of the bubble would hinder diffusion of material to the electrode surface and thus reduce the current recorded at the microelectrode tip. In this case the system is said to be operating under negative feedback conditions and the current recorded at the microelectrode depends on the R_{glass} value.[49] This subject will be examined in detail in section 3.1a.

The previous sections have discussed how the presence of a static gas bubble could alter the concentration of species close to the microelectrode surface. In the majority of the work

presented in this thesis the bubble is irradiated with sound. This results in motion of the bubble wall and thus induces a convective flow of liquid to the microelectrode surface. The next section discusses the different motions of a bubble wall.

1.3 Motions of the Bubble Wall

A bubble can undergo several different types of motion; translation, pulsation and shape oscillations. Pulsation and shape oscillations can be excited acoustically on the bubble while translational motion of the bubble does not require acoustic excitation. Pulsation (breathing mode) is the zero order spherical harmonic motion of the bubble. In this case the bubble expands and contracts spherically symmetrically at the driving frequency (under the conditions employed in this thesis (bubble radius (R_0) *ca.* 1 - 2 mm) the wall displacement amplitude is of the order of a few microns; see figure 1.4).[25] This was calculated from equation 1.6 below derived by Leighton:[24]

$$R_{\varepsilon_0} = \frac{P_A}{R_0\rho((\omega_0 - \omega^2)^2 + (\omega^2 d_{tot})^2)^{1/2}} \qquad (1.6)$$

where $R_{\varepsilon 0}$ is the radial displacement amplitude of the bubble, P_A is the pressure amplitude, ω is the driving frequency, ω_0 is the resonant frequency, ρ is the liquid density and d_{tot} is the total non-dimensional damping coefficient. It must be noted that this displacement was calculated adopting low pressures *i.e.* P_A *ca.* 50 Pa which is the order of magnitude that will be adopted in experiments later on in this thesis.

The first order harmonic corresponds to translation of the entire bubble. The higher orders correspond to shape oscillations on the surface of the bubble wall. These oscillations of the bubble wall can cause surface displacement (in the order of 100 μm under low pressure conditions, see figure 1.4)[25] due to inherent instability of the interface, which ultimately leads to surface waves.[51] The surface wave that requires the least threshold pressure to excite is the Faraday wave, a subharmonic motion of the bubble wall that occurs at half the driving frequency. Higher driving pressures excite additional surface waves at other frequencies, and all are superimposed on the underlying pulsation motion of the bubble wall.

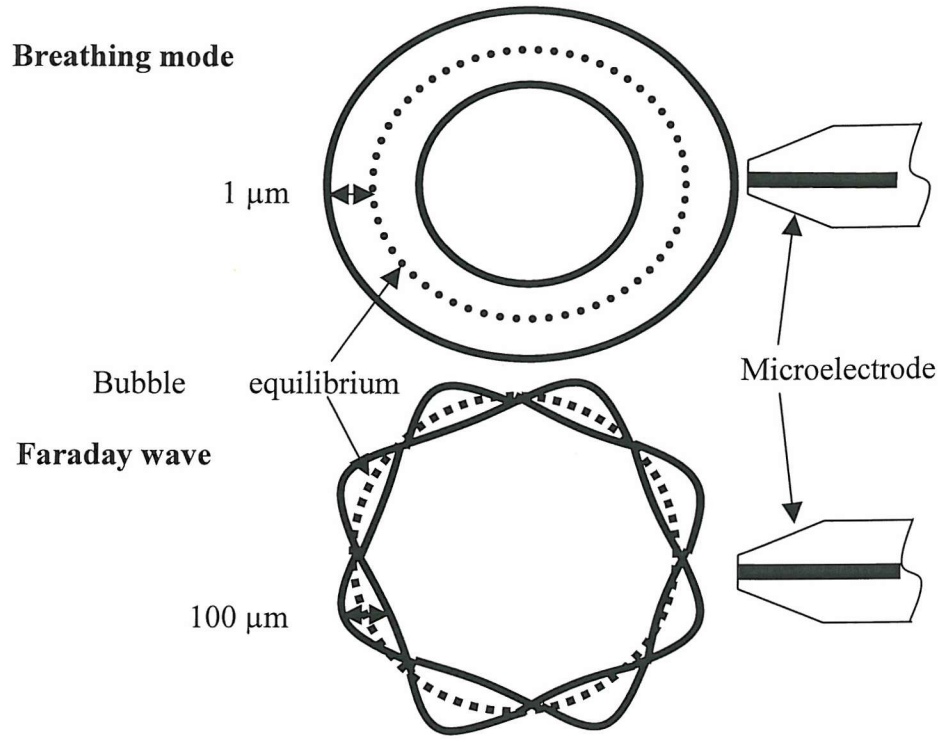

Fig 1.4 Schematic illustration showing the position of the bubble wall at equilibrium (dotted line) and at two extreme displacements, during the oscillatory cycle of: the pulsation (or breathing) mode and the mode corresponding to surface waves on the bubble wall. Note that the amplitude of the wall oscillation for surface waves is around 100 times greater than for the pulsation mode.

Pulsation and subharmonic motion of a bubble have not yet been exploited in industry. Therefore investigation of these motions is the main topic of this thesis. However, translation motion of bubbles has beneficial effects, which have been used extensively in industry.[52-55] These will be discussed in detail in the subsequent section.

1.4 Translational Bubble Motion

In many industries electrochemical generation of bubbles can be used to improve the efficiency of the system. Fouad *et al.*[15] investigated the effects of gas evolution at electrodes in cells such as those used in the chlor-alkali industry. They used a rectangular cell separated into two compartments by a tight moveable diaphragm, with nickel electrodes on either side of the diaphragm. The effect of hydrogen and oxygen evolution on the mass transfer rate to the electrode surface when monitoring the reduction of $Fe(CN)_6^{3-}$ was examined.

During this redox reaction, bubbles of gas appeared at an electrode. These bubbles detached and moved upwards through the solution, parallel to the electrode, carrying the

solution next to the electrode in the form of a gas/liquid dispersion. At the surface of the solution, some of the bubbles were lost to the atmosphere and the remaining bubbles moved horizontally along the surface of the liquid with the solution. When the flow reached the diaphragm, the bubbles were reflected back down into the solution and moved vertically parallel to the diaphragm, leading to two streams of bubbles moving in opposite directions *i.e.* one stream at the electrode surface and the other at the diaphragm. This in turn enhanced mass transfer of material to the electrode surface. Eventually, the recycled stream of bubbles lost its velocity due to the solution viscosity and formed a motionless dispersion.[15] Bubbles in this motionless dispersion rose by virtue of buoyancy force and contributed to increasing convection. Three zones can be distinguished in the cell during electrolysis; the upper zone where eddies are formed, the middle zone where a motionless gas-liquid dispersion is formed and the lower zone which is composed of a clear solution free of gas bubbles (see figure 1.5). In industrial processes where the gas evolved is not formed as a result of the desired redox reaction, the production of hydrogen or oxygen at the electrode would be beneficial if the energy needed to produce the gas at the electrode was less than the mechanical energy needed to stir the solution.

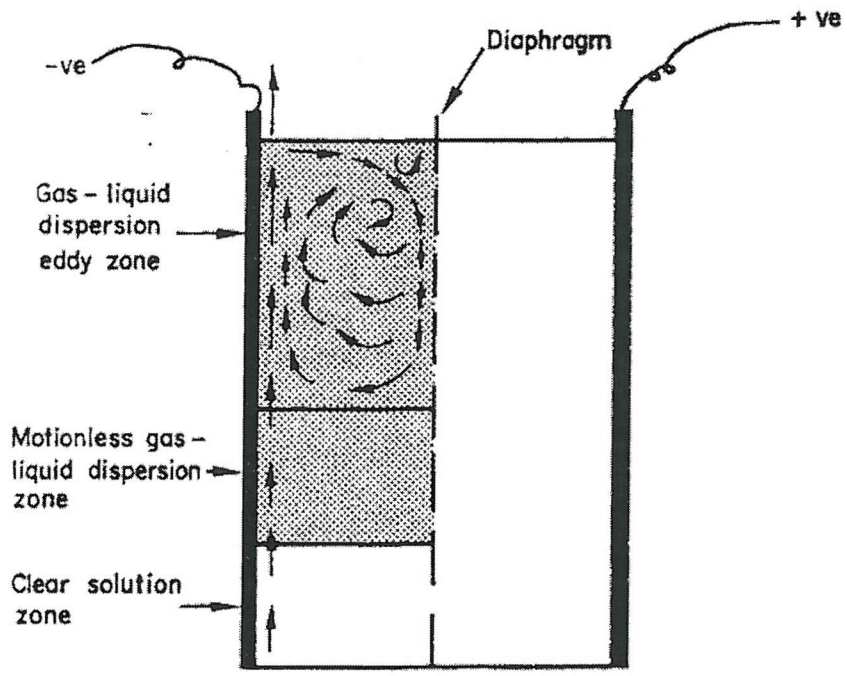

Figure 1.5 Schematic of flow of the gas-liquid dispersion in the cathode compartment. Reproduced from Foaud *et al.*.[15]

In other industries such as wastewater treatment plants air sparging is employed in bioreactors to remove contaminants in water.[12-14] The rising bubbles carry the contaminants

to the surface of the water where they are then removed. In addition, the presence of oxygen enhances biodegradation of contaminants.

The advantageous effects of translational bubble motion has resulted in extensive investigations of mass transfer enhancement at electrodes caused by this bubble motion.[5,15,56-60] The motion of electrochemically generated bubbles during their generation and subsequent release from the electrode has been studied extensively to understand their contribution to mass transfer to the electrode surface.[5,15,56-60] Three models have been developed which describe a particular mechanism of this mass transfer enhancement to an electrode. The three models are the penetration model, the hydrodynamic model and the microconvection model.[5]

Higbie[61] first proposed the penetration model, or surface renewal effect, in 1935 in relation to the absorption of a gas into a liquid, but Ibl and Venczel[56] adopted it in 1970 for electrolytic gas evolution. In this model, a volume of liquid in the mass transfer boundary layer, having been depleted of reactant by the presence of a bubble at the electrode surface, is renewed as each bubble detaches from the electrode *i.e.* fresh electrolyte with bulk concentration of reactant replaces the void left by the bubble at the surface of the electrode. Transport of the reactive species to the nucleation site [62,63] at the electrode is by diffusion, which occurs over a time known as the 'waiting period' before a new bubble is nucleated. The 'waiting period' is inversely proportional to the frequency with which the bubbles form at the electrode. In this case, the current and mass transfer coefficient will depend on the volumetric rate of gas evolution per unit area to the power of a half.[5]

The hydrodynamic model was discussed in relation to gas evolution by Janssen *et al.*[57,58] and described quantitatively by Janssen *et al.*.[59] This treatment emphasises the electrolytic flow caused by the buoyant lift of rising bubbles in the vicinity of the electrode. This model states that the mass transfer coefficient is proportional to the gas evolution rate to the power of a third.[5]

Vogt *et al.*[60] developed the microconvection model in 1979. Their approach treats the mass transfer caused by the local convection generated by the growth of a bubble attached to the electrode. In this model, single bubbles disturb the mass transfer boundary layer, (diffusion layer) causing the mass transfer coefficient to depend on the gas evolution rate to the power of a half.[5]

The work undertaken by Tobias *et al.*[5] is particularly noteworthy when considering mass transfer effects of bubble streams (generated electrolytically). The authors investigated the effects of bubble streams rising near vertical electrodes by using electrochemistry to

produce and monitor mass transfer disturbances. They used a micromosaic working electrode. This electrode was fabricated on a 7.62 cm silicon wafer. The active area consisted of a 5 mm Pt square. The centre 1 mm square of the active area shown in figure 1.6 comprised of a 10 x 10 array of Pt electrodes. Each electrode area was 96 μm^2 and the inter electrode distance was 100 μm. The remaining part of the active area acts as a buffer segment to eliminate edge effects in the centre region. In addition, there are twelve satellite segments positioned within the buffer segment at distances of 100, 300 and 500 μm from the segmented area (see figure 1.6). Bubble streams were generated at the electrode surface by using one of the satellite segments and making the potential at that segment several hundred millivolts more cathodic than the rest of the electrode. The experiments in which the bubble stream was generated away from the electrode surface were conducted by modifying the cell top to include a platinum wire electrode that produced the bubbles.

Bubbles generated at one of the satellite segments were 45 to 100 μm in diameter by the time that they detached from the electrode. Once detached, the bubble was seen to slide along the electrode for a distance of several bubble diameters (see figure 1.7) before separating and rising through the solution at a distance of approximately one bubble radius from the electrode.

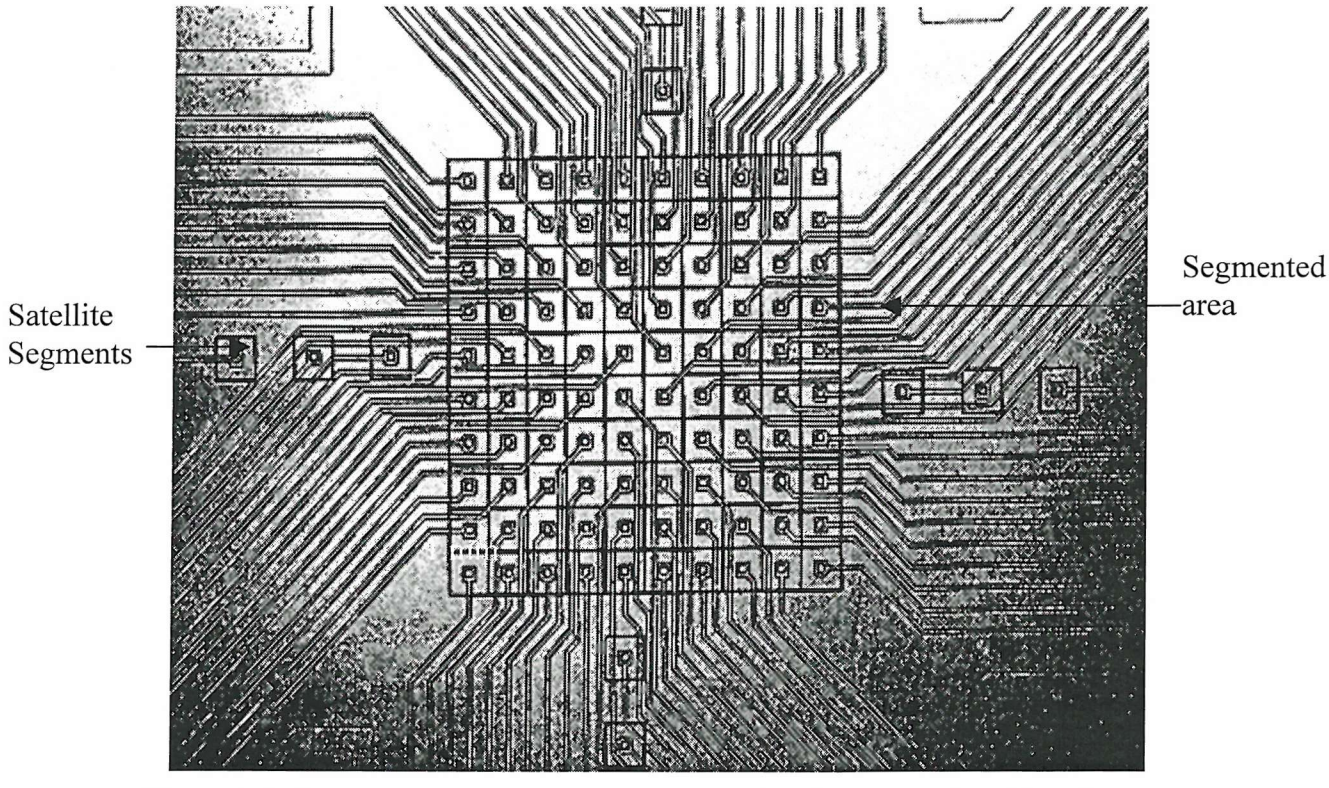

Figure 1.6 Diagram of the micromosaic electrode used to investigate the effect of bubble streams rising near vertical electrodes. Reproduced from Tobias *et al.*.[5]

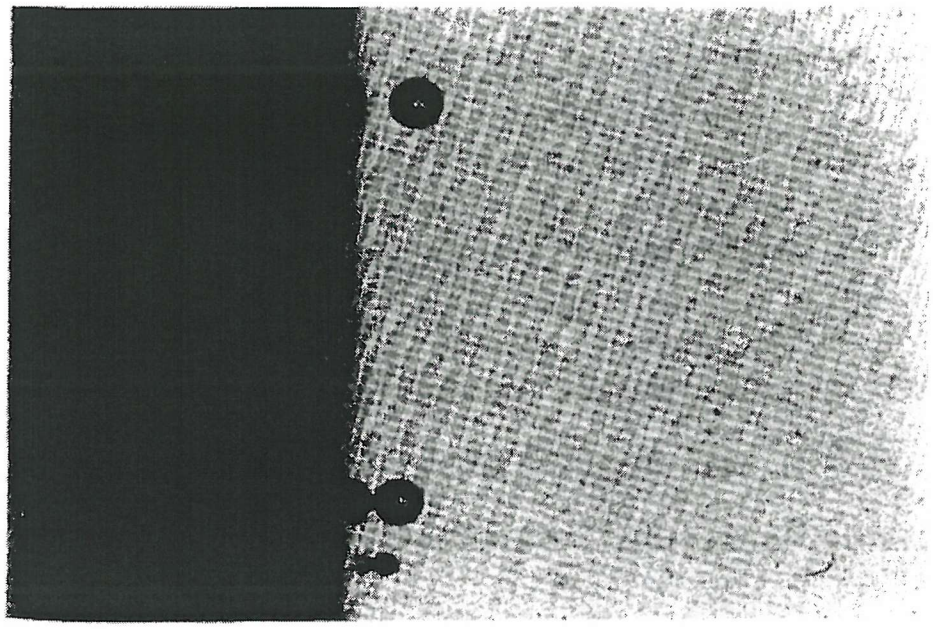

Figure 1.7 Bubbles rising along the micromosaic strip electrode. Reproduced from Tobias *et al.*.[5]

The average mass transfer rate resulting from bubbles rising within the mass transfer boundary layer increased by a factor of approximately 1.5, and then decreased until the next bubble arrived. Mass transfer enhancement to the electrode was fluctuating and fairly localised as shown by figure 1.8. This agreed with trends predicted by the surface renewal model (penetration model).

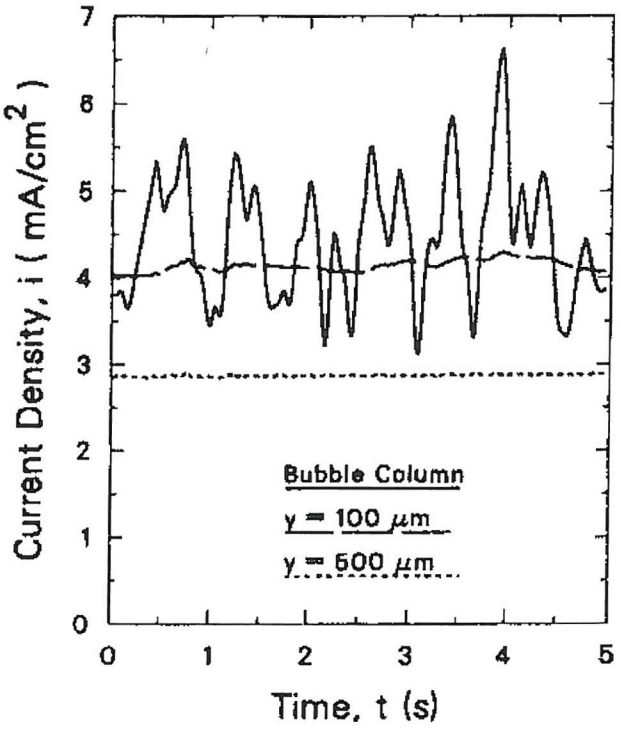

Figure 1.8 Graph showing the current density against the time for one of the monitoring segments directly in the path of the bubble stream. Reproduced from Tobias *et al.*.[5]

The current response recorded at the electrode for bubbles rising outside the mass transfer layer was steadier in time than for bubbles rising at one of the satellite segments because the effects of individual bubbles were averaged out. The magnitude of mass transfer enhancement was dependent upon the position of the bubble stream, with enhancement decreasing with increasing distance from the electrode surface. In this case the enhancement was less localised than before and resulted from an increasing velocity gradient near to the electrode (macroconvection).

This section discussed extensively the enhancement in mass transfer at electrodes caused by translational motion of bubbles. However, mass transfer enhancement associated with the breathing mode and surface wave motion has not been previously investigated. Both motions will be discussed in detail in the subsequent sections, as electrochemical detection of these modes of oscillation and the mass transfer enhancement associated with each mode is the central topic of investigation in this thesis.

1.5 The Pulsating Spherical Bubble

Minnaert[64] first calculated the natural frequency of a spherical gas bubble in a liquid, undergoing low-amplitude simple harmonic oscillations (pulsations). Figure 1.9 illustrates this motion and if these oscillations are at the bubble's resonant frequency (ω_0) the deviation of the bubble wall from its equilibrium radius (R_0) is given by equation 1.7:

$$R_\varepsilon = -R_{\varepsilon 0} e^{i\omega_0 t} \tag{1.7}$$

where $R_{\varepsilon 0}$ is defined as the maximum amplitude of radial displacement and R_ε is the amplitude of radial displacement. Note the negative sign is because a small increase in pressure would cause a decrease in radius.

The bubble radius (R) is therefore given by equation 1.8:

$$R = R_0 + R_\varepsilon(t) = R_0 - R_{\varepsilon 0} e^{i\omega_0 t} \tag{1.8}.$$

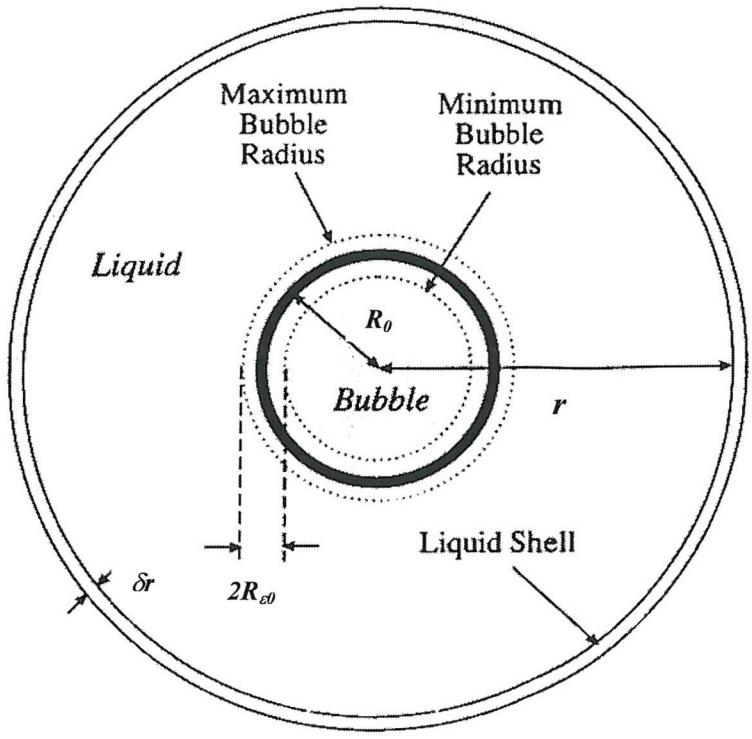

Figure 1.9 Bubble of radius R_0 surrounded by concentric shells of liquid, of which one of these having radius r and thickness δr. The bubble is executing small linear oscillations of amplitude $R_{\varepsilon 0}$. Reproduced from Leighton.[24]

The resonant frequency[24] of the bubble (ω_0) is defined by equation 1.9. The derivation of this equation was undertaken using the conservation of energy principle and assuming the effect of viscosity and surface tension is negligible. The effect of heat conduction from the bubble is incorporated through the use of the polytropic index (κ). The other terms of the equation are p_0, which is hydrostatic pressure and ρ is density of the liquid.

$$\omega_0 = \frac{1}{R_0}\sqrt{\frac{3\kappa p_0}{\rho}} \tag{1.9}$$

Equation 1.9 was first derived in adiabatic form by Minnaert,[64] who similarly assumed surface tension was negligible. The assumption of negligible heat flow (adiabatic conditions) has been shown to be a good approximation for large freely oscillating bubbles.[65,66] The Minnaert resonance frequency is defined by equation 1.10:

$$\omega_M = \frac{1}{R_0}\sqrt{\frac{3\gamma p_0}{\rho}} \tag{1.10}$$

where, γ is the adiabatic constant. Thus $\omega_M \sim \omega_0$ when surface tension and heat conduction are negligible. For air bubbles in water less than 1 atmosphere, equation 1.10 reduces to equation 1.11:

$$\upsilon_0 R_0 \approx \quad 3 \text{ m s}^{-1} \tag{1.11}$$

where $\upsilon_0 = \omega_0/2\pi$ is the linear frequency of bubble pulsations. Thus bubbles of radii larger than 100 μm will exhibit resonant frequencies in the audio range. This is particularly evident in the case of a liquid dripping from a tap and impacting upon a water surface. The characteristic 'plopping' noise is not due to the initial impact pulse but instead emanates from bubbles, which are entrained, just after the drop impacts on the water's surface, and ring at their natural frequencies.[24] The previous analysis assumed that the bubble behaved as an unforced linear system. However, in the presence of sound field of pressure amplitude (P_A) and driving frequency (ω) (assuming that the vapour pressure is negligible and that the bubble is undergoing small amplitude variations) the bubble radius can be expressed by equation 1.8 where $R_\varepsilon << R_0$. In this case the resonant frequency of a bubble can be expressed by equation 1.12:

$$\omega_0 = \frac{1}{R_0\sqrt{\rho}}\sqrt{3\kappa(p_0 + \frac{2\sigma}{R}) - \frac{2\sigma}{R} - \frac{4\mu^2}{\rho R_0^2}} \tag{1.12}$$

where σ is surface tension and μ is dynamic viscosity. This equation is produced by a small amplitude linearised approximation of the Rayleigh Plesset[67] equation. If both viscosity and surface tension forces are negligible equation 1.12 reduces to equation 1.9. This section discussed the background theory behind the pulsating bubble. The next section introduces the theory behind subharmonic Faraday wave motion.

1.6 Subharmonic Faraday Wave Motion

According to Neppiras[68] there are three possible mechanisms for direct subharmonic bubble motion occurring. The first was based on the work of Eller and Flynn.[69] They theorised that the subharmonic motion was due to non-linear oscillations of the bubble's volumetric pulsations. However, the minimum threshold pressure for the onset of this effect occurred when the frequency was twice the resonance frequency of the bubble.

Lauterborn[70] derived the second mechanism, which was again based on non-linear volumetric pulsations of the bubble. Lauterborn[70] suggested that the system became more chaotic as it was driven harder. This state of chaos was reached after a series of bifurcations, the first that resulted in period doubling. However, it was later discovered[2] that the threshold pressure for subharmonic emission by these effects, was *ca.* 10^5 Pa for bubbles resonant at several kHz. The third mechanism involved the onset of the surface wave described previously which was first noted by Faraday.[71] He was the first to notice these waves occurred at $\omega/2$ on the surface of a water column which was vertically vibrated water at frequency ω. These 'Faraday waves' are known to occur when the amplitude of oscillation of the liquid/gas interface exceeds a threshold value.[2]

Results from Hullin[72] provided the first experimental proof that surface waves were a viable source of subharmonic response of a stable bubble. Hullin[72] used an optical-electrical method to measure the amplitude of surface waves on pulsating gas bubbles in liquids. The experimental set-up evaluated the critical amplitude above which surface waves were spontaneously created on bubbles resonant in the range 2 to 15 kHz. For example, a 0.9 mm radius bubble in water driven at its resonance frequency of approximately 3650 Hz was measured as having a threshold displacement amplitude of 2.7 μm. Also by stroboscopic illumination it was shown that the surface deformed at exactly half the excitation frequency, and so the wave, which was stimulated, was of subharmonic character.

Phelps and Leighton[2,73] calculated the onset threshold pressure for these Faraday waves on a plane surface and correlated this with the threshold pressure amplitude for the onset of subharmonic motion measured experimentally for bubbles resonant between 2 and 3.2 kHz. The theoretical onset threshold pressure (P_A) for surface waves calculated from the plane-surface theory is given as follows:

$$P_A = \frac{6\mu\gamma p_0 d_{tot}}{R_0}\sqrt[3]{\frac{2}{\omega\sigma\rho^2}} \qquad (1.13)$$

where ω is the driving frequency. Figure 1.10 shows the correlation between the experimental data and theoretical data as obtained by Leighton *et al.*.[2,73] There was a slight offset between the theory and experimental data because of the plane surface approximation.

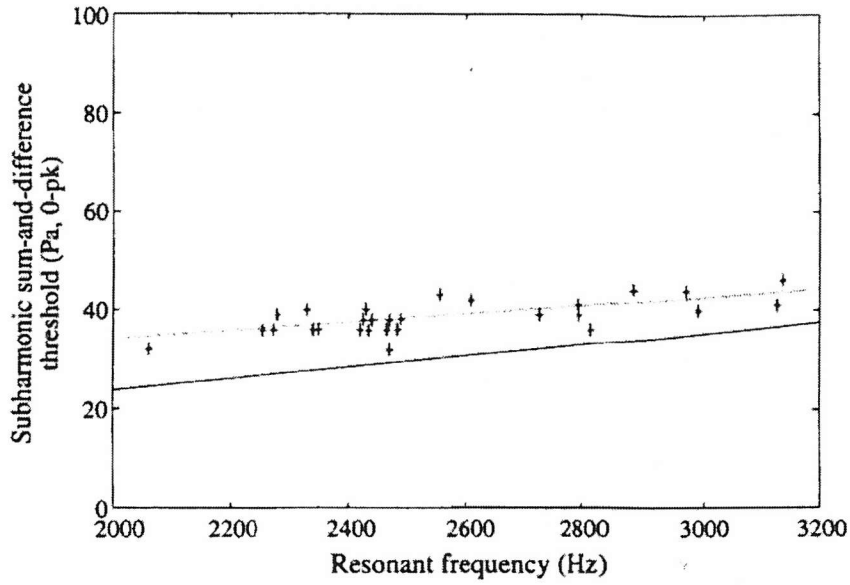

Fig 1.10 Plot showing the thresholds for subharmonic excitation for various bubble sizes at 15 cm depth (+), and their line of regression (upper). The plot additionally shows the surface wave onset threshold (lower) pressure calculated from the plane-surface theory. Reproduced from Leighton *et al.*.[73]

This theory was extended further to investigate the generation of surface waves on a spherical cavity.[74] The normalised theoretical wall displacement amplitude (C_t) to generate these surface waves was first devised by Francescutto and Nabergoj[51] and is given by equation 1.14 below:

$$C_t = [\frac{(a_1 - 1)^2 + 4p}{(-1.5a_1 + 2p + 2(n + 0.5))^2 + q^2}]^{0.5} \tag{1.14}$$

where n is the integer number of the particular mode being stimulated and

$$a_1 = \frac{4(n-1)(n+1)(n+2)\sigma}{\rho\omega^2 R_0^{\ 3}} \tag{1.15}$$

$$p = [\frac{(2(n+2)(2n+1)\mu}{\rho\omega R_0^{\ 2}}]^2 \tag{1.16}$$

$$q = \frac{6(n+2)\mu}{\rho\omega R_0^{\ 2}} \tag{1.17}.$$

As part of this thesis project, this was modified by Birkin, Watson and Leighton[75] to accommodate the desired theoretical threshold pressure (P_T) for the onset of surface waves on a spherical cavity:

$$P_T = R_0{}^2 \rho C_t [(\omega^2 - \omega_0{}^2)^2 + (\omega^2 d_{tot})^2]^{1/2} \qquad (1.18)$$

where C_t is the normalised theoretical wall displacement amplitude for surface waves. This will be correlated with experimental data for the onset of subharmonic motion and will be discussed later in the thesis (see chapter 5).

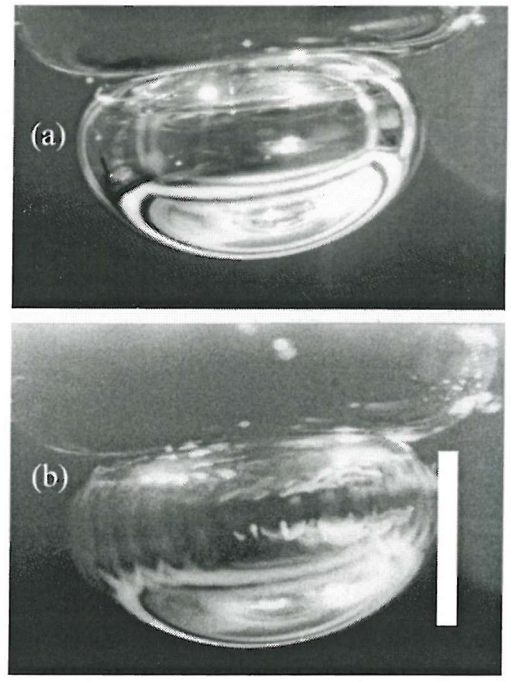

Figure 1.11 (a) Illustrates a bubble held under buoyancy forces under a glass rod in the absence of acoustic driving while (b) illustrates a bubble in the presence of acoustic driving showing the presence of Faraday waves.[76] Scale bar represents 2 mm.

Faraday waves can be visually observed by varying the driving frequency until the bubble begins to 'shimmer'. Figure 1.11 (a) illustrates a bubble in the absence of acoustic excitation while figure 1.11 (b) illustrates a bubble in the presence of acoustic excitation showing the presence of Faraday waves. This figure shows that visual shimmering can occur when the surface waves are excited on a bubble held against buoyancy forces on a glass rod. However, as well as this optical effect, bubbles that oscillate in this manner can interact with sound in a variety of ways. This interaction and its consequences will now be discussed.

1.7 Detection of Faraday Waves employing a Combination Frequency Technique

Numerous acoustic techniques exist which are capable of detecting the resonant bubble pulsation or breathing mode.[19-22] These techniques are based on the principle that the bubble scatters maximally when the applied field is tuned to the bubble resonance (see figure 1.12 (a)). One might expect the relative amplitude of Faraday waves in comparison to breathing modes (*e.g.* 1 μm compared to 100 μm) would result in enhanced acoustic emission. However, although the amplitude of wall motion associated with Faraday waves exceeds that due to bubble pulsation by several orders of magnitude,[25] the acoustic emission from the bubble is dominated by the monopole pulsation emission. The subharmonic mutipole acoustic emissions associated with Faraday waves do not propagate to distance and cannot be detected by a hydrophone (see figure 1.12 (b)). This is because when a bubble wall is executing Faraday wave motion the volume of the bubble does not change because the bubble is oscillating subharmonically. Hence the acoustic emission associated with subharmonic Faraday wave motion is very weak.

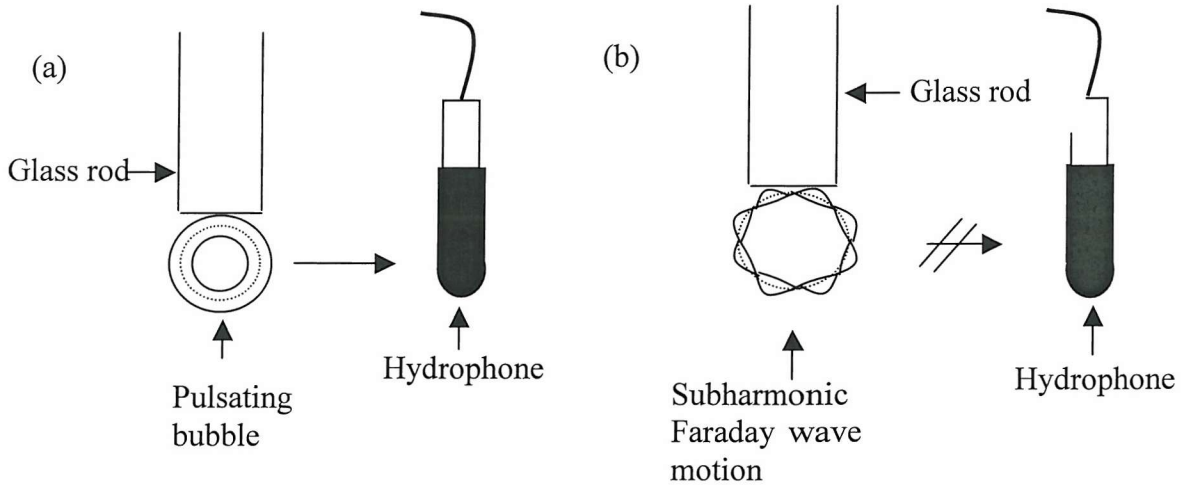

Figure 1.12 (a) Schematic illustrating monopole acoustic emission from a pulsating bubble that propagates to distance and can be detected by a hydrophone. (b) Schematic illustrating multipole acoustic emission associated with Faraday waves that do not propagate to distance and cannot be detected by a hydrophone.

Nevertheless it is possible to detect the Faraday wave by employing an acoustic technique reliant on scattering rather than acoustic emission. Such a system has been developed by Leighton *et al.*[24,73,74,77] and is termed 'combination frequency'.[24,73,74,77] The combination-frequency system is the only acoustic technique, that has been successful in detecting Faraday waves. The experimental set-up is illustrated in figure 1.13. The procedure involves two sound fields that are specifically directed at the bubble, one which is

driven at the bubble resonance of frequency ω (see figure 1.13 T_a) and the other is the scatter of the high frequency 'imaging' field of frequency ω_i (see figure 1.13 T_b). The motion of the bubble wall modulates the scattered imaging signal at the frequency of the relevant wall motion (ω for the pulsation and $\omega/2$ for the Faraday waves).

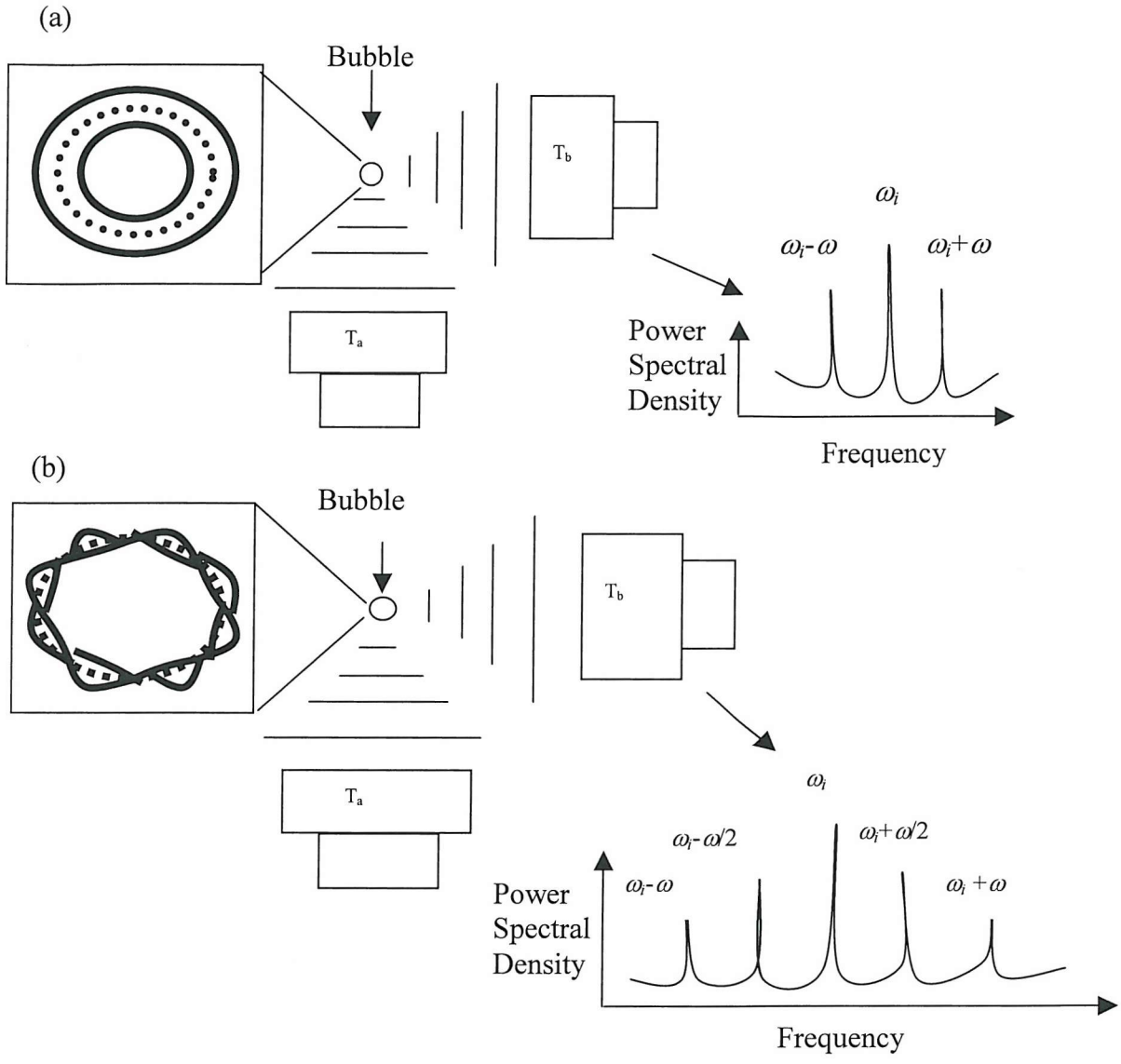

Figure 1.13 Schematics of the experimental set-up for detecting the breathing mode (a) and Faraday waves (b) using the combination-frequency technique. T_a applies the resonant driving signal (ω) while T_b applies a high frequency (ω_i). The schematics also include images of the resultant signals obtained and blown up versions of the bubble oscillating fundamentally (a) and subharmonically (b).

If the bubble is only oscillating fundamentally the high frequencies only contain signals at ω_i and $\omega_i \pm \omega$ (see figure 1.13 (a)). However, if the amplitude of the driving pressure is sufficient to generate surface waves, the high frequencies will contain additional signals at $\omega_i \pm \omega/2$ (see figure 1.13 (b)). In addition figure 1.13 illustrates the resultant signals obtained in both cases.

This method is insensitive to the presence of large off-resonance bubbles because it can differentiate between geometric scattering and resonant scattering.[78] The detection of these signals has provided the most precise means of sizing bubbles.

Although the combination frequency technique is very successful at determining bubble size and populations, it is very equipment intensive. This thesis introduces, for the first time, a new way of detecting the onset of surface waves on bubble walls, by examining the effect of the bubble wall motion on the electrochemistry at a nearby microelectrode.

1.8 Faraday Wave and Breathing Mode Detection and Electrochemistry

When a gas bubble in a liquid is driven into oscillation, a departure from spherical shape can be observed on account of surface waves. This can be observed visually on figure 1.14. These waves have been detected acoustically using a combination-frequency technique (see previous section 1.7).

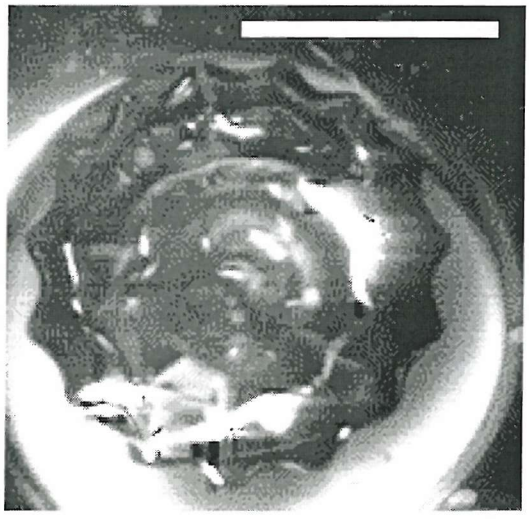

Figure 1.14 Image taken from underneath a bubble held against buoyancy forces on a glass rod representing the non-spherical bubble due to the presence of surface waves. Scale bar represents 3 mm.

A number of electrochemical studies report mass transfer enhancements due to the motion of a bubble under buoyancy forces alone.[5,15] However, when a bubble is driven into oscillation in a liquid both the breathing mode and surface waves can move the liquid phase of the media to a greater or lesser extent. The contribution to mass transfer to an electrode as a result of bubble oscillation can be described as a measure of microstreaming.

Microstreaming arises from the frictional forces between a boundary and a medium carrying vibrations of circular motion.[24] It is confined to a restricted volume near a sound

source. Mass transfer enhancement brought about by microstreaming (bubble oscillation) is one of many mechanisms thought to be responsible for the extreme mass transfer rates detected in the presence of cavitation. However, no direct electrochemical evidence has been presented which isolates this individual effect. It should be possible to characterise the frequency of mass transfer fluctuations due to an oscillating bubble in terms of subharmonic motion and fundamental motion electrochemically and determine mass transfer rates. This will be demonstrated later on in chapter five of the thesis.

The previous sections discussed how the interaction of a bubble with sound could induce a number of oscillations of the bubble wall. Prior to achieving steady state surface wave motion there is a ring-up period. Whilst steady state behaviour of bubbles has been studied by Phelps and Leighton[2,73] and Francescutto and Nabergoj,[51] understanding of this ring-up behaviour is at a very early stage.

1.9 Ring-up Time of Surface Waves and the Breathing Mode.

Recently, Ramble *et al*[74] have discovered that there exists a significant difference in the transient times taken to establish steady-state subharmonic and fundamental combination frequency signals (the so-called 'ring-up' times).

Further work has been undertaken by Maksimov and Leighton,[79] to determine theoretical values for these ring-up times. The theory explains the significant difference in the ring-up times of the surface and breathing modes, which have been experimentally observed using the combination-frequency technique. Their suggested explanation is based on the fact that the observed discrepancy takes place near the threshold for the excitation of distortion modes, where the growth of an instability is very slow. Consequently this leads to a very long duration transient interval while establishing steady state surface oscillations.

Although Maksimov and Leighton[79] have developed a theory no experimental evidence against which to test this theory exists. This was one of the aims of this thesis. Electrochemical experiments were undertaken in an effort to validate their theory (see chapter 7).

While bubble motion is important, understanding bubble growth by the process of rectified diffusion[80-83] is another basic fundamental phenomenon associated with motion of the bubble wall. This process is detected employing the acousto-electrochemical technique developed in this thesis (see chapter 9).

1.10 Rectified Diffusion

Gas bubbles in an acoustic field under the correct physical conditions will grow by the process known as rectified diffusion.[80-83] This process comes about through the active pumping of gas, initially dissolved in the liquid, into the bubble, using the energy of the sound field. Two elements contribute to the description of the process: an 'area effect' and a 'diffusion field effect'. These have been extensively discussed by Leighton.[24] The following explanations are based on the material of Leighton.[24]

Area Effect

When the radius of the bubble is less than the equilibrium radius (R_0) the pressure of the gas inside the bubble is greater than at equilibrium. As a result the gas diffuses out into the liquid. Conversely if the bubble radius is greater than its equilibrium value the internal gas pressure is less than at equilibrium. Consequently the gas diffuses from the liquid into the bubble interior. During the compressed and expanded states of the bubble the net flow of gas is not equal, because the area of the bubble wall is greater in the latter case than the former. Therefore, over a period of time, there will be an overall net influx of gas from the liquid to the bubble interior. A schematic of the process is illustrated in figure 1.15 where R is the instantaneous bubble radius, R_0 is the equilibrium bubble radius, p_g is the instantaneous gas pressure inside the bubble and $p_{g,e}$, is the equilibrium gas pressure inside the bubble.

$R > R_0$	$R = R_0$	$R < R_0$	$R = R_0$	$R > R_0$
$p_g < p_{g,e}$	$p_g = p_{g,e}$	$p_g > p_{g,e}$	$p_g = p_{g,e}$	$p_g < p_{g,e}$
Gas flow: liquid to bubble	Gas flow: none	Gas flow: bubble to liquid	Gas flow: none	Gas flow: liquid to bubble
Interfacial area large		Interfacial area small		Interfacial area large

Figure 1.15 The 'area effect'. The pressure within a pulsating bubble, and the surface area of transfer (bubble wall), both oscillate about an equilibrium value, causing a flux imbalance. Reproduced with permission from Leighton.[24]

Diffusion Field Effect

The rate of diffusion of a gas in a liquid is dependent on the concentration gradient of dissolved gas and is given by Fick's First law (see equation 1.1 page 2). The concentration gradient will change as the bubble pulsates. Consider the bubble at equilibrium shown in figure 1.16 (a). Two liquid diffusion fields surrounding the bubble are also illustrated. When the bubble is expanded each liquid diffusion field surrounding the bubble contracts (figure 1.16 (b)). According to Henry's law[84] the concentration of dissolved gas close to the bubble wall is reduced, however, the liquid diffusion field is thinner so the gradient across the diffusion field is greater. Therefore the rate of diffusion into the bubble interior is high. Conversely when the bubble is contracted the liquid diffusion fields surrounding the bubble are expanded (figure 1.16 (c)) so the concentration of dissolved gas close to the bubble wall is greater but the concentration gradient across the diffusion field is not as great as when the bubble is expanded. The two factors *i.e.* gas concentration at the bubble wall and diffusion field thickness will work together when the bubble is expanded but against each other when the bubble is contracted. Therefore there is a large concentration gradient driving across a shorter distance in the expanded case and a lesser gradient driving across a longer distance in the contracted case. The former effect being the more dominant.

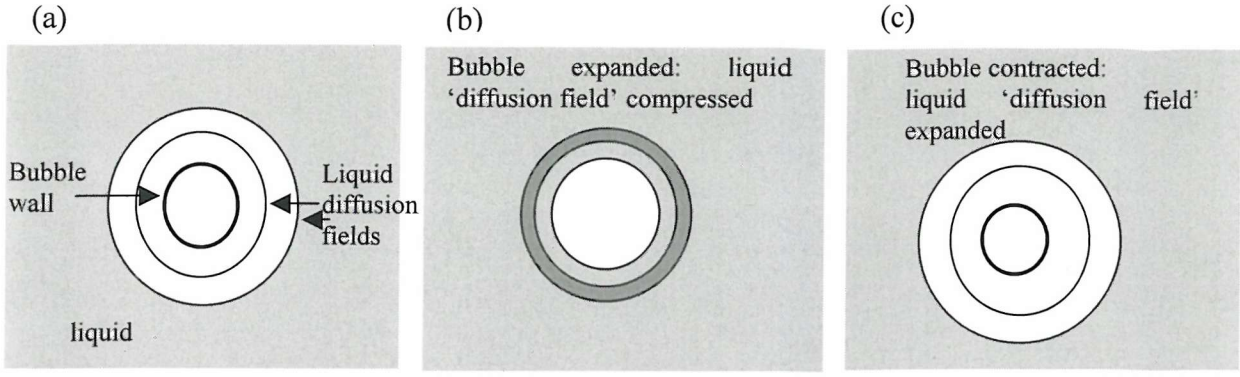

Figure 1.16 The 'diffusion field effect': the bubble and two of the liquid diffusion fields surrounding are shown. (a) The bubble is at equilibrium size. (b) The bubble expands, and the liquid diffusion fields contract. (c) The bubble contracts and the liquid diffusion fields expand. Reproduced by permission from Leighton.[24]

Therefore both the area in the expansions and contractions and the diffusion rate are asymmetrical. Both effects reinforce one another and the combined effects will cause the bubble radius (R_0) to increase.

The rate of growth of a bubble can be categorically predicted in the presence (caused by surface oscillations) and absence of microstreaming. Church[80] devised a theoretical model to predict growth rates in the absence and presence of these phenomena produced by rectified diffusion (see equations 1.19 and 1.20 respectively):

$$\frac{dR_0}{dt} = \frac{DR_gT}{R_0}(p_0 + \frac{4\pi}{3R_0})^{-1}[A + R_0(\frac{B}{\pi Dt})^{1/2}]C_{sn}(\frac{C_i}{C_{sn}} - \frac{A}{B}) \text{ non-microstreaming} \qquad (1.19)$$

$$\frac{dR_0}{dt} = \frac{DR_gT}{R_0}(p_0 + \frac{4\pi}{3R_0})^{-1}[A + R_0(\frac{BU}{\pi DR_0})^{1/2}]C_{sn}(\frac{C_i}{C_{sn}} - \frac{A}{B}) \text{ microstreaming} \qquad (1.20)$$

where, R_g is the universal gas constant, T is temperature, C_i is the concentration in the bulk and U is the streaming velocity. The terms A, B and C_{sn} are given below:

$$A = \frac{1}{T_b}\int_0^{T_b}\frac{R}{R_0}dt = 1 \qquad (1.21)$$

$$B = \frac{1}{T_b}\int_0^{T_b}(\frac{R}{R_0})^4 dt = 1 + 3\{[\frac{P_A}{3p_0}(1 + \frac{4\sigma}{3R_0p_0})^{-1}(1 - \frac{\omega^2}{\omega_0{}^2})^{-1}]^2\}\{1 + \frac{\omega^2}{\omega_0{}^2}\} \qquad (1.22)$$

$$C_{sn} = C_0(1 + 2\sigma / R_0 p_0) \qquad (1.23)$$

where T_b is the period of the pulsating bubble, C_{sn} is the concentration of gas at the bubble wall and C_0 is the saturation concentration of gas in the liquid. Figure 1.17 is a plot illustrating bubble growth rates in a 26.6 kHz field (acoustic pressure = 2 x 10^4 Pa) with and without microstreaming as a function of bubble radius predicted by Church.[80] The experimental results obtained by Eller[82] are also plotted. The local maxima at 37 μm and 56 μm represent the third and second harmonic resonance responses respectively.

As predicted by Church[80] the growth rates are enhanced in the presence of microstreaming. For a bubble with $R_0 < 35$ μm the experimental data fits with the model of no microstreaming. However, above this size, the data fits with the model predicted for microstreaming.

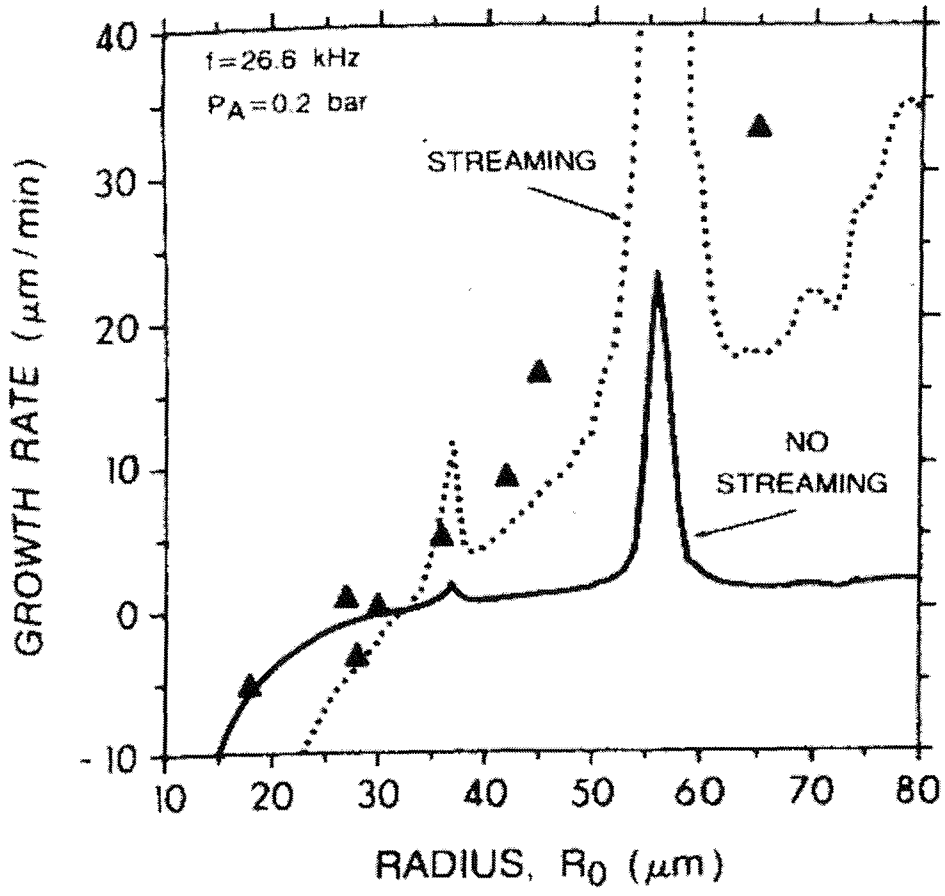

Figure 1.17 Bubble growth rates at 26.6 kHz and 2 X 10^4 Pa. (▲) represents data from Eller[82] and the solid line (—) and dotted line (....) represent rates predicted by Church[80] without streaming and with streaming respectively. Reproduced from Church.[80]

Microstreaming occurs in the presence of surface waves[24] and in this particular sound field these waves are generated when R_0 is greater than 35 μm. The effect of

microstreaming is to enhance the rate of growth of the bubble.[24] The reason for the increased rate is clear. As a bubble grows by rectified diffusion the gas near the bubble/liquid interface diffuses into the bubble. In the absence of microstreaming the rate is dependent on the conditions outlined above (area and diffusion field effect). As the region around the gas/liquid interface becomes depleted of dissolved gas the rate of growth decreases. However, in the case of microstreaming (*i.e.* the presence of surface waves) gas will tend to flow from farther out in the bulk solution caused by a convective flow of solution induced by the motion of these surface waves. This convective flow effectively increases the mass transfer to the gas/liquid interface and hence will increase the growth rate of the bubble. The process of microstreaming will continually refresh the region around the bubble wall, giving it a concentration of dissolved gas close to that found in the bulk solution.

The ability to detect surface waves electrochemically and monitor the current close to the bubble wall in the absence of sound irradiation (which can be used as a measurement of bubble wall-electrode distance; see section 1.2 and 3.1) will enable electrochemical detection of rectified diffusion. This is discussed in chapter 9 where comparisons to Church's theory will be undertaken.

It is also possible to envisage that subharmonic surface wave bubble motion would have other useful applications. One such application would be the use of bubble oscillation to provide a suitable AC component to mass transfer to an electrode. In this case detection of trace species may be possible using lock-in techniques. One such example of this application is now discussed.

1.11 Hydrodynamic Modulation Voltammetry

Hydrodynamic modulation voltammetry (HMV)[85] is a technique reliant on a periodic mass transfer oscillation and is capable of detecting low concentrations of species in solution.

In HMV a potential is applied to a working electrode, in most cases to bring about the transport-limited detection of an analyte. At the same time, the mass transfer rate to the electrode surface is oscillated by either varying the solution flow rate over a static electrode or by modulating the motion of an electrode with respect to the solution. Subsequent extraction of the alternating current (AC) component of the signal enables mass transport controlled processes to be separated from those which are not, the so-called background

processes, which include electrode surface reactions, double layer charging and solvent decomposition. In this way, quantitative limiting current measurements can be made for analytes at low concentration where the DC process would be masked by background processes. Using this technique,[85] the detection limit of species is of the order of 10^{-9} mol dm^{-3}. Indeed, concentrations of 5 x 10^{-10} mol dm^{-3} have been detected by Pratt *et al.*[86] using vibrating microwire electrodes.

The AC character of acoustoelectrochemistry has been recognised as a possible alternative to conventional HMV techniques. As an example Dewald *et al.*[87] used pulsed ultrasound to obtain a detection limit of the order of 0.1 μmol dm^{-3}. Coury *et al.*[88] in a similar manner (but using complicated filtering techniques and continuous ultrasound) also produced a detection limit of *ca.* 0.1 μmol dm^{-3}. However, both of these techniques were limited by either the chaotic nature of the cavitation process, or by the mechanical limitation of the equipment. Hence because the oscillation of a bubble could produce a continuous mass transfer modulation of the current detected at an electrode positioned close to the gas/liquid interface, an improvement in the detection limit maybe possible. This idea will be discussed further in chapter 10.

1.12 Objectives

The objectives of this project are to employ electrochemical sensors (microelectrodes) to study the motion of large gas bubbles in liquids driven into oscillation by an acoustic field. The microelectrodes are employed to,

- Detect and assess mass transport across the air/liquid interface.
- Detect the motion of surface waves on the bubble wall.

This thesis introduces a novel acousto-electrochemical technique capable of detecting surface waves and the breathing mode of an oscillating bubble.

To illustrate the method used to achieve these objectives this thesis is divided into 10 chapters. Chapter two entitled *Experimental Techniques*, presents the apparatus and techniques developed to investigate bubble dynamics electrochemically.

Chapter 3 is entitled *Static Bubble* and explores the variation in mass transport of species to an electrode surface as the electrode approaches a gas/liquid interface in the absence of sound irradiation. Two processes are explored. In the first case the bubble acts as a shield and hinders diffusion of species to the electrode surface as the bubble wall-microelectrode distance decreases. This can be termed negative feedback in SECM terms. In the second

case the bubble acts as a source of oxygen and there is an increase in current recorded at the microelectrode as the bubble wall-microelectrode distance decreases. The effect of surfactant on this electrode reaction is also examined.

Chapter 4 entitled, *The Dynamic Bubble Wall*, presents the initial electrochemical detection of the oscillating bubble. The variations in mass transfer of species to the electrode surface as the electrode approaches an oscillating bubble is explored for both the reduction of $Fe(CN)_6^{3-}$ and the reduction of oxygen.

In Chapter 5 entitled, *Modes of Oscillation of the Bubble Wall*, the frequencies of mass transfer fluctuations caused by the motion of an oscillating bubble are characterised. The oscillating bubble is found to have two classes of bubble oscillation; the fundamental or breathing mode and a second type of non-symmetric oscillations of which the shape oscillations called Faraday waves are members. Both were detected electrochemically. It must be noted that there are an infinite number of shape oscillations, which are not Faraday waves. A model is developed that determines the threshold pressure for the onset of Faraday waves and a comparison is made with experimental data obtained for the onset of subharmonic motion.

Chapter 6 entitled, *Threshold Pressure versus Surface Tension*, explores the effect of surface tension on the threshold pressure for the onset of Faraday waves. Theoretical, electrochemical and photographic techniques are used to explore this phenomenon.

Chapter 7 entitled, *Ring-up Time of Surface Waves,* presents an exploration into the time it takes for surface waves to rise following insonification.

Chapter 8 entitled, *Rising Bubbles*, presents the first application derived from the electrochemical detection of surface waves. Individual bubbles are detected from a rising stream and Faraday wave motion is detected for an individual rising bubble. This technique could be potentially useful in sizing bubble populations.

Chapter 9 entitled, *Rectified Diffusion*, introduces a second potential application of electrochemical surface wave detection. Bubble growth by the process of rectified diffusion is detected employing electrochemical techniques.

Chapter 10 entitled, *Detecting Trace Species*, discusses a new mode of hydrodynamic voltammetry. In this chapter detection of trace species is possible by locking into the AC current associated with an oscillating bubble.

Finally Chapter 11 entitled, *Conclusions and Future Work*, summarises the amassed insight acquired from using an acousto-electrochemical technique to explore bubble dynamics.

Experimental Techniques

Chapter 2

2.1 Electrodes

Microelectrodes[26,27] were extensively used throughout the course of the project because they have properties suited to the study of bubble motion. The main electrochemical system that was employed consisted of a two-electrode arrangement; a 25 μm diameter Pt working electrode sealed in glass and a silver wire counter/reference electrode. This system was used because the currents recorded were relatively small (*i.e.* in the order of nA) so polarisation effects are not important and in addition parasitic noise is reduced.

In order to study the air/liquid interface between the bubble wall and solution, an L-shaped microelectrode was required. Such an electrode would enable electrochemical monitoring around the 'equator' of the bubble wall. This type of microelectrode was fabricated in two different ways. In the first case an L-shaped glass tube was pulled into a

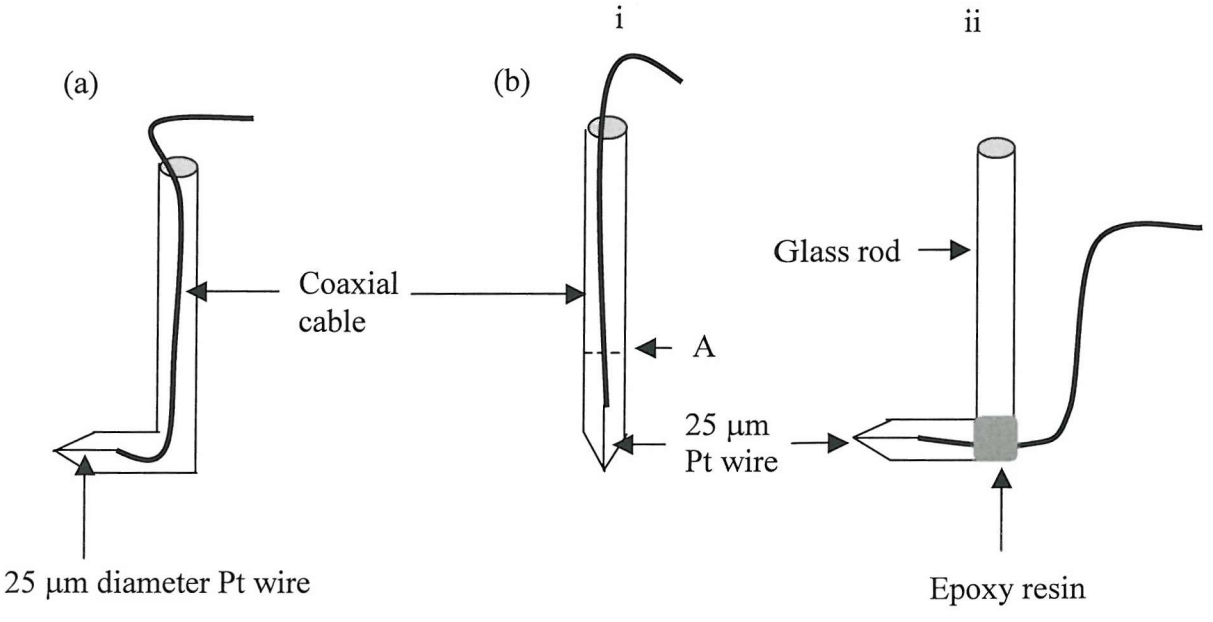

Figure 2.1 Schematics of the microelectrodes fabricated to electrochemically monitor the equator of the bubble wall where (a) represents the electrode fabricated employing the L-shaped capillary and (b) i represents the straight electrode initially constructed and cut at point A before being attached to a glass rod (b) ii.

capillary at one end and the microelectrode was fabricated as previously described.[26] The electrode was then polished and shaped to a point (R_{glass} *ca.* 5 which was determined using an optical microscope) as in conventional SECM practice[42,89] (see section 1.2). A schematic of this electrode is illustrated in figure 2.1 (a). In the second case a straight microelectrode was fabricated, shaped and polished to a point and cut at point A (see figure 2.1 (b) i) using a glasscutter. This was sealed at the top with epoxy resin and then attached to a glass rod at an angle of 90° using epoxy resin (see figure 2.1 (b) ii). In fabricating this electrode the electrical connection was made using coaxial cable to minimise background electrical noise. This fabrication technique was much easier than the former technique for two reasons. First, it was difficult to collapse the glass around the conducting wire when the glass tube was L-shaped. Second, it was much easier to shape the straight electrode to a point of correct R_{glass} value than to shape an L-shaped electrode. However, both techniques were successful in producing robust electrodes suitable for electrochemical monitoring of a gas bubble retained against buoyancy forces within the acoustic cell.

In order to monitor ring-up times for surface waves following irradiation, an L-shaped 0.5 mm diameter Pt macroelectrode was also employed. This type of electrode has a slower response time than a microelectrode (a true 'steady state' is never reached, see section 1.1), therefore an accurate measure of the bubble to electrode distance in the absence of sound irradiation is difficult to achieve. However, the measurement of rise times is simplified because the enhanced current due to bubble oscillation does not suffer from oscillations due to 'bouncing' of the bubble on the solid support. However, there are certain limitations associated with this electrode, which are discussed in detail in Chapter seven.

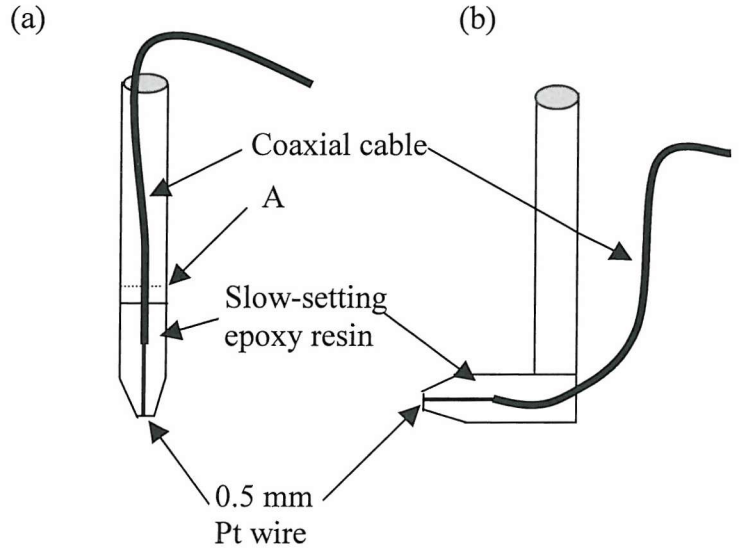

Figure 2.2 A schematic of the electrode constructed to determine ring-up times where (a) represents the straight macroelectrode initially constructed and cut at point A before being attached to a glass rod in (b).

Fabrication of this electrode required a straight glass capillary tube. The capillary tube containing approximately 3 cm of 0.5 mm Pt wire attached to insulating wire (coaxial cable to reduce background electrical noise) was then filled with slow setting epoxy (Struers Epofix). Enough resin was employed to cover the Pt wire and *ca.* 2 cm of the insulated wire. The electrode assembly was then heated to 40° C to prevent air bubbles (see figure 2.2 (a)) and allowed to set over a 24-hour period. The electrode was than cut at point A with a glasscutter and attached to a glass rod at an angle of 90° as described previously (see figure 2.2 (b)). This robust electrode allowed the equator of the bubble to be addressed.

2.2 Cells

Figure 2.3 shows a schematic of the experimental cell used to measure gas exchange reactions at liquid/air interfaces and also detection of bubble oscillations and surface waves. The cell was fabricated from a Mylar speaker and PMMA (polymethyl methacrylate). This enabled sufficient room for a glass rod to support a bubble, a hydrophone, electrodes and visual observation of the phenomena occurring within the cell. Noise on the electrochemical signal was minimised by insulating the electrical connections to the loudspeaker via silicon adhesive and a piece of acetate, which acted as a cap over the connection wires. The glass rod support was constructed with a 'dimple' (1 mm depth and 3 mm diameter). Therefore a single bubble could be isolated and maintained against buoyancy over long periods of time. Air bubbles ranging in radii from 1.5 – 2.5 mm were injected into the solution and tethered to the glass rod using a syringe and U-shaped hypodermic needle.

Figure 2.4 shows a schematic of the cell employed to measure risetimes of surface waves following insonication and rates of rectified diffusion. The cell was fabricated from a Mylar speaker and glass tubing. Bubbles in the radius range 1.5 to 2 mm were tethered to an insulated nickel wire shaped into a ring. The wire was attached to a glass rod at an angle of 90° with masking tape and then glued with quick setting epoxy resin to maintain rigidity. The wire was constructed with a loop at the base in order to sustain a bubble against buoyancy forces for long periods of time. The bubbles were attached to the wire as described previously.

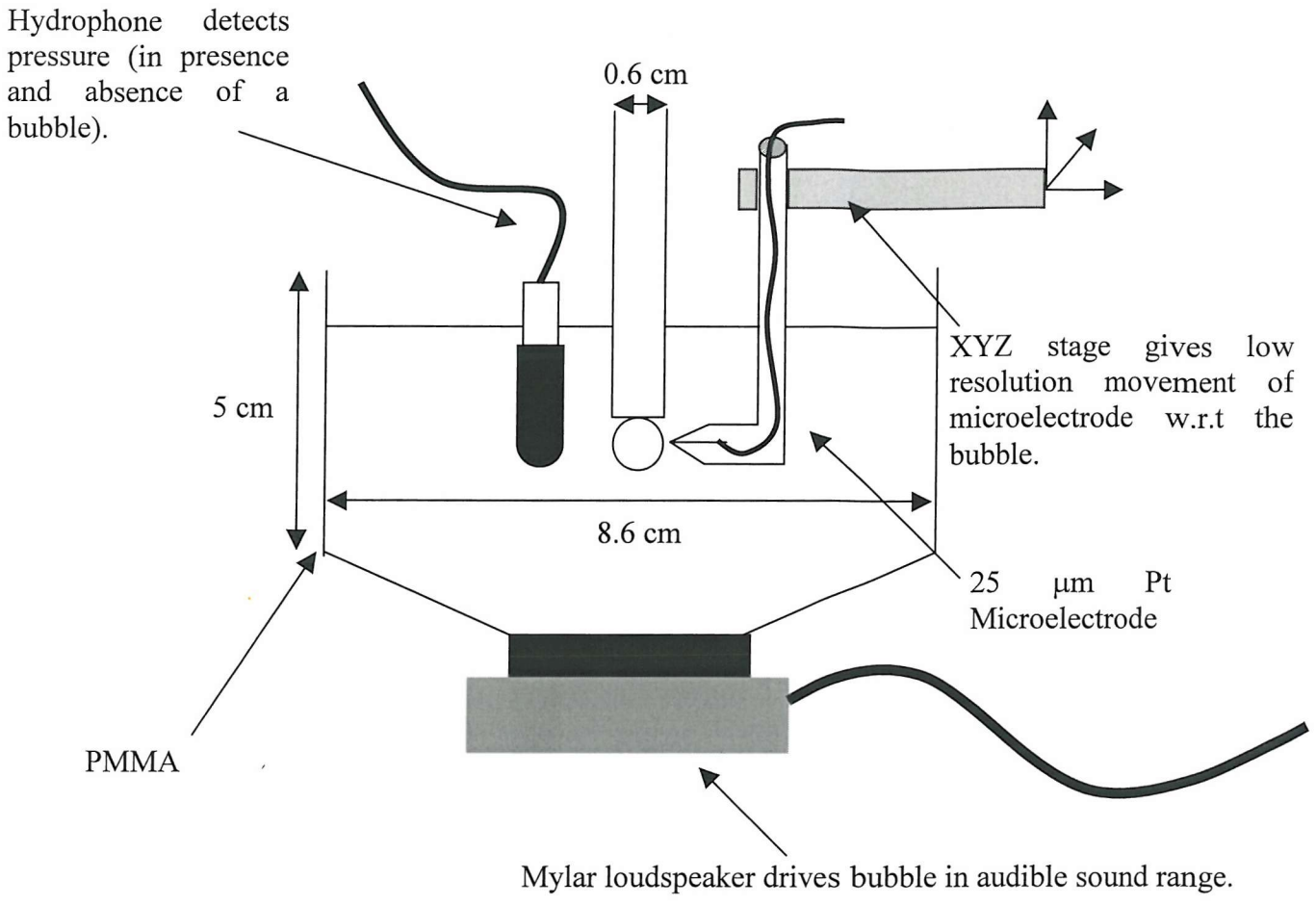

Figure 2.3 Schematic representation of the acousto-electrochemical cell employed to study gas exchange reactions at air/liquid interfaces and surface waves on the bubble wall. The cell was not thermostated. The dimensions of the cell were 8.6 cm x 8.6 cm x 5 cm.

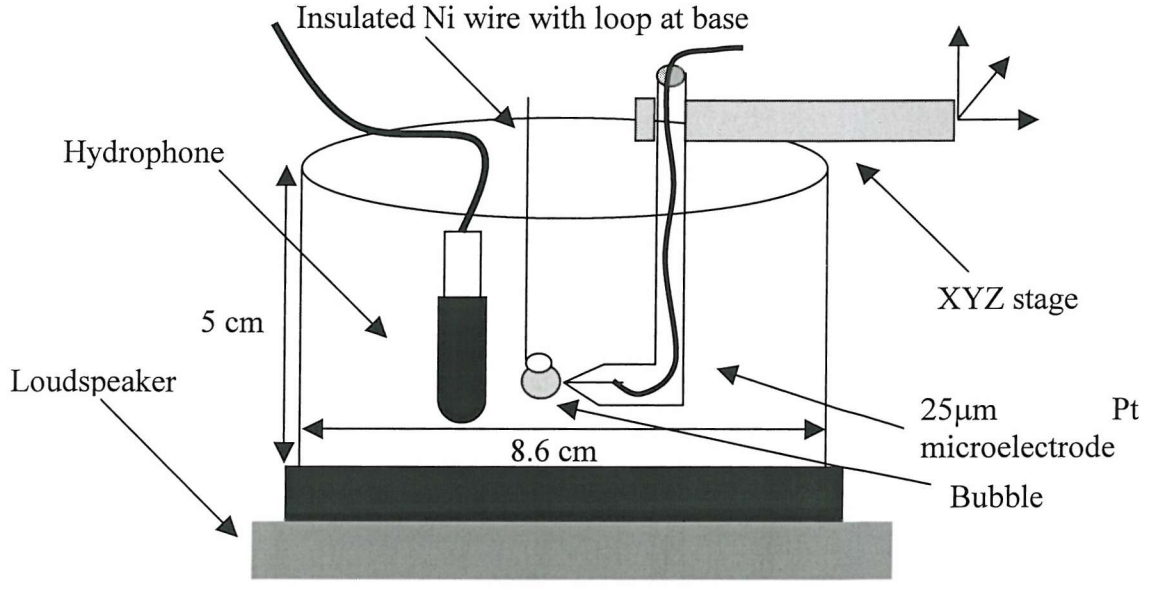

Figure 2.4 Schematic representation of the acousto-electrochemical cell employed to measure risetimes and rectified diffusion. The cell was not thermostated.

Figure 2.5 shows a schematic of the 'fly-by' experimental cell fabricated to detect the motion of bubbles through the cell under buoyancy forces alone. This cell enabled bubble injection using a fibreglass needle at the side and the bubbles travelled upwards towards the electrode surface. The needle was constructed by initially gluing the needle (0.1 mm internal diameter, length 67 mm, World Precision Instruments) to a Teflon plate using fast setting epoxy resin (see figure 2.6 (a)). Once this had set a plastic tube was placed around the needle and was filled with slow setting epoxy resin (Struers Epofix) (see figure 2.6 (b)). After a 24-hour drying period the needle was removed and connected to the side of the cell. Individual air bubbles were passed through the solution by manually pressing down on an air filled syringe attached to the needle. A hydrophone was also incorporated to enable monitoring of the passive acoustic emission that is associated with bubble injection.[90,91] At the top of the cell a 25 μm diameter platinum microelectrode was positioned within the path of the bubbles. The bubbles were driven by a loudspeaker attached to the base.

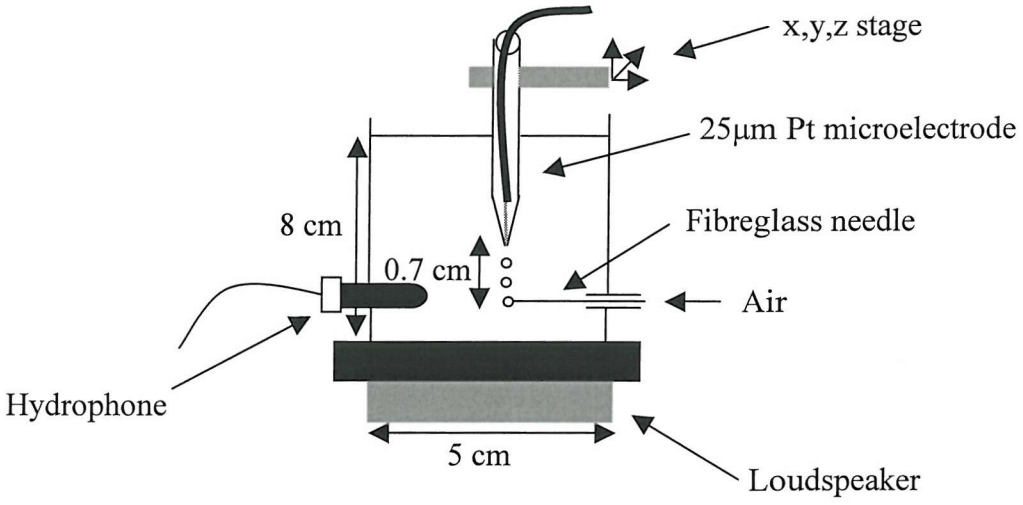

Figure 2.5 Schematic representation of the fly-by cell developed. This cell enabled both the acoustic emission associated with bubble injection to be monitored and additional electrochemical data associated with the motion of the injected bubbles close to the electrode surface.

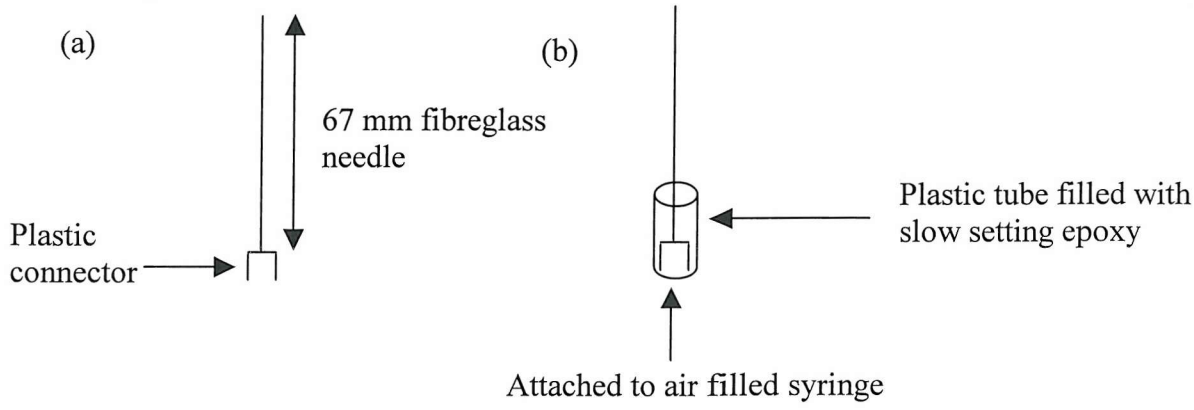

Figure 2.6 A schematic of the system used for bubble injection where (a) represents the initial fibreglass needle and (b) represents the final version of the needle employed for bubble injection.

Figure 2.7 is a schematic of the experimental set-up used to detect low levels of target analytes (see chapter 10). The electrochemical cell employed was as in figure 2.3. The measured current time data and pressure of the sound field recorded employing high temporal resolution equipment were passed through an ADC acquisition card described in the following section. Fast Fourier analysis was undertaken on the data to distinguish between the first harmonic and subharmonic signals. The potential was then varied and the same process repeated.

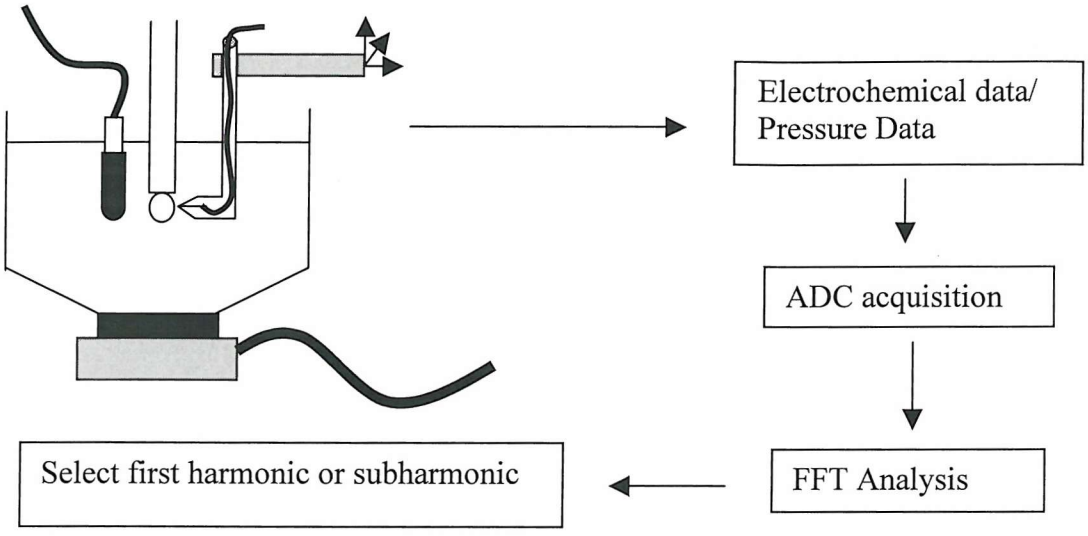

Figure 2.7 Schematic of the electrochemical set-up employed for the detection of low concentrations of target analytes.

2.3 Associated Equipment

A two-electrode arrangement (see section 1.1) was employed in all experiments with a home built current follower enabling both high gain (up to 1 X 10^8 V A^{-1}) and low noise acquisition of the experimental data. An (x, y, z) Newport micrometer and stage, (with 25 mm travel and 20 μm resolution in the z direction and 16 mm travel with 20 μm resolution in the x and y directions) was used to position and move the microelectrode around the cell in order to obtain an accurate idea of the relative position of the microelectrode with respect to the bubble.

The electrochemical data, which required only low temporal resolution, was recorded on a Computer Boards PCI-DAS1602/16 card. The equipment was interfaced to a PC using a HP VEE interface program. The results of experiments requiring higher temporal resolution were recorded using two different techniques. In the first case a Gould 200 Ms/sec, 100 MHz, 465 digital oscillosope was employed. The data obtained was transferred to a PC through an RS 232 cable and commercially available software. In the second case, data was

transferred directly to a PC over a 2 – 3 s period at high sample rates (*e.g.* 50,000 points over 2.5 s) using the Computer Boards PCI-DAS1602/16 card. All Cyclic Voltammograms (CV), current time plots and frequency analysis were performed using in-house written HP VEE software. A TG 101 programmable 10 MHz DDS function generator and a TPA 50 - D power amplifier drove the sound sources. A Bruel and Kjaer hydrophone (type 8103, sensitivity 96 x 10^{-3} pC/Pa), taking real time measurements of the acoustic pressure from the sound source, was connected to an oscilloscope via a BK 2685 charge amplifier. This was used to take pressure readings indicating the strength of the sound field in the solution at a certain frequency and driving voltage. The hydrophone output was recorded as voltage against time. This was transformed to a pressure time trace by equation 2.1:

$$P_A = \frac{V_A}{V_u x 0.1} \qquad (2.1)$$

where P_A is pressure amplitude, V_A is the voltage amplitude of the pressure signal and V_u is the 'voltage/out' setting on the charge amplifier (Bruel and Kjaer 2685).

All electrochemical experiments were performed in a Faraday cage in an effort to reduce electrical noise. The Faraday cage enables small changes in current (due to bubble oscillation) to be measured accurately. In all experiments undertaken, a single bubble was held against buoyancy forces on a glass support. Stray bubbles were removed using a brush. The frequency and pressure ranges employed with this equipment were 1.0 - 2.5 kHz and 10 - 200 Pa respectively. All experiments were performed at room temperature. The solutions employed were not thermostated due to restrictions in space within the cell. Hence a temperature range of 18 – 22 °C is quoted in the subsequent chapters. However it should be noted the experimental results were reproducible over the course of the project. This indicates that temperature variations are not expected to have major significance in the interpretation of the experimental data.

2.4 Scanning Electrochemical Microscopy (SECM)

Scanning electrochemical microscopy is a technique used to investigate reactivity at surfaces immersed in electrolytic solutions on the micrometer scale. In this work the technique is used to explore the variation in current recorded at the microelectrode tip with distance on approaching a bubble wall (approach curves). Both high and low spatial

resolution SECM techniques were employed. In the latter case a Newport micrometer and stage (described in section 2.3) was used, which allowed manual movement of the electrode in the x, y, and z directions in increments of 20 μm. A schematic of this system and the electrochemical cell employed is shown in figures 2.3 and 2.4.

Higher spatial resolution equipment was employed to monitor the current over shorter distances between the bubble wall and microelectrode surface. In this set-up (figure 2.8) the electrode was mounted onto a three dimensional stage (two TS-100 and one TS-300) driven by three piezoelectric Inchworm motors (model IW-710) which were controlled by an X, Y, Z, Inchworm motor controller (model 6200); all from Burleigh Instruments, UK. This particular SECM device is capable of moving the microelectrode within a cube of 25 mm with a nominal resolution of 4 nm.*

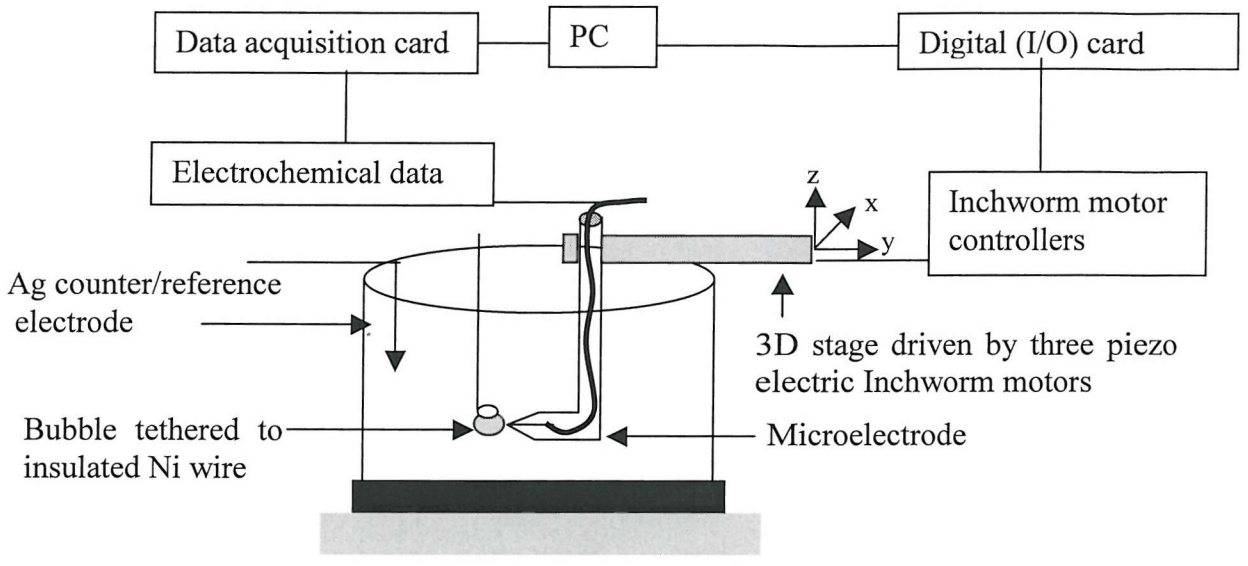

Figure 2.8 Schematic illustrating the experimental set-up used to record high resolution SECM data.

This instrument was completely controlled using a personal computer equipped with two interface cards purchased from Integrated Measurement Systems. A digital input/output (I/O) card (PCL - 724) was used to control inchworm movement and a data acquisition card (PCL - 818L) was used to collect the electrochemical data. The electrochemical cell illustrated in figure 2.4 was employed in this system. Approach curves were obtained by first adjusting the Y Inchworm to approximately 0.25 mm from the bubble wall. The equator of the bubble was then approached and the position of the X and Z Inchworms adjusted until the current signal recorded was hindered by 75 % close to the bubble wall compared to the current recorded in the bulk.

* These experiments were performed on apparatus designed and constructed by Dr G. Denuault.

2.4a SECM and Surfactants

During the course of this work approach curves were obtained in solutions containing varying concentrations of surfactant. In this series of experiments a continuous flow pump (PQ – 12 DC from Greylor, USA) (see figure 2.9) was employed to mix the solution. The solution was stirred for five minutes after each addition of surfactant. The pump was controlled by a DC power supply (Thandar TS30215). The flow rate of the liquid through the pump could be adjusted by adjusting the current manually. The flow rate at a current of 1 A was 0.45 cm^3 s^{-1}. The piping required to pump the solution from the cell into the pump and then back into the cell was Polytetrafluoroethylene (PTFE) (approximately 20 cm, 1.6 mm outside diameter, 0.8 mm internal diameter). The silicon tubing connected to the pump (see figure 2.9) had an outside diameter of 9 mm and internal diameter of 5 mm.

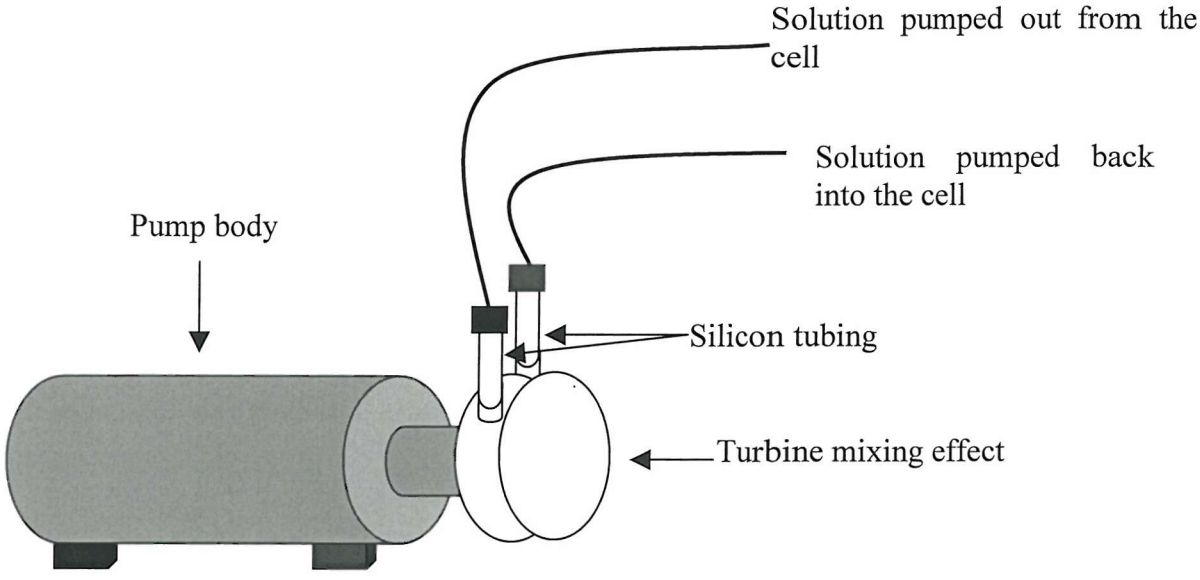

Figure 2.9 Schematic of the continuous flow pump.

2.5 High-Speed Camera

A Kodak HS 4540[§] high-speed video camera was used to record images of bubbles of various radii driven into oscillation or moving under buoyancy forces. A photograph of this camera is illustrated in figure 2.10. This system records at 4,500 frames per second (fps) with a full size picture and up to 40,500 fps with a reduced picture size. The faster the recording speed, above 4500 fps, the smaller the picture becomes until an image the size of

[§] On loan from the EPSRC Instrument pool.

a match box is produced at 40,500 fps. The system will record 3072 full frames, so at 4500 fps, a recording time of 0.66 of a second is available. However, the time increases if the recording rate is slowed down. The resolution of this system is 256 x 256 pixels. A monozoom lens was used to focus the images required.

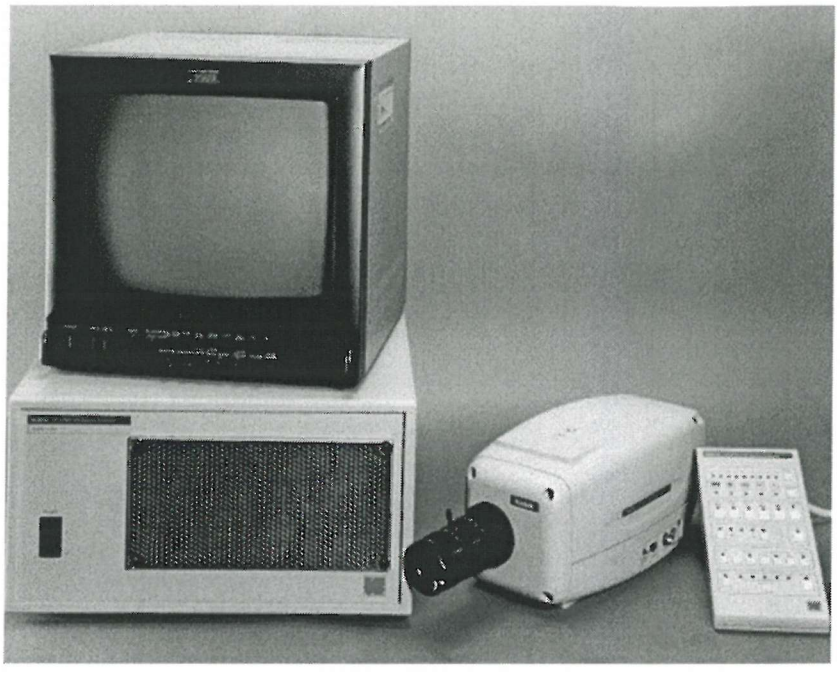

Figure 2.10 A photograph of the Kodak HS 4540 high-speed video camera used to record images of an oscillating bubble.

A schematic of the experimental set-up used to record the pictures is illustrated in figure 2.11. Small mirrors were positioned around the cell to maximise the amount of light entering the cell via a spotlight attached to the video camera. The position of the camera was also adjusted until a clear image was seen on the monitor. Recording rates of 4500, 9000 and 13500 frames per second were used to capture the images. Each individual image was recorded on the video over a longer time period so that blocks of frames could be viewed. Individual frames or groups of frames were transferred to a PC.

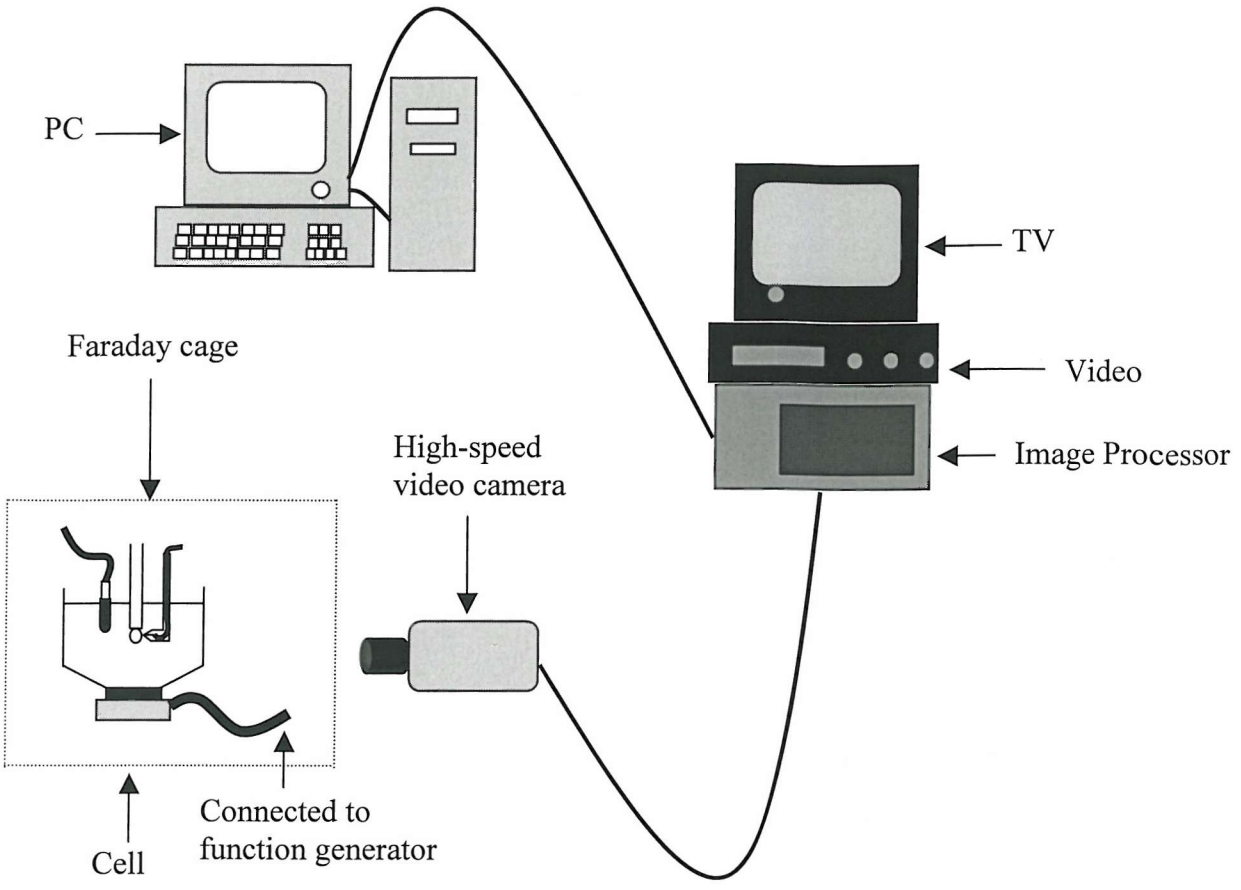

Figure 2.11 Schematic illustrating the experimental set-up employed to photograph an oscillating bubble.

2.6 Chemicals

All solutions were made up from water purified through a Vivendi Purelab Option 10 purification system. Throughout the project, electrochemical reactions were carried out using three different redox couples. The first consisting of a solution of 5 mmol dm^{-3} potassium ferricyanide ($K_3[Fe(CN)_6]$, 99.5% A.C.S. Reagent, Sigma) in 0.2 mol dm^{-3} strontium nitrate ($Sr(NO_3)_2$, 99% A.C.S. Reagent, Aldrich). The electrochemical reaction monitored was as follows:

$$Fe(CN)_6^{3-} + e \rightarrow Fe(CN)_6^{4-} \qquad (2.2).$$

The second consisting of a solution of 0.1 mol dm^{-3} potassium chloride (KCl, BDH, AnalR). The reaction monitored in this case was:

$$O_2 + 4H^+ + 4\,e \rightarrow 2H_2O \qquad (2.3).$$

The third consisting of a solution of 5 mmol dm^{-3} potassium ferrocyanide ($K_4[Fe(CN)_6]$, 99.5% A.C.S. Reagent, Sigma) in 0.2 mol dm^{-3} strontium nitrate ($Sr(NO_3)_2$, 99% A.C.S. Reagent, Aldrich). The electrochemical reaction monitored was as follows:

$$Fe(CN)_6^{4-} \rightarrow Fe(CN)_6^{3-} + e \qquad (2.4).$$

Concentrations of Triton X-100 (Sigma) below the CMC (critical micelles concentration) were also used when investigating surfactant effects.

2.7 Procedures

2.7a Detecting Subharmonic Surface Wave Motion

The experimental set-up in figure 2.3 was employed. The microelectrode was first moved in increments of 20 μm towards the equator of the bubble wall in the absence of sound irradiation. The position of the microelectrode was adjusted via the x, y, z micrometer and stage until the reduction current (when monitoring the reduction of $Fe(CN)_6^{3-}$) was hindered by 75% compared to the current recorded in the bulk. Sound irradiation was commenced and the frequency varied until a maximum in the observed mass transfer enhancement, caused by convective flow of solution due to the motion of the bubble wall, was seen on the HP VEE current time plot. Additionally the current time signal was observed in real time on an oscilloscope. Surface oscillations were noticed as an additional signal (when compared to the background) at $\omega/2$ (where ω is the driving frequency).

2.7b Determining the Onset of Subharmonic Motion

In determining the onset of subharmonic motion a combination of both high temporal (50 kHz) and low temporal resolution (1 Hz) equipment was employed. The bubble was irradiated with sound and the frequency of the sound field was adjusted until a maximum in the observed mass transfer enhancement was seen on the HP VEE current time plot. The frequency was then adjusted to the point where this large mass transfer enhancement was first noticed in comparison to the current time signal recorded in the absence of insonification. At this frequency the current signal on the oscilloscope showed a measurable

component above the noise at half the driving frequency. This is due to subharmonic surface wave motion. The extreme frequencies and pressures at which this motion was initiated were noted.

2.7c Electrochemical determination of the Breathing Mode

In determining the breathing mode of the bubble the electrode was positioned close to the bubble until the current was hindered by 75% in the absence of sound irradiation. The frequency was scanned until the current signal on the oscilloscope showed a frequency component at the same frequency as the driving pressure. Additionally the HP VEE current time plot showed an increase in current in comparison to the current recorded in the absence of sound irradiation. However, the increase in current is less significant than that recorded for Faraday wave motion. This is not surprising considering the amplitude of motion of both modes (see Chapter 1).

2.7d Measuring the Surface Tension of a Liquid

The surface tension of a liquid was determined using a DuNouy Tensiometer (see figure 2.12). To measure surface tension the liquid was placed in a clean container such as an evaporating dish, watch glass or beaker at least 4.5 cm in diameter and then placed on the sample table (see figure 2.12). The entire sample table assembly was raised until the ring was immersed approximately 5 mm into the liquid. The table was lowered until the ring was just below the surface of the liquid and was centred with respect to the container. The liquid was lowered further by means of screw B until the ring was just in the surface of the liquid and the index was approximately on zero. The torsion of the wire was increased by rotating knob A and at the same time the sample table was lowered by means of screw B to keep the index on zero. The index was to be kept on zero even though the surface of the liquid was distended. Adjustment of the knob and the screw simultaneously was continued until the film broke. The scale reading at breaking point on the film was a measure of the surface tension (σ) in mN m^{-1}.

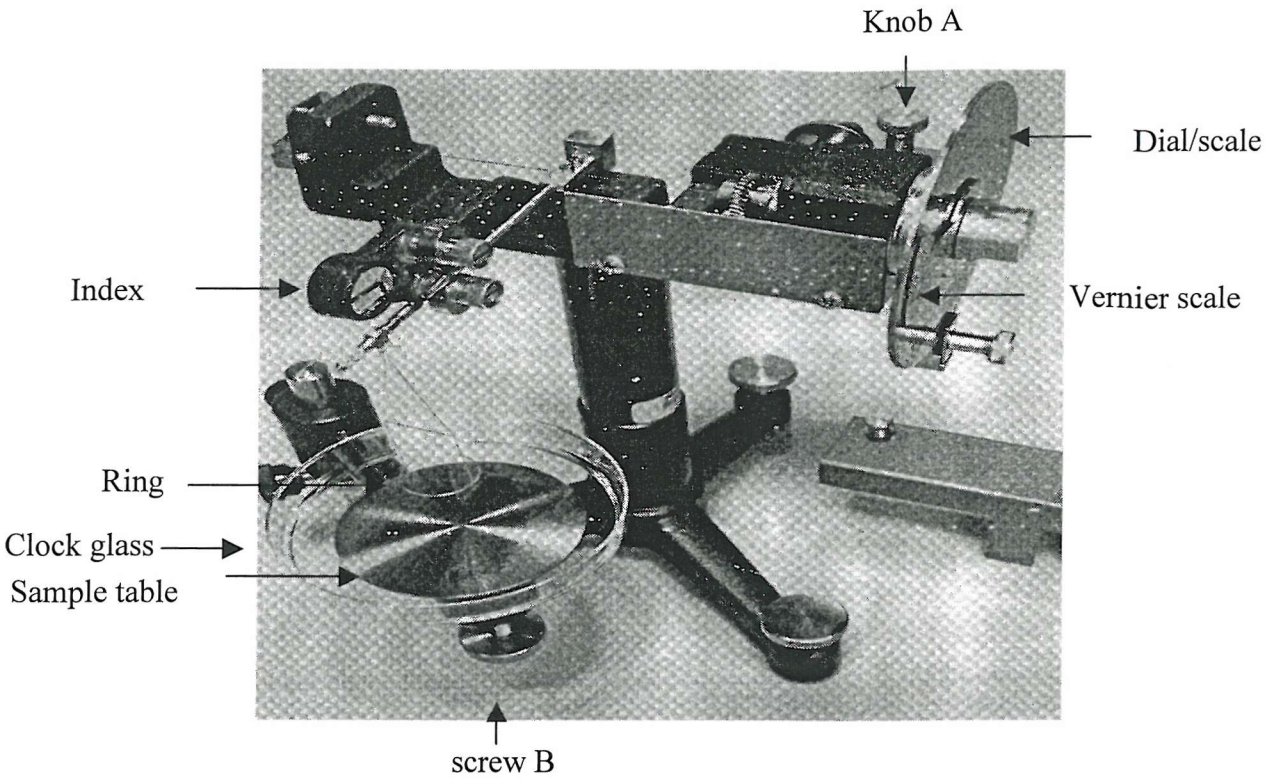

Figure 2.12 Experimental set-up employed to measure surface tension.

2.8 Conclusions

This chapter has presented a description of the experimental equipment and techniques that will be used to investigate the physical and chemical nature of an air/liquid interface and to explore bubble dynamics. Chapter three will characterise the electrochemistry at the gas/liquid interface employing SECM techniques in the absence of sound irradiation. This will be followed by a detailed description of the interaction of sound with a bubble and how this interaction affects the electrochemistry at a nearby microelectrode in chapters 4 -10.

Static Bubble

Chapter 3

3.0 Introduction

This thesis investigates the motion of a gas bubble driven into oscillation by an appropriate acoustic field. The motion itself is measured by an electrochemical technique employing microelectrodes positioned close to the gas/liquid boundary. Before description of these investigations can be undertaken, the study of the effect of the static gas/liquid boundary on the electrochemistry of the systems employed is necessary. In order to characterise this interaction the technique of Scanning Electrochemical Microscopy (SECM) will be employed.

SECM (see section 1.2) has yielded some interesting results with regard to the nature of the gas/liquid interface. In general two types of electrode response can occur on approaching a phase boundary. These have been termed 'positive' and 'negative' feedback depending on whether the current is enhanced or retarded respectively by the interface. Clearly a gas bubble can act as either an inert or active substrate depending on the gas content and electrochemical system employed. In order to illustrate these effects, a number of experiments were undertaken in solutions containing 5 mmol dm^{-3} $Fe(CN)_6^{3-}$ in 0.2 mol dm^{-3} $Sr(NO_3)_2$ and in solutions containing 0.1 mol dm^{-3} KCl. The results of these investigations are now presented.

3.1 Approach Curves

3.1a Reduction of $Fe(CN)_6^{3-}$

The electrochemistry of $Fe(CN)_6^{3-/4-}$ redox couple has been studied under a variety of different conditions. According to Pletcher *et al.*[92] the ionic strength of the media and the nature of the supporting electrolyte can influence the electrode kinetics of this redox system. They showed that the standard rate constant for comparable concentrations of electrolyte

increased along the series $Li^+ < Na^+ < K^+ < Sr^{2+}$. Therefore all experiments were carried out in a solution of $Fe(CN)_6^{3-}$ in 0.2 mol dm^{-3} $Sr(NO_3)_2$ to maintain facile and reproducible electrochemistry.

A Cyclic Voltammogram of a 25 μm diameter Pt microelectrode in 10 mmol dm^{-3} $Fe(CN)_6^{3-}$ was recorded. This is illustrated in figure 3.1. This figure shows that the electrochemistry is well defined due to the extended steady state region below 0 V *vs.* Ag. A series of potential steps from -0.2 V and 0.5 V versus Ag were recorded. These are illustrated in the insert of figure 3.1. This experiment shows that the steady state current recorded under mass transfer limited conditions (-0.2 V *vs.* Ag) was reproducible and stable with respect to time.

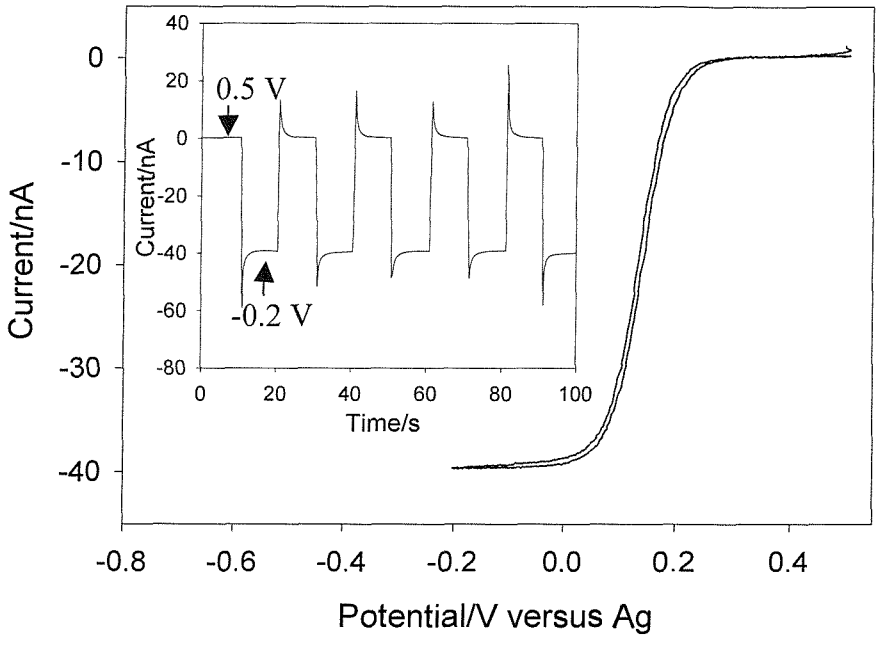

Figure 3.1 Plot showing the cyclic voltammogram recorded at a 25 μm diameter Pt microelectrode at a sweep rate of 10 mV s^{-1}. The anaerobic solution contained 10 mmol dm^{-3} $Fe(CN)_6^{3-}$ in 0.2 mol dm^{-3} $Sr(NO_3)_2$. The temperature of the solution was 18 - 22 °C. The insert in the plot shows a series of potential steps from –0.2 V *vs.* Ag to 0.5 V *vs.* Ag recorded under the same conditions.

In order to investigate the influence of the gas/liquid interface of an air bubble on the electrochemical reduction of the $Fe(CN)_6^{3-}$ redox system, the potential of the microelectrode was held at –0.2 V *vs.* Ag. This corresponded to the mass transfer limited potential for this redox system. The experimental set-up was as in figure 2.3. However, the loudspeaker and hydrophone were not required for this sequence of experiments. An air bubble was retained against buoyancy forces on a glass rod. The microelectrode was moved in increments of 20 μm towards the bubble interface (via an X, Y, Z micrometer and stage) until the steady state current was hindered by *ca.* 50 - 75% when compared to the current recorded under similar

conditions in the bulk of the solution. This reduction in current (termed negative feedback) can be used to predict the distance between the tip of the microelectrode and the bubble wall and can be compared to predictions by Amphlett *et al.*.[49] A reduction in the current of *ca.* 50-75% corresponds to a distance of approximately 5-10 μm between the microelectrode and the bubble wall. The presence of the bubble hindered the diffusion of $Fe(CN)_6^{3-}$ ions to the electrode surface and thus reduced the current recorded at the microelectrode. Figure 3.2 illustrates a schematic of the motion of ions as the microelectrode approaches the bubble wall holding the potential of the electrode at the mass transfer limiting potential for $Fe(CN)_6^{3-}$ reduction. In this case the bubble wall is acting as the inert substrate. It must be also noted that the hindrance in current depends on the R_{glass} (the ratio of the radius of the insulating sheath to the electroactive wire) and can be determined using equation 3.1, which is described in the subsequent section.

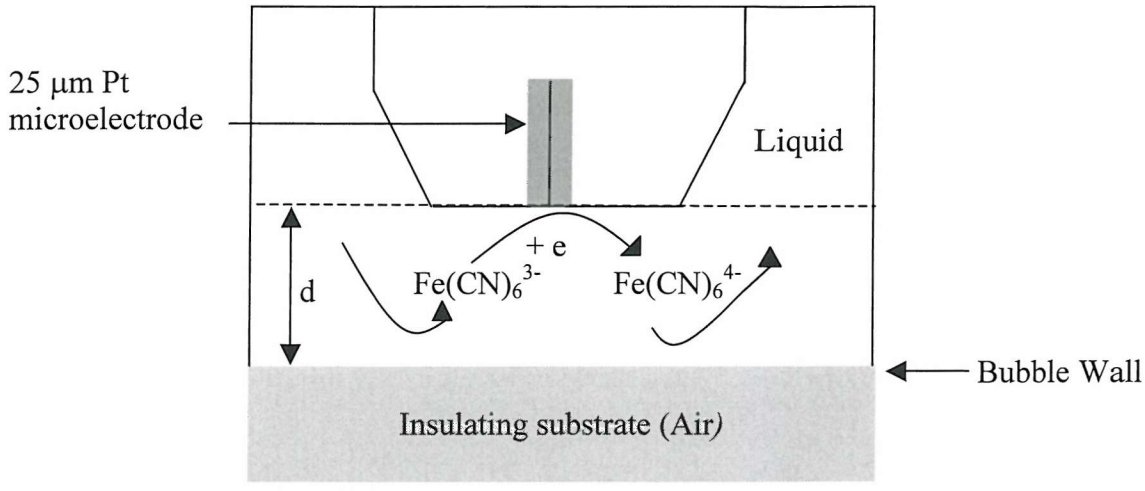

Figure 3.2 Schematic illustrating the motion of $Fe(CN)_6^{3-}$ as a microelectrode approaches an air/liquid interface where *d* represents the microelectrode-bubble wall distance.

The current was plotted as a function of time for each distance moved by the microelectrode towards the bubble. This is illustrated in figure 3.3. Figure 3.3 shows that as the microelectrode approaches the bubble wall, the current drops due to the hindered diffusion of $Fe(CN)_6^{3-}$ to the microelectrode surface caused by the presence of the bubble wall.

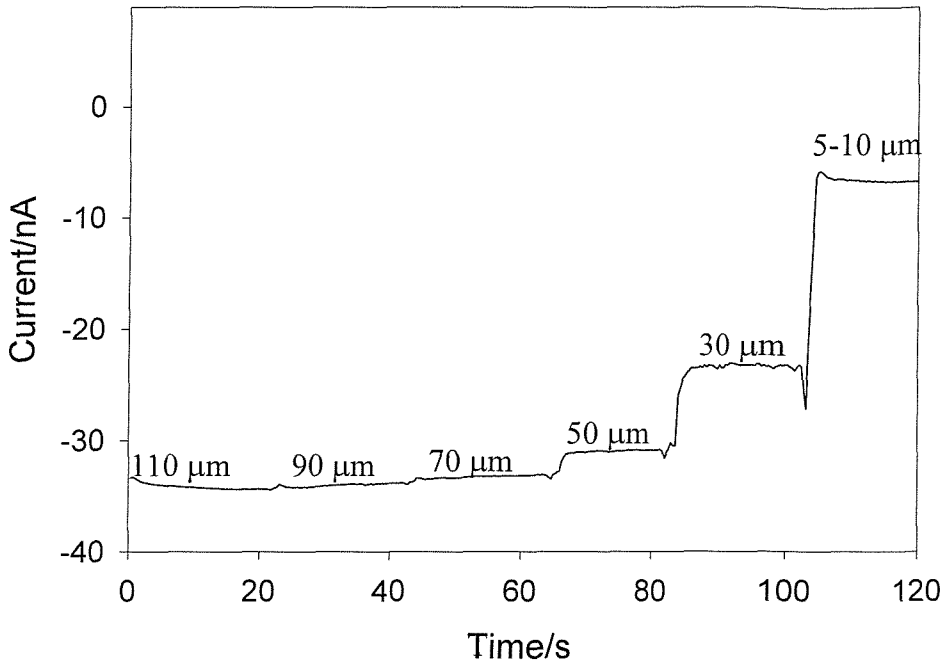

Figure 3.3 Graph of current versus time recorded at a 25 µm diameter Pt microelectrode in 10 mmol dm^{-3} $Fe(CN)_6^{3-}$/0.2 mol dm^{-3} $Sr(NO_3)_2$ on approaching the surface of an air bubble wall (*ca.* 2 mm radius). The potential was held at -0.2 V *vs.* Ag. The electrode was moved in increments of 20 µm every 20 seconds. The distances in the plot represent the approximate distance from the bubble wall (± 5-10 µm). The temperature of the solution was 18 - 22 °C.

Figure 3.4 shows the normalized current (i_{tip}/i_{inf}) (the current recorded at the microelectrode tip divided by the current recorded in the bulk far away from the bubble wall) recorded as a function of normalised distance (d/a) (distance between the bubble wall and microelectrode divided by the microelectrode radius). The solid line represents the current predicted under negative feedback conditions using equation 3.1 as determined by Amphlett and Denuault:[49]

$$\frac{i_{tip}}{i_{\inf}} = \frac{1}{k_1 + \frac{k_2}{L} + k_3 \exp\frac{k_4}{L}} \qquad (3.1)$$

where i_{tip} and i_{inf} represent the tip current at a given tip-substrate distance (d) and in the bulk respectively and k_1, k_2, k_3 and k_4 are constants which depend on R_{glass}. L stands for d/a, the tip-substrate distance divided by the electrode radius. In the experiment in question the value for *Rglass*[49] was taken to be 10.2. Hence, k_1 was 0.40472, k_2 was 1.60185, k_3 was 0.58819 and k_4 was –2.37294.

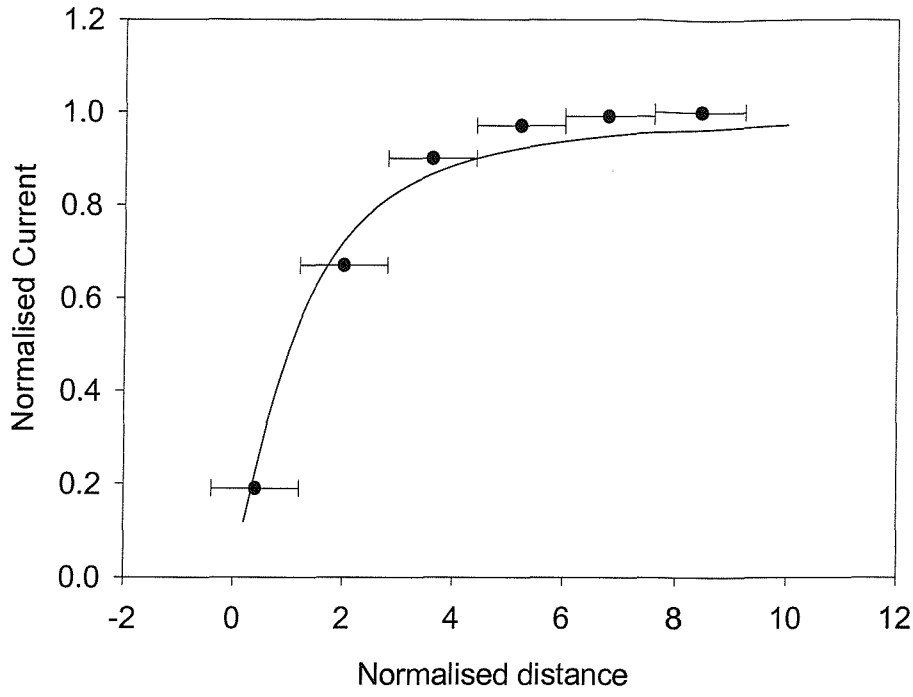

Figure 3.4 Graph of i_{tip}/i_{inf} (normalised current) versus d/a (distance from the air bubble (~ 2 mm radius) wall divided by electrode radius) recorded at a 25 μm diameter Pt microelectrode in 10 mmol dm^{-3} $Fe(CN)_6^{3-}$/0.2 mol dm^{-3} $Sr(NO_3)_2$. The solid line represents the theoretical data obtained from equation 3.1. The temperature of the solution was 18 - 22 °C. The error in the x-axis was ± 10 μm.

The fit between the experimental data and prediction is acceptable considering the resolution of the technique employed *i.e.* the electrode was moved in increments of 20 μm in this case however, it is moved in increments of 1-10 μm in common SECM practice.[42,89] The error in the x-axis was ± 10 μm divided by electrode radius, which in this case was 12.5 μm.

The resolution of the equipment employed (the micrometer and stage (20 μm)) resulted in a 'low resolution' SECM response. Hence to gather further information an experiment was performed employing a high-resolution SECM. The mass transfer limited current for the reduction of $Fe(CN)_6^{3-}$ was monitored as a function of distance. In this technique the electrode was moved in increments of 1 μm. The speed at which the electrode moved could be varied from 1.33 x 10^{-5} mm s^{-1} to 0.7156 mm s^{-1} and the instrument was completely controlled using a computer. The speed employed here was 7.3 x 10^{-3} mm s^{-1}. The position of the electrode was adjusted to approximately 0.25 mm from the bubble wall in the y direction (see section 2.4). The bubble was then approached and the x and z directions adjusted until the current signal recorded at the microelectrode was hindered by *ca.* 75 % to that recorded in the bulk solution. Figure 3.5 is a plot of normalised current (i_{tip}/i_{inf}) against normalised distance (*d/a*). The solid line represents the data obtained employing this high-

resolution technique while the dotted line represents the theoretical prediction employing equation 3.1 as described previously.[49] In this case R_{glass} was taken to be 5.09 employing k_1 as 0.48678, k_2 as 1.17706, k_3 as 0.51241 and k_4 as –2.07873. The fit between theory and experimental data is acceptable considering the difficulty in positioning the microelectrode at a normal with respect to the bubble wall.

This sequence of experiments illustrates how the current recorded at the microelectrode varies as an inert substrate (bubble wall) was approached. The distance between the bubble wall and microelectrode can be easily controlled and is very reproducible. However, as well as acting as an inert substrate, gas transfer can occur across the gas/liquid interface of an air bubble if the potential of the microelectrode is held at a potential sufficient to reduce molecular oxygen. The current versus bubble-microelectrode distance in the presence of oxygen reduction will now be explored.

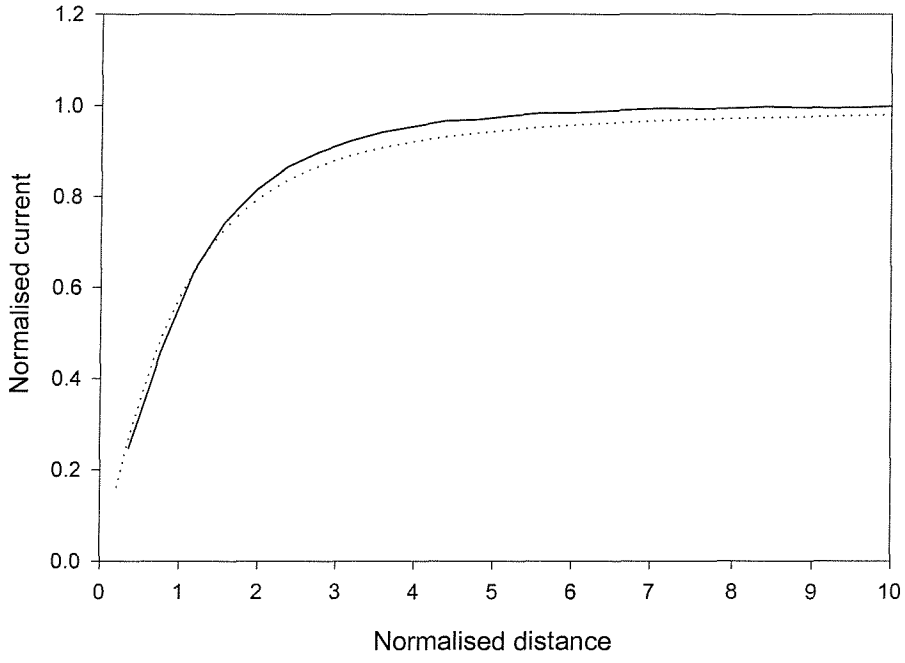

Figure 3.5 Graph of i_{tip}/i_{inf} (normalised current) versus d/a (distance from the air bubble wall divided by electrode radius) recorded at a 25 μm diameter Pt microelectrode in 5 mmol dm^{-3} $Fe(CN)_6^{3-}$/0.2 mol dm^{-3} $Sr(NO_3)_2$. The dotted line represents the theoretical data obtained from equation 3.1. The temperature of the solution was 18 - 22 °C.

3.1b Reduction of Oxygen

The electrochemistry of molecular oxygen reduction has been studied under a variety of conditions. The two electron reduction involves the production of hydrogen peroxide[93,94] (equation 3.2), while the four electron process involves full reduction to water[95] (equation 3.3):

$$O_2 + 2H_2O + 2e \rightarrow 2OH^- + H_2O_2 \quad (3.2)$$

$$O_2 + 4H_2O + 4e \rightarrow 4OH^- + 2H_2O \quad (3.3).$$

All oxygen reduction studies were carried out in 0.1 mol dm^{-3} KCl. Figure 3.6 shows a series of potential steps from –0.7 V (potential where oxygen reduction occurs) to 0.2 V versus Ag. This experiment shows that the steady state current recorded under mass transfer limited conditions (-0.7 V *vs.* Ag) was reproducible and stable with respect to time.

The steady state current recorded was 10 nA in this case and equation 3.4 can used to predict whether the reduction was a 2 or 4 electron process (*i.e.* either whether the reaction proceeded via equation 3.2 or 3.3 respectively):

$$i_{MTL} = 4n_eFaDc \quad (3.4)$$

where all the terms have their usual meanings (see page 4). The value for the number of electrons (n_e) was determined to be 3.77 using a diffusion coefficient (D) of 2.29 x 10^{-5} cm^2s^{-1} and oxygen concentration[96,97] of 0.24 mmol dm^{-3}.

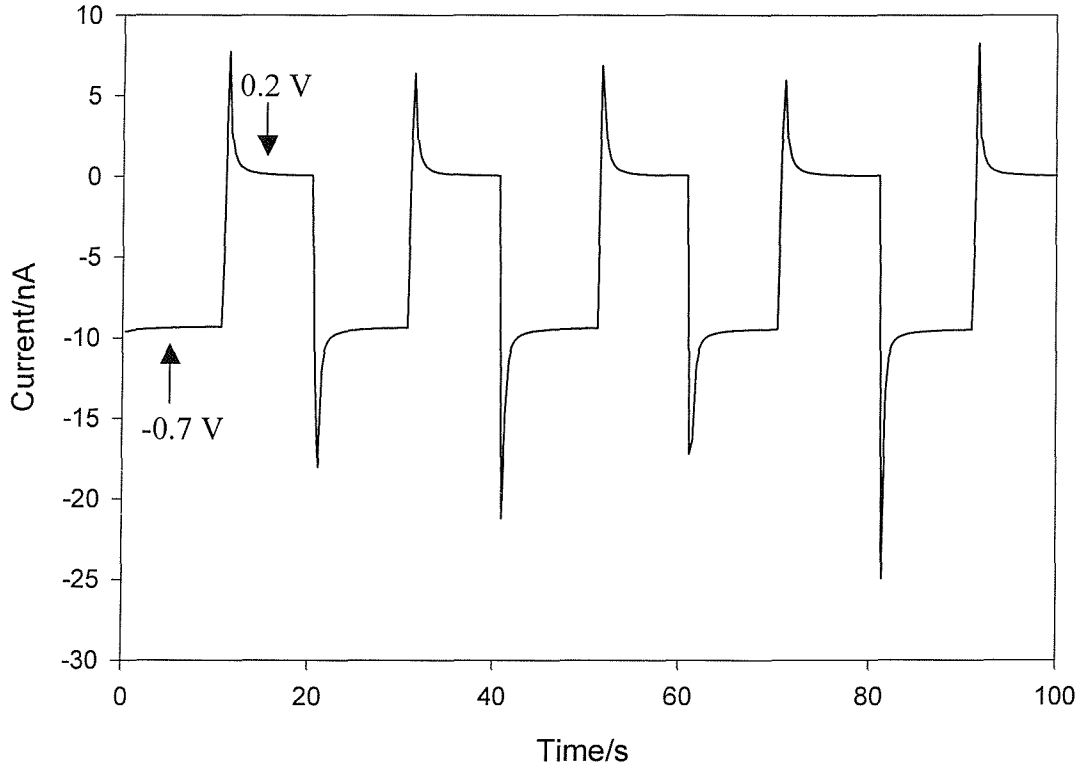

Figure 3.6 Current time plot recorded at a 25 μm diameter Pt microelectrode in 0.1 mol dm^{-3} KCl where the potential was stepped between –0.7 and +0.2 V *vs.* Ag. The temperature of the solution was 18 - 22 °C.

The microelectrode was then held at the potential at which molecular oxygen reduction occurred under mass transfer limited conditions (*i.e.* –0.7 V *vs.* Ag). The experimental set-up was as illustrated in figure 2.3. However, the hydrophone and loudspeaker were not required in this sequence of experiments. An air bubble (*ca.* 2 mm) was retained against buoyancy forces on a glass rod. The microelectrode was moved towards the bubble using the micrometer and stage in increments of 20 μm. The output current was measured as a function of time for each distance travelled (see figure 3.7). However, on examining the oxygen reduction current it was found that there was an increase in current as the air/liquid interface was approached. This suggests that oxygen was transferring across the air/liquid interface of the bubble wall in response to the concentration depletion in the bulk caused by the proximity of the diffusion field created by the microelectrode.

This result coincides with the work of Slevin *et al.*[40] who suggested that reduction of oxygen at a microelectrode creates a depleted region adjacent to the interface between a gas and liquid, and that this provides a thermodynamic driving force for the transfer of oxygen from the air to liquid phase. In the experiment reported by Slevin *et al.*[40] a planar air/liquid interface was created using a Langmuir trough.

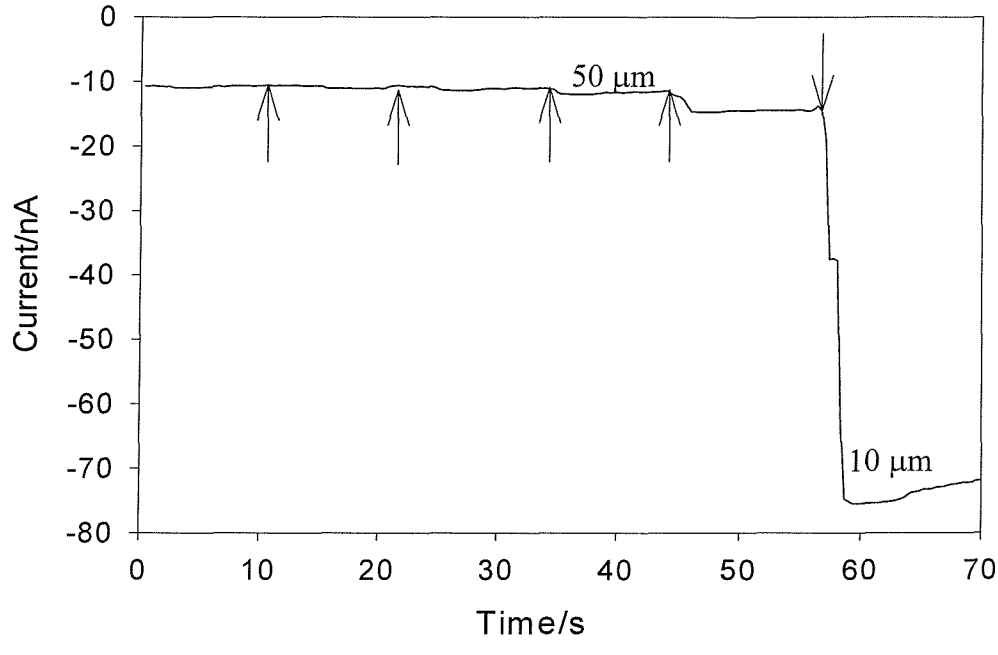

Figure 3.7 Graph of current versus time recorded at a 25 μm diameter Pt microelectrode in 0.1 mol dm^{-3} KCl on approaching the surface of an air bubble wall (*ca.* 2 mm radius). The potential was held at -0.7 V *vs.* Ag. The electrode was moved in increments of 20 μm. The distances in the plot represent the approximate distance from the bubble wall (± 5 - 10 μm). Each arrow on the plot represents the time the microelectrode was moved towards the interface. The temperature of the solution was 18 - 22 °C.

Slevin *et al.*[40] also stated that the rate of oxygen transfer across the interface was dependent on the accessible free area of the interface. The increase in current in figure 3.7, which has a positive feedback appearance,[†] was caused by the replacement of the depleted molecular oxygen from the 'reservoir of the bubble'.

Figure 3.8 is a schematic illustrating the flow of oxygen as the microelectrode approaches the bubble wall. As the microelectrode-bubble wall distance decreases the concentration of molecular oxygen in the bulk liquid becomes exhausted and thus provides a thermodynamic driving force for the transfer of oxygen across the interface. The response obtained from this experiment is akin to that expected for 'positive' feedback conditions (see figure 3.9).

Both processes show an enhancement in current as the electrode-interface distance is reduced. However, the mechanisms causing the increase in current differ. The increase in current recorded at the microelectrode on approaching a conducting substrate in the positive feedback case is caused by the regeneration of the original redox mediator. However, on approaching the gas/liquid interface of a bubble an effective shortening of the diffusion length of the species involved brings about the current enhancement.

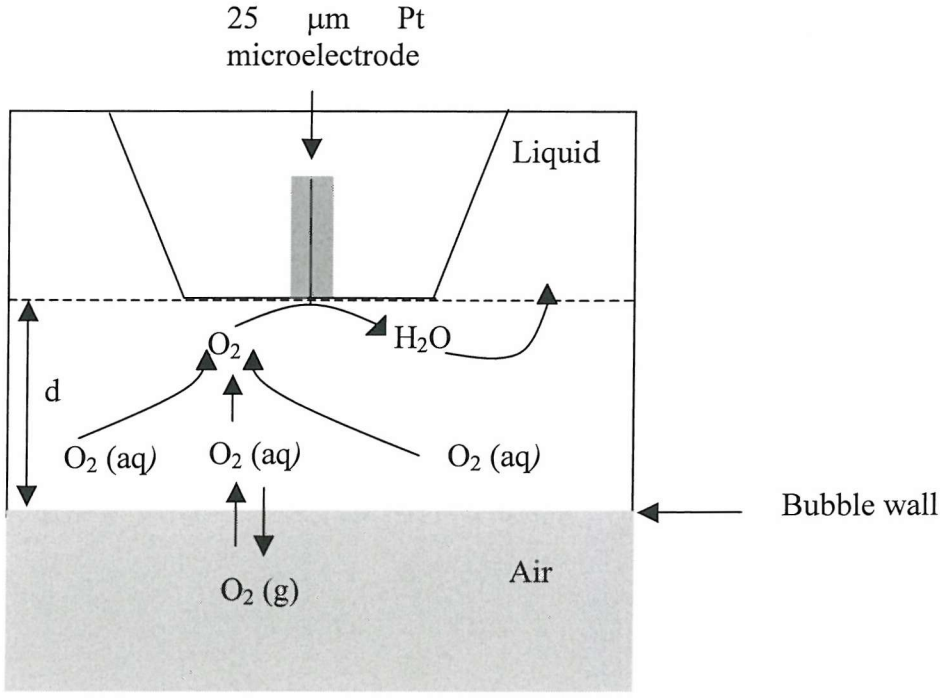

Figure 3.8 Schematic illustrating the motion of oxygen as a microelectrode approaches an air/liquid interface where *d* is the microelectrode-bubble wall distance.

[†] Strictly speaking this situation is different to a classical feedback experiment.

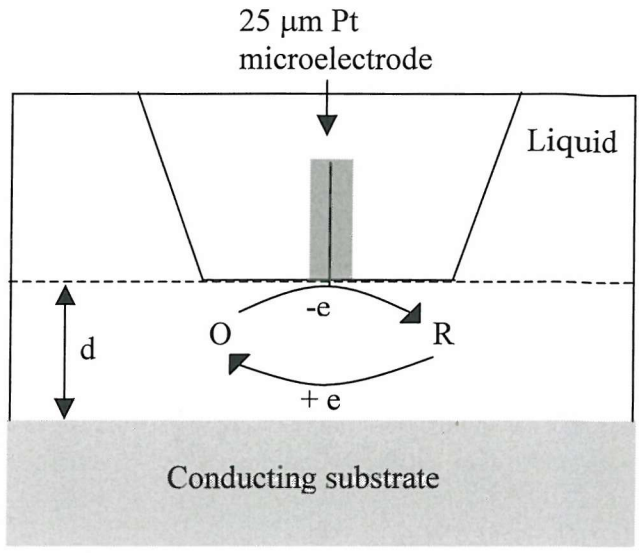

Figure 3.9 Schematic illustrating the motion of species under positive feedback conditions.

In order to explain this phenomenon, figure 3.10 shows a schematic of the concentration profile as the microelectrode tip approaches the gas/liquid interface of the air bubble. In figure 3.10 (a) the electrode is positioned far from the gas/liquid interface (d_4). Ficks first law of diffusion (see section 1.1) predicts that the flux and hence current recorded at the microelectrode is dependent on the concentration gradient.

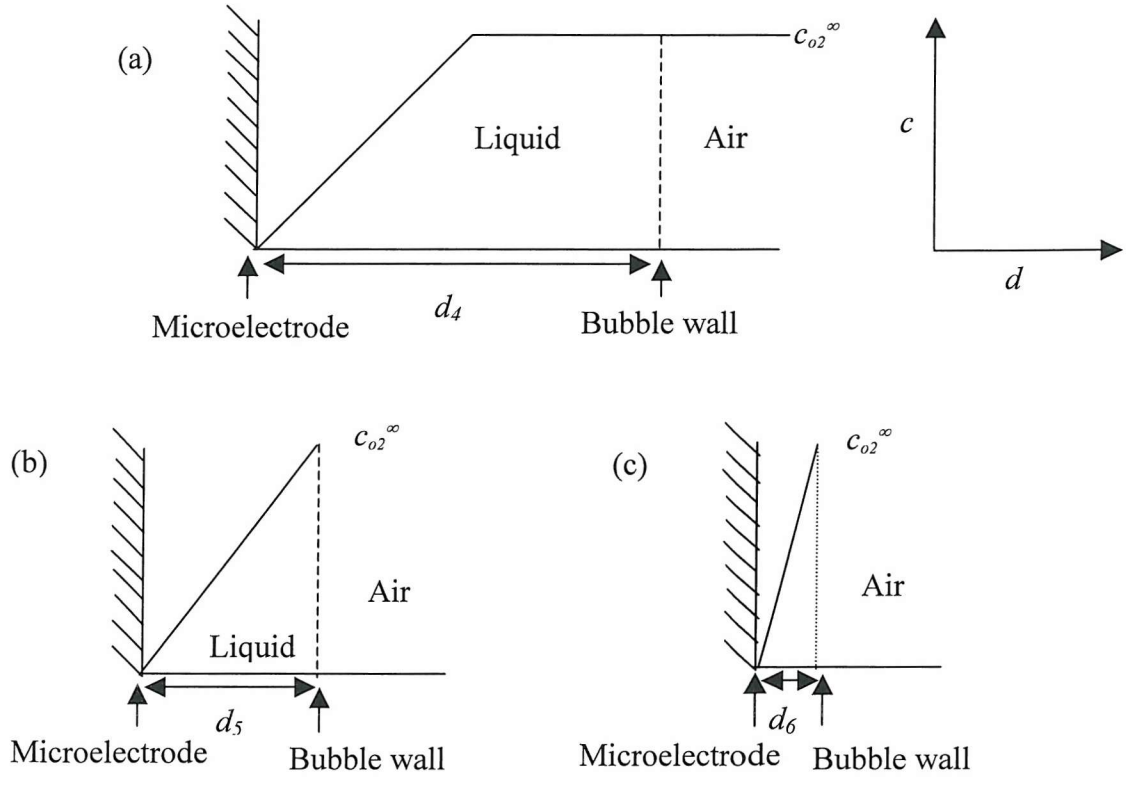

Figure 3.10 A schematic illustrating the effect of electrode-bubble wall distance on the current recorded at the microelectrode when monitoring oxygen reduction. (a), (b) and (c) represent decreasing distances between the bubble wall and microelectrode respectively. In all three schematics c_{o2}^{∞} is the bulk concentration of oxygen.

As the microelectrode bubble distance decreases (see figure 3.10 (b)) the value of *dc/dx* increases. Hence the flux of material reaching the electrode and the current increase. When the electrode-bubble wall distance is very small, *dc/dx* is very large (see figure 3.10 (c)) and the current recorded at the microelectrode is much greater than that recorded in the bulk solution.

Even though the mechanism causing the increase in current is different, it is interesting to compare the experimental findings with the prediction for positive feedback.[49] Figure 3.11 illustrates a plot of normalised current (i_{tip}/i_{inf}) against normalized distance (d/a). The solid line represents the current predicted under positive feedback conditions using equation 3.5 as determined by Amphlett and Denuault:[49]

$$\frac{i_{tip}}{i_{\inf}} = k_1 + \frac{k_2}{L} + k_3 \exp(\frac{k_4}{L}) \qquad (3.5).$$

All of the terms have been defined previously (see page 49). Again in this case the value for R_{glass} was taken to be 10.2 where k_1 was 0.72627, k_2 was 0.76651, k_3 was 0.26015 and k_4 was –1.41332. Although there is a good fit between the experimental and theoretical data the resolution of the experimental apparatus is low. Hence there are a number of different routes the theoretical curve could potentially take between the enclosed dashed lines on figure 3.11. However the experimental data shows close similarities with data obtained by Slevin *et al.*.[40]

Figure 3.12 is a plot of normalised current against electrode-interface distance on approaching a clean air/liquid interface as determined by Slevin *et al.*.[40] There is a large increase in current as the electrode-interface distance is reduced caused by rapid oxygen transfer rates across the interface, which coincides with the work reported here. Solving the diffusion equation for oxygen within the SECM geometry simulated the theoretical prediction included in this plot. This work was undertaken by Barker *et al.*.[98]

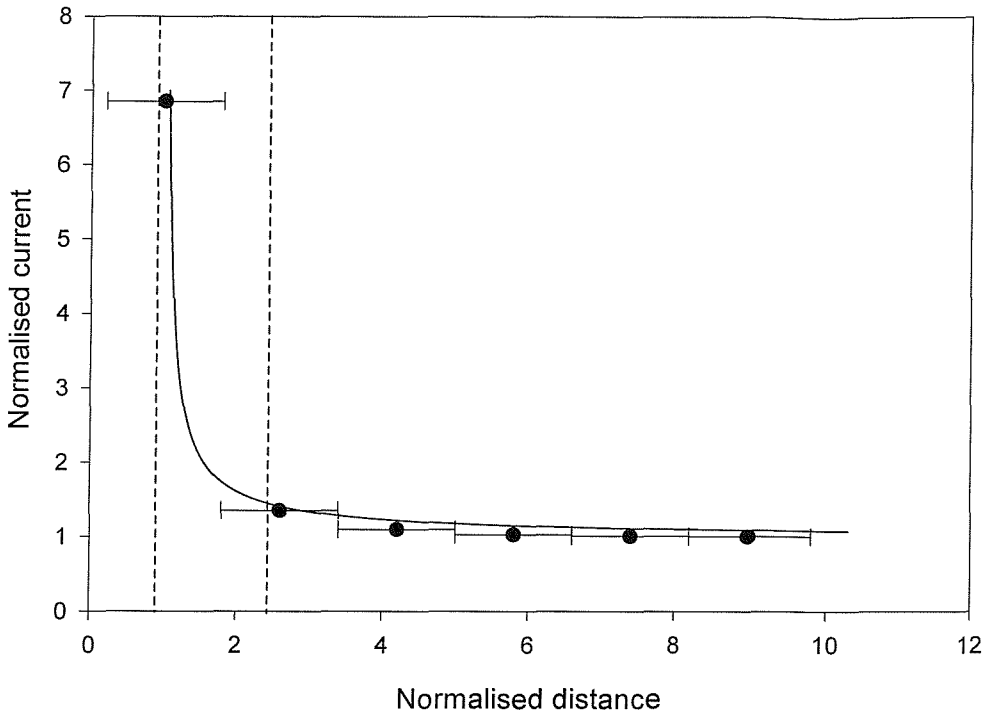

Fig 3.11 Graph of i_{tip}/i_{inf} (normalised current) versus d/a (distance moved towards the electrode surface divided by electrode radius) recorded at a 25 μm diameter Pt microelectrode in 0.1 mol dm^{-3} KCl on approaching a bubble wall. The solid line represents the curve predicted under positive feedback conditions. The temperature of the solution was 18 - 22 °C. The error in the x-axis is ± 10 μm.

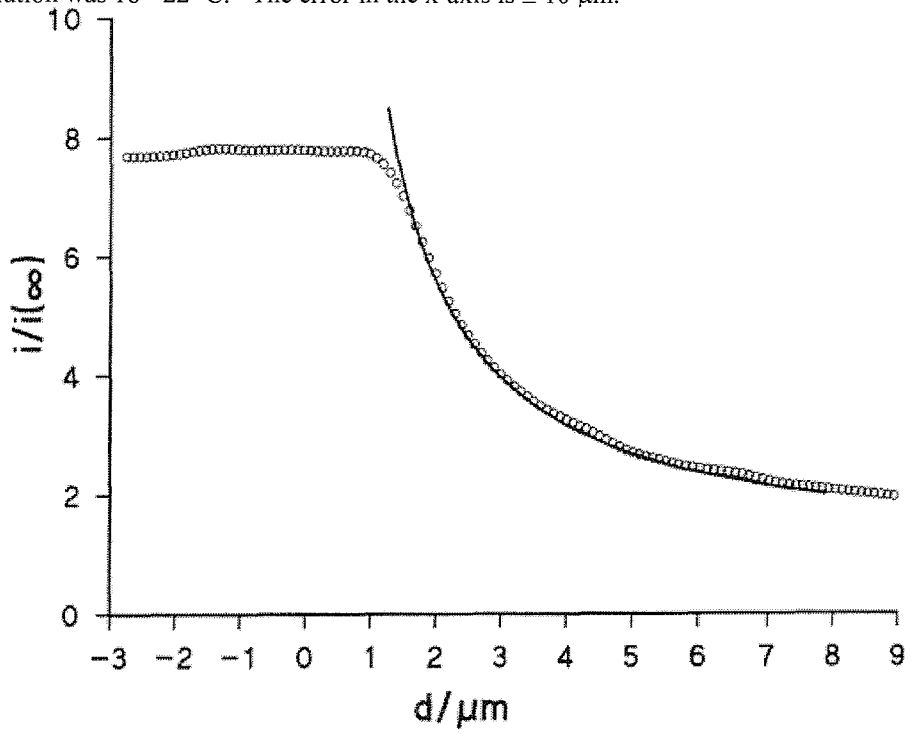

Figure 3.12 Plot of the normalised steady state current against distance from the interface recorded at a microelectrode on approaching an air/liquid interface. The reduction of oxygen (o) was monitored. The flattening of the curve to a constant value is indicative of a layer of water 1.5 – 2.0 μm thick being trapped by surface tension as the microelectrode pushed against the interface. The solid line represents the theoretical response for the transfer of oxygen from the air phase to the liquid phase. Reproduced from Slevin *et al.*.[40]

High resolution SECM (see sections 2.4 and 3.1a) was also employed to record the variation in current at the microelectrode tip with bubble-microelectrode distance in a solution of 0.1 mol dm^{-3} KCl. Identical experimental conditions to those reported in section 2.4 were employed. The electrode was moved in increments of 1 μm at a speed of 7.33 x 10^{-3} mm s^{-1}. The y direction was adjusted to *ca.* 0.25 mm (see section 3.1a). The bubble was approached and the x and z directions adjusted until a maximum increase in negative current, caused by the diffusion of oxygen from inside the bubble in response to depletion of the liquid region in between the bubble wall and microelectrode, was obtained. Figure 3.13 is a plot of normalised current (i_{tip}/i_{inf}) against normalised distance (d/a). The solid line (—▲) represents the data obtained employing this high-resolution technique while the dotted line represents the theoretical prediction employing equation 3.5 under positive feedback conditions.[49] The dotted plot represents experimental data obtained employing the low resolution SECM. In this case R_{glass} was taken to be 5.09 employing k_1 as 0.72035, k_2 as 0.75128, k_3 as 0.26651 and k_4 as –1.62091. The fit between the low-resolution technique and the high resolution SECM is excellent. However, considering the enhancement in current is not strictly positive feedback the discrepancy between the experimental data and the theoretical prediction is not surprising.

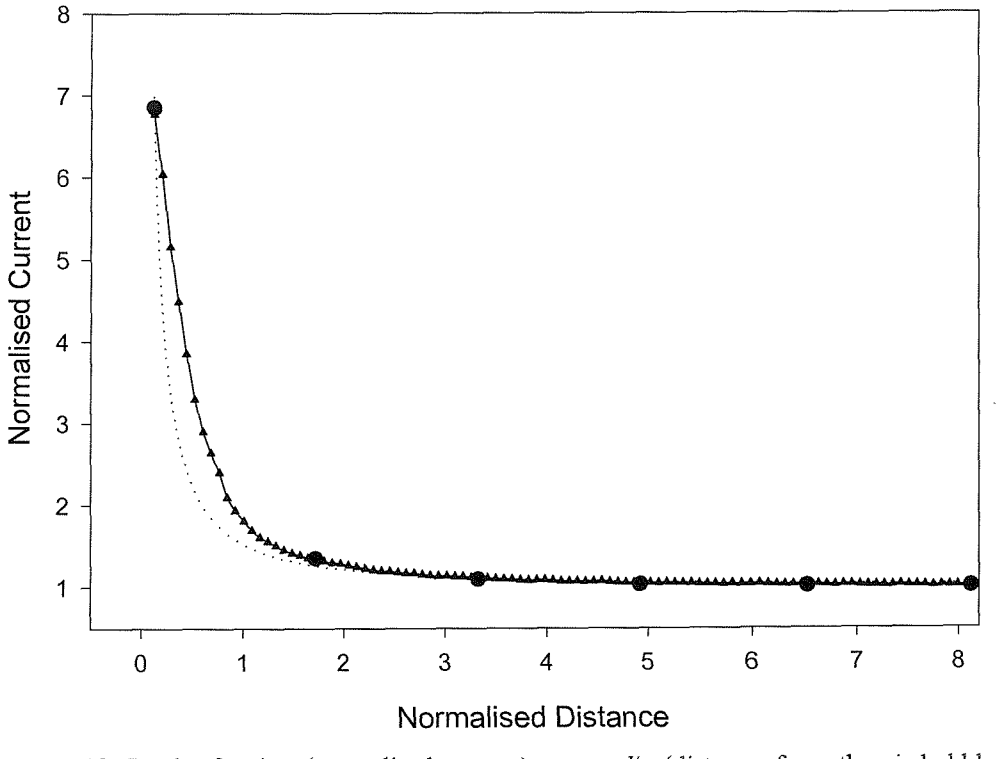

Figure 3.13 Graph of i_{tip}/i_{inf} (normalised current) versus d/a (distance from the air bubble wall (*ca.* 2 mm radius) divided by electrode radius) recorded at a 25 μm diameter Pt microelectrode in 0.1 mol dm^{-3} KCl. The dotted plot (...) represents the theoretical data obtained from equation 3.5 while (-▲) represents data obtained employing high resolution SECM equipment. The scattered plot (•) represents experimental data obtained employing low-resolution equipment. The temperature of the solution was 18 - 22 °C.

In this sequence of experiments (section 3.1b) attention was paid to water quality and hence 'clean' approach curves were obtained. However, it is also possible to envisage that contaminants present in the aqueous solution could have parasitic effects on the response of the microelectrode placed in close proximity to the interface. A number of effects were encountered which had to be overcome prior to obtaining a clean approach curve. These are discussed in detail in Appendix A. Once a 'clean' interface had been achieved it is possible to measure the effect of a known surfactant at controlled concentrations on the electrochemistry at a nearby microelectrode. The results of this study are now presented.

3.2 The Addition of Surfactant Triton X-100

The surfactant Triton X-100 was employed in this study. Triton X-100 is part of a family of polyoxyethylene-based surfactants that have been used extensively in polarography as maximum suppressers.[99] The "X" series of Triton detergents are produced from octylphenol polymerised with ethylene oxide. The number ("-100") relates only indirectly to the number of ethylene oxide units in the structure. Triton X-100 has an average of 9.5 ethylene oxide units per molecule, with an average molecular weight of 625 g. Its structure is illustrated in figure 3.14 and it is soluble in water at 25 °C. In analytical applications, Triton X-100 has been used to promote cation transfer across polarised water/oil interfaces, allowing amperometric detection of alkali metal ions.[100] In another study Zhang *et al.*[101,102] reported the effect of Triton X-100 adsorption at the interface between two immiscible electrolyte solutions (ITIES) on the oxidation of decamethyl ferrocene 1,2-dichloroethane by aqueous $Ru(CN)_6^{3-}$. The authors stated that the electron transfer reaction employed in this experiment only occurred in regions free from surfactant. In this work Triton X-100 was added to a solution of 0.1 mol dm^{-3} KCl and the effect it has on oxygen transfer across a gas/liquid interface was explored.

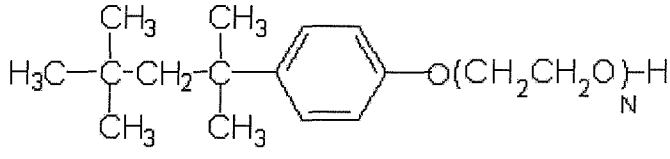

Figure 3.14 Molecular structure of Triton X-100.

Initially a 'clean' approach curve was obtained in a solution of 0.1 mol dm^{-3} KCl monitoring the reduction of oxygen. Increasing additions of a 2 mmol dm^{-3} solution of Triton X-100 were then added to 250 ml of a 0.1 mol dm^{-3} solution of KCl varying the concentration of the surfactant in this solution from 40 μmol dm^{-3} to 100 μmol dm^{-3}. The potential was held at –0.7 V *vs.* Ag where the reduction of oxygen occurs at the mass transfer limiting potential. The microelectrode was positioned approximately 150 μm from the air bubble wall (*ca.* 2 mm radius). The interface was approached in increments of 20 μm (employing low resolution SECM equipment) every 10 s for each concentration of Triton X-100 added. A current time plot at each concentration of surfactant is shown in figure 3.15. From this figure it is evident that increasing concentrations of surfactant led to a decrease in the output current recorded at the electrode close to the bubble wall. This suggests that molecular oxygen transfer was inhibited by the Triton X-100 and was only occurring in regions free from surfactant.

Similar results were obtained by Slevin *et al.*[40] who in an eloquent study reported the effects of a monolayer, accumulated at a gas/liquid interface, on oxygen transfer rates across a planar air/liquid interface. They reported that primarily the accessible free area of the interface governed the rate of oxygen transfer across the interface.

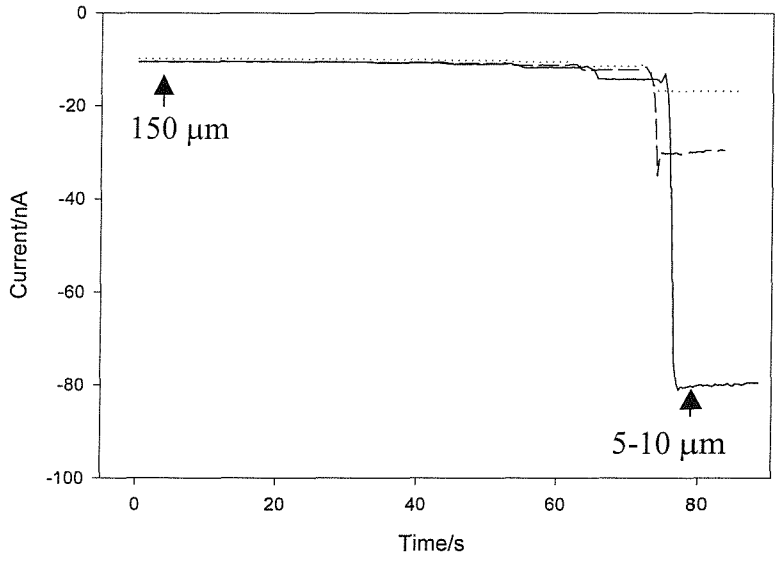

Figure 3.15 Current time plot recorded at a 25 μm diameter Pt microelectrode in a 0.1 mol dm^{-3} solution of KCl with increasing additions of Triton X-100. The potential was held at –0.7 V *vs.* Ag. The electrode was moved in increments of 20 μm every 10 s towards an air bubble wall (*ca.* 2 mm radius). Approach curves are shown for bulk aqueous Triton X-100 concentrations of 4 x 10^{-5} mol dm^{-3} (- - -), 10 x 10^{-5} mol dm^{-3} (...) and 0 (—). The current close to the electrode surface decreased with increasing concentration of the surfactant. The distances on the graph represent approximate bubble-microelectrode distances. The temperature of the solution was 18 - 22 °C.

A similar experiment in Triton X-100 was performed using high resolution SECM described previously (see sections 2.4 and 3.1). Employing a solution of 0.1 mol dm^{-3} KCl a 'clean' approach curve was obtained monitoring the reduction of molecular oxygen. An identical experimental procedure was employed as described in previously (see section 3.1b). Increasing amounts of Triton X-100 were then added to this 'clean' solution of 0.1 mol dm^{-3} KCl varying the concentration of Triton X-100 from 4 x 10^{-5} mol dm^{-3} to 8 x 10^{-5} mol dm^{-3} and finally to 1.2 x 10^{-4} mol dm^{-3}. After each addition the solution was stirred for 5 minutes employing a continuous flow pump powered by a DC power supply (see section 2.4a) and an approach curve was obtained. The flow rate employed was 0.315 cm^3 s^{-1} at a current of 0.7 A.

Figure 3.16 is a plot of normalised current (i_{tip}/i_{inf}) against normalised distance (d/a) recorded by a 25 μm diameter Pt microelectrode approaching the bubble wall. It can be clearly seen from this plot that the current recorded at the microelectrode close to the bubble wall decreases as the concentration of surfactant increases. Thus the transfer of oxygen across the gas/liquid interface is inhibited and oxygen transfer is only occurring in regions free from surfactant.

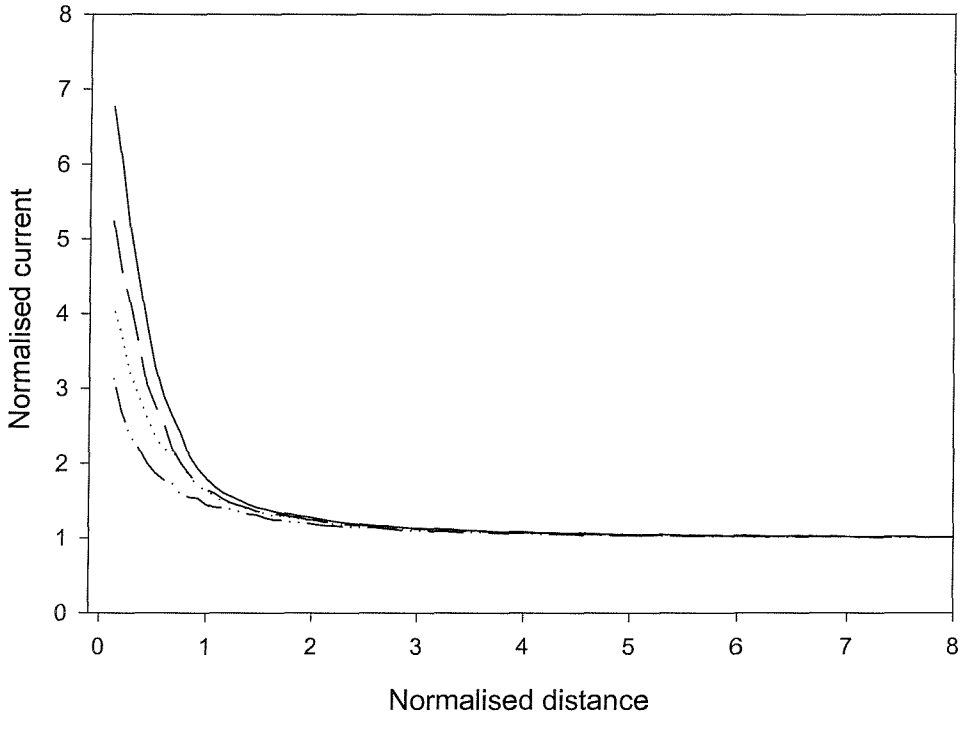

Figure 3.16 Plot of normalised current (i_{tip}/i_{inf}) against normalised distance (d/a) recorded at a 25 μm diameter Pt microelectrode on approaching an air bubble wall (R_0 *ca.* 2 mm) in a clean solution of 0.1 mol dm^{-3} KCl (—), 4 x 10^{-5} mol dm^{-3} Triton X-100 (- - -), 8 x 10^{-5} mol dm^{-3} Triton X-100 (...) and 1.2 x 10^{-4} mol dm^{-3} Triton X-100 (-..-). This experiment was performed employing high resolution SECM equipment. The temperature of the solution was 18 - 22 °C.

It must be noted that after obtaining the approach curve in a clean solution of 0.1 mol dm^{-3} KCl the electrode automatically returned to its original position (*i.e.* 0.25 mm away in the y direction) before the next scan. However, when an approach curve was recorded after the first addition of surfactant the bubble-electrode distance had decreased (see figure 3.17). Therefore the bubble-electrode distance had to be readjusted (see figure 3.16) to obtain an approach curve over the same distance range as the former. This readjustment had to be repeated after each addition of surfactant. The addition of a surfactant lowers surface tension. This is known to have an effect on the shape of the bubble within a liquid. The technique employing a 'pendant drop' is an established method relying on the effect of surface tension on the drop shape.[103] Bubbles trapped on solid surfaces tend to 'bow' outwards under the stress of buoyancy forces particularly if the surface tension is reduced.[104] Therefore the change in distance can be attributed to a change in bubble shape.

Figure 3.17 is a plot of normalised current (i_{tip}/i_{inf}) against normalised distance (d/a) obtained in a clean solution of 0.1 mol dm^{-3} KCl. The figure also includes the plots obtained after each addition of surfactant without any readjustment of the position of the microelectrode. This series of plots clearly illustrates that the bubble wall electrode distance changed after each addition of surfactant.

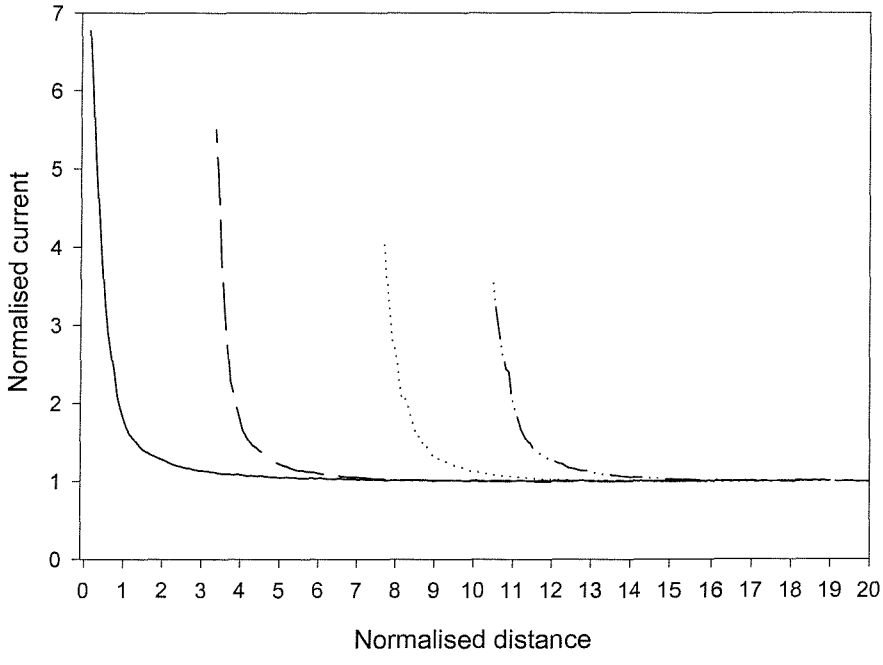

Figure 3.17 Plots of normalised current (i_{tip}/i_{inf}) against normalised distance (d/a) recorded at a 25 μm diameter Pt microelectrode on approaching a bubble wall. The potential of the electrode was held at –0.7 V *vs.* Ag where (—) represents a clean solution of 0.1 mol dm^{-3} KCl, (---) represents 4 x 10^{-5} mol dm^{-3} of Triton X-100, (....) represents 8 x 10^{-5} mol dm^{-3} of Triton X-100 and (-..-) represents 1.2 x 10^{-4} mol dm^{-3} of Triton X-100. There was no readjustment of the electrode position after each addition of surfactant. This series of plots were recorded employing a high resolution SECM technique.

3.3 Conclusions

This chapter explored the electrochemistry at the interface of a tethered static bubble in the absence of sound irradiation. Two cases were explored. First, the bubble acted as an inert substrate and blocked the diffusion of $Fe(CN)_6^{3-}$ ions to the electrode surface as the bubble wall electrode distance decreased. In the second case, the bubble acted as a source of oxygen when monitoring the reduction of oxygen. As the region between the microelectrode and bubble decreased, the concentration of oxygen close to the electrode became depleted and this provided the thermodynamic driving force for the transfer of oxygen across the interface. The current recorded at the microelectrode increased as the bubble wall was approached in this case. Both high and low spatial resolution SECM techniques were employed to monitor the variation in current recorded at the microelectrode as the bubble wall-microelectrode distance decreased. The agreement between the low-resolution experiments and the high-resolution experiments is excellent. The approach curves obtained showed good agreement with curves predicted by Amphlett and Denuault.[49]

It is also possible to envisage that the presence of contaminants accumulated on the bubble wall would hinder the transfer of oxygen across the interface. This is discussed in detail in Appendix A. In the sequence of experiments discussed in this chapter attention was paid to water quality. However, the effect of a known surfactant on the transfer of oxygen was discussed in detail. Increasing concentrations of Triton X-100, decreased the current recorded at the microelectrode close to the bubble wall *i.e.* oxygen transfer was only occurring in regions free from surfactant. This coincides with work undertaken by Slevin *et al.*[40] on planar air/liquid interfaces.

The most important points must be noted. First, a clean bubble surface behaved in a similar fashion to a planar interface. Second, surfactants block oxygen transfer from air bubbles. Clearly considering the importance of gas/liquid transfer, these results are significant and have implication on a global/environmental sense.

This sequence of experiments established a greater understanding of the electrochemistry occurring at the air/liquid interface. The electrode response varied depending on which reaction was being monitored. The bubble wall-microelectrode distance could be easily controlled employing SECM techniques and the electrochemistry recorded at the microelectrode was reproducible.

The thorough characterisation of the effects of the static gas/liquid interface enables the study of the dynamic interface to be achieved under controlled conditions. Therefore this

study will now be presented. In the following chapter the effect of mass transfer to the electrode surface in the presence of sound will be explored in detail.

The Dynamic Bubble Wall

Chapter 4

4.0 Introduction

In the previous chapter, the interface between a gas bubble, retained against buoyancy forces on the surface of a glass rod, and a liquid was explored extensively in the absence of sound irradiation. We now present an initial investigation of the interaction of a bubble with sound and the effect of this interaction on mass transfer to the electrode surface when monitoring the reduction of $Fe(CN)_6^{3-}$ and the reduction of molecular oxygen. No attempt is made at this stage to characterize exactly what form of motion the bubble wall is undertaking. That issue is explored extensively in chapter 5. The distinction in this chapter is between a stationary bubble and one whose wall is undergoing some unspecified form of oscillation. Nonetheless, a shimmering bubble seems to indicate surface wave motion. All experiments were performed employing time averaged acquisition techniques.

4.1 The Effect of Bubble Wall Motion on Mass Transfer to the Microelectrode Surface when Monitoring the Reduction of $Fe(CN)_6^{3-}$

In order to investigate the effect of an oscillating bubble on mass transfer to a microelectrode, the cell (figure 2.3) was filled with 5 mmol dm^{-3} $Fe(CN)_6^{3-}$ in 0.2 mol dm^{-3} $Sr(NO_3)_2$. An air bubble was retained against buoyancy forces on the end of the glass rod. The potential of the microelectrode was held at -0.1 V versus Ag wire where the reduction of $Fe(CN)_6^{3-}$ takes place at the mass transfer limiting rate. A 25 μm diameter Pt microelectrode ($^{35,42}R_{glass}$ *ca.* 5) was positioned close to the gas/liquid interface using an X-Y-Z micrometer and stage (see section 3.1a). When the electrode was < 100 μm away from the interface, the presence of the bubble wall could be detected as a reduction in the steady state current recorded at the microelectrode (see section 3.1a). This was owing to hindered diffusion (negative feedback) as a result of the blocking nature of the bubble wall under the conditions stated. The microelectrode was then moved in increments of 20 μm towards the bubble wall until the current recorded at the microelectrode was hindered by *ca.*75% (this

corresponds to a bubble wall-microelectrode distance of *ca.* 5 - 10 μm). The sound was switched on and the frequency and pressure of the sound field varied until the bubble was seen to shimmer (see figure 1.11). It was noted that under these conditions this shimmering corresponded to a large enhancement in current recorded at the microelectrode. This was attributed to forced convection of the liquid, produced by the oscillation of the bubble wall.

Fig 4.1 shows current-time plots at different microelectrode-bubble wall distances in the absence and presence of sound irradiation. Maintaining the microelectrode at *ca.* 5 - 10 μm from the bubble wall, the steady state current in the absence of sound irradiation was recorded (see figure 4.1 region A). Insonification commenced in region B, where the enhancement in current due to forced convection caused by the motion of the bubble wall was recorded. The microelectrode was then moved away from the bubble wall and similar current-time plots were recorded at various distances from the bubble wall. Figure 4.1 shows the series of plots obtained. Mass transfer enhancement due to bubble oscillation decreased with increasing distance between the microelectrode and interface. This was repeated until no enhancement due to bubble oscillation was observed. It must be noted that the enhancement in current in the presence of bubble oscillation is much greater than the current recorded in the bulk in the absence of the bubble *i.e.* 120 nA compared to 20 nA respectively.

As well as observing a large enhancement in direct current caused by a convective flow of the solution to the microelectrode surface, there appears to be fluctuations in mass transfer to the microelectrode. However, the frequency of these fluctuations cannot be determined from these plots. Shimmering of the bubble nevertheless seems to indicate surface wave motion. This will be explored further in chapter 5.

Figure 4.1 shows that the enhancement in the mass transfer can be detected at extended distances away from the gas/liquid interface. Figure 4.2 shows that a enhancement in the time averaged steady state mass transfer to the microelectrode was observed up to distances of *ca.* 2500 μm away from the bubble wall *i.e.* in comparison to the steady state current recorded in the bulk of the solution.

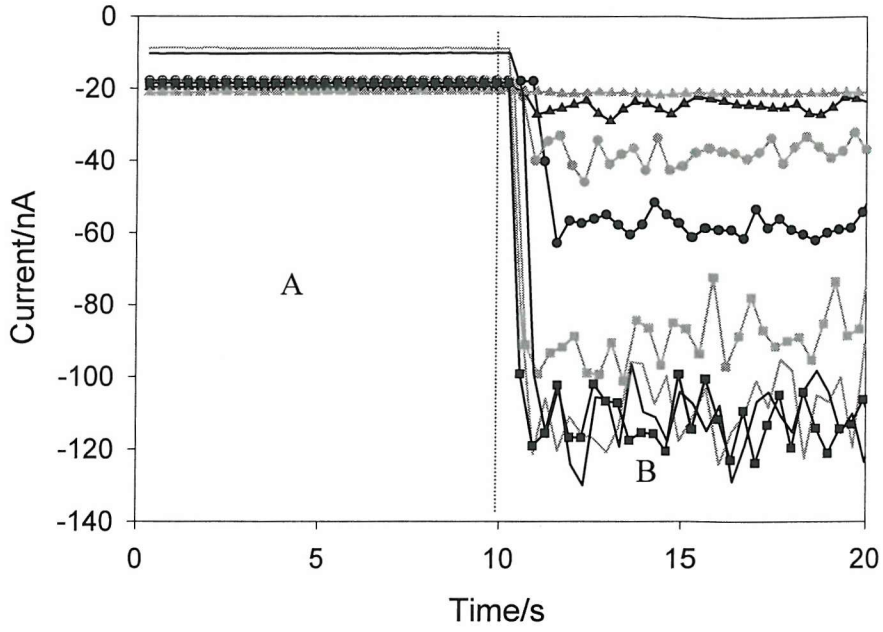

Figure 4.1 Current time plots recorded at a 25 μm diameter Pt microelectrode at distances of *ca.* 5 - 10 μm (—), 30 μm (—), 70 μm (—■), 150 μm (—■), 250 μm (—●), 510 μm (—●), 1310 μm (—▲) and 2510 μm (—▲) from the bubble wall (R_0 *ca.* 2.2 mm). Region A represents the current recorded in the absence of irradiation followed by irradiation in region B with a sound field operating at 1.46 kHz and 50.4 Pa. The solution was 5 mmol dm^{-3} $Fe(CN)_6^{3-}$ in 0.2 mol dm^{-3} $Sr(NO_3)_2$. The vertical dashed line divides region A from region B.

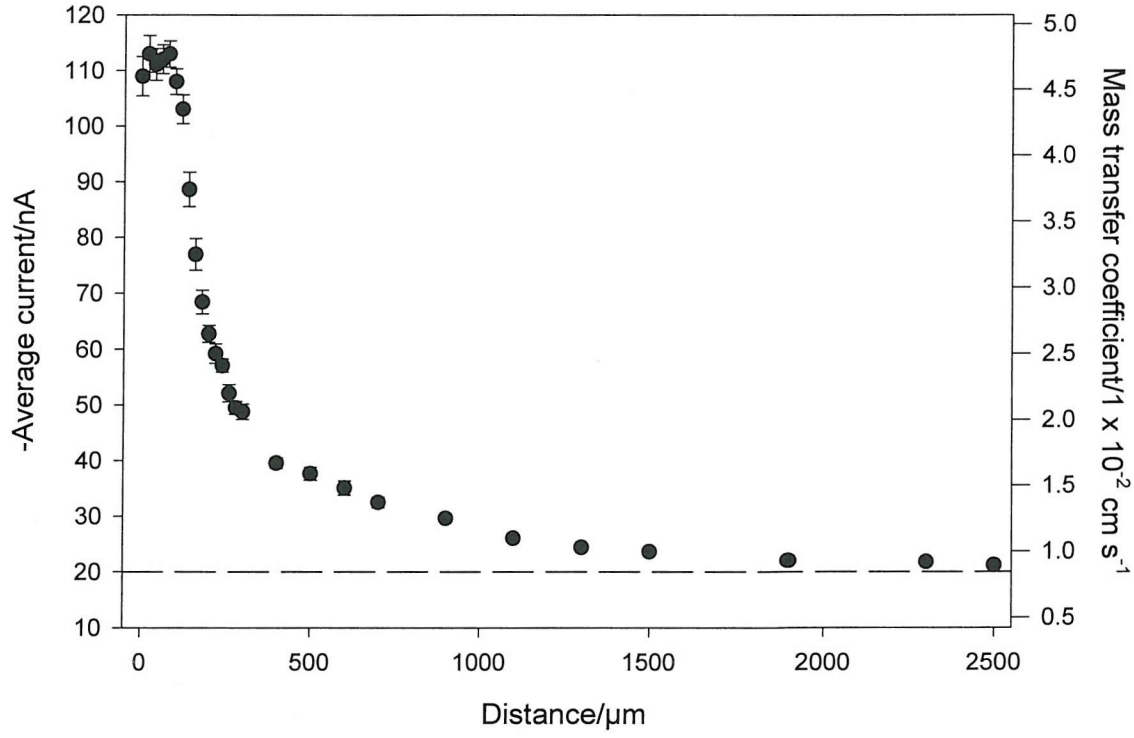

Figure 4.2 Plot showing the average current (•) and associated mass transfer coefficient recorded at a 25 μm diameter Pt microelectrode for a single air bubble (R_0 *ca.* 2.2 mm) driven into oscillation by a sound field operating at 1.46 kHz and 50.4 Pa. The solution contained 5 mmol dm^{-3} $[Fe(CN)_6]^{3-}$ in 0.2 mol dm^{-3} $Sr(NO_3)_2$. The error bars show the 95% confidence interval. The experiment was performed at *ca.* 20 - 23 °C under aerobic conditions. (- - -) represents the steady state current or mass transfer coefficient for the microelectrode in a stagnant solution far from the bubble.

In figure 4.2 the average current over a 10 second period was calculated for each distance moved away from the bubble wall in the presence of sound irradiation. The dashed line represents the mass transfer coefficient of a 25 μm diameter Pt microelectrode in stagnant solution (0.008 cm s^{-1} which was calculated using equation 1.4). However, the enhancement in mass transfer brought about by bubble oscillatory motion exceeds this value significantly with a maximum value of the coefficient as 0.0477 cm s^{-1}. It is important to note that this is brought about by a relatively small pressure amplitude (zero to peak < 100 Pa). This is a significant point as this clearly demonstrates that enhancing the mass transfer of material to an electrode in this manner would be a significantly more efficient way when compared to the employment of ultrasound to induce cavitation (a relatively high pressure amplitude phenomenon). Previous studies have shown that ultrasound (via cavitation) can enhance mass transfer significantly.[105-111] Mass transfer rates of between 0.1 - 1 cm s^{-1} have been measured. However, the magnitude of the pressure field required to achieve inertial cavitation is considerably higher. As an example to generate cavitation in water under standard conditions requires a pressure amplitude in excess of *ca.* 1 atmosphere (101,000 Pa).[24] Also above the cavitation threshold mass transfer can be difficult to quantify owing to processes such as microstreaming, jetting and acoustic streaming.[24]

It is important to show that the signal observed in figure 4.1 was a direct result of bubble wall motion and not erroneous electrical noise from the loudspeaker. Figure 4.3 shows the response of a microelectrode positioned next to the bubble wall in absence and presence of sound irradiation employing the experimental set-up in figure 2.3. At $t = 0$ the potential of the microelectrode was +0.5 V *vs.* Ag (a potential at which reduction of $Fe(CN)_6^{3-}$ was not observed). At $t = 20$ s the potential of the microelectrode was stepped to –0.1 V *vs.* Ag where mass transfer steady state reduction of $Fe(CN)_6^{3-}$ occurs. The distance from the microelectrode to the bubble wall at this stage was approximately 50 μm. This was followed by two-step changes of 20 μm towards the bubble wall, which are marked by 'A_1' and 'A_2' to adjust the microelectrode-bubble distance to *ca.* 5 - 10 μm. The current falls after each step due to hindered diffusion caused by the presence of the bubble wall (see section 3.1a). For the remainder of the figure the average microelectrode/bubble distance was fixed at *ca.* 5 - 10 μm. Sound irradiation commenced at 'B'. The additional enhancement in mass transfer to the microelectrode tip was due to the forced convection of the surrounding liquid, caused by the motion of the bubble wall. However, when the sound was switched off, the current immediately fell back to the steady state value in the absence of irradiation. The process was repeated and a similar current enhancement was observed.

In order to prove that the mass transfer enhancements to the microelectrode were caused by bubble oscillation, the potential was stepped to +0.5 V *vs.* Ag (D). The bubble was irradiated at the same frequency/pressure conditions to induce bubble oscillation but no enhancement was observed. This is because at this potential no reduction of $Fe(CN)_6^{3-}$ occurs (see figure 4.3 'E' and 'F'). Hence it can be concluded that signal observed at 'B' was due to mass transfer enhancement caused by the oscillating bubble and not an erroneous noise process. It should also be noted that the current recorded in the bulk in the absence of the bubble and sound irradiation was 20 nA compared to 120 nA recorded close to the bubble wall in the presence of sound irradiation.

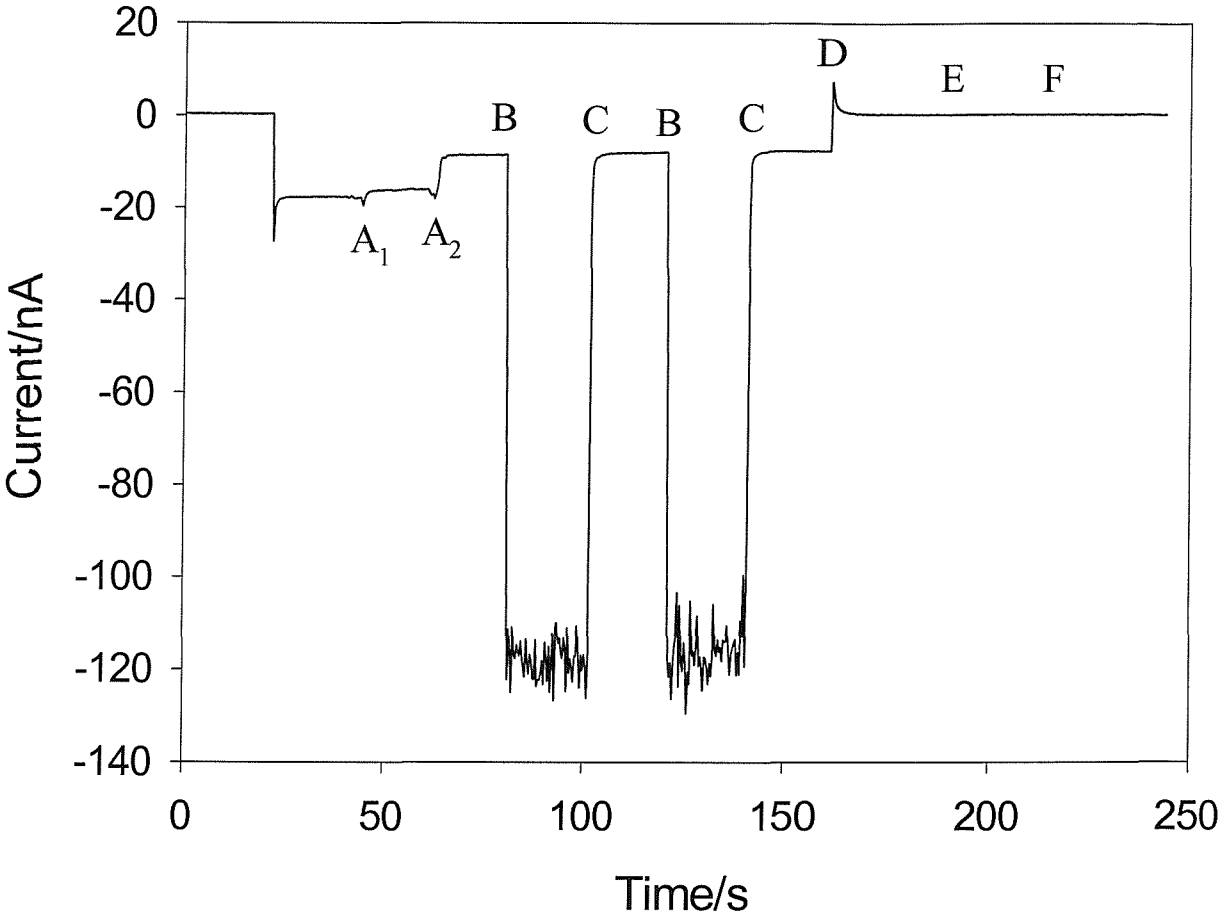

Figure 4.3 Plot showing the current time trace recorded for a 25 μm diameter Pt microelectrode approaching a bubble (R_0 *ca.* 2.5 mm) retained against buoyancy forces in the absence and presence of sound irradiation. 'A' indicates manual positioning of the microelectrode towards the bubble wall in increments of 20 μm. 'B' and 'C' represent the initiation and termination of sound irradiation of the air bubble driven into oscillation at 1.2835 kHz and 52 Pa pressure amplitude respectively. 'D' represents the point where the potential of the microelectrode was changed from -0.1 V *vs.* Ag (a potential corresponding to mass transfer limiting steady state conditions) to 0.5 V *vs.* Ag (corresponding to no reduction of the $[Fe(CN)_6]^{3-}$). 'E' and 'F' show the times when sound irradiation was commenced and terminated respectively.

This series of experiments represents the initial electrochemical detection of an oscillating gas bubble. However, as well as monitoring mass transfer enhancement of $Fe(CN)_6^{3-}$ to the electrode surface, caused by convective flow induced by the oscillating

bubble, it is also interesting to determine how the reduction of molecular oxygen present in the solution and bubble is affected by a similar bubble oscillation.

4.2 The Effect of Bubble Wall Motion on Mass Transfer to the Microelectrode Surface when Monitoring the Reduction of Molecular Oxygen

In order to investigate the effects of bubble oscillation on molecular oxygen electrochemistry at a microelectrode placed next to a gas/liquid interface, mass transfer enhancements caused by the oscillatory motion of the bubble wall were investigated in 0.1 mol dm^{-3} KCl. In this case, the potential of the microelectrode was held at -0.7 V *vs*. Ag where oxygen reduction occurs at the mass transfer limited rate. The frequency of the sound field was varied until the bubble was seen to 'shimmer' (see figure 1.11). The electrode was then positioned close to the bubble wall (*ca*. 5 - 10 μm away) until maximum enhancement in current due to the transfer of molecular oxygen through the bubble wall was seen (see section 3.1b), in the absence of sound irradiation. It must be noted that all efforts were performed to keep the gas/liquid interface free from surfactant material (minimisation of non-glass components of the cell and pure water obtained from a Vivendi Purelab Option 10 purification system). This mass transfer steady state current was recorded (see figure 4.4 region 'A'). This was followed by sound irradiation, which commenced at t = 11 s (see figure 4.4 region 'B'). The microelectrode was then moved away from the gas/liquid interface and a current time plot in the absence and presence of sound irradiation was recorded at various distances from the bubble wall. The series of plots obtained is illustrated in figure 4.4.

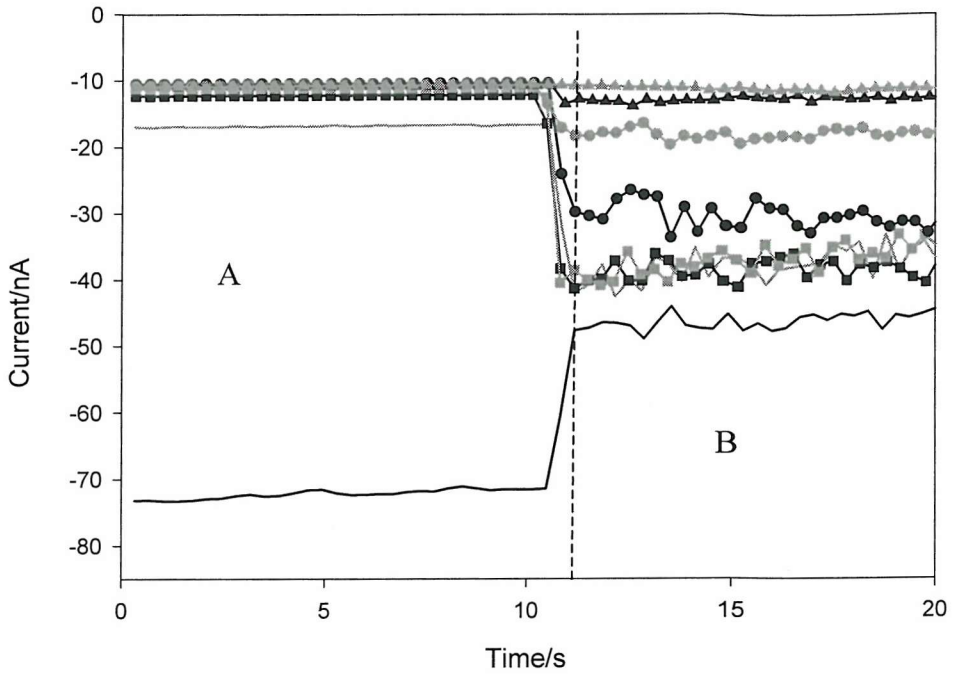

Figure 4.4 Current time plots recorded at a 25 μm diameter Pt microelectrode at distances of *ca.* 5 - 10 μm (—), 30 μm (—), 50 μm (—■), 70 μm (—■), 260 μm (—●), 510 μm (—●), 1010 μm (—▲) and 2510 μm (—▲) away from the bubble wall (R_0 *ca.* 2.6 mm). Region A represents the current recorded in the absence of sound followed by sound irradiation in region B with a sound field operating at 1.22 kHz at 44.78 Pa pressure amplitude. The solution was 0.1 mol dm^{-3} KCl. The vertical dashed line divides region A and region B. ▲

At bubble to microelectrode distances of ≥ 30 μm an enhancement in current occurs in figure 4.4, brought about by convective flow of solution due to the oscillating bubble. However, when the electrode was positioned at a closer bubble/microelectrode distance (*e.g. ca.* 5-10 μm away), sound irradiation caused a reduction in the current recorded at the microelectrode. An explanation for this observation could be that forced convection caused by the bubble wall introduces fresh solution between the microelectrode/bubble gap. Under these conditions the thermodynamic driving force for oxygen transfer across the gas/liquid interface is removed and the current falls to the mass transfer steady state reduction of molecular oxygen from the bulk of the solution to the microelectrode. This will be discussed in more detail later on in this section (see page 73).

Figure 4.5 shows the mass transfer coefficient against distance away from the bubble wall in the presence of sound irradiation. Enhancements in the mass transfer coefficient, in comparison to the mass transfer coefficient recorded in the stagnant solution far from the bubble, were noticed up to 2500 μm from the bubble wall.

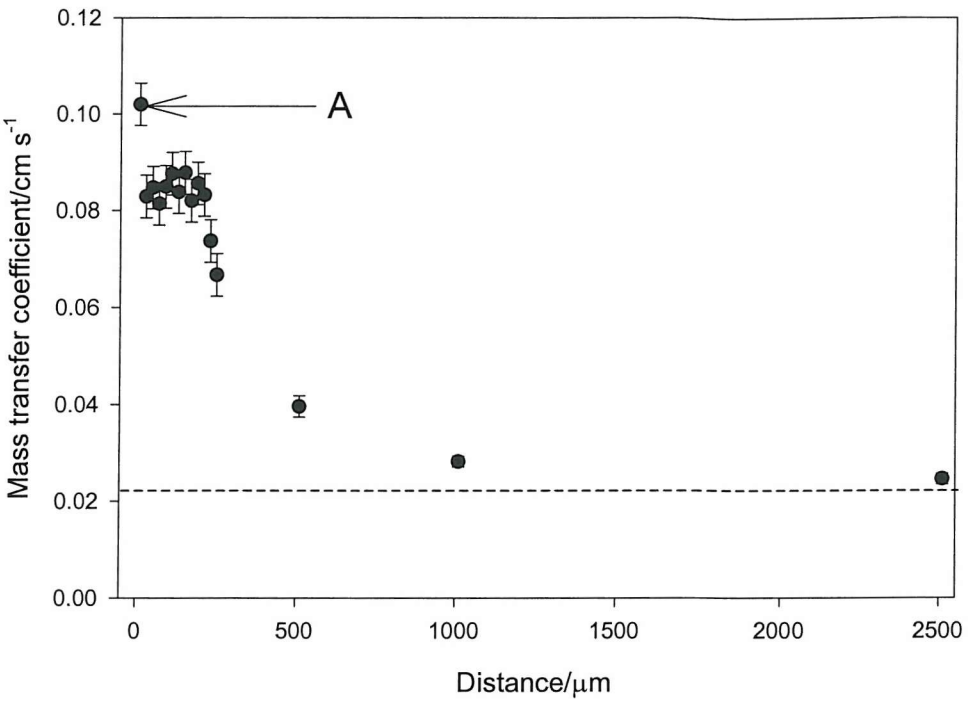

Figure 4.5 Plot showing the mass transfer coefficient (•) recorded at a 25 μm diameter Pt microelectrode for a single air bubble (R_0 *ca.* 2.6 mm) driven into oscillation by a sound field operating at 1.22 kHz at 44.78 Pa pressure amplitude. The solution contained 0.1 mol dm^{-3} KCl. The error bars show an error of ± 0.0044 cm s^{-1} up to distances of 250 μm, ± 0.0022 cm s^{-1} up to distances of 510 μm and 0.0011 cm s^{-1} there after. The errors were calculated from the variation in experimental data. The experiment was performed at *ca.* 20 - 23 °C under aerobic conditions. The dashed horizontal line represents the mass transfer coefficient for the microelectrode in a stagnant solution far from the bubble wall. The mass transfer coefficients were calculated employing $n_e = 4$. 'A' represents the mass transfer coefficient recorded at *ca.* 5 – 10 μm from the bubble wall.

This figure can be compared to a similar plot recorded when monitoring the reduction of $Fe(CN)_6^{3-}$ (see figure 4.2). In figure 4.2 the mass transfer coefficient remained approximately constant up to 130 μm. At distances greater than 130 μm the mass transfer coefficient decayed, but still remained significant in comparison to that recorded in stagnant conditions up to 2500 μm away. In figure 4.5 a maximum in the mass transfer coefficient is noticed close to the bubble wall (*ca.* 5 - 10 μm away, see point A). Between 10 μm and 210 μm away from the bubble wall the mass transfer coefficient remains approximately constant. This suggests that there is actually some contribution to mass transfer resulting from oxygen transfer across the interface close to the bubble wall in the presence of sound irradiation at distances of *ca.* 5 - 10 microns from the bubble wall (see point A). When the bubble to microelectrode distance exceeds 10 μm mass transfer of oxygen occurs from the bulk solution to the microelectrode. At distances greater than 210 μm the mass transfer coefficient decreases but is still significant up to distances of 2500 μm in comparison to that recorded for the 25 μm diameter Pt microelectrode under stagnant conditions in the bulk solution.

The reduction in current close to the bubble wall in the presence of sound irradiation can be further explained (see figure 4.4). In this experimental situation it is important to consider the time it takes for the microelectrode to reach a 'steady state' close to the bubble wall, compared to the time the bubble wall is close to the microelectrode surface. To date there is no relationship, which is capable of predicting the time it takes for a microelectrode to reach a steady state current in the presence of a convective flow of solution caused by sound irradiation of a bubble. The visible 'shimmer' (see figure 1.11) enabled us to assume surface wave motion of the gas/liquid interface. The total surface displacement induced by surface wave motion will be assumed as 30 μm amplitude (see section 5.4c i). For the purpose of this calculation minimum microelectrode-gas/liquid interface separations of 10 μm and 1 μm are employed. Figure 4.6 shows a plot of the bubble wall to microelectrode distance against time considering the period of a typical surface wave excited in the work reported in this thesis.

The time it takes for the microelectrode to reach a 'steady state', when examining the reduction of oxygen, can be calculated. Two methods are available for calculating the response time of a microelectrode. In the first method equation 4.1 was employed.[16-18] This shows an expression assuming a diffusion only mass transfer regime and considering planar diffusion in particular.[†]

$$\frac{l^2}{D} = t_{ss} \qquad (4.1)$$

Here t_{ss} is the time required for a diffusion boundary to cross a finite distance, l is the diffusion length or distance covered and D is the diffusion coefficient of the species under question.

[†] A valid approximation of the gas/liquid-electrode geometry at short distances.

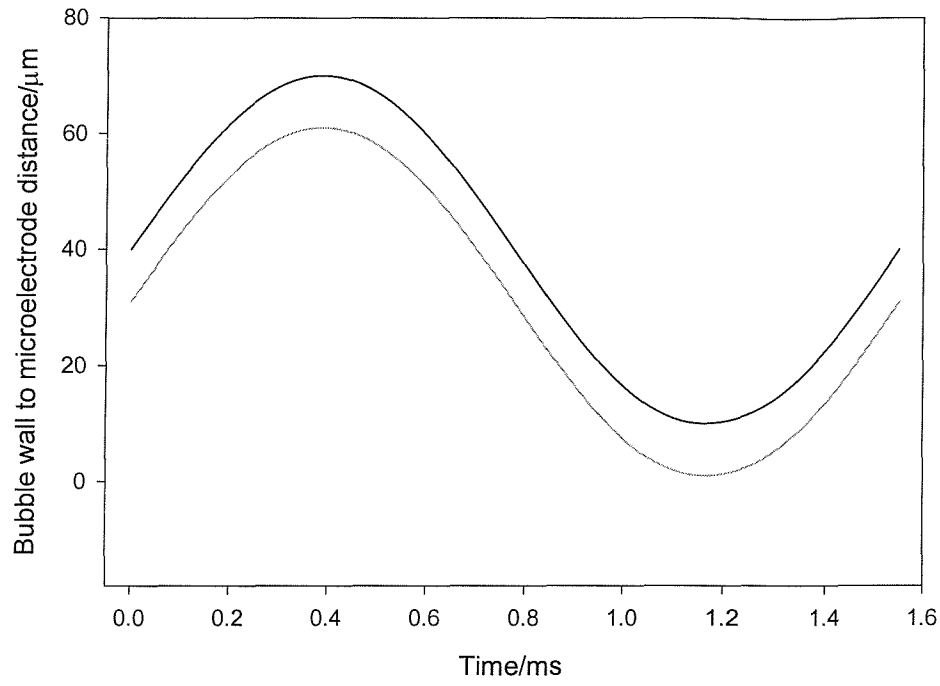

Figure 4.6 Plot of bubble wall-microelectrode distance against time of one cycle of surface wave motion on the bubble wall in the presence of a sound field operating at 1.2886 kHz. (—) represents a minimum microelectrode bubble distance of 10 μm and (—) represents a minimum microelectrode bubble distance of 1 μm. The total bubble wall amplitude displacement was 30 μm.

In the second model diffusion/convection was assumed, a suitable analogy to the real experimental system. In this case a model derived for the rotating disk electrode (RDE) is adopted. In the RDE set-up the rotated structure acts as a pump (it pulls the solution vertically upwards (convective flow) and then throws it outwards because the solution cannot pass through the solid material).[16] When the rotation rate (ω_{RD}) is fixed and the mass transfer limiting potential for the species in question applied to the electrode, a steady state limiting current is recorded at the electrode. This is in contrast to the current recorded at a planar stationary electrode, which never obtains a true 'steady state' and current decays towards zero at infinite time. This mass transfer limiting current (i_l) for the RDE is defined by the Levich equation:[16]

$$i_l = 0.62 n_e F A_1 D^{2/3} \omega_{RD}^{1/2} \upsilon^{-1/6} c \qquad (4.2)$$

where υ is the kinematic viscosity, A_1 the electrode area and c the concentration of electroactive species in the bulk solution. In addition for a RDE the diffusion layer thickness,[16] (δ) is given by equation 4.3:

$$\delta = 1.61 D^{1/3} \omega_{RD}^{-1/2} \upsilon^{1/6} \tag{4.3}$$

$$\omega_{RD} = \left(\frac{D^{1/3}\upsilon^{1/6}1.61}{\delta}\right)^2$$

The time required for the rotating disk electrode to attain a steady state current† value can be determined from equation 4.4:

$$\omega_{RD} t_{ss} \left(\frac{D}{\upsilon}\right)^{1/3} 0.51^{2/3} = 1.3 \tag{4.4}$$

where t_{ss} is the time taken to reach a steady state. Therefore, substituting ω_{RD} from equation 4.3 into equation 4.4 and rearranging allows the time it takes the RDE to reach a steady state (t_{ss}) to be calculated as a function of the other physical parameters of the system (equation 4.5):

$$t_{ss} = 1.3\left(\frac{D}{\upsilon}\right)^{-1/3} (0.51)^{-2/3} \left(\frac{D^{1/3}\upsilon^{1/6}1.61}{\delta}\right)^2 \tag{4.5}.$$

Figure 4.7 is a plot of the estimated time taken to reach steady state, for a system responding to planar diffusion alone (▬) or a convective/diffusion case (▬) *e.g.* the rotating disk electrode, against the period of surface wave motion. The thick solid lines represent a minimum bubble-wall microelectrode separation of 10 μm while the thick dashed lines represent a minimum bubble-wall microelectrode separation of 1 μm. The times to steady state were calculated from equations 4.1 and 4.5. The straight line (—) in the figure is a plot of the total time taken for one cycle of surface wave motion.

† Here the time represents a chronamperometric response to the steady state.

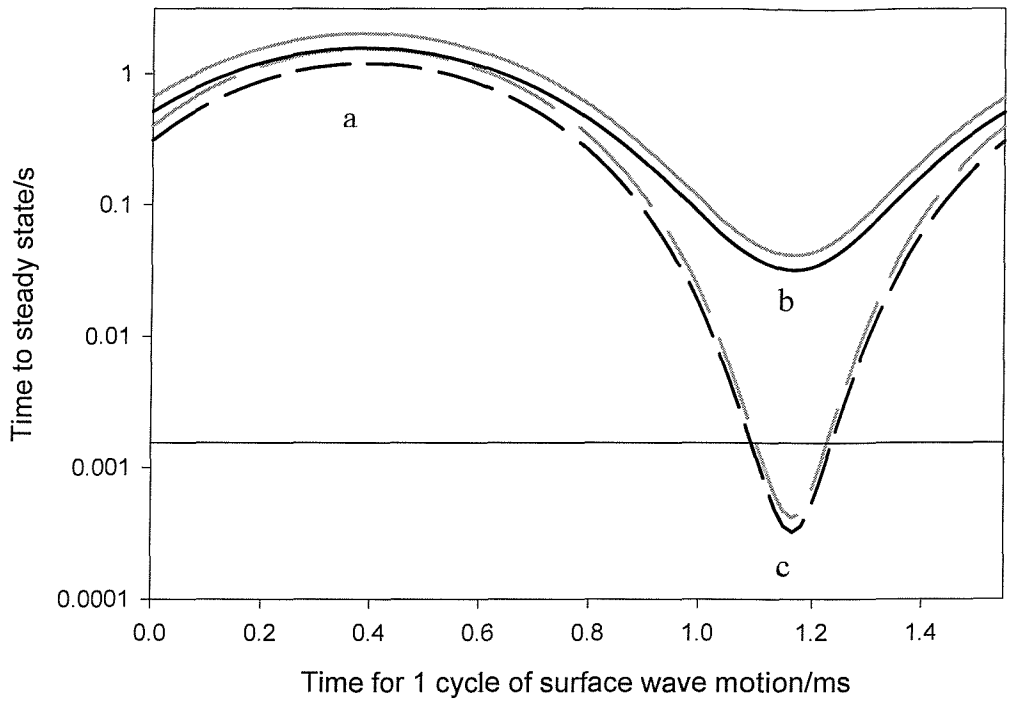

Figure 4.7 Plot of the time to steady state for an electrode undergoing planar diffusion (—) and a rotating disk electrode (—) against the time taken for 1 cycle of surface wave displacement. The thick solid lines represent a minimum bubble microelectrode distance of 10 μm while the thick dashed lines represent a minimum distance of 1 μm. a, b, c indicate far from the bubble wall, *ca.* 10 μm and 1 μm away respectively. The solid line is a plot of the total time taken for one cycle of surface wave motion.

The data represented by the thick solid lines (indicating both the planar diffusion case and the convective/diffusion case) on figure 4.7 will be discussed first. It can be seen from these plots that when the bubble is far away from the electrode surface (*ca.* 70 μm away) the time taken to reach steady state is nearly 1000 times greater than the time it takes for the surface wave to undergo one cycle of surface wave motion (indicated by a). Conversely, when the electrode is close to the bubble wall (10 μm away) the time taken to reach steady state is approximately 100 times greater than the time for one cycle of surface wave motion (indicated by b). Therefore the electrode is never close to the bubble long enough to reach a steady state and induce the transfer of molecular oxygen across the gas/liquid interface required to account for the enhancement in current observed close to the bubble wall (see figure 4.4 region A). However, on examining the data represented by the thick dashed lines (*i.e.* a minimum bubble microelectrode distance of 1 μm), the time taken to reach a steady state at 61 μm is similar to that recorded at 70 μm (see a). Conversely, the time taken to complete one cycle of surface wave motion exceeds the time taken for the microelectrode to reach a steady state at bubble wall microelectrode distances approaching 1 μm (indicated by c). Therefore there will be some contribution to the current close to the bubble wall in the

presence of sound irradiation from oxygen transfer across the interface. This can be seen on figure 4.5 as the point labeled 'A' is the closest to the bubble wall (*ca.* 5 μm away) and is significantly higher than the other data points. Clearly the microelectrode will never be close to the bubble wall for long periods to cause significant enhancements in current due to oxygen transfer across the interface. Therefore, the argument that there is some contribution to mass transfer from oxygen transfer across the bubble wall close to the bubble proves reasonable. However, at distances greater than 5 - 10 μm mass transfer occurs from the bulk solution to the microelectrode.

4.3 Conclusions

Investigation of single bubbles retained against buoyancy forces to a glass rod provided many informative results. It was shown to be possible to monitor bubble oscillation, driven by an acoustic field, employing novel electrochemical techniques. Bubble oscillation could be seen as a distortion of the bubble surface and could be detected as a fluctuation in the current recorded at the microelectrode. Enhanced mass transfer due to forced convection caused by the motion of the liquid was observed when the microelectrode was positioned close to the surface of the bubble when examining the reduction of $Fe(CN)_6^{3-}$. This enhancement in mass transfer dropped off with increased distance between the bubble equator and microelectrode. Significant enhancements in current were noticed (in comparison to the current recorded in the bulk) up to a bubble-microelectrode distance of 2500 μm.

However, the effect of bubble oscillation on mass transfer to the microelectrode surface when monitoring oxygen reduction showed differences to the $Fe(CN)_6^{3-}$ system. When the microelectrode was positioned close to the bubble wall (*ca.* 5 - 10 μm away), bubble oscillation induced a decrease in current recorded at the microelectrode. However, there was some contribution to the current caused by oxygen transfer across the interface at short distances (*ca.* 5 - 10 μm away). As the distance between the bubble and microelectrode was increased the current falls due to decreased mass transfer of oxygen to the microelectrode. An explanation for these observations was presented which modeled the system under forced convection conditions using an RDE analogy. At this stage it is important to determine the frequency of the mass transfer fluctuations owing to the oscillation of the bubble wall. However, this will require employment of high-resolution equipment.

Electrochemical detection of the breathing mode, surface waves and higher order surface waves will be discussed in detail in the next chapter.

Modes of Oscillation of the Bubble Wall

Chapter 5

5.0 Introduction

Chapter four introduced the initial investigation of how an electrochemical technique could be used to detect the interaction of a bubble, retained against buoyancy forces, with sound. This technique relied on the effect of bubble motion on mass transfer to a microelectrode positioned close to the gas/liquid interface of a bubble. In this chapter, the modes of oscillation of a bubble wall (*i.e.* breathing, surface waves and higher order surface waves) are specifically detected using this electrochemical technique for the first time.

A bubble in a liquid oscillates when placed in a sound field because the difference in compressibility between the gas and the liquid enables the bubble to couple to the pressure fluctuations caused by the sound wave.[24] When a gas bubble is irradiated with sound the wall displacement amplitude of the bubble will be greatest (*i.e.* the response of the bubble wall to time varying pressure will be greatest) at the bubble resonance. If that frequency component is present, then the magnitude of bubble oscillation will be significant because it can effectively absorb and scatter sound energy of this particular frequency. If the frequency component to which the bubble is responding to is known, then the radius can be calculated from equation 1.12 (see chapter 1). This reduces to the so-called Minnaert[64] equation when surface tension and viscosity effects are negligible (see equation 1.10 chapter 1). Sound of the correct frequency and pressure can induce a number of different oscillations of the bubble wall (fundamental motion, surface wave motion and higher order surface waves). Electrochemical detection of these modes of a bubble will now be presented.

5.1 Investigation of Subharmonic and Fundamental Motion of an Oscillating Bubble

The experimental set-up was described previously (see figure 2.3). The aqueous solution employed in the cell contained 5 mmol dm^{-3} $Fe(CN)_6^{4-}$ in 0.2 mol dm^{-3} $Sr(NO3)_2$. An air bubble was positioned under the glass rod. The potential of the electrode was held at –0.1 V *vs.* Ag where the reduction of $Fe(CN)_6^{3-}$ is mass transfer controlled. The microelectrode was positioned close to the bubble wall (*ca.* 5 - 10 μm away) using the X, Y, Z micrometer and stage, in the absence of sound irradiation (see section 4.1). The sound was switched on and the frequency and pressure of the sound field adjusted until there was a large enhancement in the time-averaged current passed at the microelectrode (see section 4.1). This large enhancement was attributed to the convective flow of solution to the microelectrode surface in response to the oscillation of the bubble wall. However, as well as observing large enhancements in mass transfer, the current was fluctuating with time (see figure 4.1). Therefore, recording equipment with a sample rate of 50 kHz (*e.g.* an oscilloscope) had to be employed to resolve the frequency component of the current time signal.

Figure 5.1 shows the current time and pressure time (recorded by the hydrophone) signals recorded under these conditions. This figure suggests that the current signal is predominantly at half the frequency of the applied sound field (frequency = 1398.5 Hz), which is confirmed by the frequency analysis of both the pressure and current signal (see figure 5.2). The signal recorded at half the driving frequency is caused by subharmonic motion of the bubble. Therefore the large enhancement in current observed in section 4.1 was in fact due to subharmonic oscillation of the bubble wall. It is also possible to see a small contribution to the current at the fundamental drive frequency (see figure 5.2). Detection of this signal will be explored in detail in the following section. The frequency analysis implies that as well as subharmonic motion of the bubble wall; the microelectrode is capable of detecting a component termed the breathing mode of the bubble wall (fundamental motion). This is understandable as there will always be some contribution from the breathing mode when the bubble is executing subharmonic motion, as it is this motion that excites subharmonic motion.

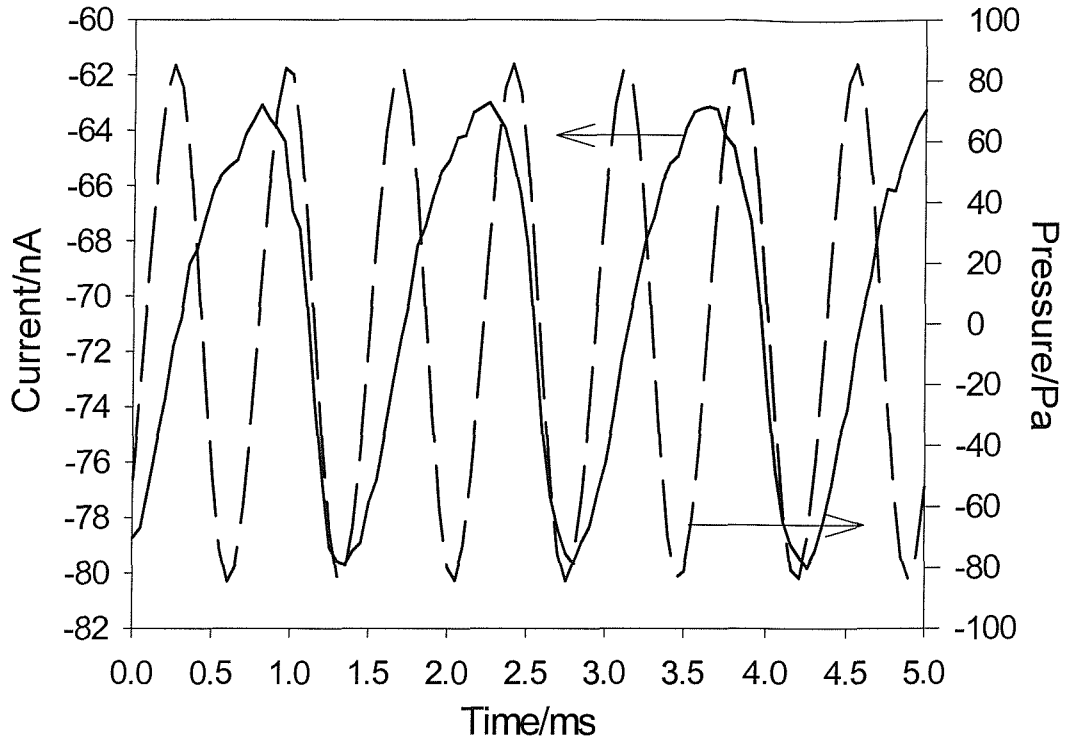

Figure 5.1 Plots showing the current/nA (—) detected at a 25 μm diameter Pt microelectrode and the pressure/Pa (---) detected by a hydrophone in 5 mmol dm^{-3} $Fe(CN)_6^{3-}$ in 0.2 mol dm^{-3} $Sr(NO3)_2$ caused by an air bubble (R_0 *ca.* 2.3 mm) interacting with a sound field at a frequency of 1.3985 kHz. The potential of the system was held at -0.1 V versus Ag wire and the pressure amplitude of the sound field was 55.6 Pa. The microelectrode bubble distance was *ca.* 5 - 10 μm.

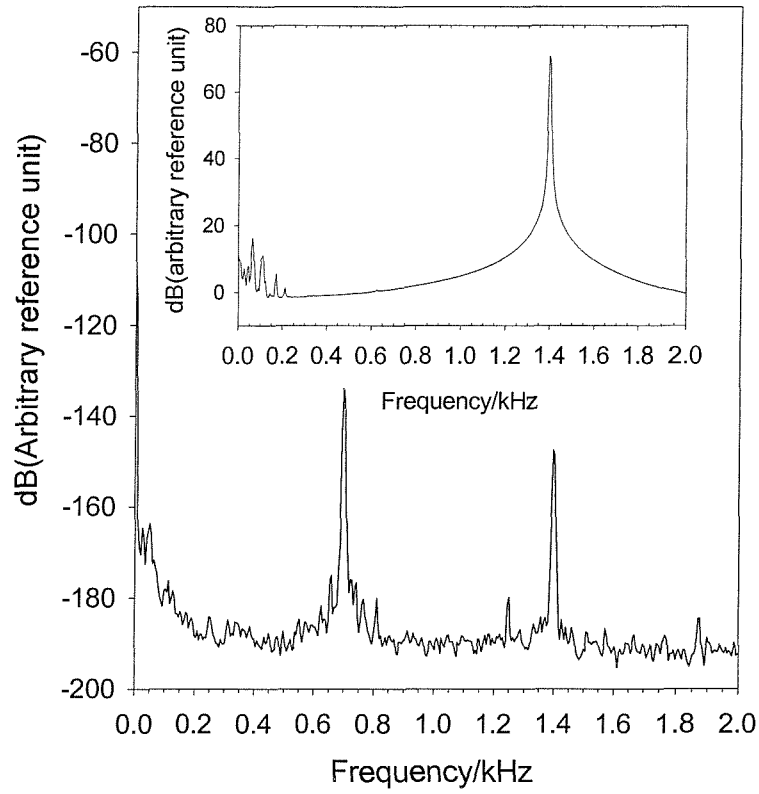

Figure 5.2 Plot showing the frequency analysis of the current time data shown in figure 5.1. The insert in the figure shows the frequency analysis of the pressure time data shown in figure 5.1. Note the y axis (dB) represents $10\log_{10}$(s/arbitrary unit) where s is the power spectral density calculated from FFT analysis of the time series data.

It was noted that subharmonic motion could be detected over a certain frequency and pressure range. This was investigated in more detail by monitoring the frequency and pressure range over which the subharmonic signal could be detected for a particular bubble using the experimental set up described previously. However, in this case a constant driving pressure was employed and the frequency adjusted until the current signal on the oscilloscope showed a frequency component at half the frequency of the driving sound field. Similarly in this case, in order to resolve the motion of the bubble wall with respect to time, recording equipment with a sampling rate of 50 kHz was employed. The extreme frequencies at which this motion began (as indicated by the subharmonic current signal) were recorded. This was repeated at a variety of drive pressures.

It is known that the pressure of a sound field varies in the absence and presence of bubbles. To illustrate this point figure 5.3 shows a plot of pressure recorded as a function of frequency[76] measured in the absence (dotted line) and presence (solid line) of an air bubble employing the experimental set-up shown in figure 2.3. Clearly the presence of a bubble affects the sound field. Therefore, the pressure amplitude of the sound field detected by the hydrophone in the above experiment was recorded in the absence of the bubble but with all other components and conditions fixed. This enabled the combinations of applied pressure and frequency at which subharmonic motion was observed to appear to be noted.

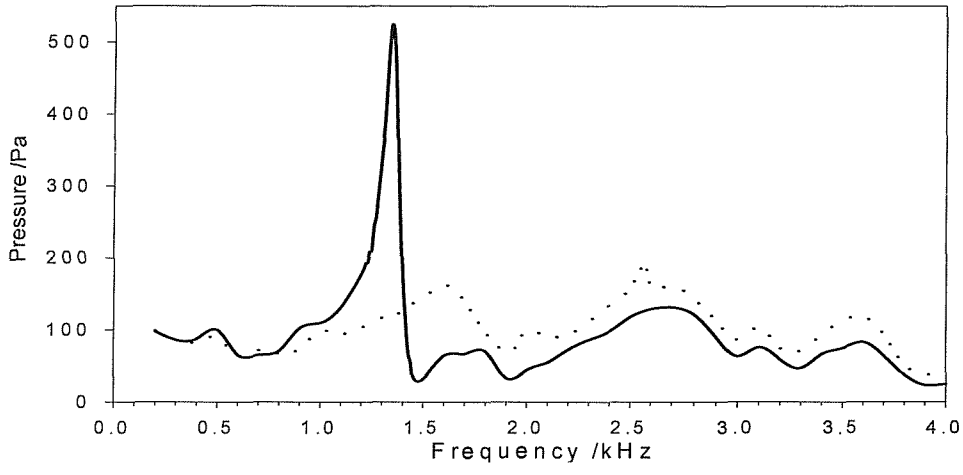

Figure 5.3 Plot of pressure against frequency in the presence (—) and absence (....) of a bubble. The radius of the bubble was *ca.* 2 mm. The solution employed was water.[76]

Figure 5.4 shows a plot of applied sound pressure amplitude (recorded in the absence of the bubble) against the sound frequency with the points indicating the pressure/frequency conditions for subharmonic motion detection using the electrochemical method described

above. Region I represents the frequency and pressure range over which subharmonic bubble motion was detected at the microelectrode for this particular bubble with a resonant frequency centered at 1.382 kHz. Outside this region (region II) subharmonic motion was not detectable. There is a minimum threshold pressure amplitude of 14 Pa (frequency = 1.382 kHz) indicating that subharmonic motion is initiated when the pressure amplitude exceeds a threshold value. As the pressure was increased above this threshold, the frequency range over which subharmonic motion was detectable gradually increased. This pressure threshold is discussed in more detail in section 5.4.

Clearly it is possible to detect subharmonic motion of the bubble wall using the electrochemical technique presented here. The fundamental breathing mode of the bubble was also investigated. The results of this study will now be discussed.

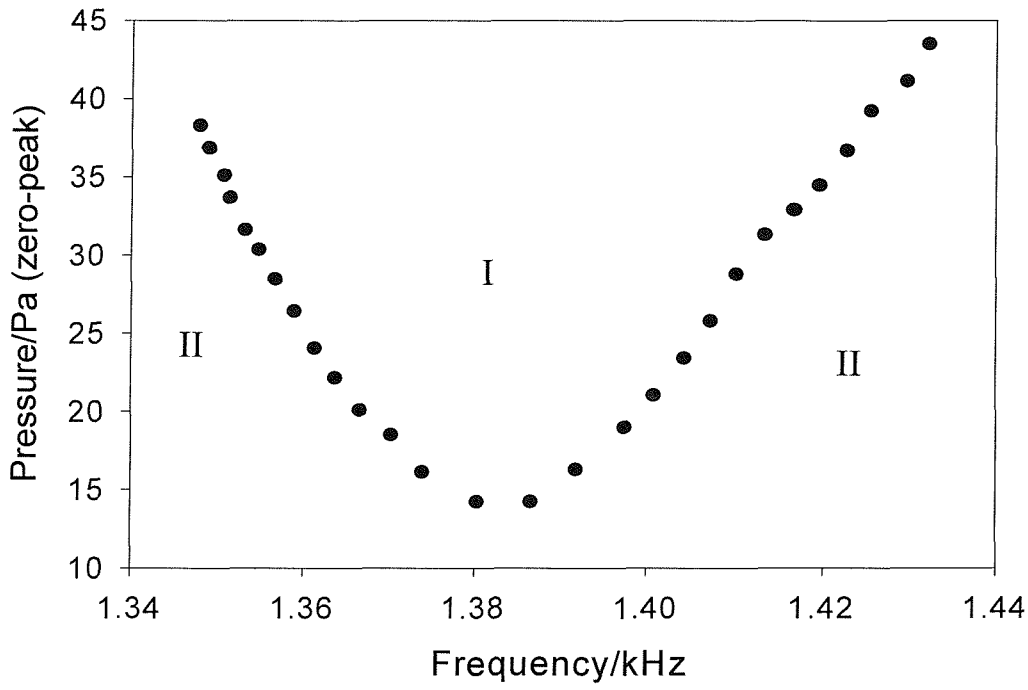

Figure 5.4 Plot showing the frequency/pressure range within which subharmonic oscillation of an air bubble resonant (R_0 *ca.* 2.3 mm) at 1.382 kHz in 5 mmol dm^{-3} $Fe(CN)_6^{3-}$/0.2 mol dm^{-3} $Sr(NO_3)_2$ can be detected by a 25 μm diameter Pt microelectrode. The potential was held at -0.1 V versus Ag wire. Region I represents the frequency and pressure range where the bubble oscillates subharmonically for this particular bubble while subharmonic oscillation is not seen in region II.

5.2 Electrochemical Detection of the Fundamental Frequency

In order to study the breathing mode motion of the bubble wall using an electrochemical technique a variety of experimental protocols were deployed. This enabled the investigation of both the effect of this motion on mass transfer to a microelectrode as a function of frequency and acoustic pressure amplitude and the temporal nature of the currents detected. The results of this study are now detailed.

5.2a Low Temporal Resolution

In section 5.1 it was determined that subharmonic motion only occurs when the driving pressure exceeds a certain threshold. It was therefore decided to reduce the driving pressure to a value below the threshold pressure required to generate subharmonic motion on the bubble wall, and initially employ equipment with the ability to record time averaged data (*i.e.* a relatively low sample rate due to averaging).

The experimental procedure was similar to that described previously (see section 5.1). The microelectrode was positioned close to the bubble wall in the absence of sound irradiation (potential held at –0.1 V *vs.* Ag). The sound was switched on and the frequency and pressure of the sound field was adjusted until the current signal on the oscilloscope showed a frequency component at half the frequency of the driving field. The extreme frequencies at which this motion was initiated were noted. The pressure of the sound field was then lowered until subharmonic motion was no longer visible in this frequency range. The time averaged current enhancement was then recorded as a function of frequency.

Figure 5.5 shows how the time averaged normalised current (I_N) at a microelectrode positioned close to a bubble wall varied as a function of drive acoustic frequency for two different bubbles. The current enhancement was small in comparison to that expected for subharmonic motion (see sections 4.1 and 5.1). Nonetheless the current frequency plot is clearly smooth with no sharp increase observed. The currents are smaller than those achieved for subharmonic motion but alter in a systematic way with respect to the applied acoustic drive frequency. The solid lines in the figure indicate the estimated bubble wall displacement amplitude calculated under the conditions using equation 1.6. Clearly the enhancement in current coincides with an increase in bubble wall displacement.

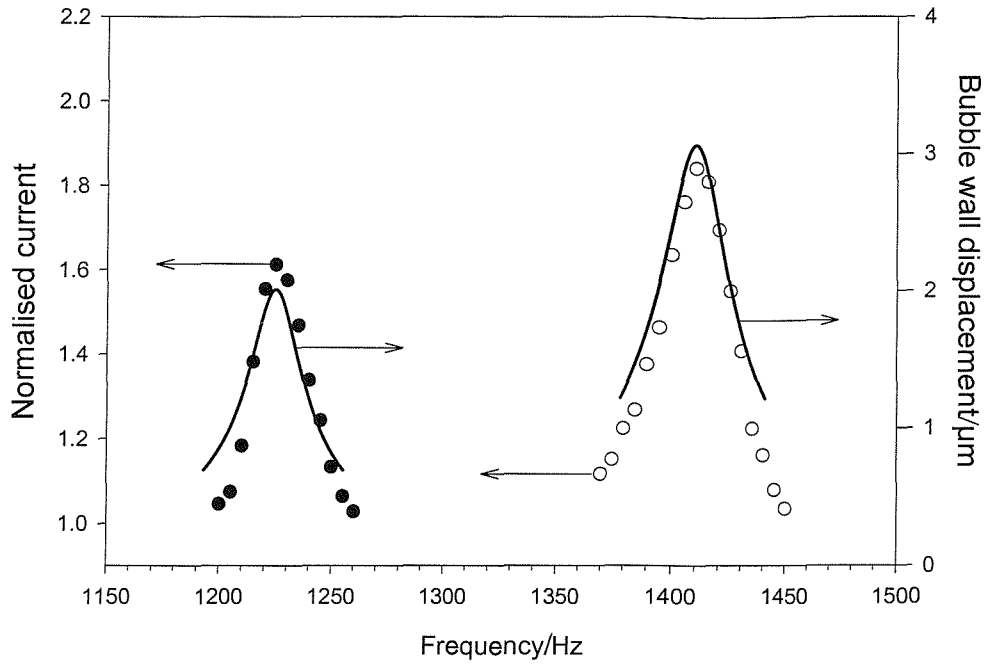

Figure 5.5 Plot showing time averaged normalised current recorded at a 25 μm diameter Pt microelectrode in 5 mmol dm^{-3} $Fe(CN)_6^{3-}$/ 0.2 mol dm^{-3} $Sr(NO_3)_2$ positioned close to the bubble wall (*ca.* 5 - 10 μm away) for two air bubbles driven into oscillation below the threshold for subharmonic excitation. In each case the excitation pressure amplitude was 5.8 Pa and 10.4 Pa for (•) and (○) respectively. The solid lines indicate the estimated bubble wall displacement amplitude[24] calculated under the conditions employing equation 1.6. The currents were normalised to the current recorded in the absence of sound irradiation (*i.e.* 6.82 nA and 8.85 nA for • and ○ respectively).

The enhancement in current is relatively small and likely to be due to the breathing mode of the bubble wall. However, further experimental evidence is required to substantiate this hypothesis. This evidence was obtained from observing the AC nature of the current enhancement and the frequency components of these mass transfer enhancements were then determined.

5.2b High Temporal Resolution

In order to resolve the motion of the bubble wall recording equipment with a sample rate of 50 kHz (*e.g.* an oscilloscope) had to be employed. This ensured that the complete current/time trace produced by the motion of the bubble wall was recorded. The potential was set at –0.1 V versus Ag where the reduction of the $Fe(CN)_6^{3-}$ ion is mass transfer controlled. The electrode was positioned close to the bubble wall and the frequency and pressure of the sound field adjusted until subharmonic motion was visible on the oscilloscope. The pressure of the sound field was then lowered until subharmonic motion

was no longer visible. However, the current signal showed a frequency component that was at the same frequency as the driving pressure (see figure 5.6 (—)). The potential was then stepped to 0.5 V *vs.* Ag wire a potential where no reduction of $Fe(CN)_6^{3-}$ takes place at the microelectrode and the current signal recorded in the presence of the sound field (see figure 5.6 (—)). This procedure was necessary to verify that signal observed at –0.1 V *vs.* Ag (—) was in fact due to the breathing mode and not due to electrical noise. At –0.5 V *vs.* Ag no alternating signal was observed. Figure 5.6 also includes the current recorded at –0.1 V *vs.* Ag (—) in the absence of an applied sound field and the pressure signal recorded by the hydrophone in the presence of the bubble (---).

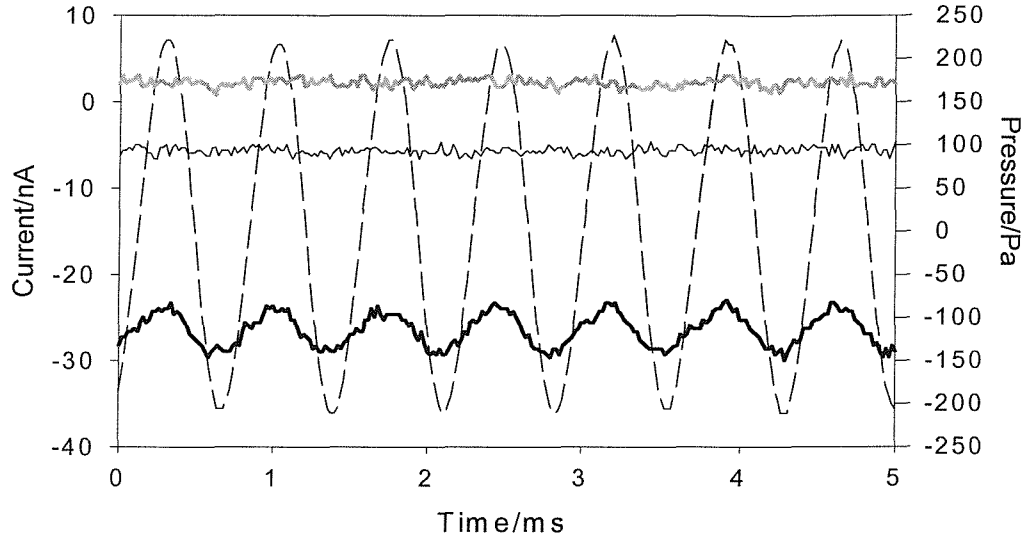

Figure 5.6 Plot showing the current recorded as a function of time in an experiment designed to measure fundamental motion of an air bubble wall (bubble radius *ca.* 2.3 mm). The traces show the current recorded at –0.1 V versus Ag with an applied sound field of 1.3839 kHz at 22.7 Pa (—), at +0.5 V versus Ag with an applied sound field of 1.3839 kHz at 22.7 Pa pressure amplitude (—) and at –0.1 V versus Ag with no applied sound field (—). The plot also includes the response of the hydrophone recorded simultaneously (---). The solution contained 5 mmol dm^{-3} $Fe(CN)_6^{3-}$ in 0.2 mol dm^{-3} $Sr(NO_3)_2$ at 20 - 22 °C under aerobic conditions. A 25 μm diameter Pt microelectrode was used to monitor the current signal.

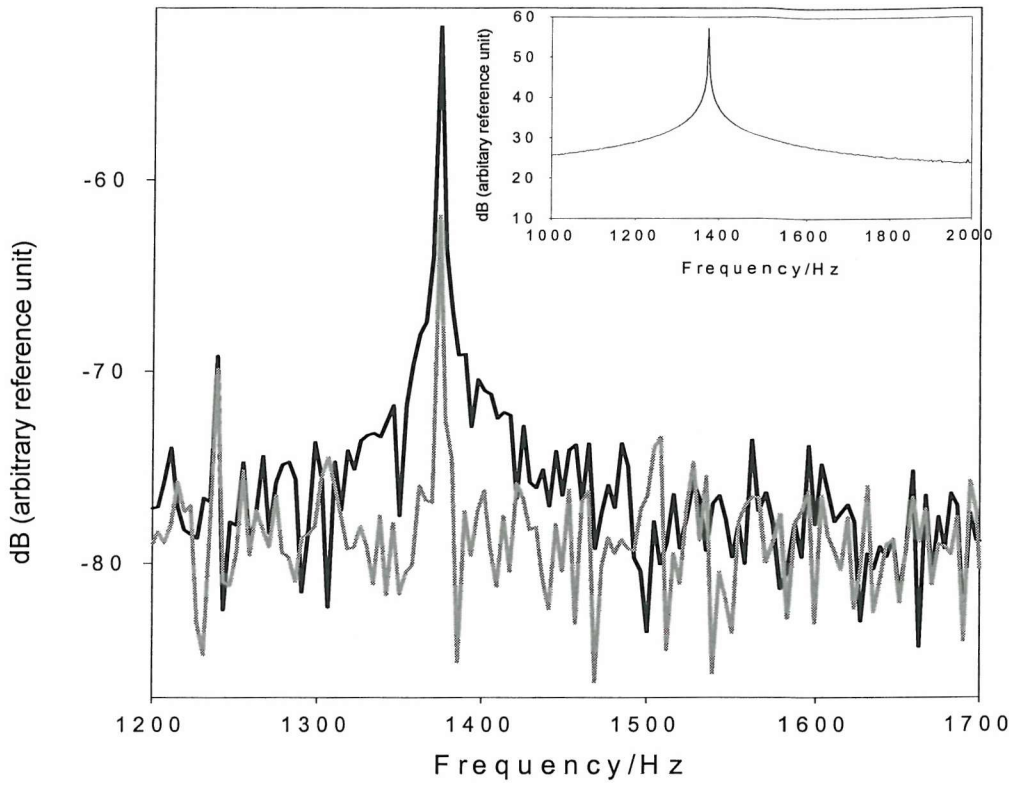

Figure 5.7 Plot showing frequency analysis of the current time data where (—) represents the sound on at –0.1 V *vs*. Ag and (—) represents the sound on at +0.5 V *vs*. Ag. The insert in the figure shows the frequency analysis of the pressure time data. Note the y axis (dB) represents $10\log_{10}(s/\text{arbitrary unit})$ where s is the power spectral density calculated from FFT analysis of the time series data.

Frequency analysis of the current time plots in the presence of sound confirmed the presence of the breathing mode (see figure 5.7 where (—) represents frequency analysis of the current/time signal in the presence of sound at –0.1 V while (—) represents frequency analysis of the current/time signal in the presence of sound at 0.5 V). The insert in figure 5.7 represents frequency analysis of the associated pressure time signal (—). Although there appears to be very little difference in the magnitudes of the signals obtained at –0.1 V and 0.5 V in figure 5.7, it must be recognised that the signal obtained at –0.1 V is *ca.* 10 dB above the signal obtained at 0.5 V (which represents background noise). This implies the signal obtained at –0.1 V is ten times stronger than that recorded at 0.5 V and thus significant in comparison to the background noise. This result shows that the signal obtained at –0.1 V in the presence of sound is in fact due to the breathing mode of the bubble and not the result of parasitic electrical pick up.

Detection of the breathing mode (fundamental bubble oscillation) is significant for a number of reasons. First, the results demonstrate that the motion of a gas bubble driven by an appropriate acoustic field, whether the breathing mode or the subharmonic oscillation is excited, can be monitored successfully by the electrochemical technique described here.

Second, the magnitude of the wall displacement of the breathing mode under these conditions (low pressures) is approximately 1 - 3 μm (see section 1.3) which is 100 times lower than that recorded for subharmonic bubble motion under similar conditions (see section 1.3). Therefore although the electrochemical detection of the breathing mode is much more difficult, it has been shown to be possible.

5.3 Individual Detection of Fundamental and Subharmonic Motion

5.3a High and Low Temporal Resolution Measurement of Fundamental and Subharmonic Motion at a Constant Frequency

The previous sections have shown that the electrochemical technique reported here, has the ability to resolve both the fundamental (see section 5.2) and subharmonic motion (see section 5.1) of the bubble wall. However, these modes exist under different conditions of pressure and frequency. The fundamental motion occurs at any pressure with the amplitude of motion highly frequency dependent, while subharmonic motion relies on some critical amplitude of oscillation to be exceeded. Hence subharmonic motion will be more easily generated at or close to the fundamental oscillation of the bubble (*i.e.* where the critical amplitude of subharmonic motion can be easily exceeded). It should be therefore possible, employing the electrochemical method described here, to measure the current contribution of each component (fundamental and subharmonic motion) as a function of pressure at a constant frequency. Such an experiment will be now described.

Employing the same experimental methodology, the electrode was positioned close to the bubble wall (potential held at –0.1 V *vs.* Ag) and the sound was switched on. The frequency and pressure of the sound field varied until the current signal on the oscilloscope showed a frequency component at half the frequency of the driving pressure (subharmonic and fundamental motion). The frequency and pressure amplitude of the driving signal were noted *i.e.* 1.167 kHz and 22.9 Pa respectively. Maintaining a constant driving frequency the driving pressure amplitude was adjusted to 14.97 Pa. At this pressure the current signal showed a frequency component on the oscilloscope at the same frequency as the driving pressure (breathing mode). As the pressure of the sound field was increased sequentially from 14.97 to 20.57 Pa an enhancement in current was noted and the AC modulation of the

current signal became more pronounced but still occurred at the same frequency as the driving pressure. This is evidence that the current enhancement is caused by the breathing mode of the bubble. Both high and low temporal resolution current time data were recorded at each driving pressure.

Figure 5.8 is a series of current time plots at different driving pressure amplitudes while maintaining a constant driving frequency of 1.167 kHz. The current increased as the driving pressure amplitude was increased from 14.97 Pa to 20.57 Pa as expected. The plot also includes the pressure time plot of the driving signal recorded by the hydrophone (—) in the presence of the bubble and the current recorded in the absence of sound (—). The low frequency modulation in figure 5.8 (slope in current from left to right) is attributed to the bubble centre moving with respect to the microelectrode.

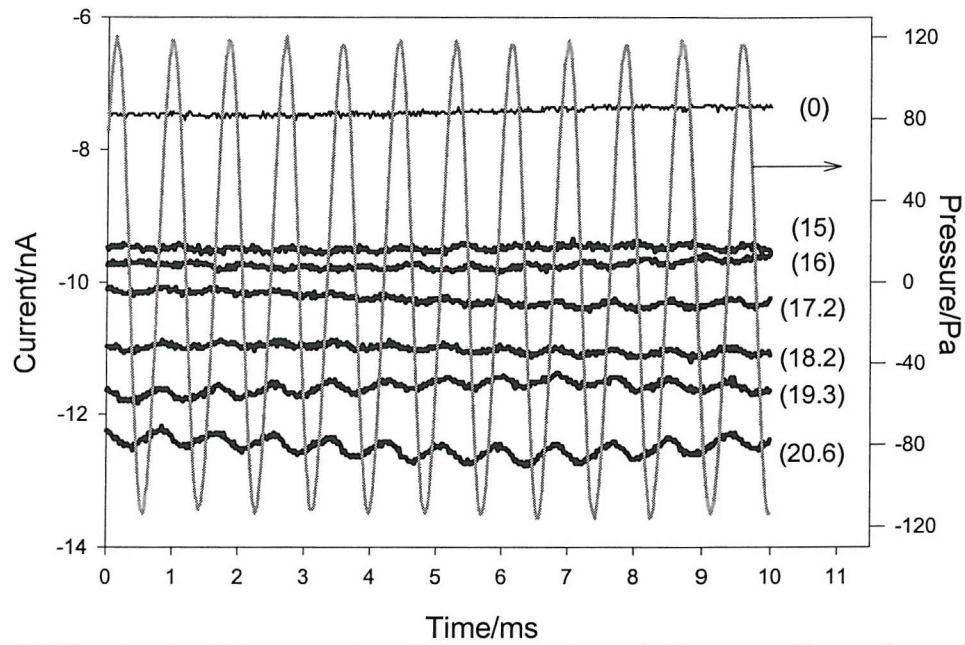

Figure 5.8 Plot showing high temporal resolution current (recorded by an oscilloscope) recorded by a 25 μm diameter Pt microelectrode in 5 mmol dm^{-3} $Fe(CN)_6^{3-}$/ 0.2 mol dm^{-3} $Sr(NO_3)_2$ as a function of time as the acoustic pressure was increased. (—) represents the current recorded in the absence of sound. (—) represents the acoustic driving pressure measured simultaneously in the presence of the bubble (R_0 *ca.* 2.75 mm) for reference. (—) represents the current recorded in the presence of sound with an increase in driving pressure amplitude from top to bottom (*i.e.* from 14.97 Pa to 20.57 Pa) at a constant driving frequency of 1.167 kHz.

Figure 5.9 shows how the time average current varied as a function of drive pressure amplitude at a constant drive frequency. The current can be seen to progress cathodically from 14.97 Pa to 20.57 Pa until a critical pressure amplitude is obtained at 20.57 Pa. As the pressure was increased above this value large enhancements in current recorded at the microelectrode were noticed which correspond to subharmonic motion of the bubble wall. This was further confirmed by analysis of the AC component of the current recorded on the oscilloscope. Figure 5.10 shows the current time relationship for 21.7 and 22.9 Pa driving

pressure amplitudes. The current time behaviour occurs at half the driving frequency and is indicative of subharmonic motion.

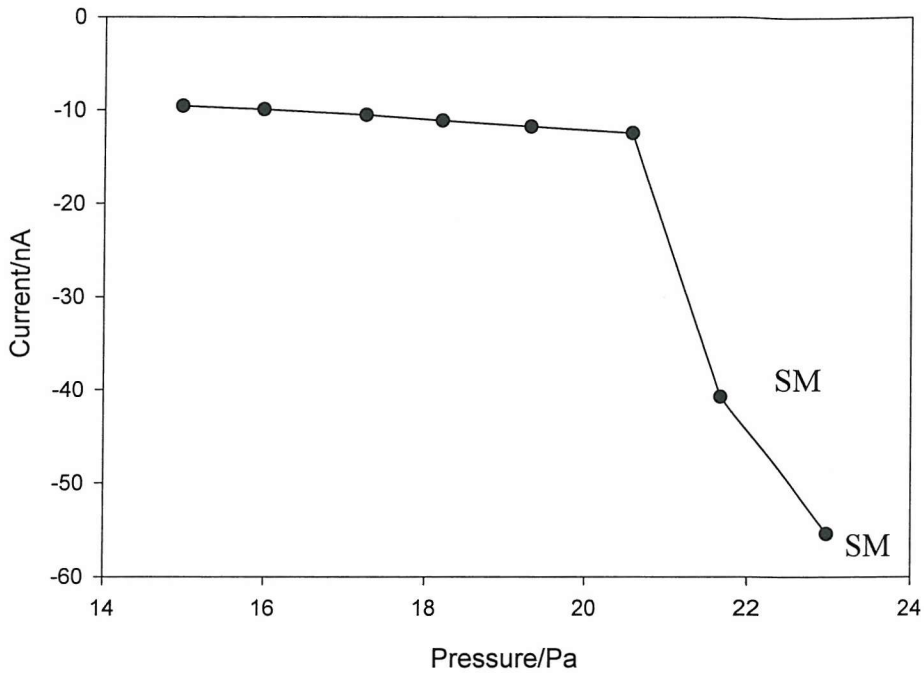

Figure 5.9 Plot showing low temporal resolution current recorded for a single air bubble (R_0 *ca.* 2.75 mm) driven into oscillation as a function of acoustic driving pressure amplitude (zero-peak). The points labelled 'SM' represent those experiments where subharmonic motion was observed. The experimental conditions were the same as in figure 5.8.

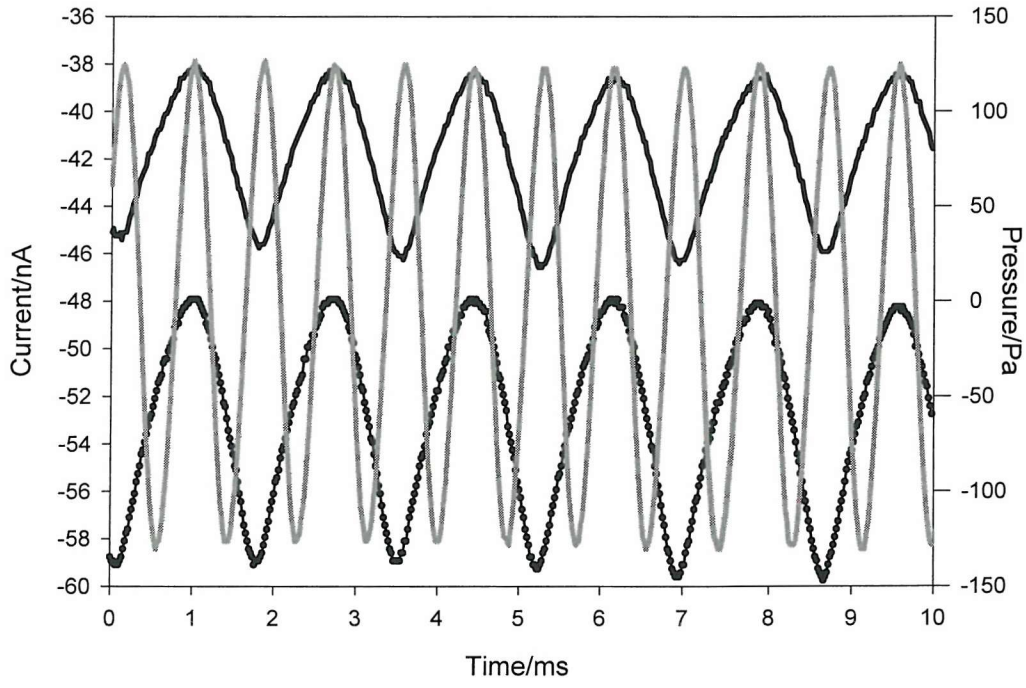

Figure 5.10 Plot showing high temporal resolution (recorded by an oscilloscope) current for the subharmonic electrochemical signals labelled 'SM' on figure 5.9. (—) represents the acoustic pressure measured simultaneously in the presence of the bubble (R_0 *ca.* 2.75 mm) for reference. The acoustic pressure amplitudes (zero-peak) were 21.7 Pa (—) and 22.9 Pa (—•) while the drive frequency was maintained at 1.167 kHz. All other experimental conditions are described in figure 5.8.

This experiment illustrated the ability of the electrochemical technique to resolve both the breathing mode and subharmonic motion of an oscillating bubble. Clearly when a critical pressure amplitude was reached subhamonic motion was initiated. It should be also possible using the electrochemical technique described here, to measure the current contribution of both components as a function of frequency but at constant driving pressure. This will be described in the subsequent section.

5.3b Low Temporal Resolution Measurement of Subharmonic and Fundamental Bubble Oscillation at a Constant Driving Pressure Amplitude

In order to quantify the contribution to the current recorded at the microelectrode placed next to the gas/liquid interface as a function of frequency, the following experiment was performed. Initially the background current in the bulk solution was recorded in the absence of sound irradiation of the bubble (potential of the electrode held at –0.1 V versus Ag where the reduction of $Fe(CN)_6^{3-}$ is mass transfer controlled). The microelectrode then was positioned close to the bubble wall (5 - 10 μm away) in the absence of sound irradiation. Maintaining a constant drive pressure, the frequency of the sound field was adjusted until the microelectrode detected a current signal with a frequency component at half the driving pressure (subhamonic motion and fundamental motion; see section 5.1). Recording equipment with a sampling rate of 50 kHz was employed in this case to resolve the motion of the bubble wall. The extreme frequencies at which this motion began were noted. This was repeated at a number of drive pressures. A plot of pressure amplitude (recorded by the hydrophone in the absence of the bubble at each combined frequency and driving pressure, see section 5.1) against frequency (threshold pressure curve, see figure 5.4) is illustrated in figure 5.11 (region II). The driving pressure amplitude was then set to 41 Pa and the frequency was swept over a large range (1.25 kHz – 1.46 kHz). The time-averaged current recorded at the microelectrode was measured over the frequency range scanned. A plot of enhanced current (caused by the motion of the bubble wall) against frequency is also included in figure 5.11.

Significant enhancements in mass transfer to the microelectrode were observed over the frequency range denoted by region II enclosed by the dashed lines in figure 5.11. This was due to subharmonic oscillation of the bubble. However, smaller mass transfer enhancements to the microelectrode (when compared to the background current) were recorded outside this frequency range (see figure 5.11 region I). This is attributed to the breathing mode of the

bubble. Observing the AC component of the current using an oscilloscope confirmed this assignment. For example in region (I) the AC component of the current occurred at the drive frequency (ω), which is indicative of the fundamental oscillating motion of the bubble wall. The long dashed line represents the current recorded in the absence of sound.

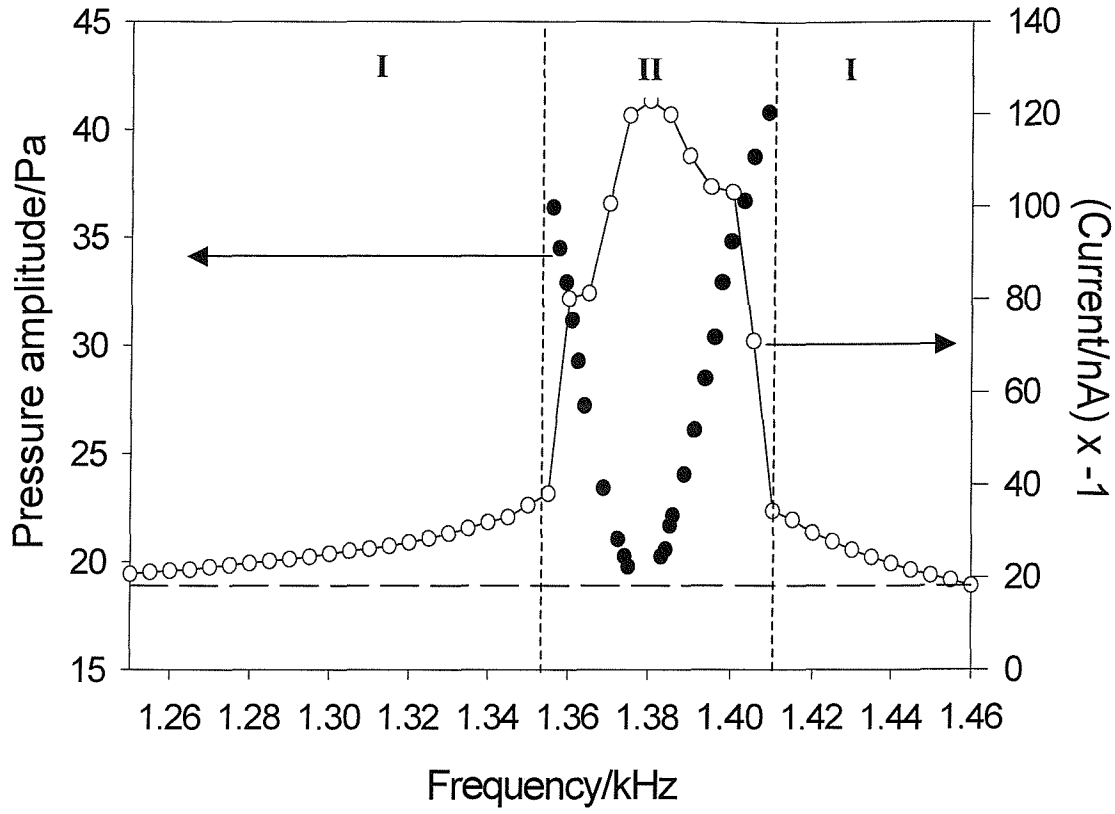

Figure 5.11 Plot showing the pressure amplitude (zero-peak) against frequency (•) (region II) within which subharmonic oscillation of an air bubble (*ca.* 0.0023 mm radius) in 5 mmol dm^{-3} $Fe(CN)_6^{3-}$ can be detected by a 25 μm diameter Pt microelectrode. The potential was held at –0.1 V *vs.* Ag. The scatter and line plot (○—) extending over the entire frequency band represents the current recorded at the microelectrode employing low temporal resolution equipment against frequency at a constant driving pressure amplitude (zero-peak) of 41 Pa. The dashed line represents the current recorded by the microelectrode in the bulk solution in the absence of sound irradiation.

The demarcation between the breathing mode and the presence of subharmonic motion of the bubble wall is clearly illustrated in this figure by plotting the threshold pressure curve on the same plot. The region at which this occurs coincides with the region in the frequency current plot where the sharp increase in current was observed.

These results demonstrated that the contribution to mass transfer by fundamental motion is significant (mass transfer coefficient k_m < 0.0148 cm s^{-1} when compared to 0.008 cm s^{-1} for a microelectrode in the bulk) and extends over a wide frequency range (1.25 – 1.46 kHz). However, the contribution to mass transfer of subharmonic motion can be seen to be significantly higher (k_m = 0.0477 cm s^{-1}) but over a narrower frequency band (1.35 – 1.41

kHz). This is a significant observation as it demonstrates that bubble oscillation (breathing mode or Faraday wave) will have a considerable contribution to mass transfer within a bubbly environment (under the correct physical conditions of frequency/pressure) but the mass transfer contribution could vary significantly depending on which mode is excited.

Clearly the ability to resolve both subharmonic and fundamental bubble motion employing an acousto-electrochemical technique has been established in sections 5.1 - 5.3. The conditions of frequency and pressure required to generate these modes was also ascertained. At this stage, it is important to determine whether the subharmonic signal observed in sections 5.1 and 5.3 is in fact due to subharmonic oscillation caused by the onset of surface waves. This will be explored in the following section.

5.4 Surface Waves Detected by a Microelectrode

When a gas bubble in a liquid is set into radial oscillating motion, a departure from the spherical shape can be observed on account of surface waves[51] (see figure 5.12). For the description of the surface distortions only the modes with $n \geq 2$ are relevant. In fact, $n = 0$ corresponds to oscillations in volume with fixed shape (pulsations), and $n = 1$ to a translation of the entire bubble. Francescutto and Nabergoj[51] derived an equation for the amplitude threshold normalised wall displacement required for the onset of these radial oscillations (ratio of the radial displacement of the bubble wall to the equilibrium radius) and compared this to results obtained by Hullin[72] who accurately measured the amplitude of these surface waves by a stroboscopic illumination method. Hullin[72] showed that the surface deformed at exactly half the excitation frequency. The normalised wall displacement amplitude (C_t) derived by Francescutto and Nabergoj[51] for the onset of surface waves was based on equation 5.1:

$$C_t = \frac{R_{\varepsilon 0}}{R_0} \tag{5.1}$$

where $R_{\varepsilon 0}$ is the radial displacement amplitude of the bubble wall and R_0 is the equilibrium bubble radius. The equation derived by Francescutto and Nabergoj[51] is given by equation 1.14 in chapter 1.

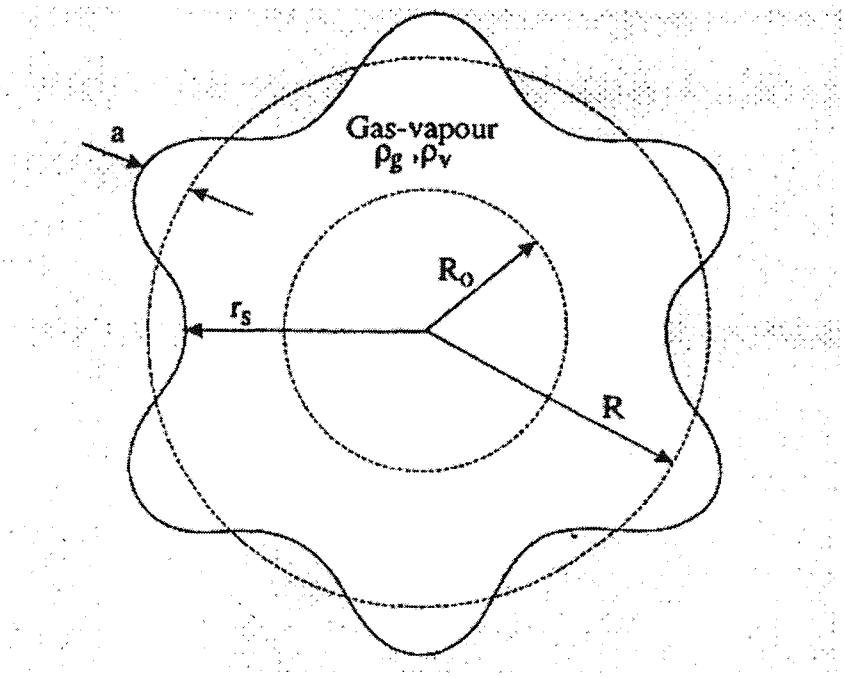

Figure 5.12 Representation of the non-spherical bubble. Here only the spherical harmonic of order $n = 6$ is considered and p_v is vapour pressure and r_s is radial distance from the centre of the bubble to its surface. Reproduced by Francescutto *et al.*.[51]

Figure 5.13 illustrates the theoretical curves reported by Francescutto and Nabergoj[51] showing C_t at resonant frequency *i.e.* C_{t0} versus equilibrium radius (R_0) relative to surface modes $n = 7$ - 12 for bubbles in water. The plot also includes the results of Hullin where there is difference between fresh and standing water. This maybe due a decrease in surface tension (see chapter 6) as a result of the accumulation of impurities into the system.[72] The agreement between with theoretical predictions and experimental is satisfactory particularly for the higher order modes. The authors also remarked that the easiest excitable mode, for a given equilibrium radius (R_0) is subharmonic which is in agreement with Hullin.[72] Previous authors[112,113] limited their analysis to the lowest mode $n = 2$ disregarding higher modes nearer to subresonance by considering them to be highly damped by viscosity.

Figure 5.14 is a plot of C_{t0} (*i.e.* C_t at the resonant frequency) against R_0 as determined from equation 1.14 in the radius range of bubbles employed in this thesis. The value of C_{t0} decreases as the bubble size increases, which agrees with the figure 5.13, derived by Francescutto and Nabergoj.[51] However, as the mode number increases from 13 through to 16 the difference in C_{t0} decreases with increasing mode number.

The subsequent section will introduce an extension to the theory proposed by Francescutto and Nabergoj[51] to determine the threshold pressure amplitude required to induce surface waves. This will be compared to the threshold pressure for the onset of

subharmonic motion determined from experimental data (see section 5.1).

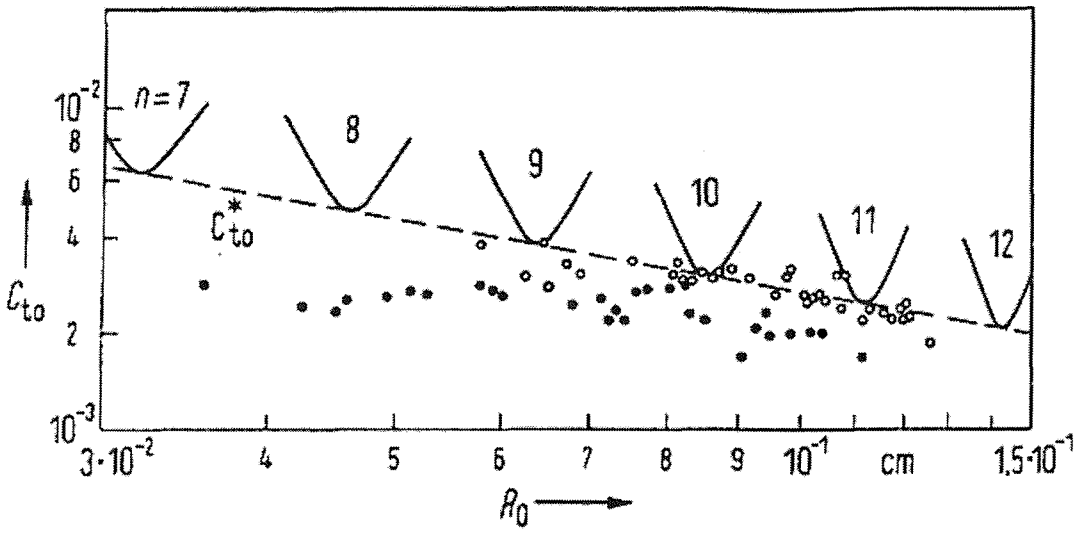

Figure 5.13 Predicted amplitude threshold wall displacement (C_{t0}) (C_t at resonant frequency) derived by Francescutto[51] versus equilibrium radius (R_0) for bubbles in water driven at resonant frequency compared with the results of Hullin[72] where (•) represents fresh tap water and (o) standing tap water. Reproduced from Francescutto and Nabergoj.[51]

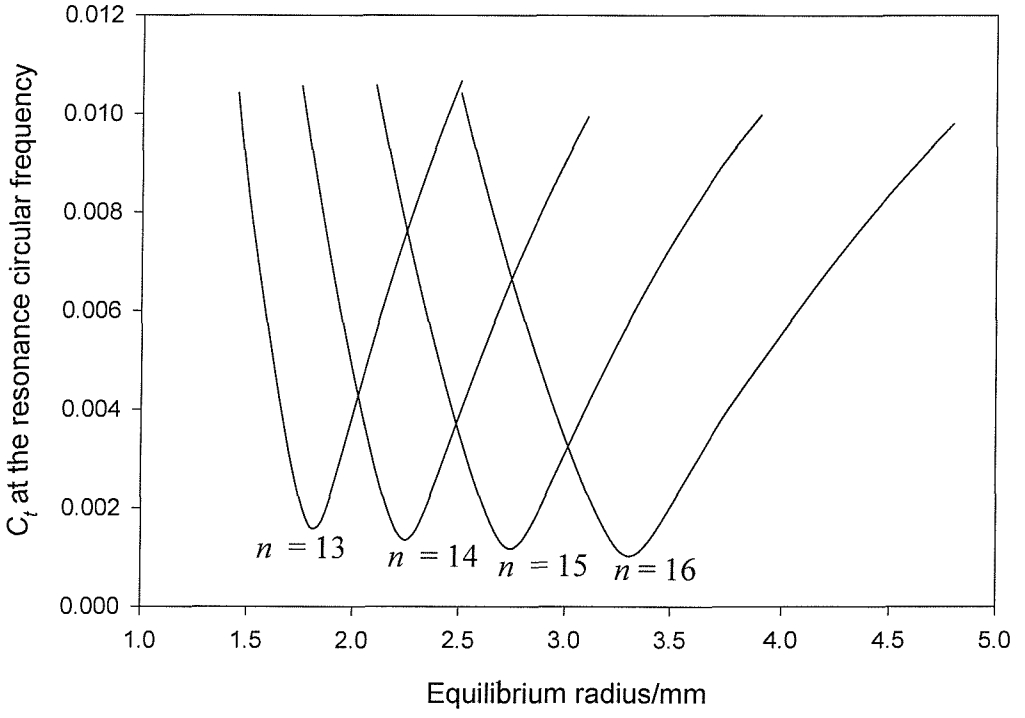

Figure 5.14 Plots of C_{t0} (*i.e.* C_t at the resonant frequency) against R_0 for bubbles in radius range employed in this thesis. C_{t0} was calculated employing equation 1.14 assuming a surface tension of 0.072 N m^{-1}, a dynamic viscosity of 8.91 x 10^{-4} kg m^{-1} s^{-1} and a density of 1000 kg m^{-3}.

5.4a Modified Theory

The pressure amplitude for Faraday motion can be calculated by substituting equation 1.6 (chapter 1) derived by Leighton and co-workers,[24,74] for $R_{\varepsilon 0}$, into equation 5.1 to generate the desired pressure threshold prediction[75] given by equation 5.2:

$$P_A = P_T = R_0{}^2 \rho C_t [(\omega_0{}^2 - \omega^2)^2 + (\omega^2 d_{tot})^2]^{1/2} \qquad (5.2).$$

Here P_A represents pressure amplitude (zero-peak), ω the driving frequency, R_0 the equilibrium radius, ρ the density of the liquid, ω_0 the resonant frequency[77] (given by equation 1.12) and d_{tot}, the dimensionless damping coefficient[74] (given by equation 5.3):

$$d_{tot} = \frac{4\omega\mu}{3\kappa p_0} + \frac{\rho(R_0\omega)^3}{3\kappa p_0 c_i} + d_{th} \qquad (5.3)$$

where μ is the dynamic viscosity, κ is the polytropic index,[114,115] c_i is the speed of sound and d_{th} is the thermal damping coefficient given by equation 5.4:

$$d_{th} = \frac{1.2\left(\left(\frac{R_0}{\sqrt{\frac{D_g}{2\omega}}}\left(\sinh\left(\sqrt{\frac{D_g}{2\omega}}\right) + \sin\left(\sqrt{\frac{D_g}{2\omega}}\right)\right)\right) + \left(2\left(\cosh\left(\sqrt{\frac{D_g}{2\omega}}\right) - \cos\left(\sqrt{\frac{D_g}{2\omega}}\right)\right)\right)\right)}{\frac{D_g}{2\omega}\left(\cosh\left(\sqrt{\frac{D_g}{2\omega}}\right) - \cos\left(\sqrt{\frac{D_g}{2\omega}}\right)\right) + \left(1.2\left(\sqrt{\frac{D_g}{2\omega}}\right)\left(\sinh\left(\sqrt{\frac{D_g}{2\omega}}\right) - \sin\left(\sqrt{\frac{D_g}{2\omega}}\right)\right)\right)} \qquad (5.4)$$

where D_g is the thermal diffusivity given by equation 5.5:

$$D_g = \frac{K_g}{\rho' C_p} \qquad (5.5)$$

where K_g is the thermal conductivity of a gas, C_p is specific heat capacity at constant

pressure and ρ' is the density of air.

The threshold pressure required to excite surface waves given by equation 5.2, will now be compared to experimental threshold pressures determined for the onset of subharmonic motion (see section 5.1) to determine whether subharmonic motion is caused by the onset of surface waves.

5.4b Electrochemical Measurement of Surface Waves

Figure 5.15 shows the results from an experiment conducted on a single bubble retained under a glass rod. The frequency and pressure range over which subharmonic oscillation occurred was determined (see section 5.1). Again the actual pressure threshold amplitude was measured under identical conditions once the bubble had been removed. Figure 5.15 shows that the pressure threshold exhibits a minimum presumably around the resonant frequency of the bubble. This is expected if Faraday waves are the source of the $\omega/2$ component detected in the current. This is because at bubble resonance, the wall displacement amplitude of the bubble wall is the greatest (*i.e.* the response of the bubble wall to time varying pressure will be greatest). Hence, the amplitude threshold will be exceeded at the lowest driving force or acoustic pressure amplitude. When the frequency of the driving frequency moves away from resonance, the amplitude of wall pulsation will decrease. Therefore this frequency shift will require the corrective measure of increasing the amplitude of the driving sound field, in order to return the bubble to the threshold condition. Final evidence was obtained by plotting on figure 5.15 the theoretical prediction for the pressure amplitude required to generate surface waves in resonant bubbles (see equation 5.2 section 5.4a).

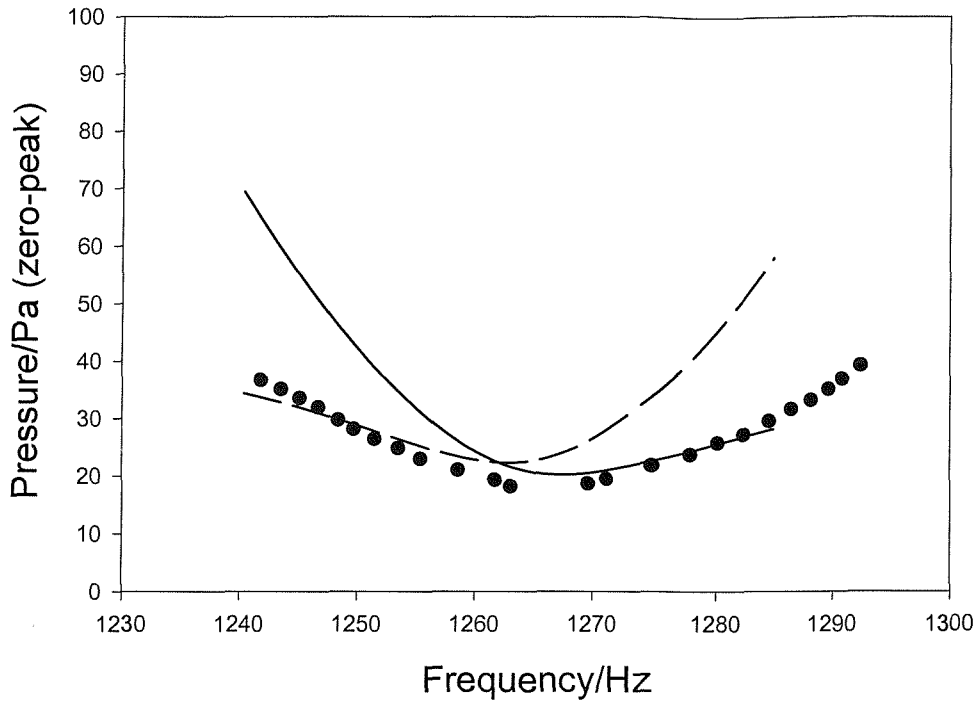

Figure 5.15 Plot showing the onset of Faraday waves (•) detected using the electrochemical detection method described in section 5.1 (bubble radius *ca.* 2.5 mm). The lines represent the pressure threshold amplitude (zero-peak) for an n (the order of the mode) = 15 (----) and n = 16 (—) modes of oscillation. The pressure thresholds were calculated using equation (5.2) and assuming a surface tension of 0.0606 N m^{-1} and 0.059 N m^{-1} for n = 15 and n = 16 mode numbers respectively. The other physical parameters were as follows: the speed of sound in the liquid was 1480 m s^{-1}, the viscosity was 8.91 x 10^{-4} kg m^{-1} s^{-1}, the hydrostatic pressure was 101 kPa, the polytropic index was 1.38, the vapour pressure was 3.54 kPa, the density of air was 1.16 kg m^{-3}, the thermal conductivity of air was 0.00253 J m^{-1} s^{-1} K^{-1}, the heat capacity was 1007 J kg^{-1} K^{-1} and the density in the liquid was 1000 kg m^{-3}.

Note that on figure 5.15 n = 15 and n = 16 are plotted indicating that the mode number, under these conditions, changes as the frequency of the driving pressure field is increased from 1.24 kHz to 1.29 kHz. However, the AC component in the current will be at $\omega/2$. Hence experimental evidence for this change is difficult to obtain from electrochemical data alone (see section 5.1). Photographic evidence would be required. It must be also noted that these modes exhibit the lowest threshold pressure amplitude under the conditions of the experiment.

Figure 5.15 shows there is good agreement between the theory and experimental data. It should be noted, however, that the model is extremely sensitive to the physical parameters, particularly the surface tension. The measured value for the system was 0.058 N m^{-1} (see experimental chapter 2). Values of 0.0606 and 0.059 N m^{-1} were employed in the theory. This results in an error of approximately 4 % between the measured and theoretical value for surface tension highlighting the sensitivity of the model to this parameter. There is also an assumption made in the comparison between the theory and the experimental data *i.e.* the

theory assumes a spherically symmetric bubble while in the experiment the presence of the glass rod will compromise this assumption.

The sensitivity of the model to surface tension (see section 2.7d) can be further exemplified in figure 5.16 which is a plot of threshold pressure amplitude (zero-peak) against frequency at varying surface tensions for a bubble resonant at 1.265 kHz and mode number n = 16. The surface tension was increased from 0.055 N m^{-1} to 0.063 N m^{-1} in increments of 0.002 N m^{-1}. It can be clearly seen that a variation in surface tension of 0.002 N m^{-1} changes the threshold pressure required to excite surface waves by *ca.* 5 Pa with the experimental data from figure 5.15 fitting at a surface tension of 0.059 N m^{-1}. The value measured experimentally was 0.058 N m^{-1}.

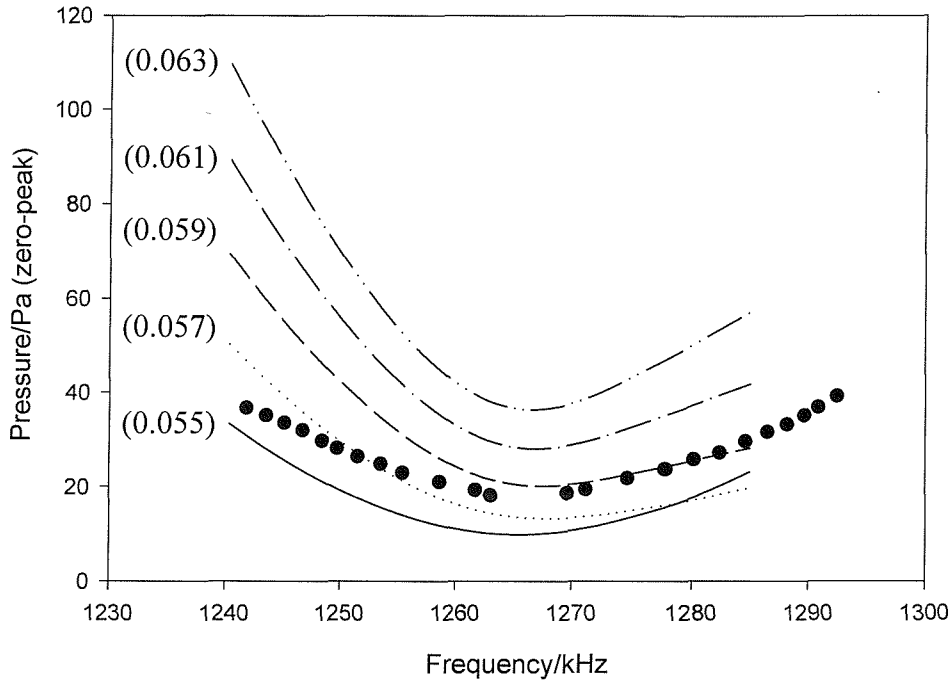

Figure 5.16 Plot of threshold pressure amplitude (zero-peak) against frequency at increasing surface tension from bottom to top for a bubble resonant at 1.265 kHz and mode number n = 16. The surface tension was increased from 0.055 N m^{-1} to 0.063 N m^{-1} in increments of 0.002 N m^{-1}. The pressure thresholds were calculated using equation (5.2) and assuming a speed of sound in the liquid of 1480 m s^{-1}, a viscosity of 8.91 x 10^{-4} kg m^{-1} s^{-1}, a hydrostatic pressure of 101 kPa, a polytropic index of 1.38, a vapour pressure of 3.54 kPa, a density of air of 1.16 kg m^{-3}, a thermal conductivity of air of 0.00253 J m^{-1} s^{-1} K^{-1}, a heat capacity of 1007 J kg^{-1} K^{-1} and a density of the liquid of 1000 kg m^{-3}. The dotted plot (•) shows the onset of Faraday waves detected using the electrochemical detection method described in section 5.1.

5.4c Photographic Detection of Surface Waves

In order to obtain complementary evidence for Faraday wave motion of the bubble wall high-speed video imaging was performed. These experiments employed a high-speed video camera (outlined in section 2.5) to record the position of the bubble wall with respect to the

microelectrode while simultaneously recording the current (recorded at the microelectrode) and pressure (recorded with a 8103 Bruel and Kjaer hydrophone placed next to the bubble retained under a glass rod). The results of this study will now be presented.

5.4c i Detecting Time Displacement Amplitude

In order to image the motion of the bubble wall with respect to the microelectrode, the position and focus of the camera was adjusted until a clear picture of the bubble and microelectrode was seen on the monitor. Figure 5.17 illustrates an image obtained using the high-speed video camera. The image shows the instantaneous position of the bubble wall with respect to the microelectrode and also gives an indication of the size of the electrode tip compared to the bubble wall.

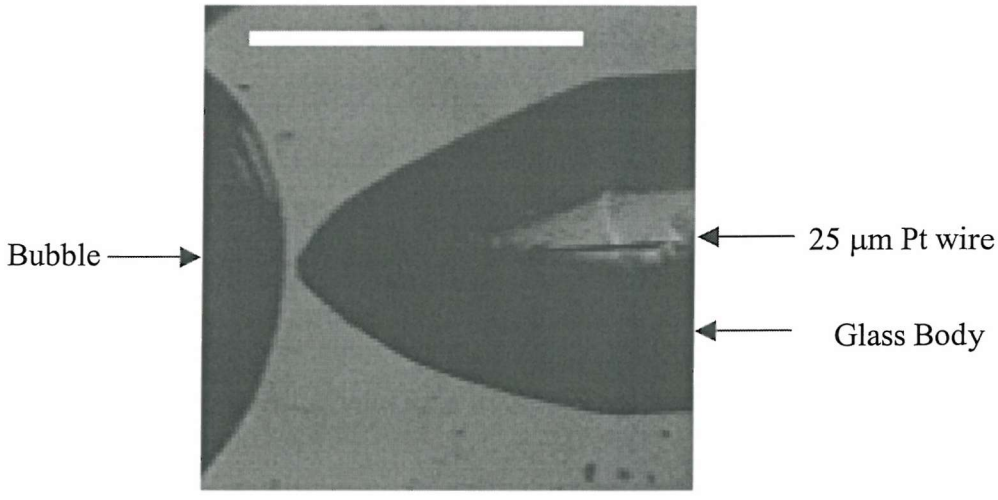

Figure 5.17 Picture taken using the high-speed video camera. The scale bar represents 0.75 mm. The recording rate was 13500 frames per second.

Figure 5.18 shows a series of images recorded at 13500 frames a second of the motion of the bubble wall driven into oscillation by an appropriate sound field. It should be noted that a subharmonic component in the current time trace (not shown) was observed indicating that surface wave oscillation had been excited. Figure 5.18 shows the first 30 individual frames as recorded. The displacement amplitude of the bubble wall can be calculated from this sequence of pictures.

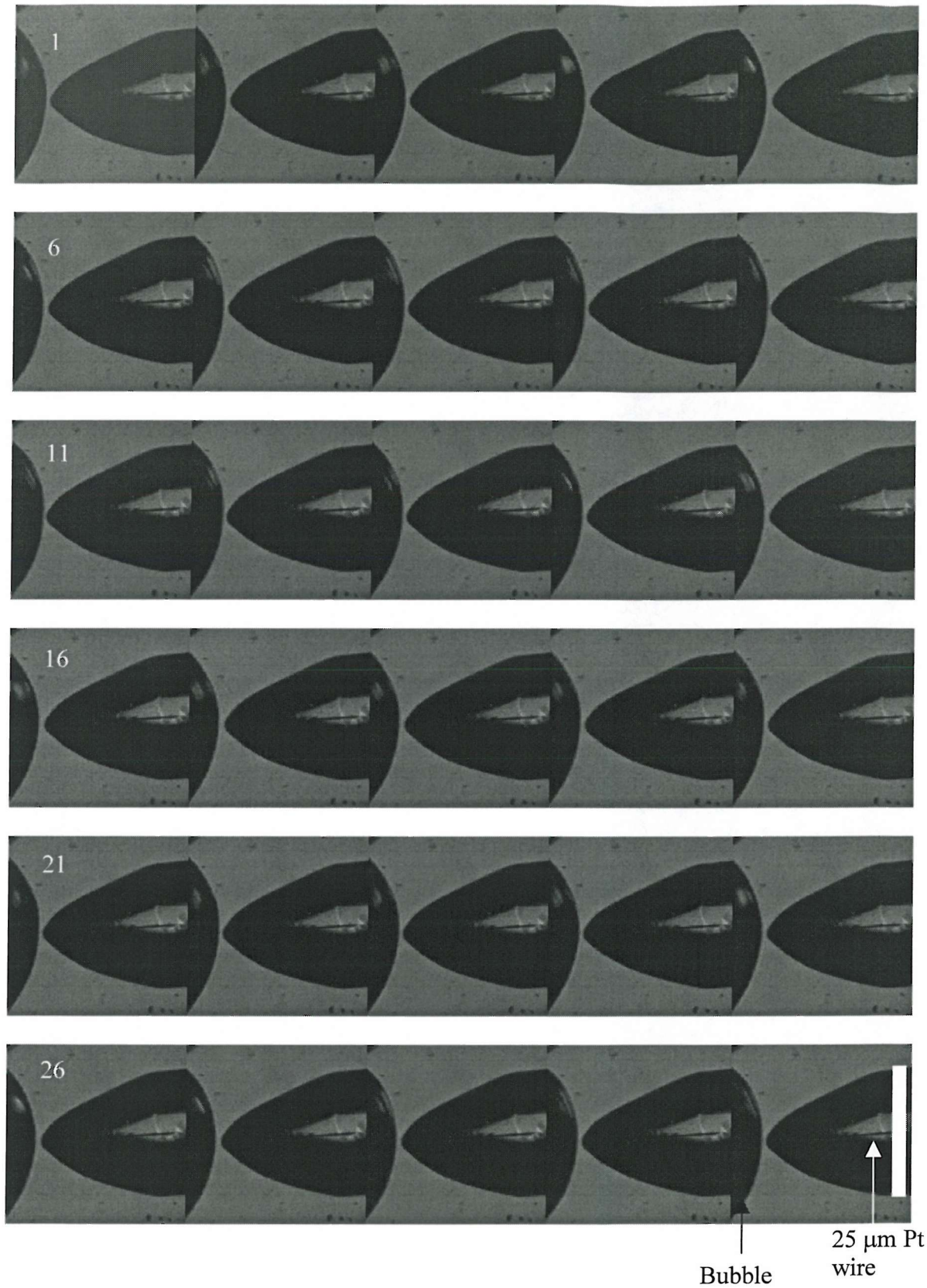

Figure 5.18 The first 30 frames recorded over a period of 2.22 ms for a bubble (R_0 *ca.* 2.5 mm) oscillating in the presence of a sound field operating at 1.2553 kHz and 62 Pa pressure amplitude. The distance between the bubble wall and the microelectrode varies over this time due to the motion of the bubble wall. Scale bar represents 0.75 mm.

Figure 5.19 is a plot of the displacement of the bubble wall against time determined by measuring the distance between the bubble wall and the tip of the microelectrode for each frame in figure 5.18. This was achieved using the 25 μm diameter Pt wire as a scale. The error in displacement data derived from the pictures was ± 10 μm. From this figure the amplitude of wave motion was determined to be *ca.* 30 μm. The driving frequency in this case was 1.2553 kHz. The dashed lines in figure 5.19 represent the bubble undergoing one period of subharmonic oscillatory motion. This corresponds to a time of *ca.* 1.6 ms and thus a frequency of 627.5 Hz *i.e.* the bubble is executing motion at half the frequency of the driving frequency, which corresponds to subharmonic surface wave motion (see section 5.4b). However, the displacement data was difficult to interpret fully as, although giving an estimate of the amplitude of oscillation, resolving the bubble wall directly next to the microelectrode tip was difficult. In essence a spatially averaged amplitude (through the depth of field of the camera) was obtained. Hence absolute displacement data cannot be obtained. This is explained by figure 5.20, which is a schematic illustrating the displacement of the bubble wall in the time it takes to complete one period of oscillatory motion. This figure can be used to explain the displacement data derived in figure 5.19.

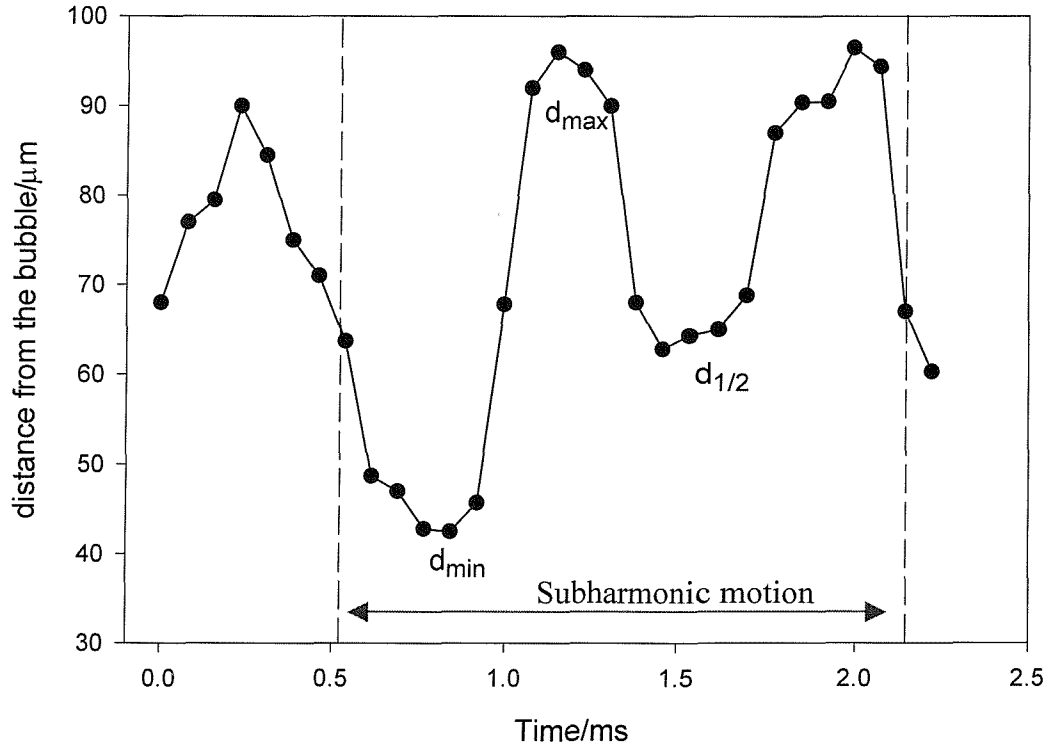

Figure 5.19 Plot of the microelectrode distance from bubble wall versus time calculated from the series of pictures shown in figure 5.18. The distance from the bubble wall was calculated using the 25 μm diameter Pt microelectrode as a scale. The sound field was operating at 1.2553 kHz and 62 Pa pressure amplitude. The displacement data (d_{min}, d_{max} and $d_{1/2}$) is explained in figure 5.20.

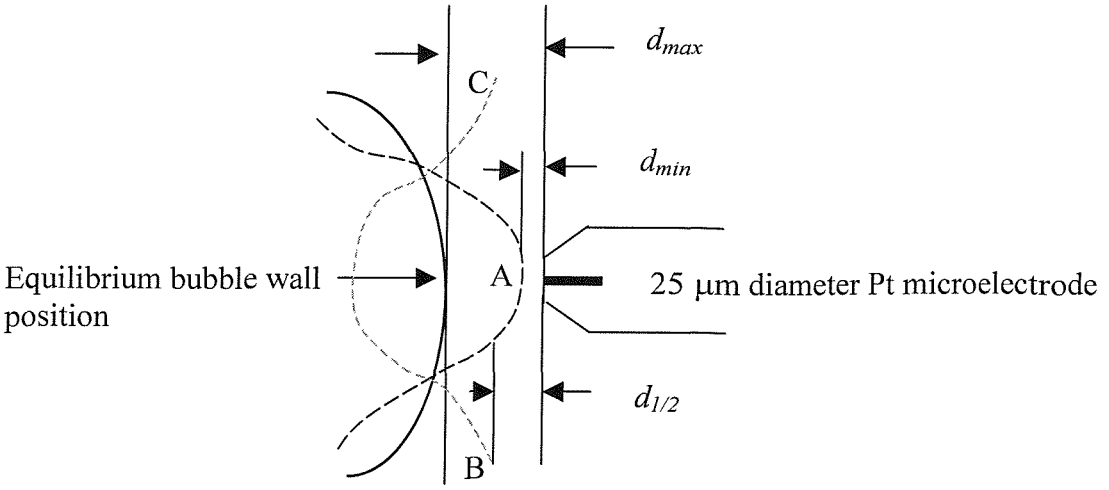

Figure 5.20 Schematic illustrating determination of the displacement amplitude using the high-speed video camera. The solid line represents the equilibrium position of the bubble wall while the dashed lines represent the extremes of displacement due to surface wave motion. The vertical solid lines represent the positions recorded from the images of the bubble wall with respect to the microelectrode. d_{min} and d_{max} represent the minimum and maximum distance determined from the images (see figure 5.19). $d_{1/2}$ is explained in the text. The points A-C represent individual waves.

At $t = 0.75$ ms ('d_{min}' in figures 5.19 and 5.20) the microelectrode-bubble wall distance is at a minimum. The distance between the bubble wall and the microelectrode increases as time progresses with maximum displacement reached at 'd_{max}' (see figures 5.19 and 5.20). At this point the displacement between the bubble wall and microelectrode would be expected to increase as wave A approaches its maximum displacement. However, the adjacent surface waves 'B' and 'C' moving in the opposite direction obscure the true microelectrode-bubble wall distance. The motion of these waves ('B' and 'C') towards the microelectrode derives the displacement data denoted by $d_{1/2}$ (see figures 5.19 and 5.20). As wave 'A' moves back towards the microelectrode maximum displacement is again reached and waves 'B' and 'C' move in the opposite direction. It must be noted that although there was a lot of error associated with this experiment the main aim was to resolve the motion of the bubble wall, which in this case was subharmonic in nature.

5.4c ii Visual Surface Wave Detection

In order to accurately determine the motion of surface waves on the bubble wall, high-speed video images were captured from below the bubble. A single bubble retained under a glass rod in water was set oscillating at a frequency 1.2966 kHz and an applied driving pressure amplitude (zero-peak) of 83.5 Pa. However, in this case a dental mirror was

positioned under the bubble to enable images from underneath the bubble to be taken. Individual frames were transferred to the PC as described before.

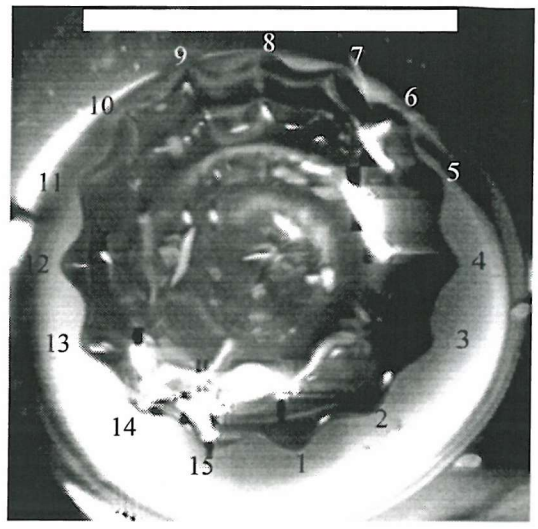

Figure 5.21 Photograph taken from below the bubble illustrating the presence of Faraday waves on the surface of an oscillating bubble (R_0 *ca.* 2.5 mm). In the photograph the bubble was set oscillating at a frequency 1.2966 kHz and driving pressure amplitude of 83.5 Pa. The scale bar indicates 5 mm. The numbers around the circumference of the bubble represent individual mode numbers.

Figure 5.21 illustrates an image of a non-spherical bubble showing evidence of Faraday waves. The mode number (n) is determined to be 15 from this image by counting the peaks around the circumference of the bubble. From the image it is possible to estimate the magnitude of the surface wave displacement as *ca.* 100 μm as expected (see section 1.3). Employing equation 5.2, derived to determine the threshold pressure required to excite surface waves, the mode number for a bubble with a resonant frequency of 1.2966 kHz can be calculated at a surface tension of 0.072 N m^{-1}.

The two modes $n = 14$ and $n = 15$ which, lie around the bubble resonance, give the lowest excitation pressure. This is shown in figure 5.22. When $\omega > \omega_0$, the mode number $n = 15$ would be seen at the bubble resonance. However when $\omega < \omega_0$, the mode number $n = 14$ would be seen at bubble resonance. There is good agreement between the theory and photographic data. However, it must be noted that it was difficult to get the absolute driving pressure. The presence of the dental mirror, employed to obtain the best image, can be expected to complicate the sound field. Also the exact resonant frequency could not be determined electrochemically (*e.g.* by measuring the minimum in threshold pressure/frequency curve). Unfortunately the presence of the dental mirror resulted in extreme difficulty in approaching of bubble wall with the microelectrode during these experiments.

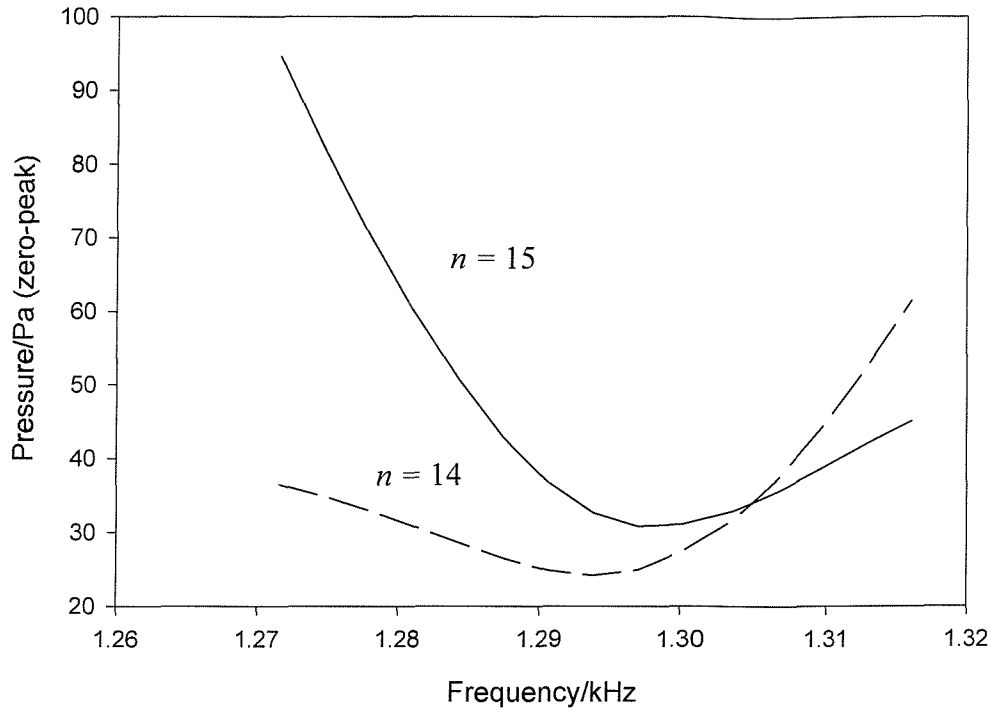

Figure 5.22 Plots showing the predicted pressure threshold for Faraday wave motion for mode numbers n = 14 (- - -) and n = 15 (—). The resonant frequency of the bubble is 1.2966 kHz. The pressure thresholds were calculated using equation (5.2) and assuming a surface tension of 0.072 N m^{-1}, a speed of sound in the liquid of 1480 m s^{-1}, a viscosity of 8.91 x 10^{-4} kg m^{-1} s^{-1}, a hydrostatic pressure of 101 kPa, a polytropic index of 1.38, a vapour pressure of 3.54 kPa, a density of air of 1.16 kg m^{-3}, a thermal conductivity of air of 0.00253 J m^{-1} s^{-1} K^{-1}, a heat capacity of 1007 J kg^{-1} K^{-1} and a density of the liquid of 1000 kg m^{-3}.

Clearly the combined electrochemical and photographic study provided evidence for the existence of Faraday waves on the surface of the bubble wall. Therefore the onset of Faraday waves was responsible for subharmonic bubble motion reported in section 5.1.

It is expected that if the driving pressure is much higher than the threshold pressure required to generate surface wave motion, higher order surface waves will be generated on the bubble wall. The following section will examine the effect of high driving pressures on the mode number of a single bubble.

5.5 Faraday Waves, Fundamental Motion and Higher Order Surface Waves

Employing equation 5.2 derived in section 5.4a the mode number was varied for a bubble of equilibrium radius 2.1 mm. Figure 5.23 illustrates a plot of pressure threshold amplitude against frequency at different mode numbers for a bubble resonant at 1.5 kHz (R_0 = 2.1 mm) at a constant surface tension of 0.072 N m^{-1}. As the mode number was increased from 14

(where the threshold pressure amplitude was a minimum) through to 18 the threshold pressure amplitude increased from 18.96 Pa through to 268.76 Pa (zero-peak). Hence, if a bubble is subjected to an acoustic pressure of the order of 100 Pa, a range of modes can be excited on its surface.

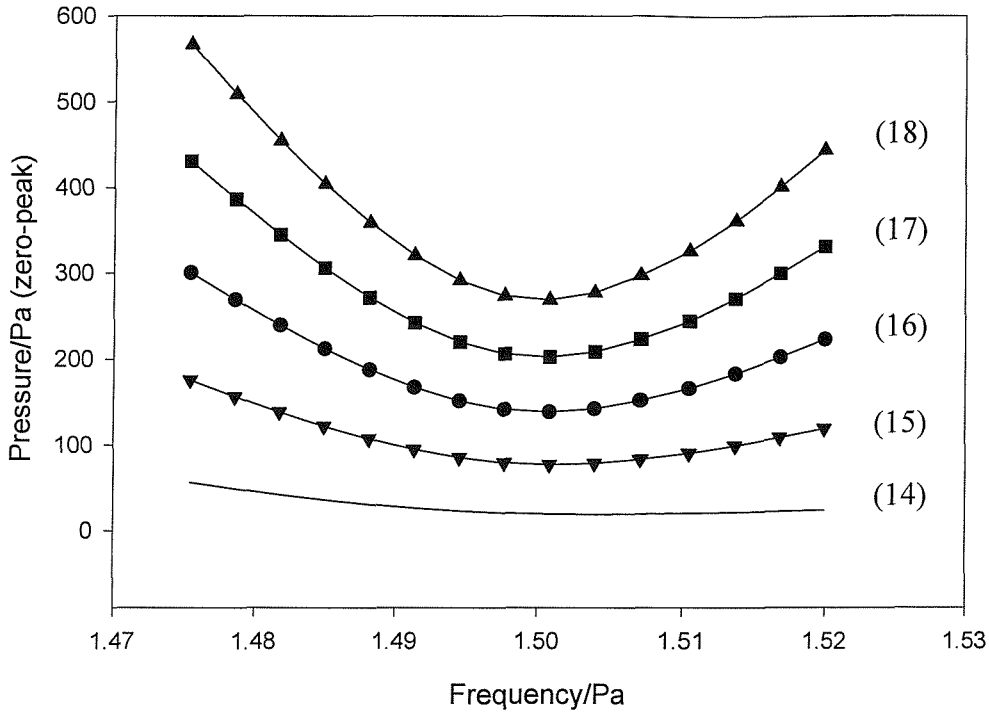

Figure 5.23 Plots of pressure threshold amplitude versus frequency for a bubble of radius 2.1 mm (resonant at 1.5 kHz) and mode numbers 14 - 18. The threshold pressures where calculated using equation 5.2 with a speed of sound of 1480 m s^{-1}, a viscosity of 8.91 x 10^{-4} kg m^{-1} s^{-1}, a hydrostatic pressure of 101 kPa, a polytropic index of 1.38, a vapour pressure of 3.54 kPa, a surface tension of 0.072 N m^{-1}, a density of air of 1.16 kg m^{-3}, a thermal conductivity of air of 0.00253 J m^{-1} s^{-1} K^{-1}, a heat capacity of 1007 J kg^{-1} K^{-1} and a density of the liquid of 1000 kg m^{-3}.

Further evidence of this phenomenon is shown in figure 5.24. These pictures were taken using the high-speed video camera described in section 2.5. In this case the driving pressure amplitude was varied from 10.9 Pa through to 139 Pa. Figure 5.24 shows that as the pressure amplitude was increased, the mode number of the surface wave increased as indicated by the chaotic behaviour apparent in pictures (d) - (f). Image (a) was below the threshold pressure required for Faraday wave excitation while (b) and above represent excitation of Faraday wave motion. Images (d) - (f) represent excitation of higher order surface waves. At high pressures within the range employed the bubble can be seen to fragment as indicated in figure 5.24 (f). In addition at higher pressures (> 80 Pa see images (e) and (f)) the whole bubble is seen to move. This is akin to 'dancing bubble' phenomena reported in the literature. [24]

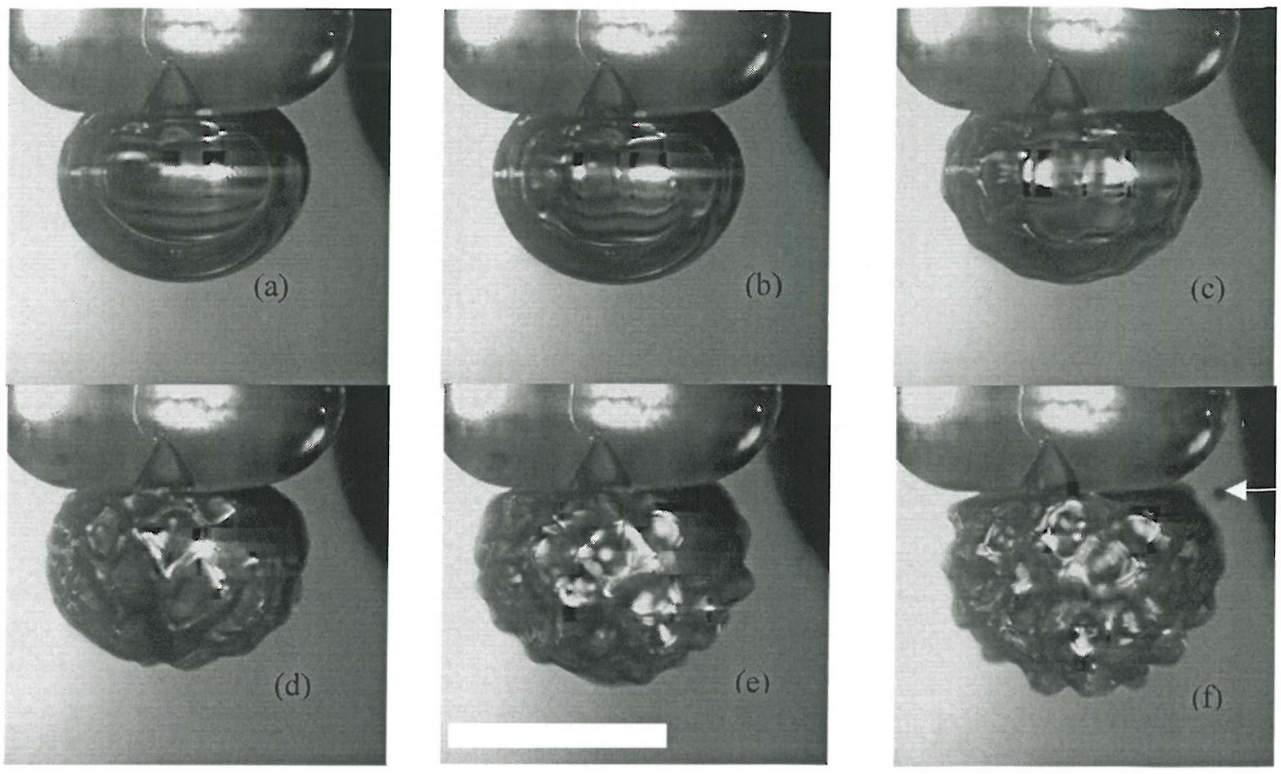

Figure 5.24 A schematic illustrating pictures of a bubble driven at 1.5006 kHz (R_0 *ca.* 2.1 mm) with a driving amplitude pressure of (a) 10.9 Pa (b) 24 Pa (c) 44 Pa (d) 79 Pa (e) 94 Pa and (f) 139 Pa. At relatively high-pressures the bubble fragments denoted by the arrow on (f). Scale bar represents 2 mm.

5.6 Conclusions

Under appropriate conditions of pressure and frequency, the current passed at a microelectrode placed close to an oscillating bubble (*ca.* 5 - 10 μm away) was found to have two main frequency components. These corresponded to the fundamental or breathing mode oscillation of the bubble (at ω) or surface wave motion, which occurred at a subharmonic frequency (*i.e.* at $\omega/2$). These modes of oscillation were found to exist under different conditions of pressure and frequency. The breathing or fundamental mode occurs at any pressure with the amplitude of motion highly frequency dependent, while subharmonic motion relies on some critical amplitude of oscillation to be exceeded. Mass transfer enhancements to the microelectrode surface in the presence of subharmonic motion exceeded that in the presence of the breathing mode alone, while the amplitudes of wall displacement vary dramatically between the two forms of oscillation.

It was determined that the onset of Faraday waves was responsible for subharmonic oscillation of the bubble wall. A model was developed which predicted the threshold pressure amplitude for the onset of these surface waves (and thus subharmonic motion) and this theory agreed favourably with electrochemical experimental data obtained. Further

complementary imaging data confirmed the presence of Faraday waves.

Finally, if the driving pressure is much greater than the threshold pressure required to excite surface waves, higher order surface waves could be excited. This was confirmed employing the model derived in 5.4a and also by high-speed imaging of an oscillating bubble.

This chapter discussed in detail the different modes of oscillation of a bubble (breathing mode, surface wave motion and higher order surface waves). A simple model was derived to determine the threshold pressures required to excite surface waves. Some of the important physical parameters affecting surface waves on a bubble wall were highlighted by Francescutto and Nabergoj.[51] These authors discussed the effect of surface tension on the normalised wall displacement. Hence it would be appropriate at this stage to discuss the effect of surface tension on the threshold pressure amplitude required to excite surface waves determined using the electrochemical technique presented in this thesis. This is explored in the following chapter.

Threshold Pressure versus Surface Tension

Chapter 6

6.0 Introduction

Chapter 3 outlined the effect of surfactants[40,101,102] on the nature of the gas/liquid interface of a stationary bubble. It was demonstrated that surfactants could inhibit oxygen transfer across a gas/liquid interface of a bubble. However, as well as gas inhibition, the presence of surfactants has the effect of reducing surface tension.[116] Surface tension plays an important role in bubble shape stability. According to Francescutto and Nabergoj[51] decreasing surface tension has the double effect of shifting the natural frequencies of the surface modes (ω_n) and raising the threshold amplitude wall displacement (C_t).

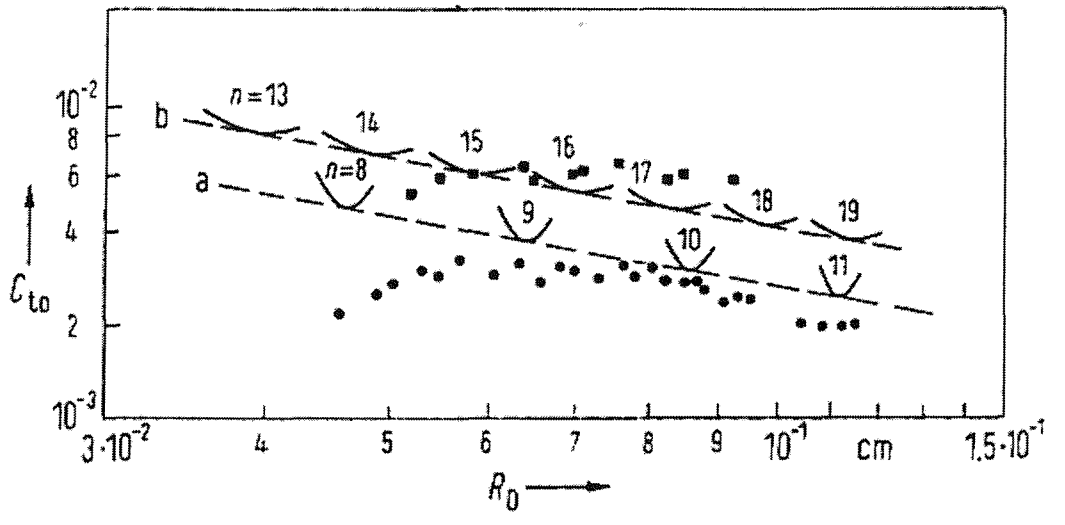

Figure 6.1 Predicted amplitude threshold normalised wall displacement (C_{t0}) (C_t at resonant frequency) versus equilibrium radius (R_0) for bubbles in water driven at the resonant frequency compared with the experimental results of Hullin to show the effects of surface tension. The curves refer to surface tensions of 0.072 N m^{-1} (line a) and 0.015 N m^{-1} (line b). The experimental points refer to bi-distilled water (•) and bi-distilled water with the addition of a surfactant (■). Reproduced from Francescutto and Nabergoj.[51]

Figure 6.1 is a plot of the predicted amplitude normalised threshold wall displacement (C_{t0}) (C_t at resonant frequency) versus equilibrium radius (R_0) for bubbles driven at the

resonant frequency determined by Francescutto and Nabergoj.[51] This data is compared to experimental results obtained by Hullin.[72] Clearly from this plot the threshold amplitude wall displacement at resonant frequency (C_{t0}) has increased as surface tension decreased (see figure 6.1 lines a and b). It must be also noted that the mode number (n) increased for a given equilibrium bubble radius with a decrease in surface tension.

Employing the model derived in chapter 5 section 5.4a the effect of surface tension on the pressure threshold amplitude (P_T) required to excite surface waves and mode number (n) will be explored here. This theoretical approach will also be combined with some experimental observations.

6.1 Factors affecting the Threshold Pressure - Surface tension

In order to investigate the effect of surfactants on Faraday wave motion, the threshold pressure at the resonant frequency was calculated as a function of surface tension for a range of modes using equation 5.2 (derived in section 5.4a). In this case a bubble of equilibrium radius 0.0023 m was considered. Figure 6.2 shows plots of threshold pressure amplitude (at the resonant frequency) as a function of surface tension (solid lines) for different mode numbers. It is clear from this figure that a reduction in surface tension, by the addition of a surfactant, has an effect on the threshold pressure. However, the plots show that if an individual mode is considered (*e.g.* $n = 15$), the pressure threshold at the resonant frequency varies as a function of surface tension in a non-linear manner. Nevertheless this cannot be considered in isolation, as the bubble is free to undergo the lowest pressure excited mode. Hence figure 6.2 shows that as the surface tension is lowered the mode number excited will increase rather than the pressure threshold varying dramatically. The dotted schematic on the plots in figure 6.2 also illustrate this point. For example starting at the surface tension illustrated by the grey dot (point A), $n = 14$ becomes excited at the bubble resonance. As the surface tension is lowered, the mode number remains at 14 until the intersection between two modes is reached (see figure 6.2 black dot). At this surface tension the mode number changes from $n = 14$ to $n = 15$ (see black circles). As the surface tension is lowered even further from the black circles where $n = 15$ is excited, to the black/grey dots and finally to the grey circles, $n = 16$ and then $n = 17$ become excited respectively. In this schematic the black dots represent the intersection between two modes. The arrow indicates the lowering of the surface tension. Hence the pressure threshold will vary, but not increase dramatically,

just 'undulate' at the bubble resonance as we 'jump' from mode to mode.

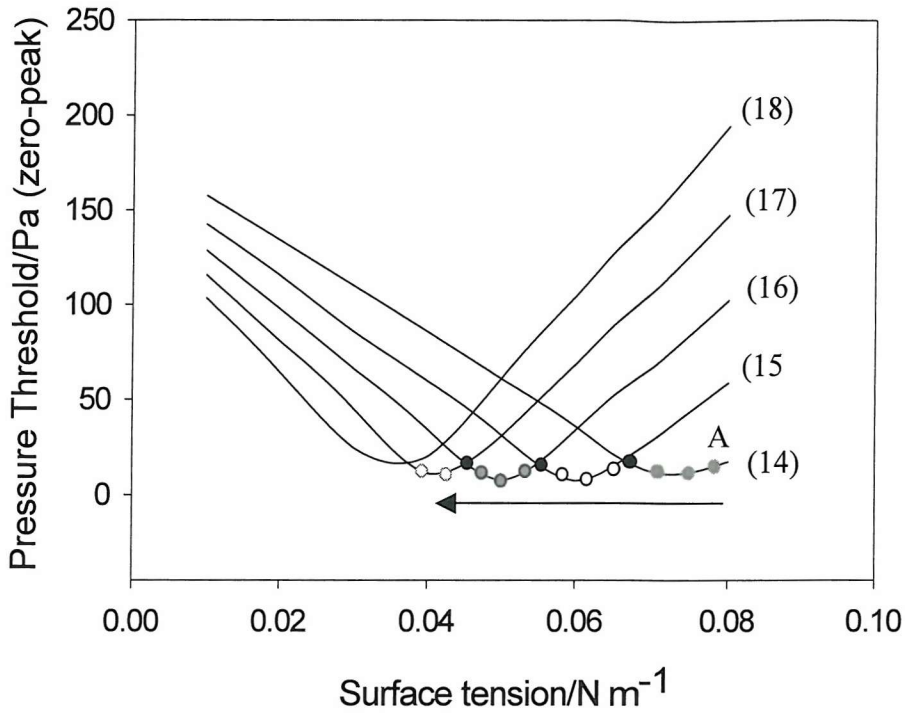

Figure 6.2 Plot of the predicted threshold pressure at the bubble resonant frequency as a function of surface tension for different mode numbers (14 - 18) (solid lines). The threshold pressure was calculated using the model outlined in section 5.4a where the equilibrium radius was 0.0023 m, the density in the liquid was 990 kg m^{-3}, the speed of sound in the liquid was 1480 m s^{-1}, the viscosity was 8.91 x 10^{-4} kg m^{-1} s^{-1}, the hydrostatic pressure was 101 kPa, the polytropic index was 1.38, the vapour pressure was 3.54 kPa, the density of air was 1.16 kg m^{-3}, the thermal conductivity of air was 0.00253 J m^{-1} s^{-1} K^{-1} and the heat capacity was 1007 J kg^{-1} K^{-1}. The dotted schematic is described in the text.

This is in apparent contrast to the work of Francescutto and Nabergoj,[51] who showed a dramatic effect of surface tension in relation to surface waves. However, this is because the data presented by Francescutto and Nabergoj,[51] was concerned with the variation of C_t and not the actual threshold pressure (as determined here). In order to illustrate this point figure 6.3 shows a plot of the C_t and $\left[\left(\omega_0{}^2-\omega^2\right)^2+\left(\omega^2 d_{\text{tot}}\right)^2\right]^{0.5}$ terms (equation 5.2) as a function of frequency. It is evident from this figure that both factors are heavily frequency dependant. Clearly figure 6.3 shows that although C_t is a central factor in determining the threshold pressure, it is important to consider all the relevant terms.

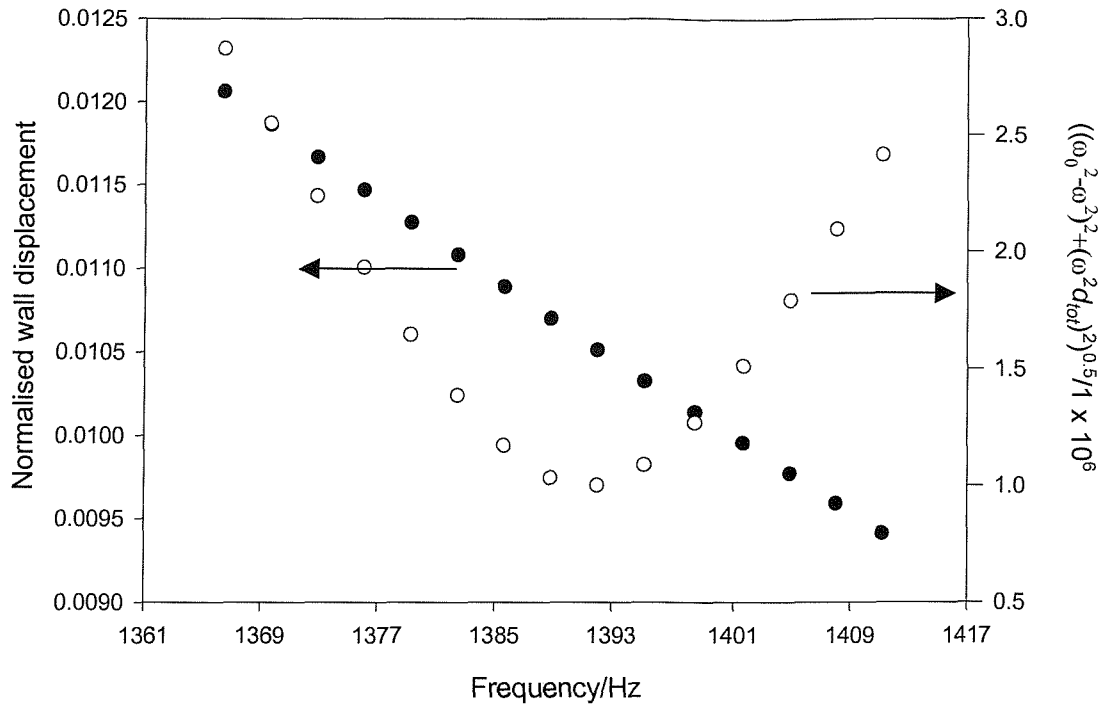

Figure 6.3 Plot of C_t and $\left[\left(\omega_0{}^2-\omega^2\right)^2+\left(\omega^2 d_{\text{tot}}\right)^2\right]^{0.5}$ against frequency. Both terms were calculated using the model outlined in section 5.4a where the equilibrium radius was 0.0023 m, the density in the liquid was 990 kg m^{-3}, the speed of sound in the liquid was 1480 m s^{-1}, the viscosity was 8.91 x 10^{-4} kg m^{-1} s^{-1}, the hydrostatic pressure was 101 kPa, the polytropic index was 1.38, the vapour pressure was 3.54 kPa the density of air was 1.16 kg m^{-3}, the thermal conductivity of air was 0.00253 J m^{-1} s^{-1} K^{-1} and the heat capacity was 1007 J kg^{-1} K^{-1}.

While the previous discussion has illustrated the behaviour of the pressure threshold as a function of surface tension, it has not explained why surface tension should have such an effect. In order to develop an explanation for this behaviour it is necessary to consider the mode frequency in relation to the excitation or drive frequency. The mode frequency[74] (ω_n) can be calculated from equation 6.1. This shows that by decreasing the surface tension of the system the natural frequency of the appropriate surface mode changes.

$$\omega_n{}^2 = \frac{(n+1)(n+2)(n-1)\sigma}{\rho R_0{}^3} \qquad (6.1)$$

Figure 6.4 shows a plot of the ratio of mode frequency (ω_n calculated using equation 6.1) to the bubble resonant frequency (ω_0) as a function of surface tension employing an equilibrium bubble radius (R_0) of 0.0023 m and a mode number (n) of 14. Clearly from this figure a decrease in the surface tension causes the ratio of ω_n/ω_0 to decrease. The figure also

includes a plot of threshold pressure amplitude (P_T) at the resonant frequency as a function of surface tension under the same physical conditions. It is evident from the plot that a variation in surface tension can cause the pressure threshold amplitude to increase or decrease. Clearly there is a minimum threshold pressure amplitude for the onset of surface waves for this particular bubble radius and mode number at a given surface tension. This minimum occurs when $\omega_n/\omega_0 = 0.5$. Therefore when the mode frequency (ω_n) is exactly half the resonant frequency (ω_0) we have the optimal set of conditions for the onset of Faraday waves at half the driving frequency. Above or below this (*i.e.* $\omega_n/\omega_0 \neq 0.5$) does not represent beneficial conditions for the onset of Faraday waves because the pressure threshold amplitude (P_T) increases. This is as expected if one considers that the most efficient 'driving signal' will occur exactly when $\omega = 2\omega_n$. At this point the bubble is driven 'twice' per surface wave cycle. Above or below this frequency the driving force is slightly out of phase with the surface oscillation. Hence away from $\omega = 2\omega_n$ the pressure threshold increases as expected.

Figure 6.5 shows a series of similar plots for different mode numbers but with the same bubble radius. In each case the threshold pressure for surface waves for any given mode number at different surface tensions has a minimum that coincides with a subharmonic frequency at half the resonant frequency of the bubble. This explains why we do not observe any large effect of surface tension (σ). As the surface tension (σ) is lowered (by the addition of a surfactant) the threshold pressure (P_T) value rises until a higher mode order is preferentially excited. Clearly it is important to validate this hypothesis with experimental data. This validation was achieved in two complementary ways; electrochemical detection of surface waves and high-speed video imaging of the bubble. This dual approach was undertaken because electrochemical data alone is insufficient to support the theory. This is because even if the surface tension was changed Faraday wave motion at $\omega/2$ would be still observed.

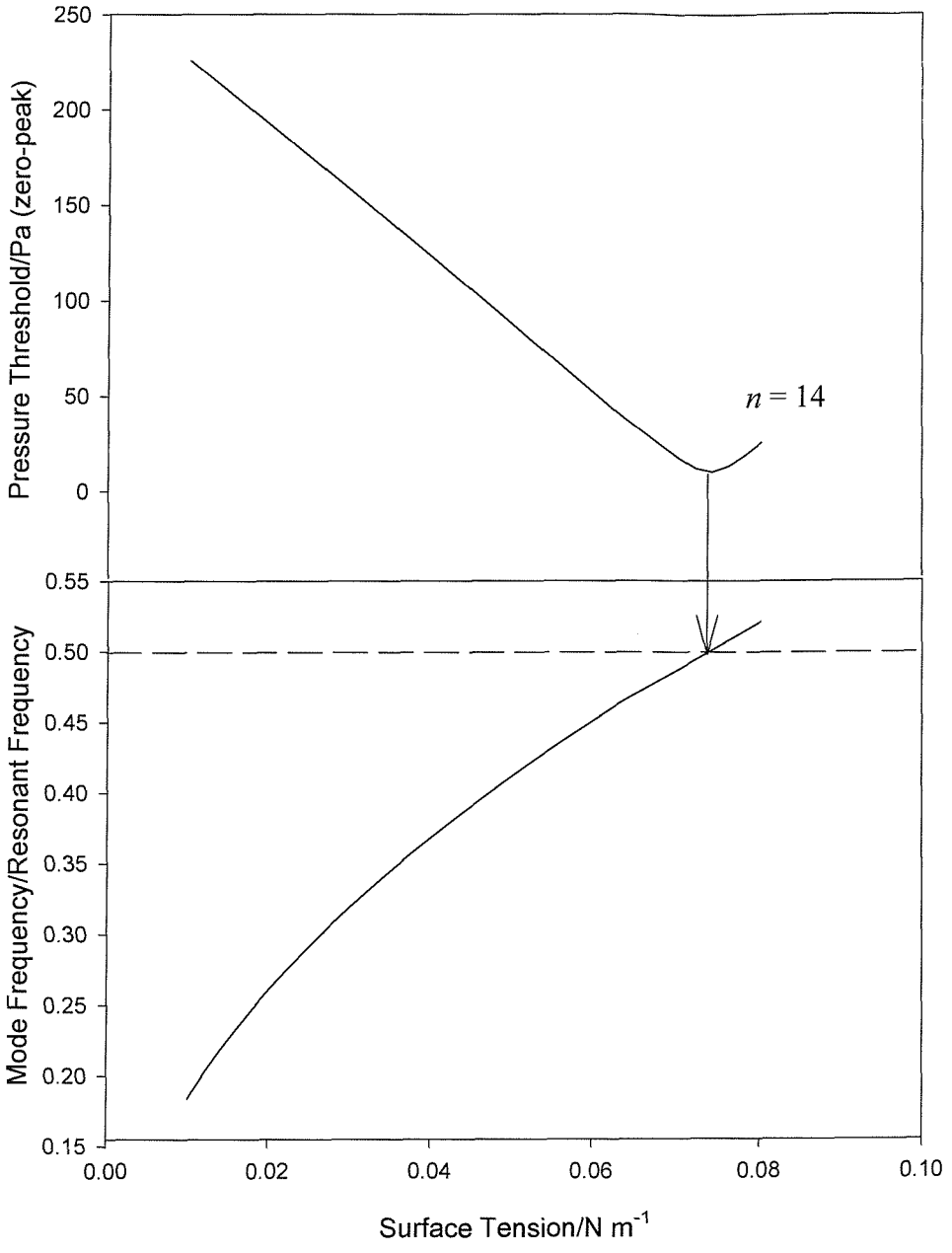

Figure 6.4 Plots of threshold pressure at the resonant frequency and the mode frequency divided by resonant frequency (ω_n/ω_0) against surface tension for n = 14. The threshold pressure was calculated using the model outlined in section 5.4a where the equilibrium radius was 0.0023 m, the density of the liquid was 990 kg m^{-3}, the speed of sound in the liquid was 1480 m s^{-1}, the viscosity was 8.91 x 10^{-4} kg m^{-1} s^{-1}, the hydrostatic pressure was 101 kPa, the polytropic index was 1.38, the vapour pressure was 3.54 kPa, the density of air was 1.16 kg m^{-3}, the thermal conductivity of air was 0.00253 J m^{-1} s^{-1} K^{-1} and the heat capacity was 1007 J kg^{-1} K^{-1}.

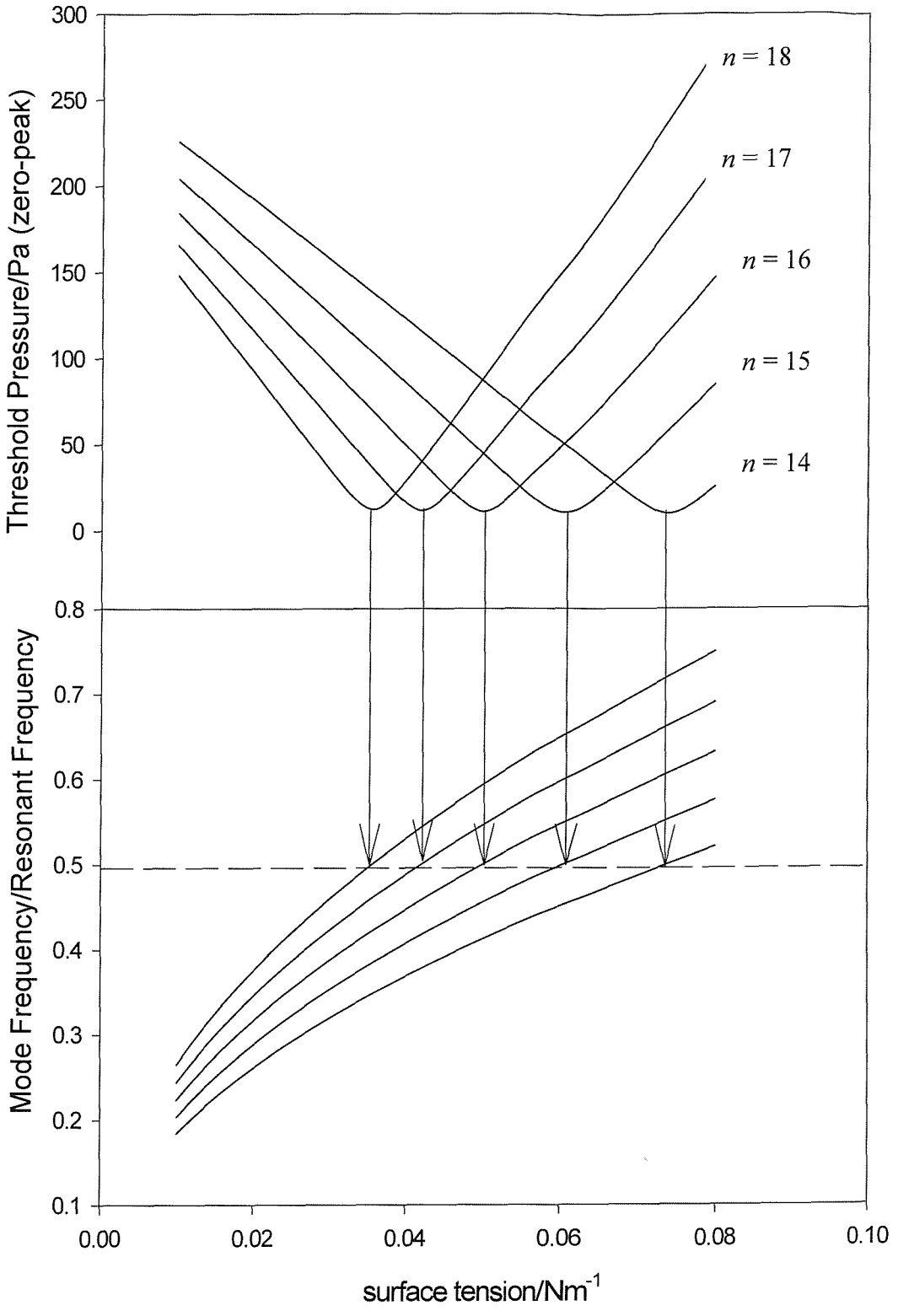

Figure 6.5 Plots of threshold pressure at the resonant frequency and the mode frequency divided by resonant frequency (ω_n/ω_0) against surface tension for n = 14 - 18. The threshold pressure was calculated using the model outlined in section 5.4a where the equilibrium radius was 0.0023 m, the density was 990 kg m^{-3}, the speed of sound was 1480 m s^{-1}, the viscosity was 8.91 x 10^{-4} kg m^{-1} s^{-1}, the hydrostatic pressure was 101 kPa, the polytropic index was 1.38, the vapour pressure was 3.54 kPa, the density of air was 1.16 kg m^{-3}, the thermal conductivity of air was 0.00253 J m^{-1} s^{-1} K^{-1} and the heat capacity was 1007 J kg^{-1} K^{-1}. Note the surface tension in pure water is normally quoted as 0.072 N m^{-1}. Hence the possible range 0.01 – 0.07 N m^{-1} is plotted in this figure.

6.2 Experimental versus Surface Tension

6.2a Electrochemical

The experimental set-up was described earlier (see figure 2.3). A solution of 5 mmol dm^{-3} $Fe(CN)_6^{3-}$ in 0.2 mol dm^{-3} $Sr(NO_3)_2$ was employed. Additions of the surfactant Triton X-100 to this electrolyte varied the surface tension from 0.068 N m^{-1} to 0.0335 N m^{-1}. A 25 μm diameter Pt microelectrode was positioned *ca.* 5-10 μm from the air bubble wall and the sound was switched on. The frequency and pressure range over which subharmonic oscillation occurred for similar sized bubbles at varying surface tensions was measured (see section 5.1). Figure 6.6 illustrates a series of threshold pressure plots measured for bubbles resonant around 1.50 kHz but at differing surface tensions. The solid lines in the plots represent the theoretical threshold pressure curves for the onset of surface waves predicted from the model (see equation 5.2 section 5.4a) under the same conditions.

A number of points must be noted from the series of plots. First, the model is particularly sensitive to physical parameters, particularly the surface tension (see section 5.4b). Therefore values of surface tension of 0.069 N m^{-1}, 0.048 N m^{-1} and 0.034 N m^{-1} were employed in the theoretical predictions for a, b and c respectively in figure 6.6 to obtain the best fit between the data and the theory. However, these compare well to the experimental measured values of 0.068 N m^{-1}, 0.047 N m^{-1} and 0.0335 N m^{-1} determined for the experimental threshold pressure plots of a, b and c respectively. Second, the theoretical pressure curves in figure 6.6 predict an increase in mode number with a decrease in surface tension *i.e.* as the surface tension is decreased from 0.069 N m^{-1} to 0.048 N m^{-1} and to 0.034 N m^{-1} the mode number increases from 14 to 16 and finally to 18. However, the variation in the overall threshold pressure between the three cases is small. This agrees with the theoretical predictions in section 6.1 *i.e.* as surface tension (σ) is lowered (by the addition of a surfactant) the threshold pressure (P_T) value rises until a higher mode order is achieved. Third, the dashed lines in figure 6.6 a-c represent mode numbers calculated, employing equation 5.2, on either side of the resonant frequency indicating that a minimum in threshold pressure amplitude occurs at the resonant frequency for mode numbers n = 14, 16 and 18 in plots a-c respectively. As the driving frequency is adjusted to above or below the resonant frequency in plots a-c the mode excited on the bubble wall does not change and remains at n = 14, 16 and 18 respectively *i.e.* the theoretical curve still fits the experimental data.

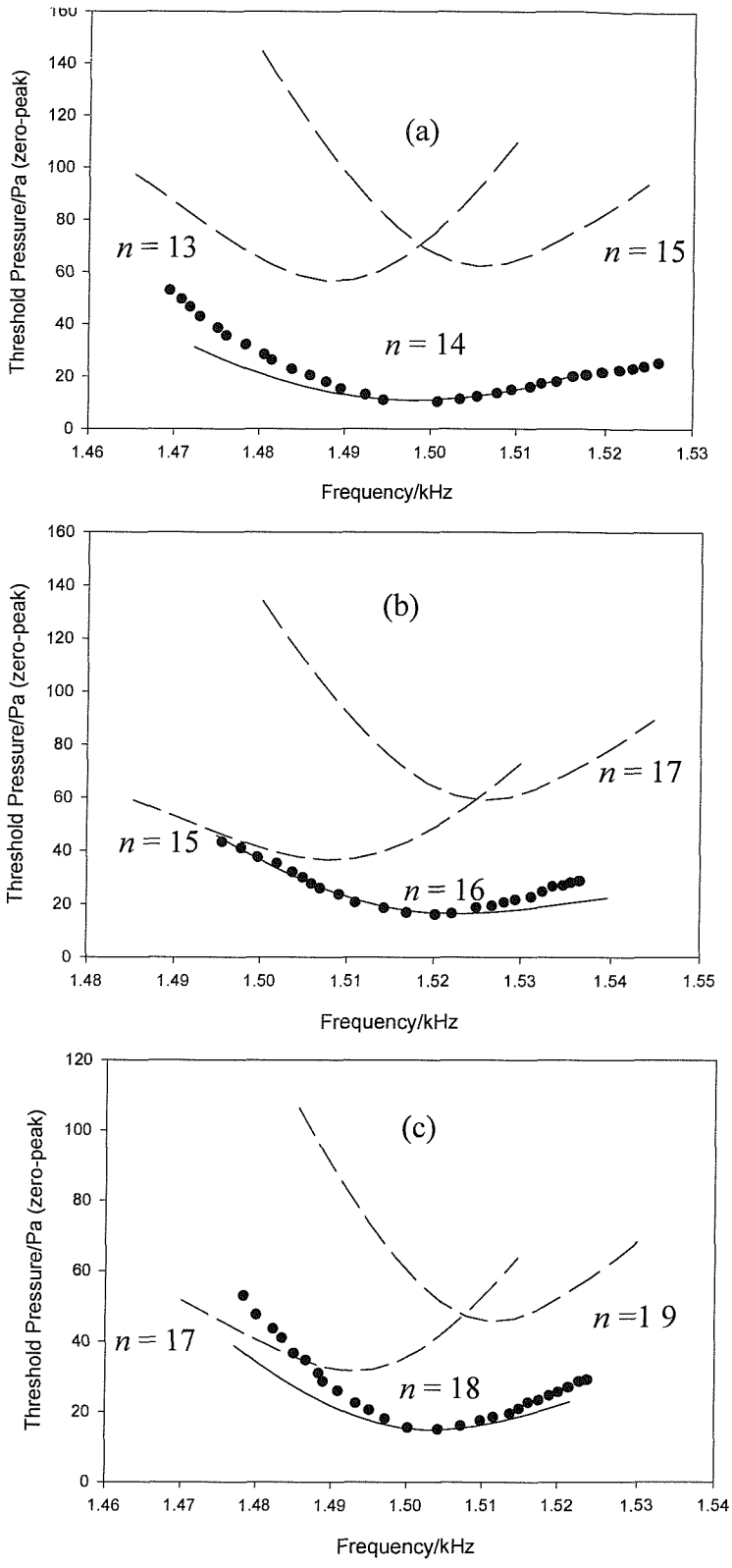

Figure 6.6 Plot showing the onset of Faraday waves (•) detected at an air bubble (R_0 *ca.* 2 mm) using the electrochemical detection method described in section 5.1. The solid lines represent the predicted pressure threshold for (a) n (the order of the mode) = 14 (b) n = 16 and (c) n = 18 modes of oscillation. The pressure thresholds were calculated using equation (5.2) and assuming a surface tension of (a) 0.069 N m^{-1} (b) 0.048 N m^{-1} and (c) 0.034 N m^{-1}, a speed of sound of 1480 m s^{-1}, a viscosity of 8.91 x 10^{-4} kg m^{-1} s^{-1}, a hydrostatic pressure of 101 kPa, a polytropic index of 1.38, a vapour pressure of 3.54 kPa and a density of the liquid of 1000 kg m^{-3}. The dashed lines in plots a - c represent mode numbers calculated, employing equation 5.2, on either side of the resonant frequency indicating that a minimum in threshold pressure occurs at the resonant frequency for mode numbers n = 14, 16 and 18 in plots a-c respectively. The error in the experimental data was ± 1.5 Pa.

The fit between experiment and theory is satisfactory. The results also agree with the results of Francescutto and Nabergoj[51] (see figure 6.1) *i.e.* a decrease in surface tension leads to an increase in mode number. However, the change in mode number with changing surface tension will be more easily identifiable with photographic data. This is discussed in section 6.2b.

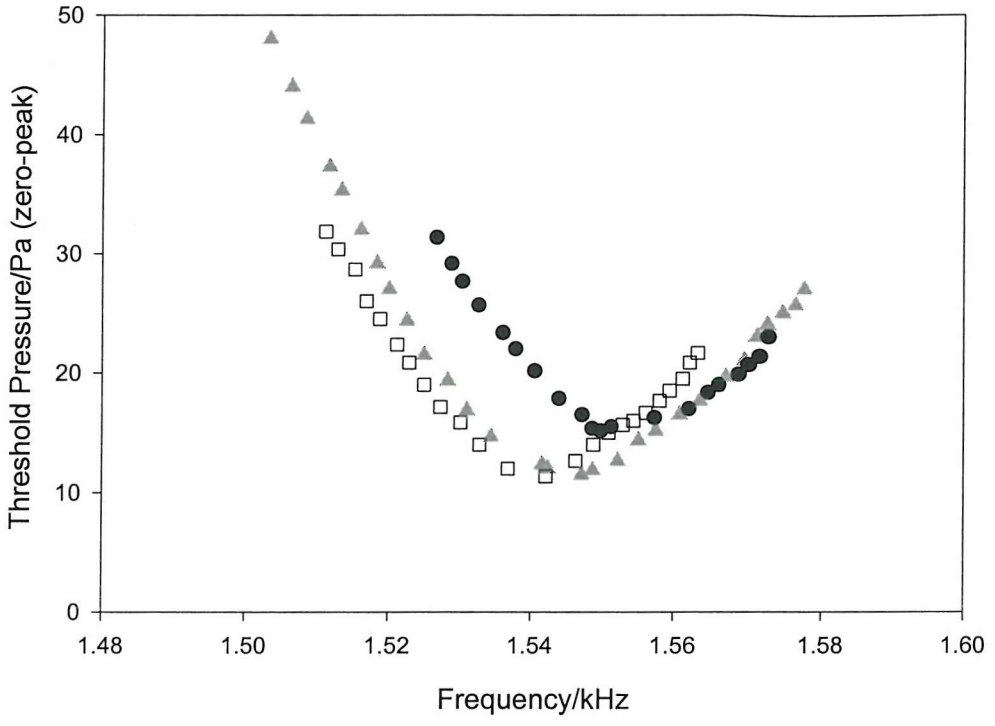

Figure 6.7 Plot showing the onset of Faraday waves (●), (□) and (▲) detected for a bubble resonant (R_0 *ca.* 2 mm) around 1.55 kHz using a 25 μm diameter Pt microelectrode in the presence of sound irradiation. The solution employed was 5 mmol dm^{-3} $Fe(CN)_6^{3-}$/0.2 mol dm^{-3} $Sr(NO_3)_2$ with increasing additions of Triton X-100. The surface tensions were measured as 0.068 N m^{-1}, 0.047 N m^{-1} and 0.0335 N m^{-1} for (●), (□) and (▲) respectively. The error in the experimental data was ± 1.5 Pa.

Figure 6.7 illustrates a similar set of experimental results obtained with bubbles resonant around 1.55 kHz. In this case all the data is plotted on one graph to illustrate the point that threshold pressure amplitude does not vary much as the surface tension was decreased.

While the electrochemical data presented so far agrees favourably with the theory proposed in section 6.1 further complementary photographic evidence is required to corroborate the theory. This data will now be presented.

6.2b High Speed Video Data

A series of bubbles of varying sizes were imaged in solutions of varying surface tensions using the high-speed video camera described in chapter 2 section 2.5. This enabled the motion of surface waves along the bubble wall to be captured and hence the effect of surface tension on mode number to be determined. Figure 6.8 shows a series of pictures of similarly sized bubbles (R_0 *ca.* 2.5 mm), taken from underneath the bubble, but at varying surface tensions. The surface tension was adjusted by the addition of known quantities of Triton X-100 to water already present in the cell (Note the surface tension was determined in each case by a DuNouy Tensiometer balance; see section 2.7d.). As the surface tension was reduced from 0.074 N m^{-1} to 0.0535 N m^{-1} and to 0.047 N m^{-1} the mode number increases from 15 to 16 and to 18 respectively at similar driving pressure amplitudes. The mode numbers were determined from the pictures by counting the peaks around the circumference of the bubble (see figure 6.8 (a)). These results agree favourably with the theory discussed in section 6.1 *i.e.* the mode number increases with decreasing surface tension. This data also supports the findings of Francescutto and Nabergoj[51] (see figure 6.1).

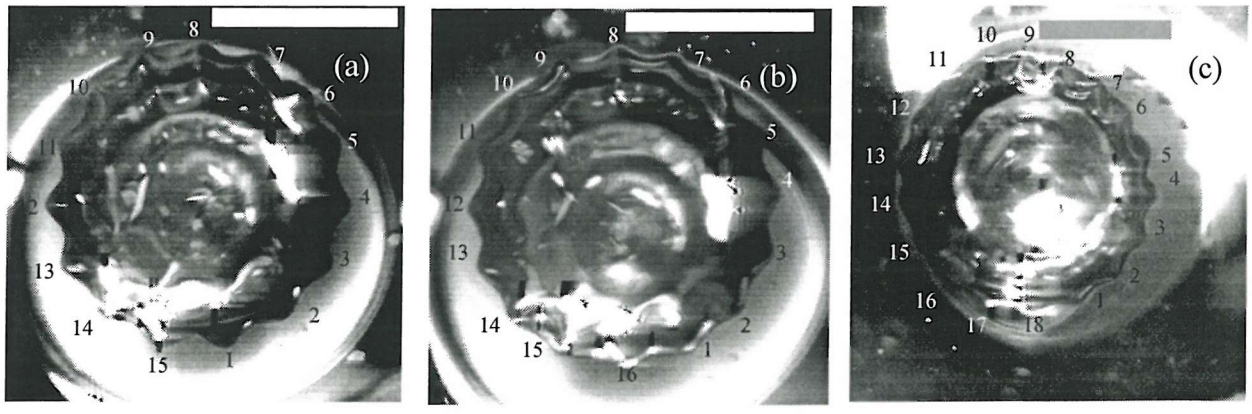

Figure 6.8 A sequence of pictures of bubbles (R_0 *ca.* 2.5 mm) taken with a high speed video camera oscillating at (a) 1.2966 kHz at 83.5 Pa (b) 1.310 kHz at 82.5 Pa and (c) 1.2995 kHz at 66.5 Pa with surface tensions and mode numbers of (a) 0.074 N m^{-1} $n = 15$ (b) 0.0535 N m^{-1} $n = 16$ and (c) 0.047 N m^{-1} $n = 18$. Scale bars represent 3 mm in each case.

Similar results were obtained with different sized bubbles (R_0 *ca.* 2.3 mm and R_0 *ca.* 2 mm) at varying surface tensions. These results are illustrated in figures 6.9 and 6.10. In both sequences of pictures the mode number increases as the surface tension decreases under similar conditions of driving pressure as expected.

However, it was difficult to calculate exact mode numbers for each bubble from the

theory derived in section 5.4a under the conditions employed in this experiment. The reasons for this were discussed on page 104. Also different bubbles were employed for each picture taken because the stability of the bubbles on the glass rod decreased with each addition of surfactant.

Nevertheless, these photographic studies verify the hypothesis that a decrease in surface tension changes the mode number under similar conditions of driving pressure amplitude.

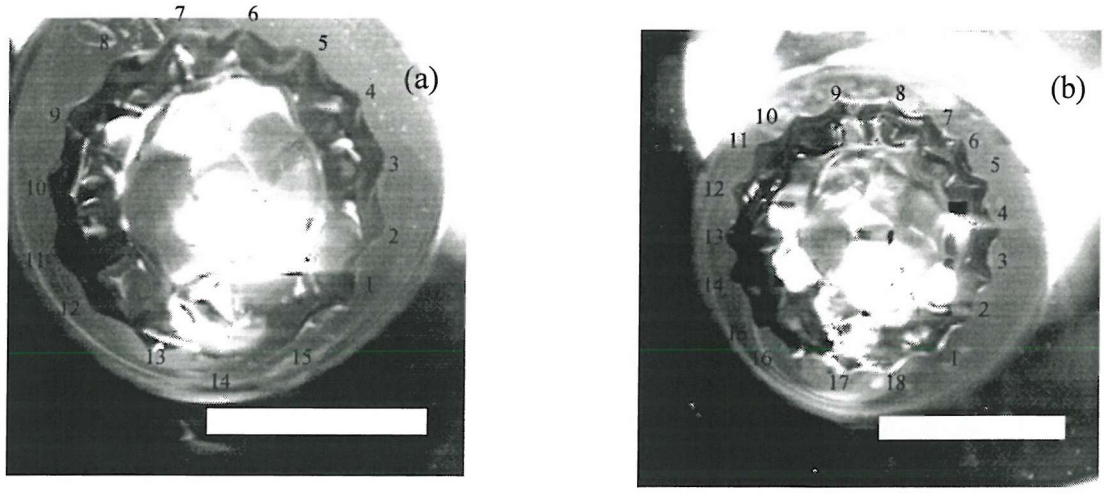

Figure 6.9 A sequence of pictures of bubbles (R_0 *ca.* 2.3 mm) taken with a high speed video camera oscillating at (a) 1.3902 kHz at 110 Pa and (b) 1.3962 kHz at 88.5 Pa with surface tensions and mode numbers of (a) 0.075 N m^{-1} n = 15 and (b) 0.047 N m^{-1} n = 18. Scale bars represent 3 mm in each case.

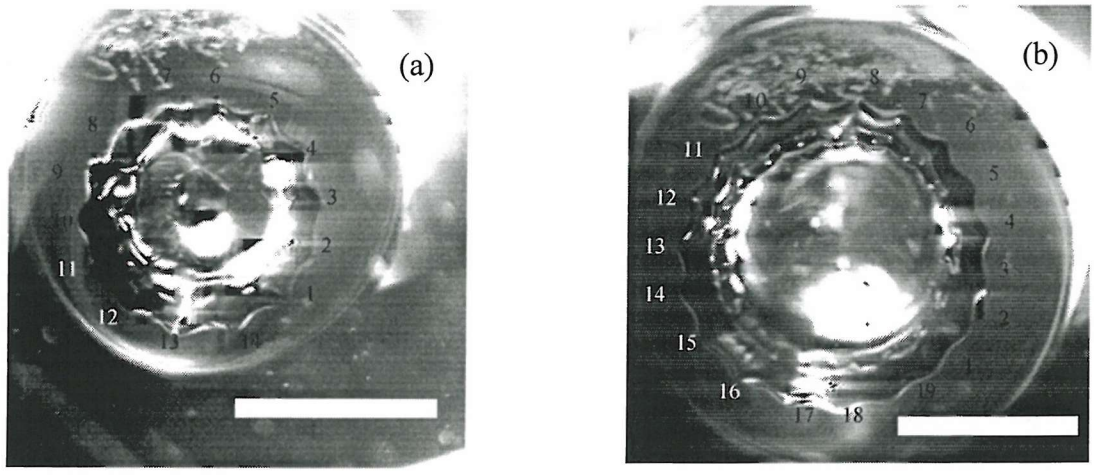

Figure 6.10 A sequence of pictures of bubbles (R_0 *ca.* 2 mm) taken with a high speed video camera oscillating at (a) 1.6051 kHz at 228.5 Pa and (b) 1.5999 kHz at 250 Pa with surface tensions and mode numbers of (a) 0.075 N m^{-1} n = 14 and (b) 0.0335 N m^{-1} n = 19. Scale bars are 3 mm in each case.

6.3 Conclusions

The effect of surface tension on the threshold pressure required to excite surface waves was extensively studied. The theory derived in chapter 5.4a predicted an increase in mode number with a decrease in surface tension which agrees with the work of Francescutto and Nabergoj.[51] Also, the threshold pressure required to excite surface waves is largely unaffected *i.e.* the threshold pressure (P_T) value rises until a higher mode order is achieved. This hypothesis was confirmed by both electrochemical and photographic evidence.

In the preceding chapters of this thesis electrochemical surface wave and breathing mode detection was extensively studied under 'steady state' conditions (*e.g.* constant sound irradiation of the bubble). While the previous findings are highly important they do not address non steady state conditions and the ensuing complications. These issues will now be discussed with particular relevance to understanding the mechanism for surface wave ring-up (*i.e.* the time for surface waves to rise following insonification). This non steady state data will be beneficial in understanding the phenomenon termed Faraday waves in general. The results of a preliminary study to see if it is possible to measure ring-up times employing the acousto-electrochemical technique introduced in this thesis is discussed in the next chapter.

Ring-up time of Surface Waves

Chapter 7

7.0 Introduction

Determining the ring-up time of surface waves (the time taken for the surface wave to be generated on the bubble wall) following irradiation of a bubble with sound of an appropriate frequency and pressure is important in developing a suitable theoretical understanding of the behaviour of such waves on a bubble wall. Leighton *et al.*[74] reported that the time taken to establish steady state subharmonic signals was significantly greater than that required to establish the signal for fundamental motion of the bubble wall. In this experiment the oscillation of the bubble was determined using a combination frequency technique. Maksimov and Leighton[79] subsequently developed a theory, to explain the significant difference[74] in ring-up times observed. However, relatively little experimental evidence is available to compare to the new theory.[79] Preliminary electrochemical experiments are presented here designed to accurately measure the rise time of the Faraday wave on the surface of a bubble, held against buoyancy forces, as a function of the physical parameters of the system, particularly the pressure amplitude and the frequency employed. The results of this study are now presented.

7.1 Experimental Preliminary Tests

The experimental set-up was as in figure 2.4. An air bubble was tethered to an insulated Ni wire in 5 mmol dm^{-3} $Fe(CN)_6^{3-}$/0.2 mol dm^{-3} $Sr(NO_3)_2$. The potential of the electrode was held at –0.1 V versus Ag. A 25 μm diameter Pt microelectrode was positioned close to the bubble wall (*ca.* 5 - 10 μm away) and the extreme frequencies and pressures at which subharmonic motion occurred were recorded (threshold pressure curve, see section 5.1). A

series of experiments were then performed. In one of the first set of experiments a 0.5 mm diameter Pt macroelectrode was employed. This electrode was chosen in an attempt to suppress fluctuations in the current due to bubble 'bouncing' observed when a 25 μm microelectrode was employed in initial trial experiments. The 0.5 mm electrode samples over a larger surface area of the interface and hence should be less prone to this effect. However, the 0.5 mm electrode will be less able to resolve the subharmonic motion of the gas/liquid interface when compared to a 25 μm diameter Pt microelectrode. Nevertheless resolution of the individual surface wave motions is not required in this experiment as the overall motion of the bubble wall leads to a mass transfer enhancement that can be detected at the macroelectrode.

Current time data was recorded at a variety of frequencies/pressures inside the threshold pressure curve. Figure 7.1 represents a typical current time plot recorded by the macroelectrode. In this example the sound was switched on at *t ca.* 0.9 s.

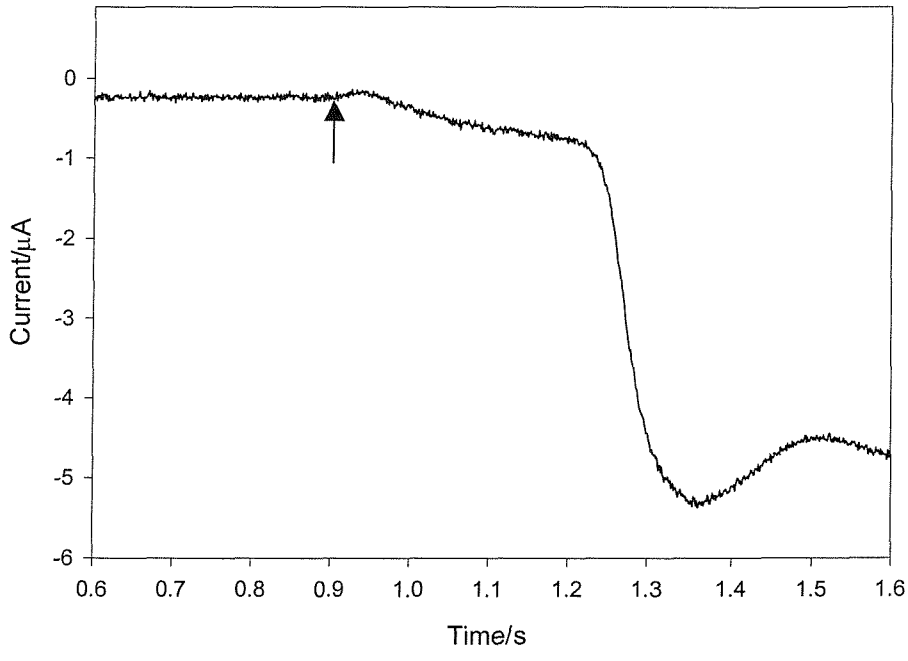

Figure 7.1 Current time plot recorded by a 0.5 mm diameter Pt macroelectrode positioned close to the bubble wall (R_0 *ca.* 1.7 mm) in 5 mmol dm^{-3} $Fe(CN)_6^{3-}$/0.2 mol dm^{-3} $Sr(NO_3)_2$ in the presence of a sound field of 1.8685 kHz at 53.481 Pa. The sound was switched on at *t ca.* 0.9 s which is indicated by the arrow. The potential of the electrode was held at –0.1 V versus Ag.

However, although the macroelectrode was less susceptible to this bouncing effect a number of problems were encountered during the course of these experiments. First, the macroelectrode and body were found to inhibit the motion of the bubble wall. This was because the macroelectrode is large in comparison to the size of surface waves. This effect was noted by visual observation of the bubble in the presence of sound irradiation. Second,

on examination of the current time plots recorded at different frequencies and pressures inside the threshold pressure curve, it was evident that the bubble had grown by the process of rectified diffusion (see chapter 9) during the experiment. The effect of rectified diffusion can be noted from figure 7.2 (a) and figure 7.2 (b). Figure 7.2 (a) represents the threshold pressure curve (•) determined by monitoring the onset of subharmonic motion with a 25 μm diameter Pt microelectrode as described previously (see section 5.1) prior to performing the experiments with the macroelectrode. The symbols (□) and (■) represents the frequency and pressure conditions employed for rise time experiments

(a)

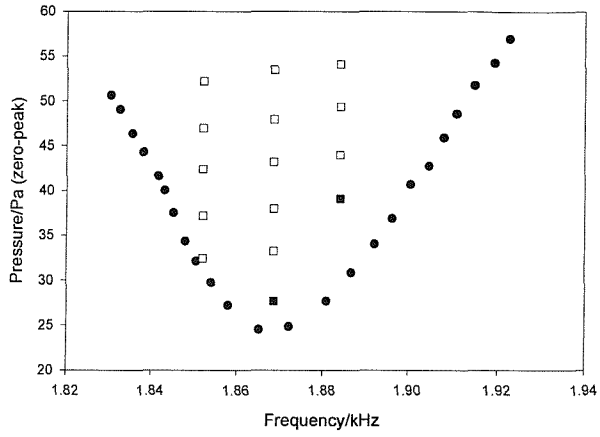

(b)

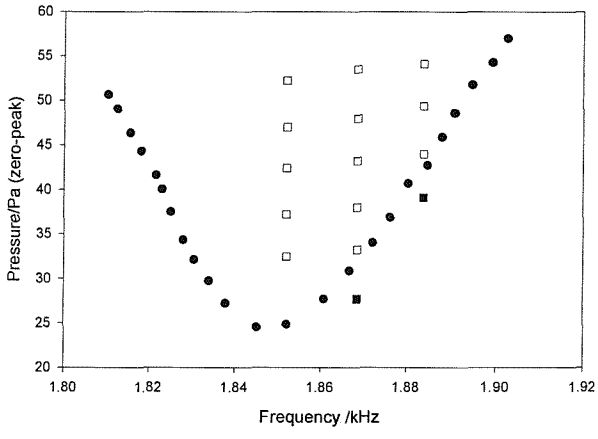

Figure 7.2 (a) Plot showing the frequency and pressure range within which subharmonic oscillation of air bubble (R_0 *ca.* 1.7 mm) in 5 mmol dm^{-3} $Fe(CN)_6^{3-}$/0.2 mol dm^{-3} $Sr(NO_3)_2$ resonant at 1.86 kHz was detected by a 25 μm diameter Pt microelectrode. The potential was held at -0.1 V versus Ag wire. (•) represents the threshold pressure curve obtained while (□) and (■) represent the frequencies and pressures picked to determine rise times. (b) Plot showing the predicted frequency pressure range within which subharmonic oscillation of air bubble in 5 mmol dm^{-3} $Fe(CN)_6^{3-}$/0.2 mol dm^{-3} $Sr(NO_3)_2$ could be detected by a 25 μm diameter Pt microelectrode after growth by rectified diffusion. The figure also includes the frequencies and pressures picked to determine risetimes (□) and (■).

Figure 7.2 (b) represents the predicted pressure threshold curve after the rise time experiment had been performed. This prediction was based on observation of the current time plots recorded at the frequencies/pressures inside the threshold pressure curve selected to investigate risetimes. In particular on examination of the current time plots at the frequencies and pressures denoted by (■) on figure 7.2 (a) no evidence of subharmonic surface wave motion was visible (no large enhancement in current similar to figure 7.1 was visible). Therefore it was presumed that these frequencies and pressures lied outside the conditions required for subharmonic motion (see figure 7.2 (b)). Hence the resonant frequency of the bubble had shifted to a lower value, which is illustrated on figure 7.2 (b). This shift in resonant frequency resulted in an estimated increase in the bubble radius from 1.71 mm to 1.73 mm. This was calculated employing equation 1.12.

In order to avoid the inhibition of the bubble motion and the growth of the bubble, it was decided to employ a 25 μm diameter Pt microelectrode (which had been polished to R_{glass} *ca.* 5) and add a known amount of a surfactant, specifically Triton X-100, to the solution. The presence of a surfactant hinders the process of rectified diffusion. This will be discussed in more detail later on in the thesis in Chapter 9. This experimental protocol was used to monitor ring-up times of the Faraday wave motion of the gas/liquid interface of the bubble. For these experiments the response time of the electrochemical sensor is critical. However, considering a first approximation of the diffusion field of the electrode (*e.g.* planar) it is possible to estimate that the electrode will respond in *ca.* < 0.2 s. In the presence of forced convection, as is expected for bubble oscillation, this response time will be even faster (estimate at 2 ms). Clearly this is sufficient to resolve the ring-up times presented later in this Chapter. The results of this particular study are now presented.

7.2 Ring-up experiments in the presence of Triton X-100

The solution employed contained 0.2 mmol dm^{-3} Triton X-100 in 5 mmol dm^{-3} $Fe(CN)_6^{3-}$ /0.2 mol dm^{-3} $Sr(NO_3)_2$. The 25 μm diameter Pt microelectrode was positioned close to the bubble wall (*ca.* 5-10 μm away) and the extreme frequencies and pressures at which subharmonic motion was initiated were determined (see section 5.1). Similarly, a number of frequencies and corresponding driving pressures were selected inside the threshold pressure curve to determine ring-up times under the conditions chosen. Figure 7.3 is a plot of the threshold pressure curve obtained (•) including frequencies and pressures chosen for

the rise time experiment (□).

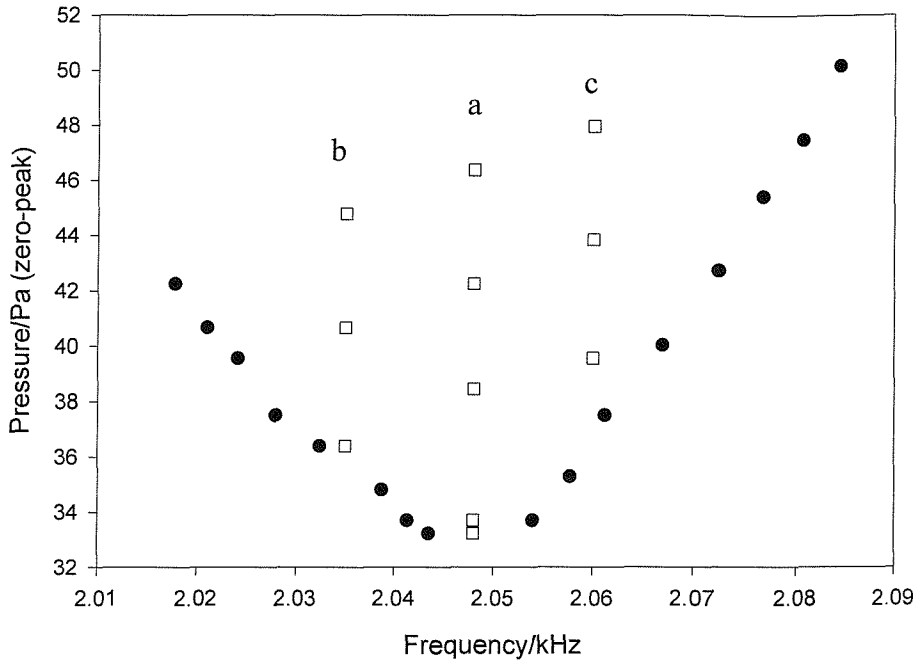

Figure 7.3 Plot showing the frequency and pressure range (•) within which subharmonic oscillation of air bubble (R_0 *ca.* 1.56 mm) in 0.2 mmol dm^{-3} Triton X-100 in 5 mmol dm^{-3} $Fe(CN)_6^{3-}$ / 0.2 mol dm^{-3} $Sr(NO3)_2$ resonant at 2.048 kHz was detected by a 25 μm diameter Pt microelectrode. The potential was held at -0.1 V versus Ag wire. (□) represents the frequencies and pressures (a, b, c) selected for the rise time experiment.

The current passed at the microelectrode and the pressure measured by an 8103 hydrophone placed in close proximity to the bubble were recorded simultaneously as a function of time. In this experiment the current time data was recorded as the bubble was exposed to sound at the frequencies and pressures selected (see □ in figure 7.3). Figure 7.4 shows an example of the current and pressure traces recorded simultaneously as a function of time under the described procedure. Figure 7.5 shows the same current time trace plotted with the time axis adjusted to reflect the exposure of the bubble to sound at time $t = 0$. Also illustrated on figure 7.5 is the annotation for the parameters assigned to the experimental data. These are defined as T_1, the time taken between the initial current perturbation and the onset of subharmonic contribution to the current (denoted by the rapid rise in current) and T_2, which is T_1 plus the time taken for the rapid rise in current. G_1 represents the gradient of the initial current maximum (denoted by *) while G_2 is the gradient of the second current maximum (*i.e.* the rapid increase in current due to the onset of subharmonic motion). These values were determined from each current time trace for the three frequency bands (a, b and c) plotted in figure 7.3. Table 7.1 illustrates the resultant data obtained.

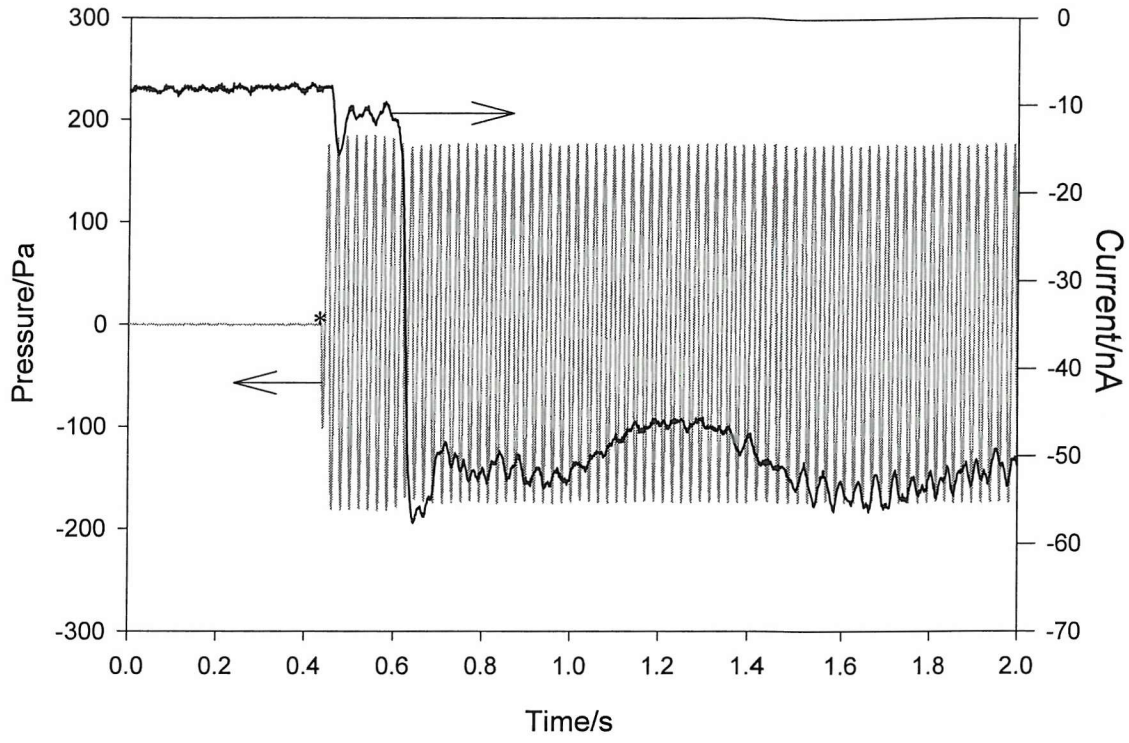

Figure 7.4 Plots illustrating the current time (—) and pressure time (·····) data recorded simultaneously. The current time data was recorded by a 25 μm diameter Pt microelectrode in 0.2 mmol dm^{-3} Triton X-100 in 5 mmol $Fe(CN)_6^{3-}$/0.2 mol dm^{-3} $Sr(NO_3)_2$ positioned close to an air bubble in the presence of a sound field of 2.048 kHz at 38.45 Pa pressure amplitude. The pressure time data was recorded by a hydrophone. The time the sound was switched on is indicated by * on the plot.

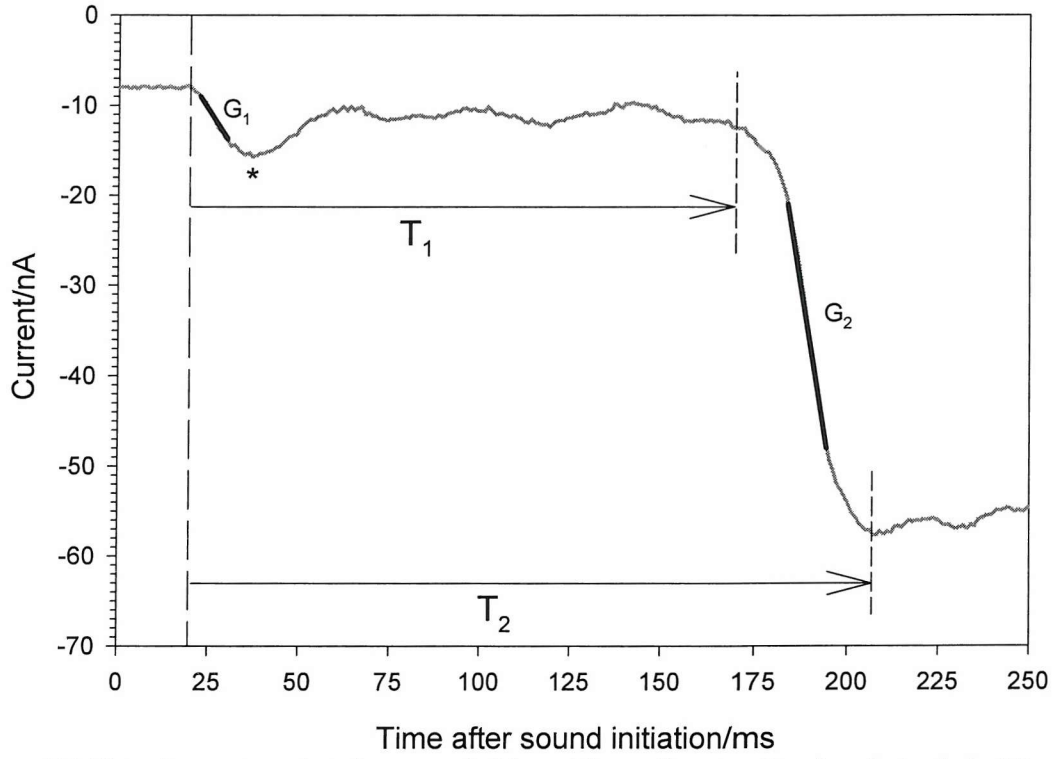

Figure 7.5 Plot of current against time recorded by a 25 μm diameter Pt microelectrode in 0.2 mmol dm^{-3} Triton X-100 in 5 mmol $Fe(CN)_6^{3-}$/0.2 mol dm^{-3} $Sr(NO3)_2$ positioned close to an air bubble in the presence of a sound field of 2.048 kHz at 38.45 Pa pressure amplitude. T_1 represents the time taken between the initial current perturbation and the onset of the subharmonic contribution to the current. T_2 represents T_1 plus the time taken for the rapid rise in current. G_1 represents the gradient of the initial current maximum (indicated by *) while G_2 is the gradient of the second current maximum (*i.e.* rapid increase in current caused by the onset of Faraday wave motion).

Important observations regarding the ring-up time of surface waves can be obtained from table 7.1. First, the initial current transient (assumed here to be the contribution to the current caused by the initial fluid motion as the result of fundamental bubble motion) following sound irradiation decreased as the driving pressure was reduced for each frequency band (a, b and c) employed. Second, both T_1 and T_2 increase as the driving pressure decreased for each frequency band employed. Therefore, the surface wave rise time increases with decreasing drive pressure at a constant drive frequency. Similarly G_1 and G_2 decrease with smaller drive pressures as expected.

Freq./ kHz	Pressure/ Pa	Initial Current max (*)/nA	T_1/s	T_2/s	T_2 in no. of cycles	[(di/dt)/A s^{-1}] /1 x 10^{-7} G_1	[(di/dt/A s^1)] /1x10^{-6} G_2
(a)	46.4	27.3	0.051	0.061	124.9	-8.992	†
	42.3	20.9	0.073	0.088	180.2	-6.539	-3.56
	38.5	15.7	0.151	0.192	393.3	-5.385	-1.652
	33.7	15.3	0.454	0.521	1067	-5.193	-0.375
	33.2	11.4	1.011	1.156	2367.4	-1.994	-0.1507
(b)	44.8	24.7	0.049	0.068	138.4	-7.287	-3.35
	40.7	15.8	0.085	0.121	246.2	-5.095	-1.796
	36.4	12.6	0.200	0.241	490.4	-3.004	-1.088
(c)	47.9	20.9	0.056	0.077	158.6	-8.787	-3.091
	43.8	17.8	0.099	0.126	259.6	-7.979	-2.353
	39.6	13.8	0.359	0.402	828.2	-5.97	-0.597

Table 7.1 Table showing the collection of experimental results obtained from the ring-up experiments. a, b and c represent the three frequency bands employed *i.e.* 2.048 kHz, 2.035 kHz and 2.06 kHz respectively (see figure 7.3). The initial current maximum, T_1, T_2, G_1 and G_2 are explained in figure 7.5.

Figures 7.6, 7.7 and 7.8 show current plotted as a function of the number of cycles of the excitation sound wave for the frequency bands a, b and c respectively. In each figure the surface wave ring-up time depicted as a number of cycles of the pumping wave from when the sound was switched on (indicated by ŧ) increases as the driving pressure decreases at constant frequency. These results can be compared to previously reported findings from combination frequency studies.[74] Figure 7.9 shows signal strength against the time in

† Gradient difficult to measure as the contribution to current caused by the onset of surface waves was difficult to establish.

cycles of the pumping wave, for a bubble resonant at 2.7 kHz (driving pressure 50 Pa), illustrating both the subharmonic and fundamental combination frequency signals recorded by Leighton *et al.*.[74] In this case the maximum subharmonic combination amplitude occurs after *ca.* 400 cycles. This can be compared to the electrochemical findings reported here were the maximum signal strength obtained using the combination frequency technique occurs in the range obtained under the conditions of this experiment *i.e.* between 125 and 2367 cycles (T_2 in table 7.1). It is also interesting to note that close to the surface wave threshold pressure (see band a figure 7.3; 2.048 kHz at 33.7 Pa and 33.2 Pa) a small pressure amplitude change (0.5 Pa) can make dramatic differences in the ring-up time (see figure 7.6). In these examples a 0.5 Pa change can result in a factor of 2 difference in the ring-up time (see figure 7.6) and other parameters (see Table 7.1).

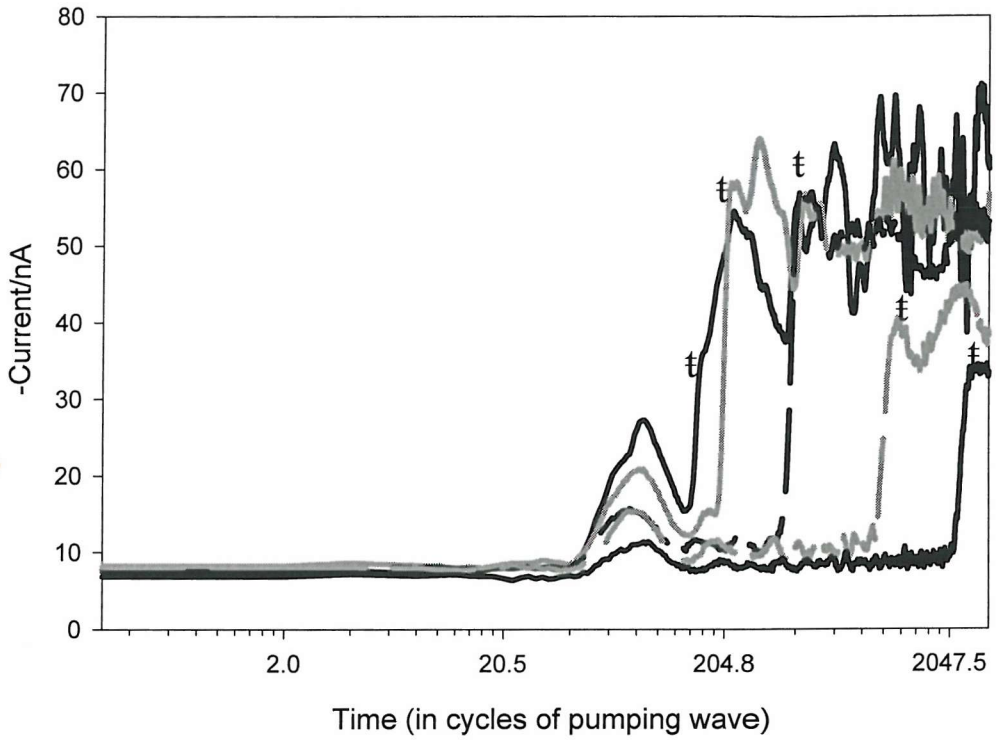

Figure 7.6 Plots of the current against time (in cycles of pumping wave) recorded by a 25 μm diameter Pt microelectrode in 0.2 mmol dm^{-3} Triton X-100 in 5 mmol dm^{-3} $Fe(CN)_6^{3-}$/0.2 mol dm^{-3} $Sr(NO_3)_2$ positioned close to an air bubble in the presence of a sound field of 2.048 kHz at 46.4 Pa, 42.3 Pa, 38.5 Pa, 33.7 Pa and 33.2 Pa pressure amplitude (left to right). The ring-up time in cycles for surface wave motion is denoted by ŧ in each plot.

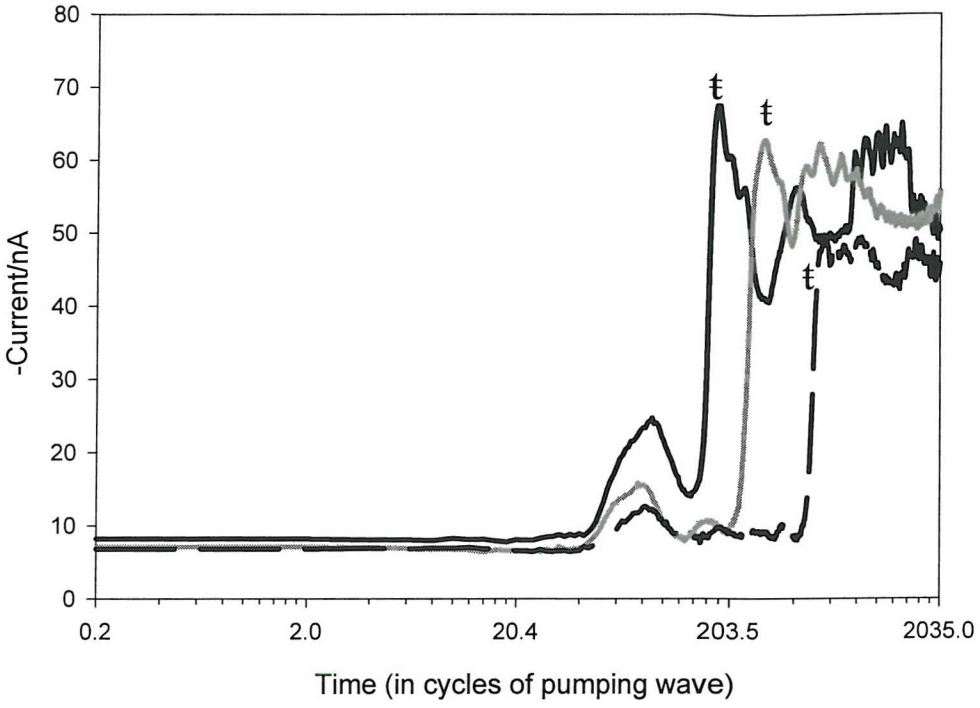

Figure 7.7 Plot of the current against time (in cycles of pumping wave) recorded by a 25 μm diameter Pt microelectrode in 0.2 mmol dm^{-3} Triton X-100 in 5 mmol dm^{-3} $Fe(CN)_6^{3-}$/0.2 mol dm^{-3} $Sr(NO_3)_2$ positioned close to an air bubble in the presence of a sound field of 2.035 kHz at 44.8 Pa, 40.7 Pa and 36.4 Pa pressure amplitude (left to right). The ring-up time in cycles for surface wave motion is denoted by t in each plot.

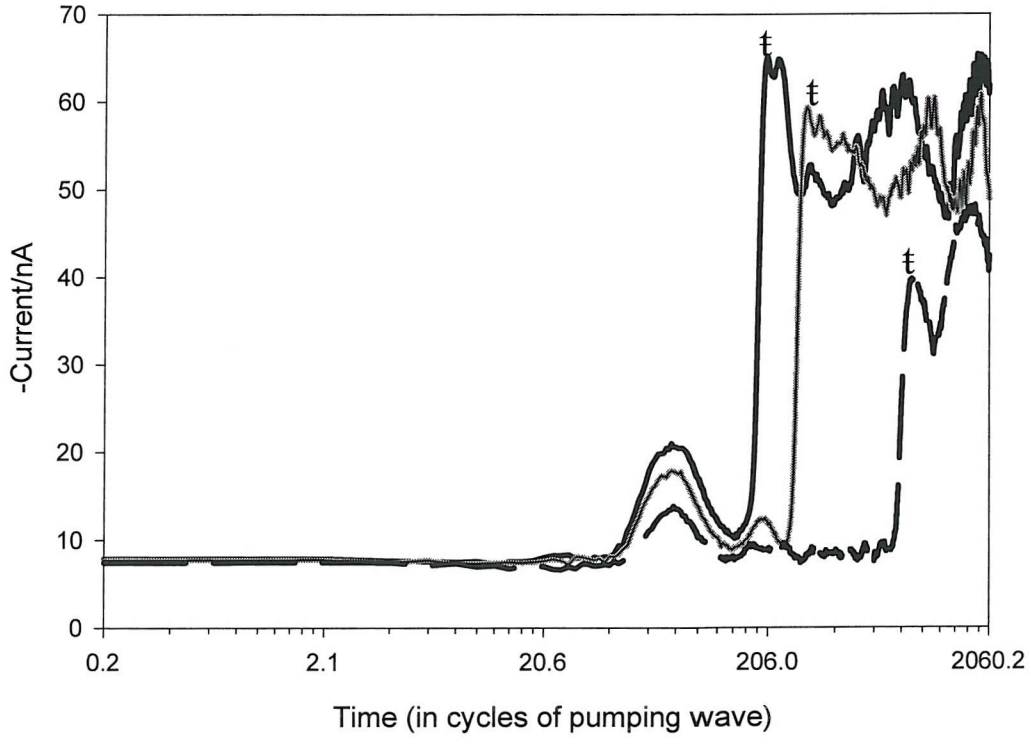

Figure 7.8 Plot of the current against time (in cycles of pumping wave) recorded by a 25 μm Pt diameter microelectrode in 0.2 mmol dm^{-3} Triton X-100 in 5 mmol dm^{-3} $Fe(CN)_6^{3-}$/0.2 mol dm^{-3} $Sr(NO_3)_2$ positioned close to an air bubble in the presence of a sound field of 2.06 kHz at 47.9 Pa, 43.83 Pa and 39.6 Pa pressure amplitude (left to right). The ring-up time in cycles for surface wave motion is denoted by t in each plot.

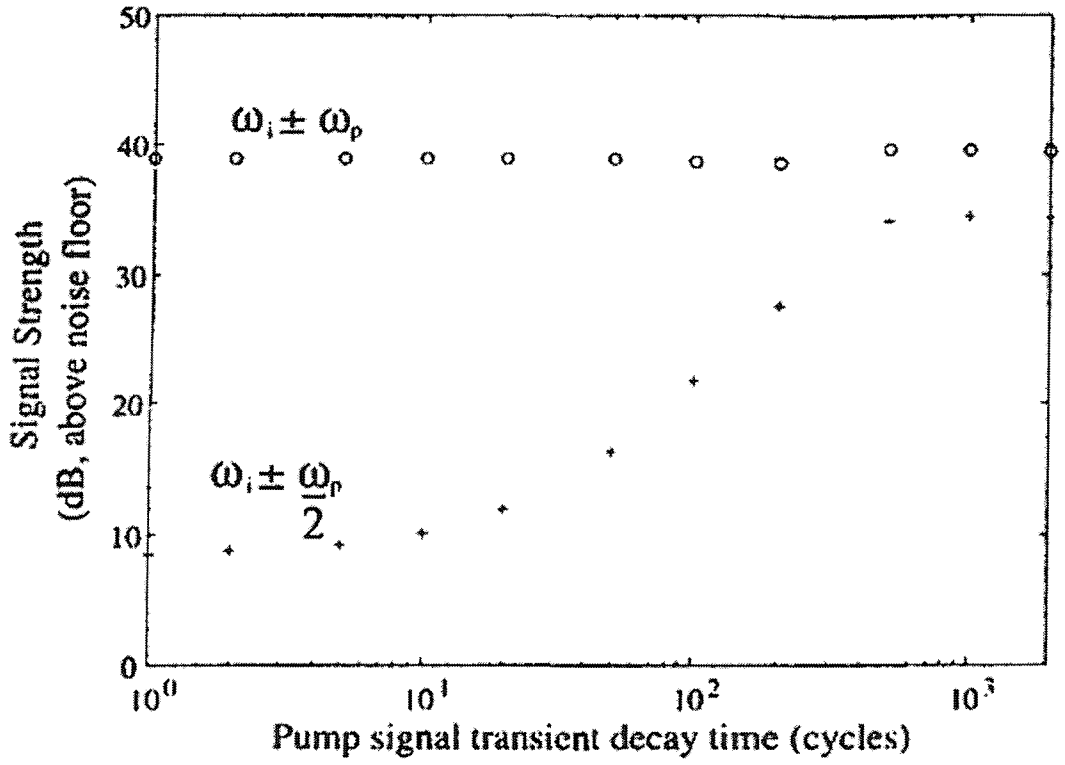

Figure 7.9 Plots of signal strength (amplitude) against time (in cycles of pumping wave) recorded for a bubble resonant at 2.7 kHz driven at 50 Pa employing the combination frequency technique described in section 1.7. The plot (+) represents the combination frequency subharmonic signal while (○) represents the combination frequency fundamental signal. Reproduced from Leighton *et al.*.[74]

The experimental data reported in this chapter is currently being analysed with respect to the theory proposed by Maksimov and Leighton.[79] However, the results are unavailable at this time. Nonetheless the data compares well to that obtained employing the combination frequency technique.[74]

7.3 Conclusions

Initial experiments performed to measure surface wave ring-up were undertaken employing a macroelectrode. However, a number of problems were encountered during the course of these experiments; bubble growth by the process of rectified diffusion and inhibition of bubble motion. Bubble growth by the process of rectified diffusion was removed by controlled addition of the surfactant Triton X-100 while dampening of bubble motion was removed by employing a 25 μm diameter Pt microelectrode. Important information regarding the ring-up time of surface waves was obtained using these experimental conditions. The initial current time transient following sound irradiation decreased with decreasing drive pressure at a constant drive frequency, while the time taken

to achieve steady state surface oscillations increased with decreasing drive pressure at a constant frequency. The data obtained compares well to similar experiments performed employing the combination frequency technique and is currently being compared to the theory proposed by Maksimov and Leighton.[79]

Clearly the results reported here and previously in chapters 4 - 6, demonstrated that electrochemistry can be employed as a successful and sensitive method for detecting bubble motion driven by an appropriate acoustic field. However, it is also possible to envisage that bubble motion induced by acoustic excitation will have useful applications. The subsequent three chapters will explore this idea and discuss three separate feasibility studies to see if electrochemical detection of Faraday wave motion can be used to size bubbles (Chapter 8), measure rates of rectified diffusion (Chapter 9) or to detect trace species (Chapter 10).

Rising Bubbles

Chapter 8

8.0 Introduction

Numerous acoustic techniques exist to detect and size bubbles. [19-23,73,74,117,118] Acoustic techniques are very suitable for bubble sizing because of a number of reasons. These include the large impedance mismatch at the gas/liquid interface and the significant difference in the compressibility of the gas and the liquid means that the bubble can couple strongly with pressure fluctuations.[73] In chapter 5 it was determined that Faraday wave motion only occurs for a range of frequencies and driving pressures. There is also a threshold pressure at which Faraday wave motion is initiated. Therefore, electrochemical detection of this mode could be potentially useful in sizing bubbles because this motion occurs over a much narrower frequency band than for fundamental oscillation of a bubble (see section 5.3b). This chapter presents the initial experimental work (employing the acousto-electrochemical technique developed in previous chapters) undertaken to detect and measure Faraday wave motion of an individual bubble in a rising bubble stream.

8.1 Electrochemical Detection of Individual Bubbles

The experimental set-up employed is shown in figure 2.5 (see chapter 2). A microelectrode was positioned in the path of the rising bubble stream so that individual bubbles could be detected. Bubble streams were generated manually using an air filled syringe attached to a fibreglass needle inserted in the side of the cell. A loudspeaker was incorporated into the cell for experiments requiring sound irradiation of the bubble stream. Initially, the cell was filled with a solution of 5 mmol dm^{-3} $Fe(CN)_6^{3-}$ in 0.2 mol dm^{-3} $Sr(NO_3)_2$. The potential was held at –0.1 V versus Ag where the reduction of $Fe(CN)_6^{3-}$ was mass transfer controlled. Individual air bubbles were injected into the solution. This experiment was performed in the absence of sound irradiation. A Kodak HS 4540 high-speed video camera was used to picture the rising stream of bubbles and also to align the microelectrode in the centre of the rising stream. Figure 8.1 shows an image of a stream of bubbles rising in the vicinity of a 25 μm diameter Pt microelectrode in the absence of sound

irradiation. The recording rate of the camera employed was 4500 fps. Figure 8.2 shows the current time plot recorded at a microelectrode placed in the bubble stream. Each peak corresponds to the effect of an individual bubble on the current recorded at the microelectrode. This figure illustrates successive bubble passes but the amplitude of the dips is not fully resolved as the inter-point time here is 1 ms which from figure 8.4 might alias the peak. Nonetheless the enhancement in current is due to the forced convection induced by bubble motion caused by buoyancy forces.

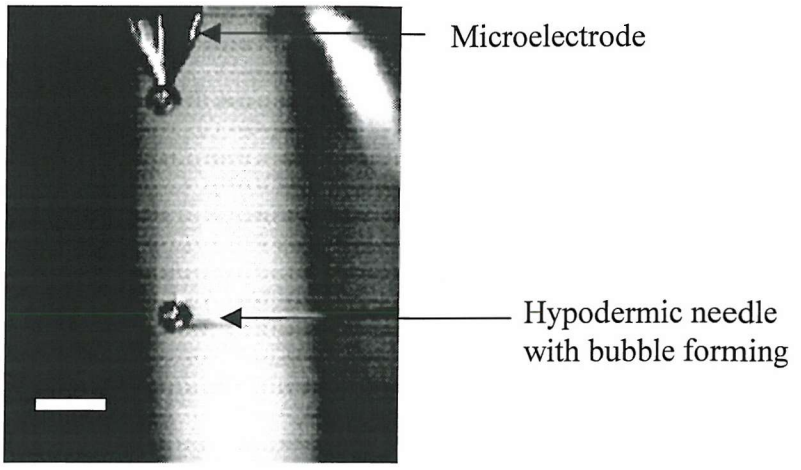

Figure 8.1 Picture of a rising bubble hitting the electrode surface recorded by the high-speed video camera in the absence of sound irradiation. The scale bar indicates 2 mm. The recording rate was 4500 fps.

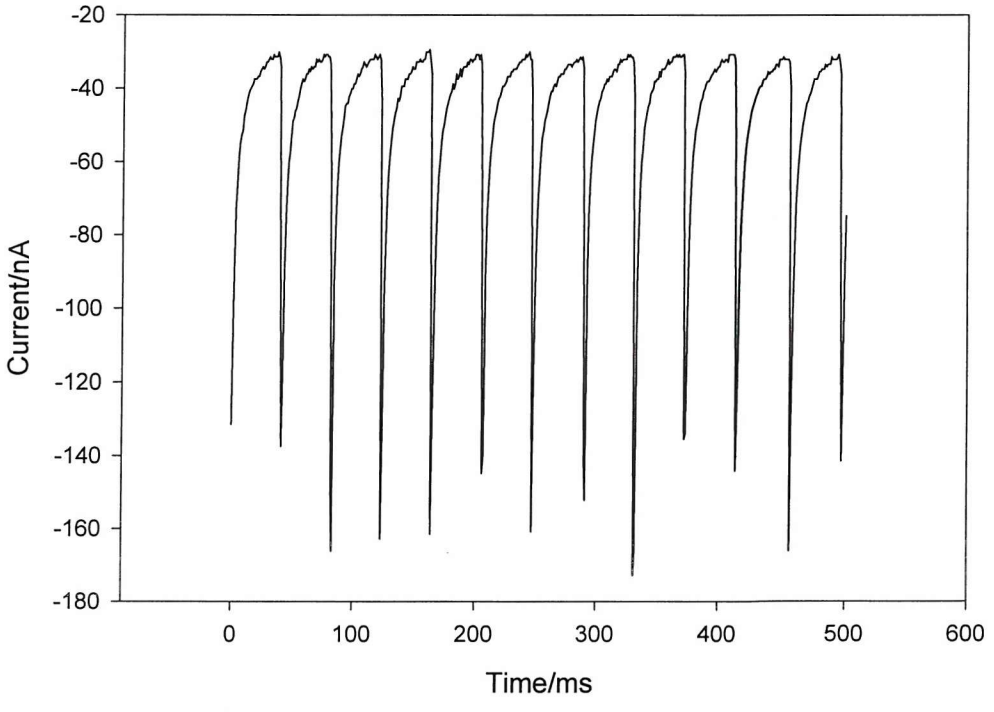

Figure 8.2 Plot of current versus time recorded by a 25 μm diameter Pt microelectrode in 5 mmol dm^{-3} $Fe(CN)_6^{3-}$/0.2 mol dm^{-3} $Sr(NO_3)_2$ under aerobic conditions where the potential of the microelectrode was held at –0.1 V versus Ag. The microelectrode was positioned in line with a stream of rising bubbles (R_0 *ca.* 0.5 mm). Each peak represents individual bubble detection.

Figure 8.3 shows a set of images illustrating the motion of an individual rising bubble. The sequence of pictures represents detachment of the bubble from the hypodermic needle (a), followed by its passage towards the microelectrode (b) and (c), subsequent momentary impact on the microelectrode surface (d), detachment (e) and finally movement away from the electrode surface (f). The approximate diameter of the bubble is determined to be 1 mm from this sequence of images.

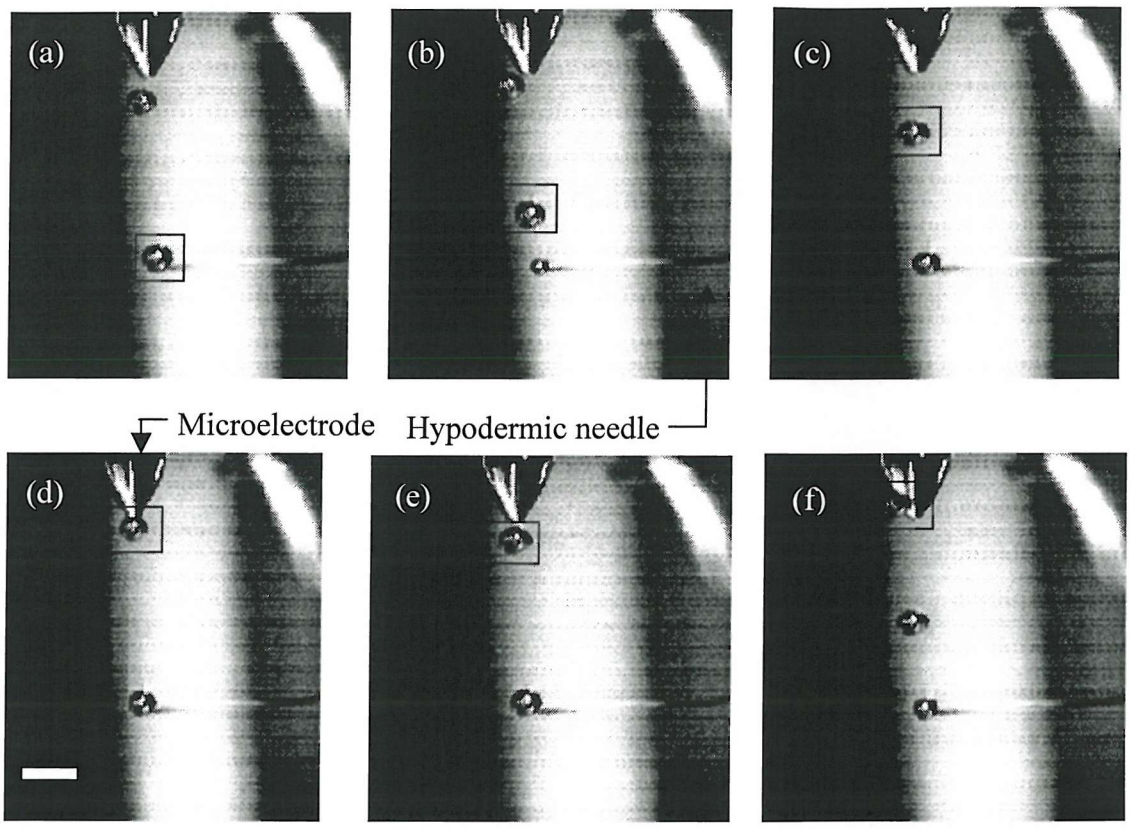

Figure 8.3 A series of pictures taken by the Kodak HS 4540 video camera of single bubble (enclosed in black box) (a) detaching from the hypodermic needle (b) moving upwards in line with the 25 μm diameter Pt microelectrode (c) moving closer to the microelectrode (d) reaching the microelectrode tip and momentarily 'sitting' (e) detachment from the microelectrode and (f) moving away from the microelectrode. This experiment was performed in 5 mmol dm^{-3} $Fe(CN)_6^{3-}$/0.2 mol dm^{-3} $Sr(NO_3)_2$ under aerobic conditions where the microelectrode was held at –0.1 V versus Ag. The recording rate of the camera was 4500 frames per second. The scale bar on picture (d) represents 2 mm.

Figure 8.4 shows the effect of an individual bubble on the current recorded at the microelectrode tip. A number of important points must be noted from this figure. In region 'A' the current increases which is attributed to mass transfer enhancements to the electrode surface as a result of the convective flow of the liquid to surface of the microelectrode induced by the motion of the rising bubble. This coincides with the 'hydrodynamic model' discussed in chapter 1 section 1.4 proposed by Janssen *et al.*.[57-59] This treatment emphasises the electrolytic flow caused by the buoyant lift of rising bubbles in the vicinity of the

electrode. Region 'B' represents the momentary impact or 'sitting' of the bubble on the end of the microelectrode prior to moving away from the microelectrode surface. This hinders diffusion of species to the electrode surface so thus the current starts to decrease. However, the current starts to increase again in region 'C' produced by the detachment of the bubble from the electrode surface. This can be correlated with the penetration model introduced in chapter 1 section 1.4 by Ibl and Venczel.[56] In this model a volume of liquid in the mass transfer boundary layer, having been depleted of reactant, is renewed as each bubble detaches from the electrode and allows fresh electrolyte with bulk concentration of reactant to replace the void left by the bubble at the surface of the electrode. Finally, in region 'D' the current starts to decrease as the bubble moves away from the electrode surface and mass transfer steady state conditions are restored.

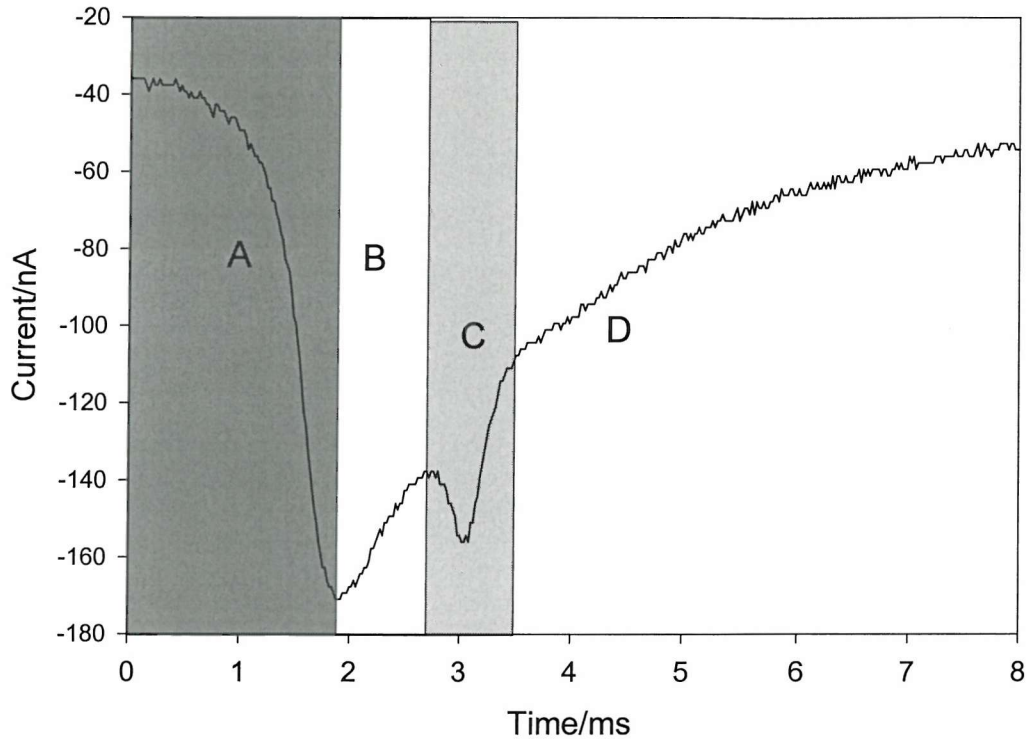

Figure 8.4 Plot of current against time recorded by a 25 μm diameter Pt microelectrode in 5 mmol dm^{-3} $Fe(CN)_6^{3-}$/0.2 mol dm^{-3} $Sr(NO_3)_2$ under aerobic conditions for a single air bubble (R_0 *ca.* 0.5 mm) rising in the path of the electrode. The potential of the microelectrode was held at –0.1 V versus Ag.

However, an alternative explanation for the current time transient observed in regions 'B' and 'C' could also be proposed. In this case the current transient could be explained in terms of a 'stop/start' flow regime as the bubble hits the microelectrode surface. This can be attributed to the deceleration of the bubble as it momentarily comes to rest on the microelectrode tip (see figure 8.4 region B). As the bubble moves away from the microelectrode, convective flow is initiated and the transient shown in figure 8.4 region C is

generated. The exact mechanism responsible for this current time transient remains to be fully ascertained.

8.2 Calculation of Mass Transfer Coefficients in the Presence of a Bubble Stream

In figure 8.4 the current recorded at the microelectrode due to an individual rising bubble was determined to be –171 nA. The mass transfer coefficient (k_m) can be calculated from equation 1.4 chapter 1. Therefore the mass transfer coefficient was calculated to be 0.072 cm s^{-1} under these conditions. This is significant when compared to an already efficient value in a stagnant solution of 0.008 cm s^{-1} *i.e. ca.* 10 times bigger (see section 4.1).

In order to determine the spatial variation of the mass transfer enhancements due to the rising bubble stream (R_0 *ca.* 0.5 mm), an experiment was performed where initially the position of the microelectrode was adjusted (via a micrometer and stage) until maximum enhancement in mass transfer to the electrode surface, due the motion of individual rising bubbles, was observed (see figure 8.4). The microelectrode was then moved in increments of 40 μm laterally in the x direction away from the centre of the bubble stream and the corresponding current time plot caused by the motion of an individual bubble in the vicinity of the microelectrode tip recorded. This was repeated at a number of distances away from the centre of the bubble stream. The mass transfer coefficient was calculated as before for each distance away from the centre of the stream. Figure 8.5 is a plot of the mass transfer coefficient against distance from the centre of the bubble stream. The dashed line (----) represents the mass transfer coefficient recorded under stagnant conditions in the bulk solution far from the bubble. It is evident from this plot that when the distance from the centre of bubble stream is greater than 0.4 mm the enhancement in mass transfer to electrode surface falls back to that recorded under steady state conditions. This implies that the microelectrode will have to be positioned close to the centre of the bubble stream to accurately determine the effects of individual bubbles on the mass transfer coefficient. It is also worth noting that the distance scale for mass transfer enhancement is approximately one bubble radii.

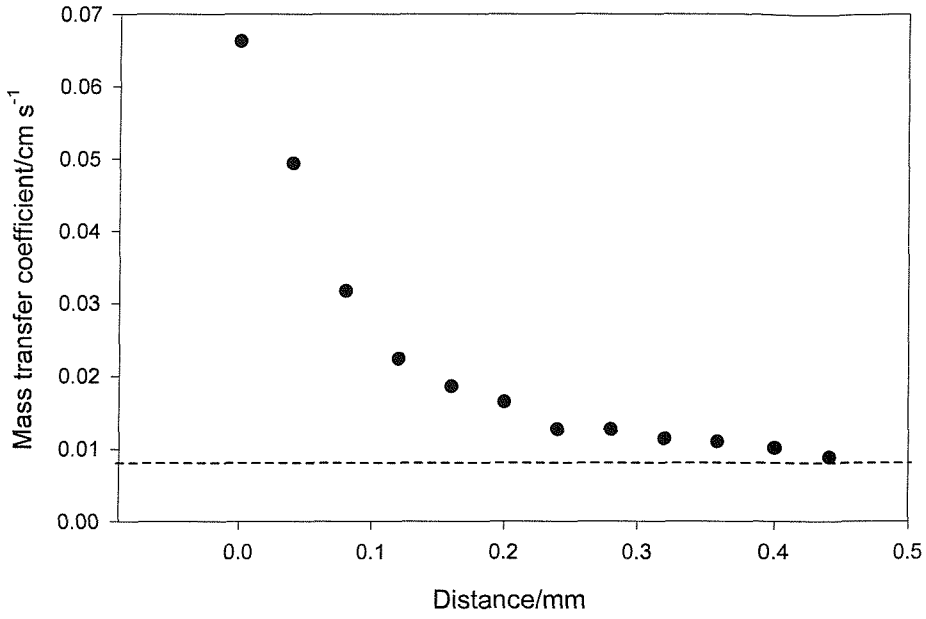

Figure 8.5 Plot of mass transfer coefficient against distance from the centre of a bubble stream (R_0 *ca.* 0.5 mm) in the x direction recorded by a 25 μm diameter Pt microelectrode in 5 mmol dm^{-3} $Fe(CN)_6^{3-}$/0.2 mol dm^{-3} $Sr(NO_3)_2$ under aerobic conditions. The dashed line represents the mass transfer coefficient in a stagnant solution. The potential of the microelectrode was held at –0.1 V versus Ag. The error in mass transfer coefficient is ± 0.001 cm s^{-1}.

8.3 Electrochemical Detection of Faraday Waves on an Individual Rising Bubble

It has been shown that the mass transfer enhancements due to bubbles rising under buoyancy forces are extremely localised. In order to determine the influence of sound irradiation on the rising bubbles an experiment was performed where initially the position of the microelectrode was adjusted (via the micrometer and stage) until maximum enhancement in mass transfer to the electrode surface was observed due to individual rising bubbles (in this case the current time plots were recorded on an oscilloscope). Images of the individual bubbles rising in the bubble stream were captured using a Kodak HS 4540 camera. These confirmed that the microelectrode was positioned in centre of the stream. An approximate estimate of the bubble diameter was determined to be 1 mm in section 8.1. Therefore, the resonant frequency of the bubble was calculated to be approximately 6.4 kHz employing equation 1.11 in chapter 1.

The bubble stream was then irradiated with sound. From the images gathered the frequency of the sound field was adjusted to 6 kHz and increased until the current time plot observed on an oscilloscope showed a frequency component that was half the frequency of the driving acoustic field. Figure 8.6 shows a plot of the current time trace recorded in this

manner. The acoustic pressure was then recorded, using a hydrophone, in the absence of the bubble stream but under identical conditions for the observation of the subharmonic signal. This is also included in figure 8.6.

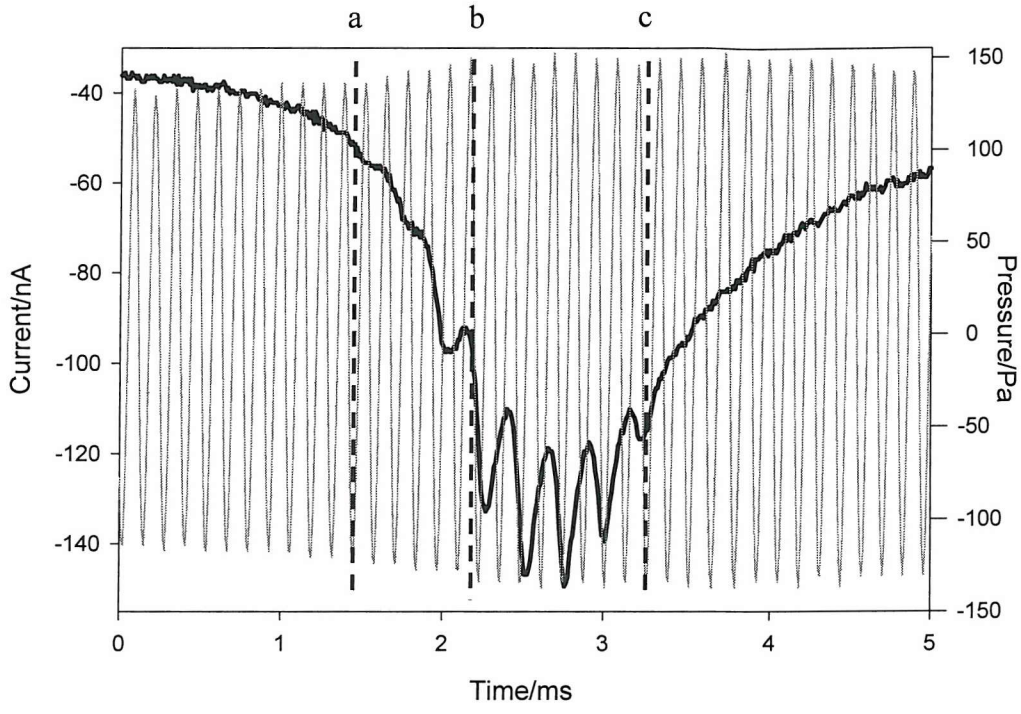

Figure 8.6 Plots showing the current (—) detected at a 25 μm diameter Pt microelectrode and the pressure (—) detected by a hydrophone (in the absence of the bubble stream) in 5 mmol dm^{-3} $Fe(CN)_6^{3-}$/0.2 mol dm^{-3} $Sr(NO_3)_2$ caused by a rising air bubble interacting with a sound field of 7.678 kHz. The potential of the system was held at –0.1 V versus Ag under aerobic conditions.

A number of important points must be noted from the figure 8.6. First, the enhancement in negative current is induced by convective flow of the solution to the microelectrode surface caused by the buoyant lift of the rising bubble (similar to figure 8.4). Second, line 'a' in figure 8.6 denotes the point of initial subharmonic signal detection by the microelectrode. Third, between lines b and c the bubble is presumed to be in close proximity to the microelectrode. In this region the magnitude of the subharmonic signal is at a maximum. The current then starts to decrease as presumably the bubble moves away from the microelectrode surface and mass transfer steady state conditions are restored. Images of the oscillating bubble were also captured by the high-speed video camera. These provided evidence that the subharmonic signal was as a result of surface wave motion of the bubble wall (*e.g.* Faraday waves). However, it was difficult to see Faraday wave motion from the still images.

It should be noted that because of the magnitude of the current time signal caused by convective flow of the solution induced by the rising bubble (see figure 8.4) in comparison

to the magnitude of signal caused by Faraday wave motion (see figure 8.6) the fundamental (breathing mode) would be difficult to detect on a rising bubble.

8.4 Determination of Bubble Size

Employing buoyant rise time measurement is a standard way of determining bubble size or measuring the bubble radius photographically. Levich[119] carried out work studying the rise velocities of bubbles in liquids based on the Rybczynski-Hadamard[120,121] equation. For Reynolds numbers (*Re*) between 50 and 800 (*i.e.* diameter between 0.5 and 2 mm see equation 8.1) Levich[119] found the velocity of bubbles to be given by equation 8.2:

$$Re = \frac{\rho v d_1}{\mu} \tag{8.1}$$

where ρ is the density of the liquid, v is the rising velocity, d_1 is the bubble diameter and μ is the liquid viscosity.

$$v = \frac{gR^2(\rho - \rho')}{9\mu} \tag{8.2}$$

where R is the bubble radius and ρ' is the gas density. This approach assumes that the bubbles were spherical, although deviation from bubble spherical shape[122] was found to occur at *Re ca.* 800.

Equation 8.2 can be used to calculate the radius of the rising bubbles employed in the experimental conditions described in section 8.1. The velocity (v) calculated from the images 8.3 b and c (the time frame between these images was known and the distance travelled by the bubble in that time was calculated employing the microelectrode as a scale) was determined to be 17.74 cm s^{-1}. The bubble radius was calculated as 382 ± 77.5 μm from equation 8.2 assuming the density of the solution is approximately the same as for water, and using the dynamic viscosity of water as 8.91 x 10^{-4} N m^{-2} s. However, this is not the most precise means of determining bubble size as the error in determining the rise velocity is relatively large and had to be accounted for *i.e.* the error in measuring the distance the bubble had moved from the images in figure 8.3 (b) and (c) was ± 0.1 mm.

Detection of Faraday wave motion is probably the most accurate means of sizing bubbles.[73,74,123] Leighton *et al.*[123] used a 'combination frequency' technique to detect

Faraday wave motion. Employing this technique Leighton *et al.*[123] sized single rising bubbles and compared their results to the buoyant rise time measurement of sizing bubbles. Single bubbles in a rising stream were determined as having a radius of 820 ± 130 μm when the buoyant rise time technique was employed while a value of 862 ± 12 μm was determined using detection of Faraday wave motion. Clearly, detection of Faraday motion is a much more precise means of sizing bubbles.

In section 8.3 Faraday wave motion was detected for single rising bubbles employing electrochemical techniques. The frequency at which Faraday wave motion was observed was 7678 ± 20 Hz. This corresponds to a radius of 417 ± 12 μm (calculated using equation 1.12) which is much more favourable than the rise time measurement of 382 ± 77.5 μm. The reduced error in the acousto-electrochemical detection technique compares well to that determined by Leighton *et al.*[123] using the combination frequency technique. Also it must be remembered that the Levich equation is only valid for bubbles with surfactant free mobile interfaces.[119] In the presence of surfactant the rise rates of bubbles has been shown to decrease[122] by up to 30 %. However, retardation effects will be less dramatic for larger bubbles[119] *i.e.* $Re > 1$. In the experiments reported in this chapter no procedures were undertaken to remove trace surfactants that maybe present in the solution apart from normal good laboratory practice. Hence the difference in the size estimations for the two techniques may result from trace residual surfactant, which is difficult to remove completely from the solution.

8.5 Conclusions

A number of important points arise from this study. It was possible to measure the effects of individual bubbles on mass transfer to a microelectrode. Individual bubbles were denoted by large enhancements in current recorded at the microelectrode due to forced convection induced by bubble motion caused by buoyancy forces. The effect of an individual bubble on the current recorded at the microelectrode could be explained in terms of the hydrodynamic model[57-59] and the penetration model[56] or by a flow 'stop/start' mechanism.

Significant enhancements in the steady state current were noticed when the microelectrode was < 0.5 mm from the centre of the rising bubble stream. The most significant result from this series of experiments was the electrochemical detection of surface wave motion of an individual rising bubble. Electrochemical detection of this

Faraday wave motion could be used to size bubbles. This detection technique was much more accurate than the buoyant rise time technique. The accuracy compared well to that obtained by Leighton *et al.*[123] who used a combination frequency technique to measure Faraday wave motion.

Other possible applications of electrochemical detection of Faraday wave motion can be envisaged. The next chapter introduces one such application where a preliminary study into the growth of bubbles in the presence of acoustic irradiation by a process known as rectified diffusion is reported.

Rectified Diffusion

Chapter 9

9.0 Introduction

A gas bubble in a liquid, in the absence of a sound field, will slowly dissolve owing to the excess internal gas pressure required to balance the surface tension or Laplace pressure ($2\sigma/R$). Thus, in the absence of a sound field and any stabilising mechanisms, all bubbles will gradually dissolve.[124] However, in the presence of a sound field growth of the bubble comes about through active pumping of the gas, initially dissolved in the liquid, into the bubble using the energy of the acoustic wave. This process has been termed 'rectified diffusion'. This chapter presents an electrochemical study of the growth of large gas bubbles (R_0 *ca.* 1 - 2 mm) through this process.

9.1 Original Theory

The prediction of the acoustic pressure threshold for rectified diffusion has been the subject of numerous studies[82,83,125-127] and predictions generally agree with available experimental results. This threshold depends on the amount of dissolved gas in the liquid, the bubble size and the acoustic frequency. The growth rates of bubbles have also been predicted, but these predictions are often considerably less than measured values.[82,128,129] The discrepancy has been identified as a failure to account for microstreaming.[130,131] Church[80] devised a theoretical model to account for bubble growth in the absence and presence of microstreaming. Church[80] combined the equation for the rate of change in the number of moles of a gas in a bubble (n_g) derived by Eller *et al.*[126] (equation 9.1) with equation 9.2, which assumes ideal gas behaviour. This gave the time average rate of change in equilibrium radius (equation 9.3).

$$\frac{dn_g}{dt} = 4\pi R_0 D[A + R_0(\frac{B}{\pi Dt})^{1/2}]C_{sn}(\frac{C_i}{C_{sn}} - \frac{A}{B}) \qquad (9.1)$$

where R_0 is the equilibrium radius of the bubble, D is the diffusion coefficient, A and B are described in chapter 1 section 1.10, C_i is the gas concentration in the bulk, C_{sn} is the concentration of gas at the bubble wall and C_0 is the saturation concentration of gas in the liquid.

$$p_0 + \frac{2\sigma}{R} = \frac{3n_g R_g T}{4\pi R_0^{\ 3}} \tag{9.2}$$

where R_g is the universal gas constant, p_0 the hydrostatic pressure, R the instantaneous bubble radius, σ is the surface tension, n_g is the number of moles of gas and T absolute temperature.

$$\frac{dR_0}{dt} = \frac{DR_g T}{R_o}(p_0 + \frac{4\pi}{3R_0})^{-1}[A + R_0(\frac{B}{\pi Dt})^{1/2}]C_{sn}(\frac{C_i}{C_{sn}} - \frac{A}{B}) \tag{9.3}$$

Church[80] described the term $1/t$ as the length of time between the moment when the acoustic pressure amplitude P_A exceeds the threshold pressure for rectified diffusion P_T and the moment rectified diffusion is observed. This term maybe referred to as the 'transient term' and represents the initial depletion of gas surrounding the bubble during the earliest stages of growth. Therefore as time passes the gas concentration gradient at the bubble wall decreases and thus the growth rate decreases. However, in the presence of microstreaming the concentration gradient is maintained because the gas content of the liquid surrounding the bubble is constantly renewed through forced convection of material from the bulk of the liquid. However, equation 9.3 does not account for this effect.

Examining equation 9.3 derived by Church[80] it is apparent that the $(p_0 + 4\pi/3R_0)$ term represents the contribution to the growth rate due to the diffusion of gas from outside the diffusion boundary layer (DBL) surrounding the bubble. The term containing the transient time represents the contribution due to dissolved gas inside the DBL. As the time progresses during irradiation, the gas concentration in the DBL decays towards an equilibrium level that is maintained by diffusion from outside the boundary layer (see figure 9.1 (a)). In the absence of microstreaming the $1/t$ affects the growth rate only during the time it takes to reach this equilibrium. This time is given by t_1 (see figure 9.1 (c)). However, in the presence of microstreaming a spatially non-uniform, dynamic gas concentration of higher average value is reached rapidly (see figure 9.1 (b)). Therefore, the

't' value in the $1/t$ term is much less. This time is given by t_2 (see figure 9.1 (c)). As t is regarded as the decay time regardless of microstreaming, the $1/t$ is more accurately known as the 'decay' term.

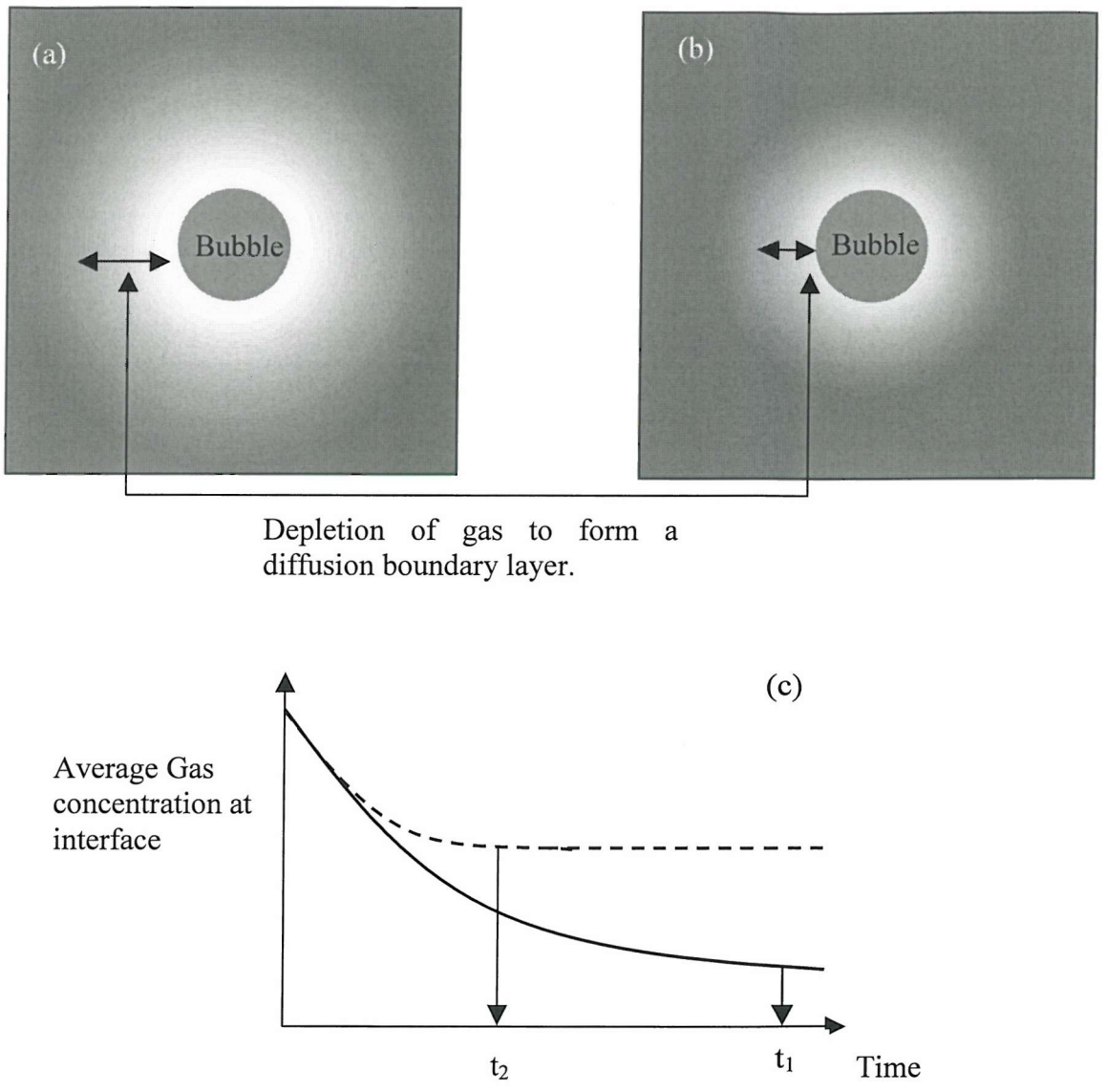

Figure 9.1 Schematic illustrating the effect of streaming on the concentration profiles surrounding the bubble and the decay term where (a) represents the formation of the diffusion boundary layer caused by gas depletion in the presence of sound irradiation but in the absence of streaming (b) represents the formation of the diffusion boundary layer caused by gas depletion in the presence of sound irradiation and the presence of microstreaming and (c) is a plot of the average gas concentration at the interface against the time where t_1 and t_2 represent the decay time in the absence and presence of microstreaming respectively.

These ideas (*i.e.* decay times) can be incorporated into the model. As the gas concentration profile surrounding the bubble wall is governed by equation 9.3, two important length scales, the equilibrium radius (R_0) and the diffusion length $(Dt)^{1/2}$ need to be considered. However, when a convective (microstreaming) field is added a new velocity

term (U) is introduced so a third length scale appears having order of magnitude of $(DR_0/U)^{1/2}$. As U increases for a given value of t or time passes for a constant U, the diffusion length scale quickly becomes greater than the convection length scale. Under these conditions the convective term dominates the gradient. As the term R_0/U is dimensionally time, the diffusion and convection lengths have the same form enabling Church[80] to substitute R_0/U for t in equation 9.3 when microstreaming is present. Under these conditions equation 9.3 becomes equation 9.4.

$$\frac{dR_0}{dt} = \frac{DR_gT}{R_o}(p_0 + \frac{4\pi}{3R_0})^{-1}[A + R_0(\frac{BU}{\pi DR_0})^{1/2}]C_{sn}(\frac{C_i}{C_{sn}} - \frac{A}{B}) \qquad (9.4)$$

However, Church[80] also stated that this order of magnitude estimate could not be used to predict the correct numerical coefficient. An exact calculation of the value of the t term (or the R_0/U term) would be difficult so an estimate has to be employed. This estimate in the decay time requires knowledge of the fluid velocity, but no theory exists for the microstreaming produced by surface waves. Church employed values for the streaming velocity measured by a number of other workers. As an example Gould[129] has measured streaming velocities in excess 1 cm s^{-1} around bubbles exhibiting surface waves at 20 kHz. Alternatively equation 9.5 given by Statnikov[131] for the flow around a bubble attached to a needle gives velocities of this magnitude, has simple angular dependence and shows an increase in velocity with increasing bubble radius for $R_0 < R_r$, the linear resonance radius. The equation is:

$$U_\theta = \frac{V_0^{\,2}}{4R_0\omega}\sin 2\theta\{1 + (\frac{C_0}{\omega R_0})^2[(\frac{\omega_0^{\,2}}{\omega^2} - 1) + d_{tot}^{\,2}]^{-1}\} \qquad (9.5)$$

where U_θ is the streaming velocity with angular dependence, V_0 is the acoustic particle velocity given by equation 9.6, ω is the driving frequency, ω_0 is the resonant frequency of the bubble and d_{tot} is non-dimensional damping coefficient:

$$V_0 = P_A / \rho c_i \qquad (9.6)$$

where c_i is the speed of sound and ρ is the density of the liquid. Owing to the nature of the derivation of equation 9.5 it should be restricted to frequencies below 100 kHz and $R_0 > 20$

μm. For frequencies above this frequency and below this radius there are no observations of streaming velocities around free bubbles. Figure 9.2 is a plot of bubble radius against time recorded by Gould[81] for a bubble growing by rectified diffusion. It also includes theoretical values calculated by Church[80] using the theory derived above. In the figure the onset of surface oscillations and acoustic streaming is concomitant with the marked increase in growth rate. Church also compared his theory to experimental data obtained by Eller[82] (see section 1.10 figure 1.17). Both Eller[82] and Gould[81] showed a marked increase in growth rates in the presence of microstreaming, determining growth rates of 0.1 - 0.5 μm s^{-1} under similar conditions of frequency and pressure. The pressure amplitude of the sound field (*i.e.* 1.2 - 2.5 kHz and < 100 Pa) employed in thesis is significantly lower in comparison to the sound field employed by Gould[81] (20 kHz and 27.27 kPa). Therefore the growth rates reported in this work will be expected to be lower than those obtained by Gould[81] and Eller.[82]

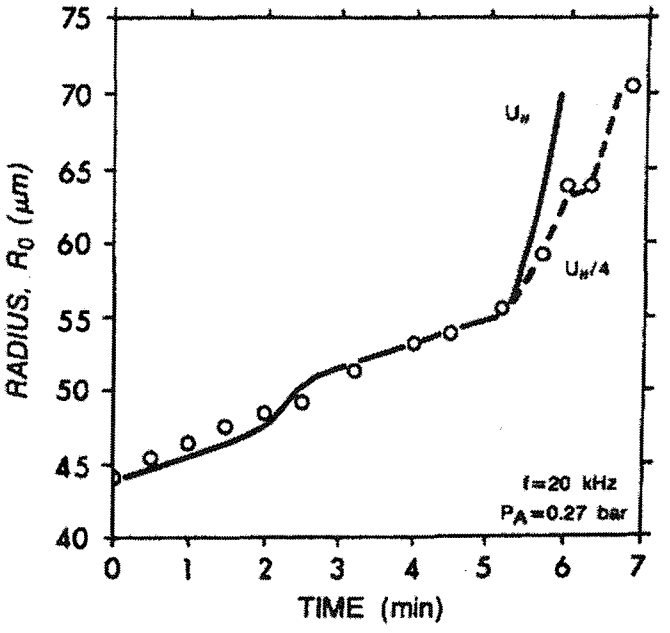

Figure 9.2 Bubble radius versus time for a bubble growing by rectified diffusion (○) measured by Gould.[81] The onset of surface oscillations and acoustic streaming was concomitant with the marked increase in growth rate. The sound pressure was 0.27 bar at 20 kHz. The solid line (—) represents theoretical calculations of Church.[80] Reproduced from Gould.[81]

In order to determine the growth rates in the presence of Faraday wave motion, a series of experiments were performed employing an electrochemical technique. The methodology and results of this study are presented in the following sections.

9.2 Experimental

9.2a Rate of Bubble Growth in the Presence of Faraday Wave Motion

The experimental set-up employed was as in figure 2.4. An air bubble was tethered to an insulated Ni wire in a solution containing 5 mmol dm^{-3} $Fe(CN)_6^{3-}$ in 0.2 mol dm^{-3} $Sr(NO_3)_2$. The microelectrode was positioned close to the bubble wall via a micrometer and stage in the absence of sound irradiation (*ca.* 20 μm away see section 3.1a). The sound was switched on. The current time trace was then observed using an oscilloscope and the frequency and pressure of the sound field adjusted until Faraday wave motion was detected. The system was set-up so that we were at the lower side of the frequency/pressure curve (see section 5.1), which enabled growth, but not loss of Faraday wave activity. Maintaining this pressure and frequency the sound field was alternated between off and on in 30 s intervals while the current at the microelectrode was monitored as a function of time (employing low temporal resolution equipment). Figure 9.3 illustrates the current time plot recorded in this manner. The insert in figure 9.3 shows $i_{MTL}/i_{int,MTL}$ (*i.e.* the mass transfer limiting current recorded at the microelectrode after a period of sound irradiation divided by the initial mass transfer limiting current recorded at the microelectrode in the absence of sound irradiation) as a function of the irradiation exposure.

A number of points must be noted from this figure. First, it is evident from both plots that the current recorded at the microelectrode in the absence of sound irradiation decreases as the time of irradiation increases. This indicates that the bubble-wall microelectrode distance has decreased (see section 3.1a). Therefore the bubble has grown (assuming that the bubble remains in one position at all times). After seven minutes of sound irradiation there is no change in the current recorded at the microelectrode in the absence of sound irradiation. This signifies the electrode (or surround) is at or touching the bubble wall (see figure 9.3 region A). Note also that once the bubble reaches resonance the growth rate slows.[24] Second, the fluctuations in current in the presence of sound vary as the time of irradiation increases. In chapter five section 5.3b it was noted that the current recorded at the microelectrode varied over the frequency and pressure range at which subharmonic motion occurred (see figure 5.11). Therefore these differences in the enhancement and fluctuation of the current are caused by a shift in the resonance frequency to a lower value indicating the bubble has grown (see equation 1.12).

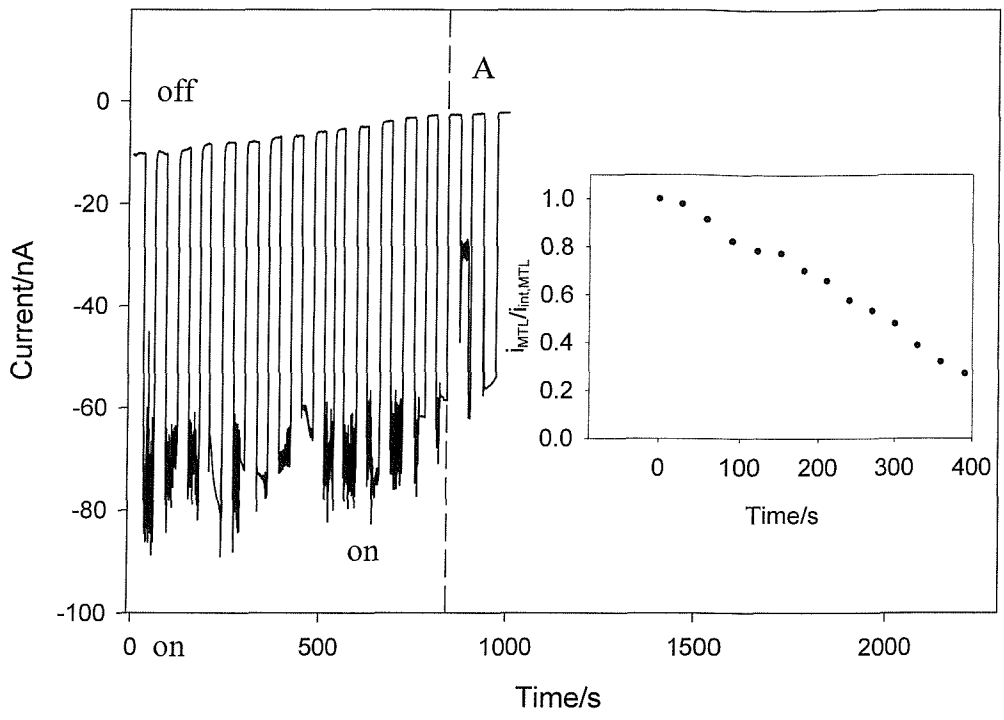

Figure 9.3 Plot of current versus time detected by a 25 μm diameter Pt microelectrode positioned at approximately 20 μm from the bubble wall (R_0 1.3 - 1.4 mm) where a sound field of 2.08 kHz at 51.74 Pa pressure amplitude was alternated between off and on in 30 s intervals. The solution used was an aerobic solution of 5 mmol dm^{-3} $Fe(CN)_6^{3-}$ in 0.2 mol dm^{-3} $Sr(NO_3)_2$. The insert shows $i_{MTL}/i_{int,MTL}$ against time of irradiation.

It is possible to calculate the rate of growth of the bubble radius from the data obtained in figure 9.3. This required a number of calculations to be undertaken. First, the normalised current in the absence of sound irradiation was calculated by dividing the average current recorded at the microelectrode in the absence of insonification after each pulse of irradiation by the current recorded in the bulk far from the bubble in the absence of sound irradiation *i.e.* i_{tip}/i_{inf} (see section 3.1). In this sequence of experiments the bubble wall is considered inert (negative feedback). Therefore, the bubble-wall microelectrode distance can be determined, employing equation 3.1 derived by Denuault and Amphlett,[49] under negative feedback conditions. The value of L, the microelectrode tip-substrate distance (d) divided by the electrode radius (a), can be calculated from equation 3.1 employing R_{glass} equal to 5.09 (ratio of the insulating glass sheath radius to that of the electroactive disk). The microelectrode tip-bubble wall distance after each pulse of sound can be determined because the radius of the microelectrode (a) was 12.5 μm.

Figure 9.4 shows a plot of the growth of the bubble radius in μm against time of irradiation. The rate of bubble growth was determined from this plot to be 0.0371 ± 0.0017 μm s^{-1}. This is a factor of 10 lower than the rates obtained by Eller[82] and Gould.[81] However,

the pressure amplitude of the sound field was significantly lower (< 100 Pa).

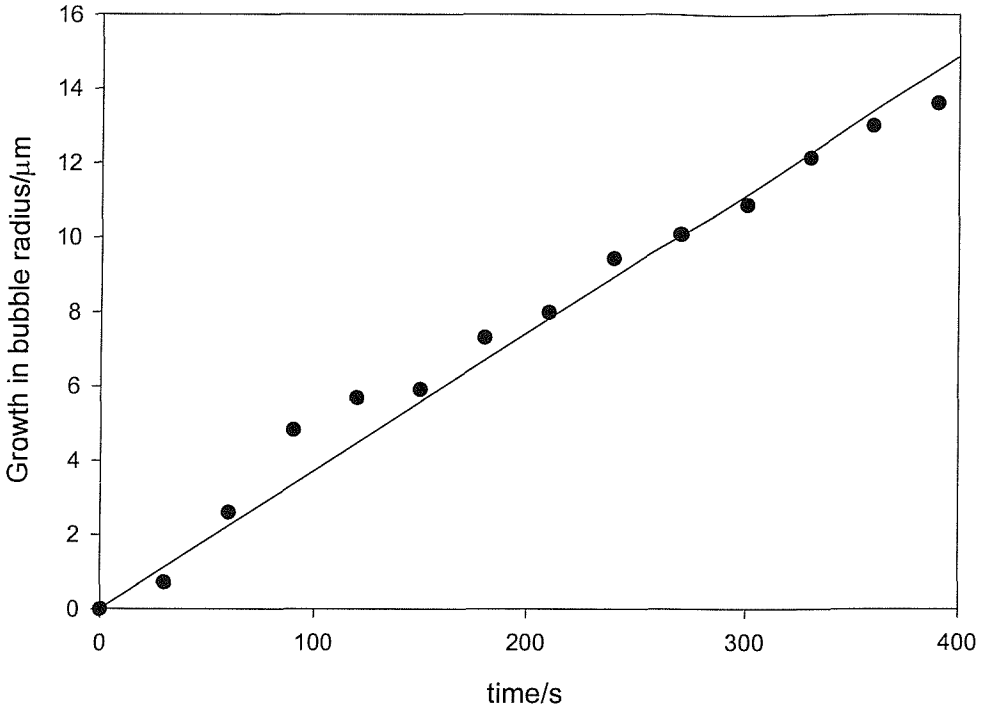

Figure 9.4 Plot of growth in bubble radius by rectified diffusion against time of irradiation for a bubble irradiated with a sound field of 2.08 kHz at 51.74 Pa pressure amplitude. The solid line was the best-fit straight line. The other experimental conditions were the same as figure 9.3.

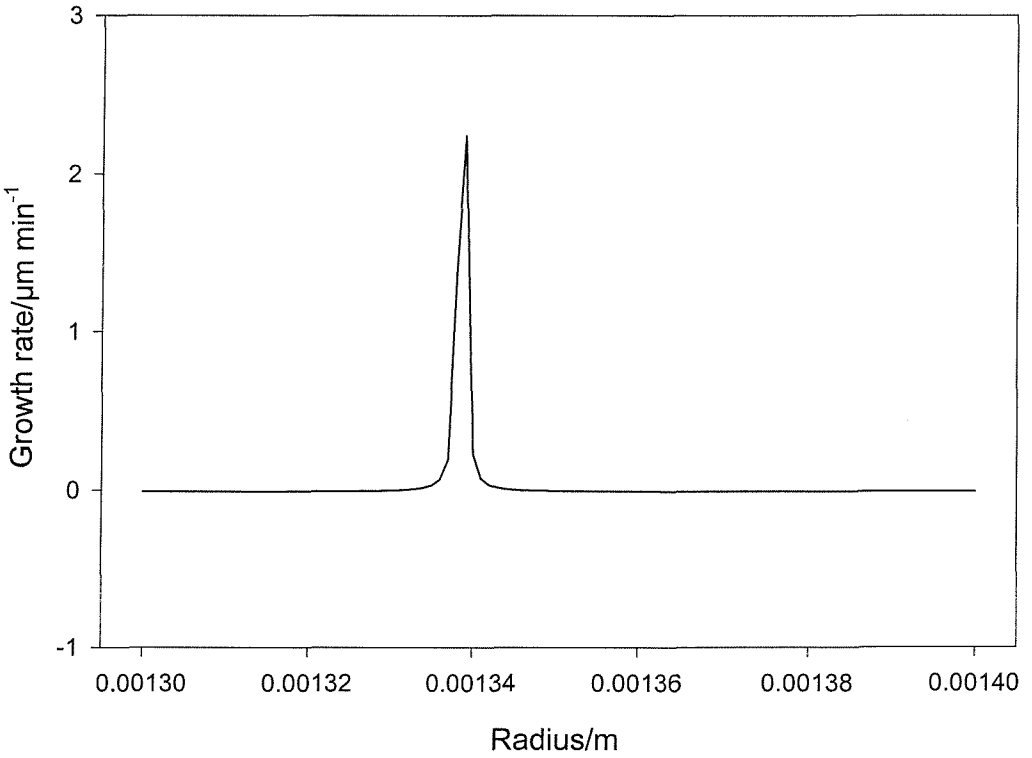

Figure 9.5 Plot of growth rate against radius predicted by equation 9.3 derived by Church[80] employing the experimental conditions in figure 9.3 *i.e.* a sound field of 2.08 kHz at 51.74 Pa pressure amplitude (see equations 1.21 and 1.22).

Figure 9.5 is a plot of growth rate in μm per minute against radius predicted using equation 9.4 derived by Church[80] employing the experimental conditions in figure 9.3. A maximum growth rate of 0.0373 μm s^{-1} was predicted from Church's theory. The theory shows good agreement with the experimental data obtained here.

The method proposed by Church[80] to account for the effects of microstreaming on growth rates by rectified diffusion is not an exact solution of the problem. First, no exact theory exists for the microstreaming velocities produced by surface waves. Second, the equations used to calculate values for *A* and *B* assume spherical symmetry of the bubble. The presence of surface waves violates this assumption. Therefore, the calculated values of *A* and *B* may not accurately represent the true physical situation.

Clearly the electrochemical method presented here is successful in determining the growth rate of a bubble attached to a wire support. However, previous chapters have discussed the effect of surfactants on both the nature of the gas liquid interface and the motion of the bubble wall. The subsequent section will explore the effects of surfactants on the rate of rectified diffusion.

9.2b Rate of Bubble Growth and Surfactants

The experimental set-up was as in figure 2.4. The rate of growth of the bubble radius was first determined in the absence surfactant. An air bubble was tethered to an insulated Ni wire in a solution containing 5 mmol dm^{-3} $Fe(CN)_6^{3-}$/0.2 mol dm^{-3} $Sr(NO_3)_2$. The electrode was positioned approximately 20 μm from the bubble in the absence of sound irradiation using methods described previously (section 3.1a). The potential of the electrode was held at –0.1 V versus Ag. The sound was again alternated between off and on in 30 s intervals at a frequency where Faraday wave motion was evident. Figure 9.6 illustrates the current time plot recorded where the insert represents $i_{MTL}/i_{int,MTL}$ as a function of time of irradiation. The features in figure 9.6 are similar to those recorded in figure 9.3. First, the current recorded in the absence of sound irradiation decreased as the time of irradiation increased thus confirming bubble growth. Second, the current in the presence of irradiation fluctuated as the time of irradiation increased further substantiating bubble growth for reasons described in 9.2a. A plot of the growth of the bubble radius against time determined from figure 9.6 is shown in figure 9.7. A growth rate of 0.0304 ± 0.0036 μm s^{-1} was calculated from this plot, which shows reasonable agreement with the rate determined in section 9.2a.

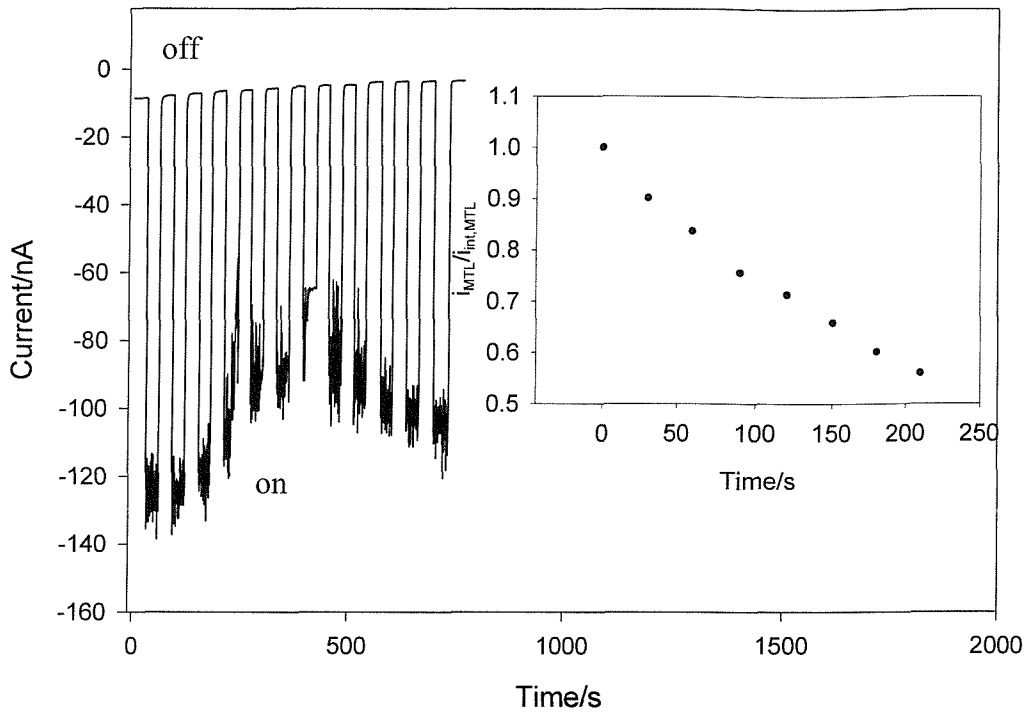

Figure 9.6 Plot of current versus time detected by a 25 μm diameter Pt microelectrode positioned at approximately 20 μm from the bubble wall (R_0 1.2 – 1.3 mm) where a sound field of 2.29 kHz at 79.6 Pa pressure amplitude was alternated between off and on in 30 s intervals. The solution used was an aerobic solution of 5 mmol dm^{-3} $Fe(CN)_6^{3-}$ in 0.2 mol dm^{-3} $Sr(NO_3)_2$. The insert shows $i_{MTL}/i_{int,MTL}$ against time of irradiation.

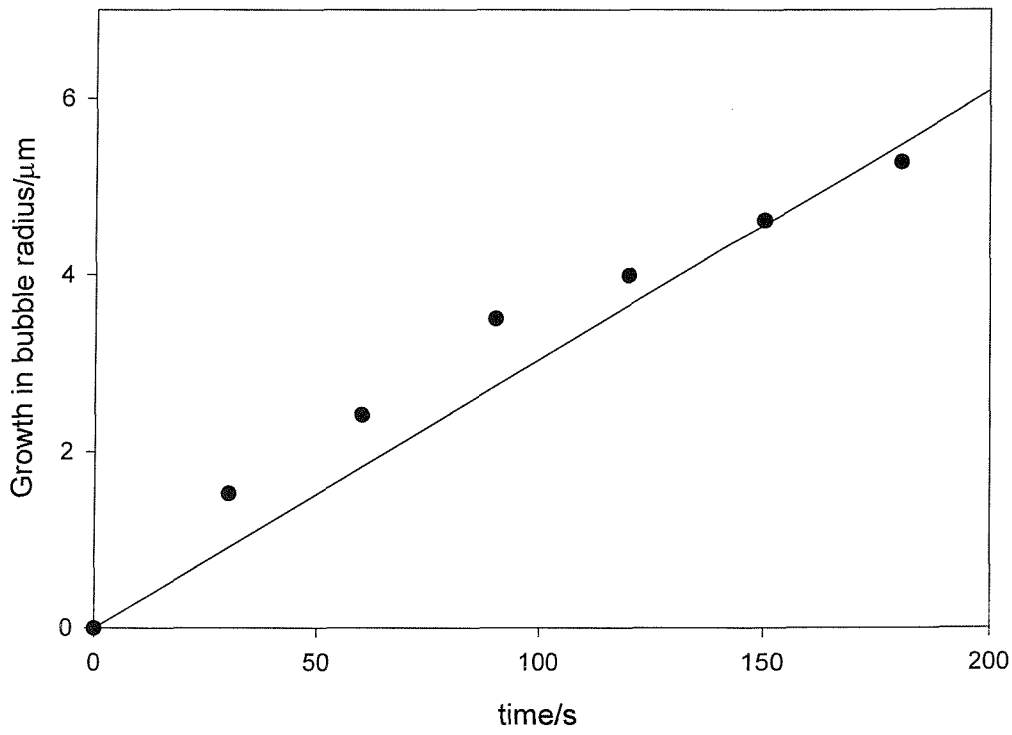

Figure 9.7 Plot of growth in bubble radius by rectified diffusion against time of irradiation for a bubble irradiated with a sound field of 2.29 kHz at 79.6 Pa pressure amplitude. The solid line indicates the best-fit straight line. The other experimental conditions were the same as figure 9.6.

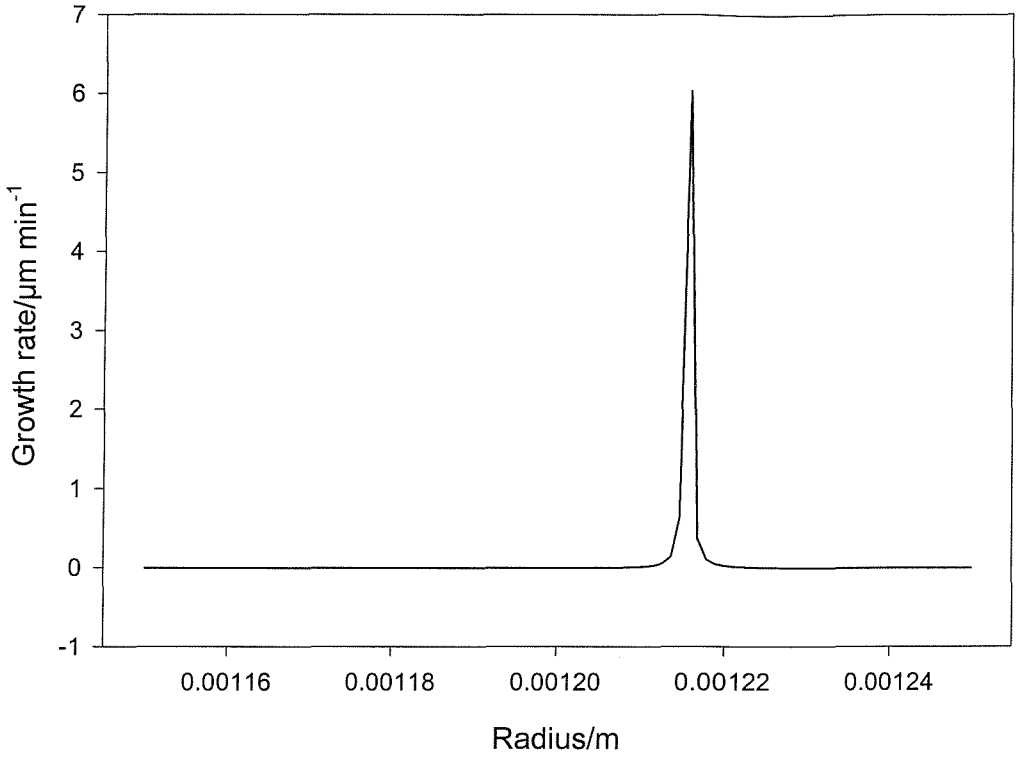

Figure 9.8 Plot of growth rate against radius predicted by equation 9.3 derived by Church[80] employing the experimental conditions in figure 9.6 *i.e.* a sound field of 2.29 kHz at 79.6 Pa pressure amplitude (see equations 1.21 and 1.22).

Figure 9.8 is a plot of growth rate in μm per minute against radius predicted using equation 9.4 derived by Church[80] employing the experimental conditions in figure 9.6. A maximum growth rate of 0.1005 μm s^{-1} was predicted from Church's theory. This does not compare well with the experimental data. However, a number of problems exist with Church's theory[80] outlined in the previous section 9.2a.

In order to investigate the effect of surfactants on the rectified diffusion induced growth of a bubble, Triton X-100 was then controllably added (28 μl) to the solution containing 5 mmol dm^{-3} $Fe(CN)_6^{3-}$/0.2 mol dm^{-3} $Sr(NO_3)_2$. The concentration of this species present in the solution was 0.2 mmol dm^{-3}. Bubble growth by rectified diffusion in the previous experiment required the microelectrode/bubble distance to be readjusted to approximately 20 μm in the absence sound irradiation. Sound was alternated between off and on in 30 s intervals at the same frequency and pressure at which Faraday wave motion occurred (*i.e.* 2.29 kHz at 79.6 Pa). Figure 9.9 illustrates the current time plot obtained. The insert shows $i_{MTL}/i_{int,MTL}$ as a function of time of irradiation for a sound field operating at 2.29 kHz/79.6 Pa with surfactant (■) and without surfactant (●) (see figure 9.6) and a sound field operating at 2.08 kHz/51.74 Pa without surfactant (○) (see figure 9.3).

From the main plot in figure 9.9 it is evident the current recorded in the absence of sound remains approximately constant as the time of irradiation increases. Therefore the microelectrode bubble distance is not varying; consequently, the bubble has not grown. This is also evident from the insert plot (■) where the current remains approximately constant as the time of irradiation increases. Note the insert also includes current time plots in the absence of surfactant. These plots clearly show that the current recorded at the microelectrode decreased as the time of irradiation increased thus confirming bubble growth for reasons previously discussed in section 9.2a. Figure 9.9 clearly shows that the fluctuations in current in the presence of sound irradiation remain constant with time. Hence, there is no shift in resonance frequency of the bubble further substantiating that the bubble has not grown.

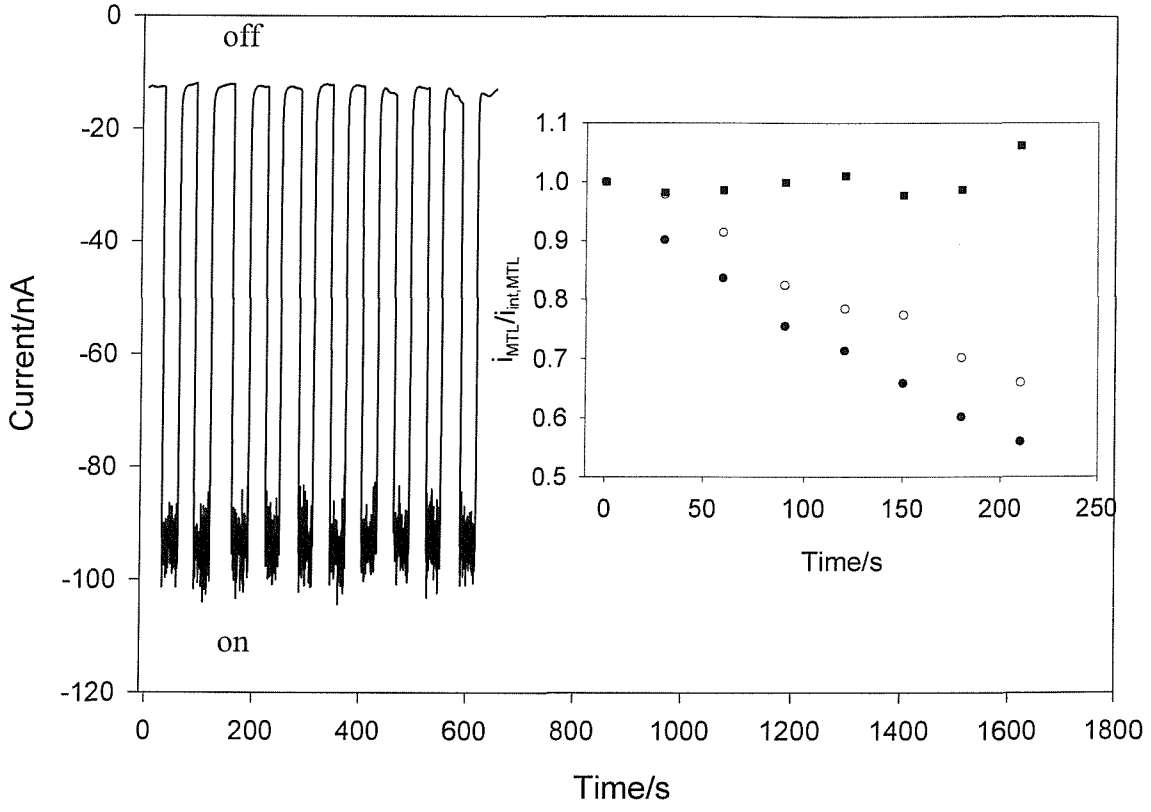

Figure 9.9 Plot of current versus time detected by a 25 μm diameter Pt microelectrode positioned at approximately 20 μm from the bubble wall where a sound field of 2.29 kHz at 79.6 Pa was alternated between off and on in 30 s intervals. The solution used was an aerobic solution 0.2 mmol dm^{-3} Triton X-100 in 5 mmol dm^{-3} $Fe(CN)_6^{3-}$/0.2 mol dm^{-3} $Sr(NO_3)_2$. The insert shows $i_{MTL}/i_{im,MTL}$ against time of irradiation in the presence of Triton X-100 (■). The insert also includes $i_{MTL}/i_{im,MTL}$ against time without surfactant and a sound field operating at 2.29 kHz /79.6 Pa (●) and a sound field operating at 2.08 kHz/51.74 Pa (○).

It can be therefore concluded that the presence of surfactants hinders the process of rectified diffusion as expected. It is known that surfactants tend to accumulate at the interface of two phases. According to Unwin *et al.*[40] the amount of accessible free area

governs the rate of transfer of oxygen across the gas liquid interface *i.e.* oxygen transfer can only occur in regions free from surfactant. This was verified for a bubble system in chapter 3 section 3.2 where the presence of a surfactant hindered oxygen transfer across the gas/liquid interface of a static bubble. These results are supportive of one another and indicate that surfactants would hinder the process of rectified diffusion.

9.3 Conclusions

Electrochemical detection of bubble growth by rectified diffusion was explored in this chapter. Previous studies[80-82] have measured the growth of bubbles in the presence of a sound field and have determined enhanced growth rates in the presence of microstreaming. This chapter introduces the first electrochemical measurement of rectified diffusion in the presence of Faraday wave motion. Growth rates of 0.03-0.04 $\mu m\ s^{-1}$ were determined experimentally. These rates were a factor of 10 lower than those obtained by Eller[82] and Gould.[81] However, the pressure amplitude of the sound fields employed by these authors were significantly higher. The results obtained compared reasonably well with theory proposed by Church.[80] However, his proposed method of accounting for microstreaming in the presence of surface waves on rectified diffusion growth rates is not an exact solution of the phenomenon.

Previous chapters have explored the effects of surfactants on gas transfer across the interface and the threshold pressure required to excite surface waves. In this chapter the presence of surfactants has been shown to hinder bubble growth through rectified diffusion.

It is also possible to envisage that electrochemical detection of Faraday wave motion would have other useful applications. In the next chapter detection of trace species is possible using lock-in techniques.

Detecting Trace Species

Chapter 10

10.0 Introduction

In the previous chapters electrochemical technology has been employed to investigate the interaction of sound with a gas bubble. Those studies clearly showed that electrochemical techniques could give valuable insight into the nature of the bubble oscillation, the gas exchange between a bubble and the surrounding liquid, the growth of a bubble through rectified diffusion, the ring-up time of surface waves and the effects of surfactants on surface wave phenomena. However, it is possible to envisage that bubble oscillation is a useful tool in applications not directly related to investigating the phenomena *per se* but exploiting the unusual characteristics available when a bubble interacts with sound. One such application is presented here where an oscillating bubble is employed in a new hydrodynamic voltammetry technique we term acoustic voltammetry (AcV). Before we introduce this technique it is useful to describe the detection limits and characteristics of hydrodynamic modulation voltammetry (HMV) found within the literature.

HMV relies on introducing an AC modulation to the convective flow of species to an electrode surface.[85] Under appropriate conditions this AC modulation is locked into and improved signal to noise ratios are obtained. This results in extreme enhancements in detection limits. As an example previous studies[85,86] have determined detection limits for ions in solution as being 0.5 nmol dm^{-3} using HMV (see section 1.11). However, electrochemical detection of surface waves could be potentially effective in HMV. In addition to efficient mass transfer of species caused by the motion of the bubble wall, the frequency of subharmonic oscillation is easily discriminated from the background noise. This is illustrated in figure 10.1. Figure 10.1 shows a plot of the frequency analysis of a typical current time plot, employing high-resolution equipment, recorded by a 25 μm diameter Pt microelectrode in the presence of subharmonic motion (see section 5.1). A signal is detected both at the driving frequency (which represents electrochemical detection of the breathing mode) and at half the driving frequency (which represents electrochemical detection of the Faraday wave, a subharmonic motion). In chapter 5 figure 5.7 it was

demonstrated that the breathing mode was easily distinguishable from background electrical noise. Therefore, as the magnitude of the subharmonic signal is *ca.* 10 times greater than the magnitude of the breathing mode signal in figure 10.1, the subharmonic signal will be easily discriminated from background electrical noise. Hence electrochemical detection of subharmonic motion could be potentially useful in identifying low concentrations of species in solution through a modified version of HMV termed here AcV. The results of a pilot study into this application are now presented.

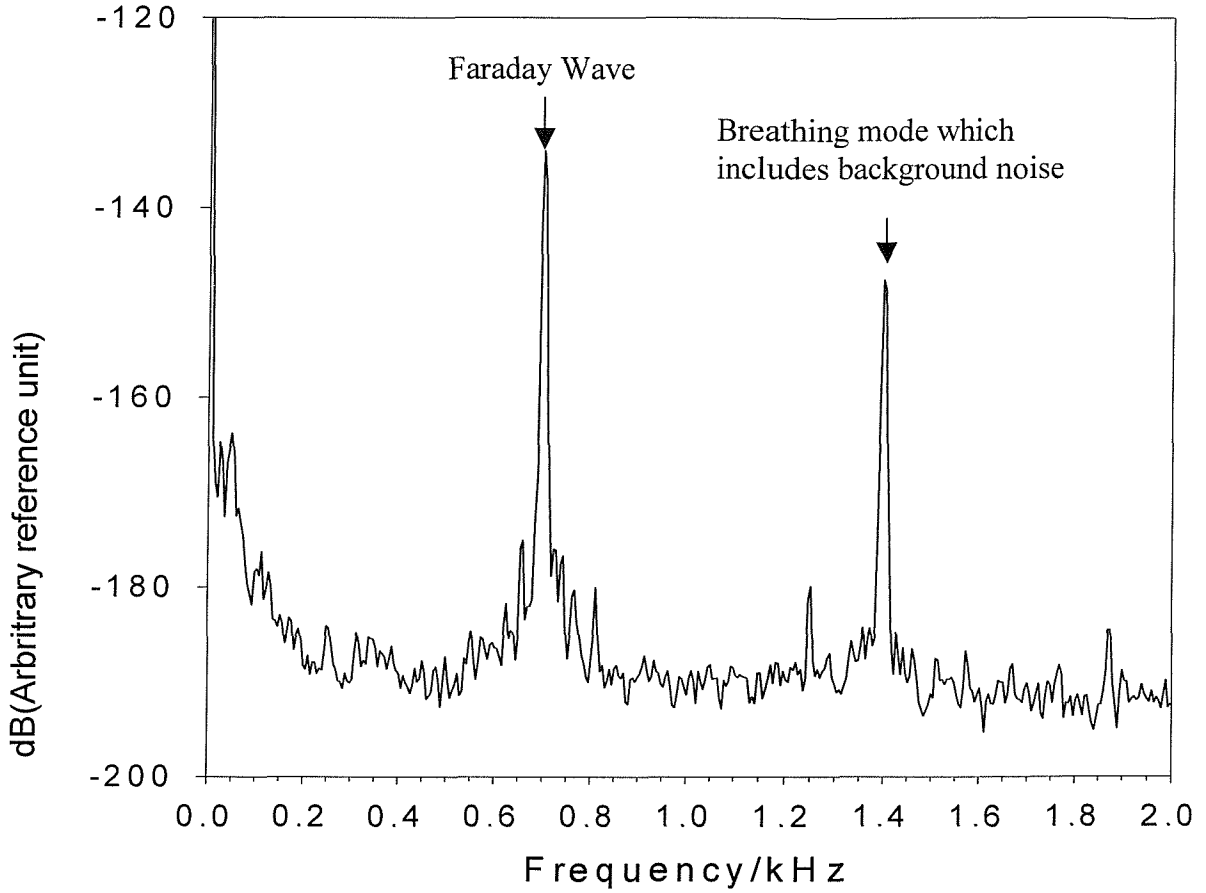

Figure 10.1 Plot showing frequency analysis of current time data recorded by a 25 μm diameter Pt microelectrode in the presence of subharmonic motion (see section 5.1). The frequency and pressure of the sound field were 1.3985 kHz and 55.6 Pa respectively. The plot shows both detection of the Faraday wave and breathing mode of the bubble wall (this signal contains some background electrical noise). Note the y-axis (dB) represents $10\log_{10}(s/\text{arbitrary unit})$ where s is the power spectral density calculated from FFT analysis of the time series data.

10.1 Experimental Results

Initially a set of experiments to determine the feasibility of employing Faraday waves for hydrodynamic modulation voltammetry were performed in $Fe(CN)_6^{3-}$ monitoring the reduction of this ion. However, for this redox system the potential that has to be employed results in the reduction of molecular oxygen as an interferent. It was difficult to differentiate between oxygen reduction and $Fe(CN)_6^{3-}$ reduction at very low concentrations of $Fe(CN)_6^{3-}$. Therefore it was decided to employ $Fe(CN)_6^{4-}$ and monitor the oxidation of this ion at +0.5 V versus Ag. At this potential there would be no conflicting reactions due to known components.

The experimental set-up (figure 2.3) and procedure is outlined in chapter 2. A 25 μm diameter Pt microelectrode was positioned close to the bubble wall (*ca.* 5-10 μm away). The frequency of the driving field was varied until the bubble was observed to shimmer. The potential was set at +0.5 V *vs.* Ag (at this potential the oxidation of $Fe(CN)_6^{4-}$ is mass transfer controlled) and the current was monitored as a function of time. The current time data was transferred directly to a PC over a 2 - 3 s period at high sample rates (*e.g.* 50,000 points over 2.5 s) using the Computer Boards PCI-DAS1602/16 card. This data was then passed through a Fast Fourier Transform (FFT)[132] and the magnitude of the subharmonic signal was noted. The magnitude of the signal can be defined as the square root of the sum of the squares of the real and imaginary parts of the transform.[122] This was repeated at a number of potentials from +0.5 V through to –0.2 V *vs.* Ag. The concentration was then varied from 50 μmol dm^{-3}, to 10 μmol dm^{-3} and to 5 μmol dm^{-3} and the same process was repeated. Figure 10.2 is a plot of the magnitude of the subharmonic signal against potential at varying concentrations. The plot also includes the magnitude of the background signal (recorded in 0.2 mol dm^{-3} $Sr(NO_3)_2$ alone) against potential.

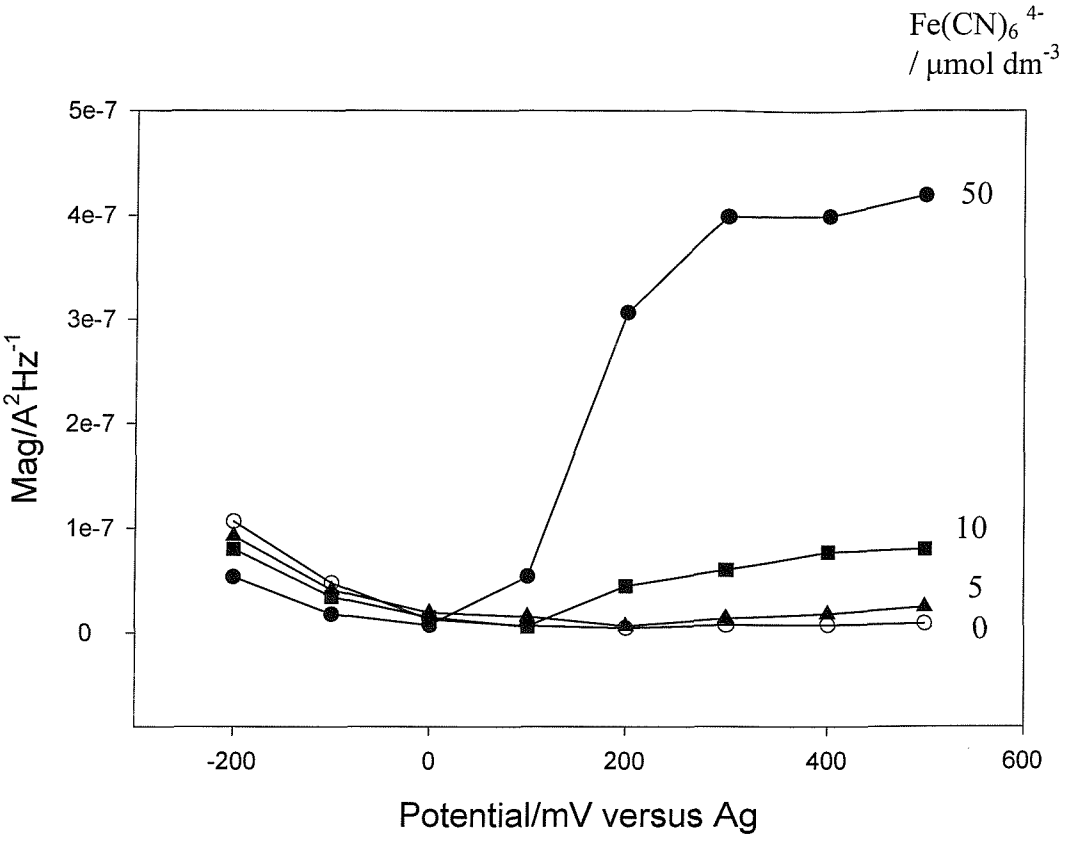

Figure 10.2 Plot showing the magnitude of subharmonic motion detected by a 25 μm diameter Pt microelectrode in varying concentrations of $Fe(CN)_6^{4-}$ against potential versus Ag under aerobic conditions (R_0 *ca.* 2 mm). These plots represent Acoustic Voltammograms (AcV).

A number of points must be noted from figure 10.2. First, in the region from +0.5 V to 0.2 V *vs.* Ag a strong subharmonic signal, when compared to the background signal, was noted particularly at 50 μm dm^{-3} which did not depend on the potential of the microelectrode. Therefore in this region $Fe(CN)_6^{4-}$ oxidation is mass transfer controlled. This agrees with voltammetry of the microelectrode in stagnant solution far away from the bubble wall. Below +0.2 V the magnitude of the signal varies over the entire potential range scanned as expected from the voltammetry of $Fe(CN)_6^{4-}$. Second, the magnitude of the subharmonic signal reaches at minimum at 0.1 V *vs.* Ag (for 10 and 5 μmol dm^{-3}) and then gradually increases below this potential as the reduction of oxygen is initiated. However, it is interesting to note that the magnitude of the signal below 0.1 V decreases as the concentration of $Fe(CN)_6^{4-}$ increases. It is known that adsorption of ions particularly $Fe(CN)_6^{4-}$/ $Fe(CN)_6^{3-}$ can alter electrode kinetics[133,134] on Pt. Hence the results indicate that the adsorption of $Fe(CN)_6^{3-/4-}$ causes inhibition of oxygen reduction as expected.

$Fe(CN)_6^{4-}$/ μmol dm^{-3}	Magnitude/A^2 Hz^{-1} at 0.5 V	Magnitude = m[$Fe(CN)_6^{4-}$] + c
50	4.2e-7	m = 8.6e-9 A^2 Hz^{-1} μmol^{-1} dm^3 c = -9.7e-9 A^2 Hz^{-1}
10	7.5e-8	
5	3.3e-8	
background	2.0e-8	

Table 10.1 Table showing the concentration of $Fe(CN)_6^{4-}$ and corresponding magnitude of subharmonic motion at 0.5 V *vs.* Ag derived from figure 10.2. The table also includes the slope and intercept of the magnitude against concentration of $Fe(CN)_6^{4-}$.

Table 10.1 shows how the magnitude of the subharmonic signal at +0.5 V *vs.* Ag varies with concentration. This data was derived from figure 10.2. On plotting the concentration against the magnitude a linear relationship was obtained indicating a detection limit of *ca.* 2.5 μmol dm^{-3}. However, below 5 μmol dm^{-3} it was difficult to distinguish between the background signal and the signal denoted by $Fe(CN)_6^{4-}$.

These results compare favourably to ultrasound studies where the detection limit for target analytes was 0.1 μmol dm^{-3}.[87,88] Previous studies have shown that ultrasound[105-111] can enhance mass transfer significantly with mass transfer coefficients reported in the order of 0.1 - 1 cm s^{-1}. The mass transfer coefficient reported in this study is 0.0477 cm s^{-1}.[135] This is approximately 25 times lower than those reported by ultrasound and the detection limit is less than 50 times higher. However, it must be noted that the pressure required to achieve inertial cavitation in water[24] under standard conditions is *ca.* 1 atmosphere (101,000 Pa). This is a factor of 1000 higher than the pressures employed here (< 100 Pa). Clearly if this technique was improved, surface wave detection as a means of sensing low concentrations of species in solution would be superior to the cavitation methods where high energy and detrimental effects (*e.g.* erosion[136-138]) can be a problem. The limits of this technique arise from the fact that the AC component is small compared to the DC offset. Lastly at concentrations less than 5 μmol dm^{-3} the purity of the solution will be paramount.

10.2 Conclusions

In this chapter electrochemical detection of surface wave motion was used to detect trace species in solution. A new technique described as Acoustic Voltammetry (AcV) has been presented. In this technique the detection of trace species was possible by locking into the AC component of the current signal obtained in the presence of Faraday wave motion of a bubble driven by an acoustic field. The detection limit was found to be *ca.* 2.5 μmol dm^{-3}, which compares well to ultrasonic studies.

Conclusions and Future Work

Chapter 11

11.0 Concluding remarks

In this thesis electrochemical sensors (microelectrodes) were employed to study the nature of bubble motion in the presence of a sound field.

Previously subharmonic and fundamental oscillations of a bubble wall have been detected both acoustically[19-23,73,74] and photographically.[72] This thesis introduced a novel acousto-electrochemical technique capable of detecting both fundamental and subharmonic bubble oscillations. However, prior to sound irradiation, the electrochemistry at the gas bubble-liquid interface was explored. This investigation allowed the bubble wall-microelectrode distance to be controlled in subsequent experiments. An extensive investigation into the interaction of sound with large gas bubbles retained against buoyancy forces on a glass rod then followed. Electrochemical detection of the fundamental (breathing) and subharmonic Faraday wave motion were explored extensively including the development of a simple model to equate subharmonic motion with surface wave motion. The effect of surface tension on this model was also investigated. Prior to achieving steady state surface wave motion there is a ring-up period. This ring-up time was explored employing the acousto-electrochemical technique developed in this thesis.

Bubble motion induced by acoustic excitation was also shown to have several useful applications. One such application is in the detecting and sizing of bubbles, which was investigated extensively. Bubble growth by the process of rectified diffusion and trace species detection were also explored.

11.1 Overall Conclusions

In the first part of this thesis an extensive investigation into the electrochemical process occurring at the gas/liquid interface was undertaken in the absence of sound irradiation. The variation in mass transfer of species to a microelectrode surface as it approaches an air bubble in the absence of sound irradiation was explored for two different reactions. First, the reduction of the ion $Fe(CN)_6^{3-}$ was examined. The current recorded at a microelectrode

tip as it approached a bubble wall decreased, indicating that the presence of the bubble was blocking the diffusion of $Fe(CN)_6^{3-}$ to the electrode surface. This agreed with the SECM negative feedback predictions, which indicate a decrease in tip current as the microelectrode approaches an inert surface.[49] Second, the reduction of oxygen was monitored as a microelectrode approached the gas/liquid interface of an air bubble. It was found that there was an increase in negative current as the electrode approached the interface due to the diffusion of oxygen from inside the gas bubble in response to concentration depletion caused by the electrochemical reduction of molecular oxygen at the microelectrode surface. In this case the bubble was acting as a source of oxygen. This sequence of experiments allowed the bubble wall microelectrode distance to be controlled. The effect of surfactants on the reduction of oxygen close to the gas/liquid interface was also explored. Increasing concentrations of Triton X-100, decreased the current recorded at the microelectrode close to the bubble wall *i.e.* oxygen transfer was only occurring in regions free from surfactant. This coincides with work undertaken by Unwin *et al.*[40] on planar air/liquid interfaces.

It was shown that the motion of a suspended bubble driven to oscillate could be detected electrochemically via mass transfer enhancements to the electrode surface. On exploring the reduction of $Fe(CN)_6^{3-}$, it was found that there was a large increase in current (compared to the current recorded in the bulk in the absence of sound irradiation) as the electrode approached the gas/liquid interface. This was due to forced convection caused by the motion of the bubble wall. Significant enhancements in mass transfer were recorded up to 2.5 mm away. However, on examining the oxygen reduction reaction there was a decrease in negative current recorded close to the interface in the presence of sound irradiation (*ca.* 5 -10 μm away). It was thought that this reduction in current was caused by forced convection of fresh solution into the gap between the microelectrode and the gas/liquid interface of the bubble wall. Hence the driving force for oxygen transfer across the gas/liquid interface (*e.g.* concentration depletion) had been removed. However, it was discovered that there was some contribution to the current caused by transfer of molecular oxygen across the interface at *ca.* 5 - 10 μm from the bubble wall. As the distance between the bubble wall and microelectrode increased the current fell to mass transfer of oxygen from the bulk to the microelectrode. An explanation for these observations was presented which modeled the system as a rotating disk electrode.

The two main oscillatory modes of an oscillating bubble (*i.e.* fundamental and subharmonic motion) have been detected electrochemically for the first time. A number of important points relating to this study must be noted. First, subharmonic motion occurs for a

certain range of driving frequencies and pressures and there is a threshold pressure amplitude at which this motion begins. However, fundamental bubble motion can occur at any pressure and the amplitude of motion was highly frequency dependent. Second, subharmonic motion occurs as a result of the onset of Faraday waves, which was confirmed by the model derived in chapter 5. Third, a reduction in surface tension did not change the threshold pressure at which surface wave motion was initiated but did change the mode number. This was confirmed by the model mentioned above with complementary photographic and electrochemical evidence. Finally, the time taken for surface waves to rise (to generate steady state oscillations) was found to increase with decreasing driving pressure. There was an initial 'fluid flow lag time' before the ring-up of the surface waves.

A number of applications derived from the electrochemical detection of an oscillating bubble were explored. First, individual bubbles were detected from a rising stream. Faraday wave motion of individual rising bubbles was electrochemically detected for the first time. This was used to size individual bubbles and was much more favourable than the rise time method of determining bubble size. Second, growth rates of bubbles by the process of rectified diffusion caused by microstreaming were determined and compared to a theoretical model. Third, low levels of ions were detected by using bubble oscillation to provide a suitable AC component to mass transfer to an electrode. The detection limit was found to be 1 - 5 μmol dm^{-3}, which compared well with ultrasonic studies but with certain limitations.

11.2 Importance to Industry and Science

The electrochemical investigation of the gas/liquid interface of both a stationary and oscillating bubble provided many useful results. First, the ability to detect enhanced mass transfer of oxygen close to a clean stationary air bubble and the capacity to detect the presence of surfactants at this interface would be important on a global/environmental sense. The results obtained compare well with the literature.[40,101,102]

Second, enhanced mass transfer to the electrode in the presence of sound irradiation (compared to that recorded in the bulk in the absence of sound irradiation) when monitoring the reduction of $Fe(CN)_6^{3-}$ was noticed. This could be potentially useful in industry in large reaction vessels. Third, detection and sizing of individual rising bubbles has both industrial and environmental applications. Fourth, detection of trace species in solution employing lock-in techniques provided an alternative to hydrodynamic modulation voltammetry.

Finally this study provided some useful contributions to fundamental science. It provided an alternative means to detecting both fundamental and surface wave motion of an oscillating bubble, previously detected by acoustic and photographic techniques. Growth rates by the process of rectified diffusion were also determined and compared to a theoretical model.

11.3 Future work

Electrochemical detection of the interaction of a bubble with sound provided many useful results but further investigations must be undertaken. The ring-up times determined in chapter 7 are currently being tested against a theory proposed by Maksimov and Leighton.[79] The data is not available at this time. Electrochemical detection of Faraday wave motion of a rising bubble could eventually be employed to detect and size bubble populations. However, further extensive investigation into this area will have to be undertaken. Finally a more extensive study into the phenomenon of rectified diffusion could be undertaken with the development of a new theory to predict bubble growth and dissolution rates.

Appendix A

A.0 Introduction

In chapter 3, attention was paid to water quality and hence 'clean' approach curves were obtained for the reduction of oxygen at a microelectrode on approaching a gas/liquid interface. However, numerous problems were encountered prior to obtaining a 'clean' approach curve, which we attribute to 'skin effects'. Malfunctioning of the water purification system and contamination of the glassware by surfactants still present subsequent to washing contributed to these effects. Certain background electrolytes also inhibited the oxygen reduction process on approaching the gas/liquid interface. Rinsing the glassware thoroughly in purified water and changing the electrolyte solution overcame this problem. A brief description of the problems encountered is explained below.

A.1 Contaminants present in $Sr(NO_3)_2$

It is a well known that the purity of an electrolytic solution is very important when studying the electrochemistry at the interface between two phases.[40,101,102] In order to demonstrate that bubbles are a rich source for contamination an experiment was performed in aqueous 0.2 mol dm^{-3} $Sr(NO_3)_2$. A 25 μm diameter Pt microelectrode was positioned within 100 μm of the bubble wall using the x, y, z micrometer and stage. At this point the potential of the microelectrode was stepped from +1 V (where the Pt is oxidised to PtO_x) to –0.7 V *vs.* Ag (where oxygen reduction occurs). This potential stepping routine was employed to clean the surface of the microelectrode. Essentially when the potential of the microelectrode was stepped from +1 V to –0.7 V *vs.* Ag a 'fresh' Pt surface was generated because PtO_x is stripped from the microelectrode surface. This enabled mass transfer controlled electroreduction of molecular oxygen. The microelectrode was then moved towards the bubble wall in increments of 20 μm in the x direction until the microelectrode-interface distance was approximately 5 – 10 μm. A current time plot was recorded for each distance moved towards the bubble wall stepping the potential each time (see figure A.1). Figure A.1 shows that there was a sharp decay in current following the potential step from

+1 V to –0.7 V *vs.* Ag (see figure A.1 region B) for each increment moved by the microelectrode towards the bubble wall. Under ideal conditions you would expect the current to relax back to mass transfer steady state conditions as in figure 3.6 chapter 3 (no bubble present). However, it appears that under the conditions employed, the current decayed over time and that the rate of decay of current with time increases with decreasing distance between the interface and microelectrode. To confirm this, the rate of decay of current with respect to time (*di/dt*) was calculated from t = 10 s to t = 20 s for each set of data. The average value of *di/dt* was plotted against distance from the bubble surface. This is shown in the insert of figure A.1 where the rate of decay is greatest close to the bubble wall. This suggests that impurities present on the bubble wall were contaminating the microelectrode surface (possibly due to $Sr(NO_3)_2$). This is important as the reduction of molecular oxygen is thought to be a surface process. Hence, surface contaminants will have marked effects on the electrochemistry of molecular oxygen. Clearly, the state of the gas liquid interface can have profound effects on the electrochemistry recorded at the microelectrode. A more extensive look at the effect of $Sr(NO_3)_2$ on the reduction of oxygen at the gas/liquid interface was undertaken.

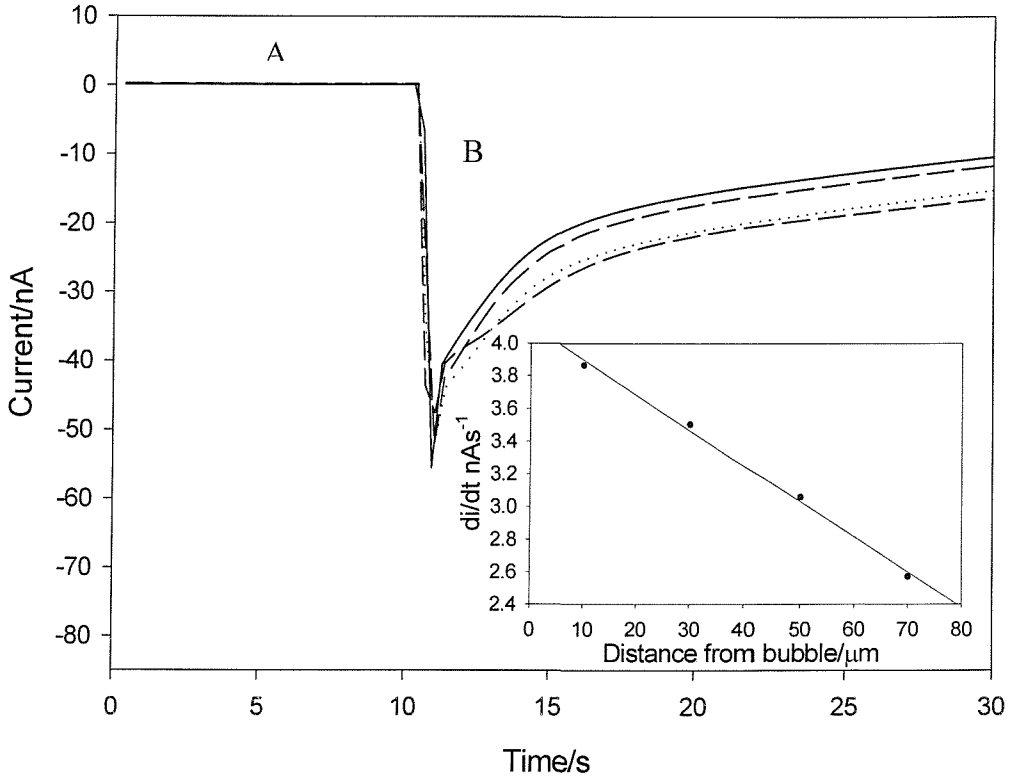

Figure A.1 The variation in current with time for a 25 μm diameter Pt microelectrode at approximately 70 μm, 50 μm, 30 μm and 10μm from the bubble wall (from bottom to top) where the potential is stepped from +1 V (A) to -0.7 V *vs.* Ag (B)(where oxygen reduction occurs) in 0.2 mol dm^{-3} $Sr(NO_3)_2$. The insert shows the rate of decay in current against distance from the bubble wall for each distance moved showing that the rate of decay increased with decreasing interface-microelectrode distance.

A similar experiment was undertaken in 0.2 mol dm^{-3} $Sr(NO3)_2$ which contains some form of impurities. However, in this case, the microelectrode was positioned at a distance >100 μm from the bubble wall and the potential was stepped from +1 V (see figure A.2 region A) to –0.7 V (see figure A.2 region B) *vs.* Ag where steady state mass transfer limited reduction of molecular oxygen occurs on the clean microelectrode surface. The interface was approached by the microelectrode using an x, y, z micrometer and stage in increments of 20 μm until there was a large enhancement in current close to the bubble wall (see figure A.2 region C). However, after each movement of 20 μm in this region there was a slight decay in current (spikes) suggesting impurities present on the bubble wall are contaminating the electrode. This decay increased as the distance between the bubble and microelectrode decreased. When the microelectrode was positioned close to the bubble wall (*i.e.* 5 - 10 μm away), indicated by region D in figure A.2, a rapid decay in current was observed as a function of time which is in agreement with the results shown in figure A.1

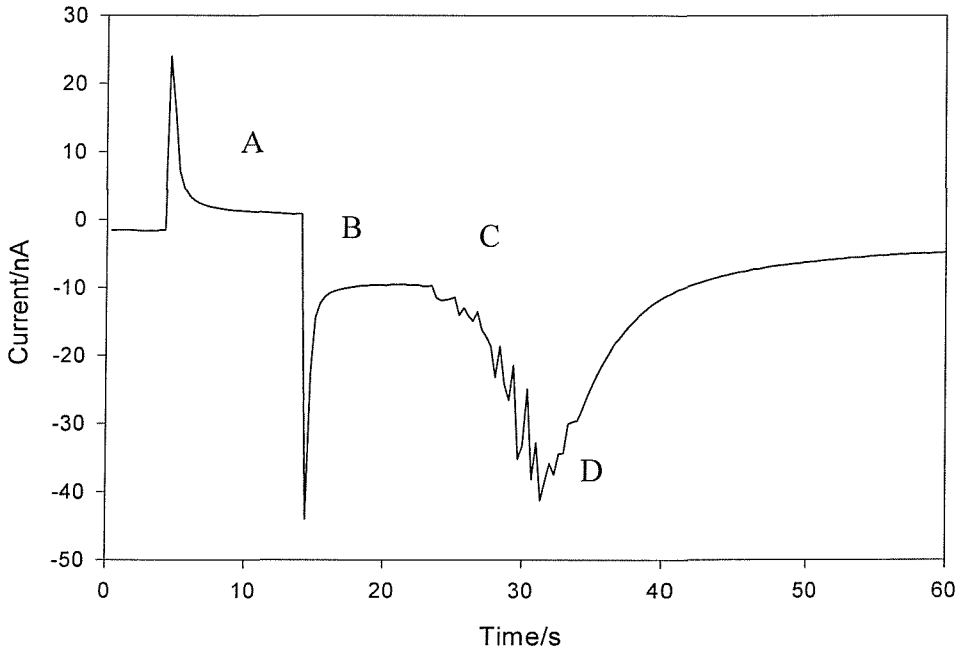

Figure A.2 The variation of current with time for a 25 μm diameter Pt microelectrode in 0.2 mol dm^{-3} $Sr(NO_3)_2$ where the potential was stepped from 1 V (A) to –0.7 V (B) *vs.* Ag followed by movement of the microelectrode towards the bubble wall (C) and than rapid decay in current due to electrode fouling (D).

These results clearly show that the interface between a gas bubble and the aqueous liquid media can be complex, and cause a variety of parasitic effects on the response of a microelectrode placed in close proximity to the interface. All experiments in chapter 3 were performed in KCl (BDH, AnalR) employing water from a Vivendi Purelab Option E10 purification system. This enabled 'clean' approach curves to be obtained for the reduction

of molecular oxygen at the microelectrode surface in the bulk solution and near the gas/liquid interface of a suspended air bubble.

Publications

1. P. R. Birkin, T. G. Leighton and Y. E. Watson, "The use of Acoustoelectrochemistry to investigate Rectified Diffusion", Submitted to *Ultrasonics Sonochemistry*.

2. Y. E.Watson, P. R. Birkin and T. G. Leighton, "Electrochemical Detection of Bubble Oscillation", *Ultrasonics Sonochemistry*, **10**, 65-69, 2003.

3. P. R. Birkin, Y. E. Watson, T. G. Leighton and K. L. Smith., "Electrochemical Detection of Faraday Waves on the Surface of a Gas Bubble", *Langmuir*, **18**, 2135-2140, 2002.

4. P. R. Birkin, Y. E. Watson and T. G. Leighton, "Efficient Mass Transfer from an Acoustically Oscillated Gas Bubble", *Chem. Comm.*, 2650-2651, 2001.

5. P. R. Birkin, T. G. Leighton, Y. E. Watson and J. F. Power, "Acoustoelectrochemistry", *Acoustics Bulletin*, **26(5)**, 24-37, 2001.

6. P. R. Birkin, Y. E. Watson, T. G. Leighton and M. D. Simpson, "Measurement of Species Flux from a Bubble using an Acousto-electrochemical Technique", *Acoustical Oceanography*, Proceedings of the Institute of Acoustics, **23(2)**, 242-247, 2001.

7. P. R. Birkin, J. M. Elliot and Y. E. Watson, "Electrochemical Reduction of Oxygen on Mesoporous Platinum Microelectrodes", *Chem. Comm.*, 1693-1694, 2000.

References

1. T. G. Leighton, D. G. Ramble, A. D. Phelps, C. L. Morfey and P. P. Harris, *Acta Acustica*, **84**, 801, 1998.

2. A. D. Phelps and T. G. Leighton, *Acta Acustica*, **83**, 59, 1997.

3. T. G. Leighton, *J. Soc. Env. Eng.*, **7**, 9, 1994.

4. T. G. Leighton, *J. Soc. Env. Eng.*, **8**, 16, 1995.

5. G. M. Whitney and C. W. Tobias, *AIChE Journal*, **34**, 1981, 1988.

6. T. J. Lin and H. G. Donnelly, *American Institute of Chemical Engineering Journal*, **92**, 1177, 1966.

7. I. Anderson and S. Bowler, *New Scientist*, **125**, 1707, 1990.

8. E. O. Belcher, *I. E. E. E. Transactions on Biomedical Engineering*, **27**, 330, 1980.

9. J. Ophir and K. J. Parker, *Ultrasound in Medicine and Biology*, **15**, 319, 1989.

10. A. J. Coleman, M. Whitlock, T. G. Leighton and J. E. Saunders, *Physics in Medicine and Biology*, **38**, 1545, 1993.

11. A. J. Coleman, M. J. Choi, J. E. Saunders and T. G. Leighton, *Ultrasound in Medicine and Biology*, **18**, 267, 1992.

12. W. H. Ting, *P. I. Civil Eng.-Geotec.*, **155**, 143, 2002.

13. I. S. Chang and S. J. Judd, *Process Biochem.*, **37**, 915, 2002.

14. S. F. Catney and R. J. Lynch, *P. I. Civil Eng.-Geotec.*, **149**, 253, 2001.

15. M. D. Fouad and G. H. Sedahmed, *Electochim. Acta*, **17**, 665, 1972.

16. D. Pletcher, *A First Course in Electrode Processes*, The Electrochemical Consultancy, 1991.

17. P. H. Reiger, *Electrochemistry*, second edition, Chapman and Hall, 1994.

18. A. J. Bard and L. R. Faulkner, *Electrochemical Methods*, Wiley, New York, 1980.

19. W. M. Fairbank and M. O. Scully, *IEEE Trans. Biomed. Eng.*, **24**, 107, 1977.

20. R. Y. Nishi, *Ultrasonics*, **10**, 173, 1972.

21. D. L. Miller, *Ultrasonics*, **19**, 217, 1981.

22. D. M. Farmer and S. Vagle, *J. Acoust. Soc. Am.*, **86**, 1897, 1989.

23. T. G. Leighton, A. D. Phelps, D. G. Ramble and D. A. Sharp, *Ultrasonics*, **34**, 661, 1996.

24. T. G. Leighton, *The Acoustic Bubble*, Academic Press, New York, 1994.

25. P. R. Birkin, T. G. Leighton, Y. E. Watson and J. F. Power, *Acoustics Bulletin*, **26(5)**, 24, 2001.

26. G. Denuault, *Chem. Ind-London*, **18**, 678, 1996.

27. D. Pletcher, *Microelectrodes: Theory and Application*, ed. M. I. Montenegro, M. A. Queiros and J. L. Daschbach, Kluwer Academic Publishers, Dordrecht, 1990.

28. J. L. Amphlett, *Numerical simulation of microelectrodes*, A thesis submitted for the degree of Doctor of Philosophy Southampton University, 2000.

29. G. Denuault, M. V. Mirkin and A. J. Bard, *J. Electroanal. Chem.*, **308**, 27, 1991.

30. P. R. Birkin, Y. E. Watson, T. G. Leighton, M. D. Simpson, *Acoustical Oceanography*, Proceedings of the Institute of Acoustics, **23(2)**, 242, 2001, T. G. Leighton, G. J. Heald, H. Griffiths and G. Griffiths (eds.), Institute of Acoustics.

31. A. W. Adamson, *Physical Chemistry of Surfaces*, Wiley, New York, 1997.

32. G. A. Somorjai, *Surface Chemistry and Catalysis*, Wiley, New York, 1994.

33. M. Tionsky, Z. G. Cardon, A. J. Bard and R. B. Jackson, *Plant Physiol.*, **113**, 895, 1997.

34. P. A. Christensen and A. Hammett, *Techniques and mechanisms in Electrochemistry*, Blackie, Glasgow, 1994.

35. A. J. Bard, F. R. F. Fan, J. Kwak and O. Lev, *Anal. Chem.*, **61**, 132, 1989.

36. M. Tionsky, A. J. Bard and M. V. Mirkin, *J. Am. Chem. Soc.*, **119**, 10785, 1997.

37. M. H. Delville, M. Tionsky and A. J. Bard, *Langmuir*, **14**, 2774, 1998.

38. Y. Shao, M. V. Mirkin and J. F. Rusling, *J. Phys. Chem. B*, **101**, 3202, 1997.

39. C. J. Slevin, J. V. Macpherson and P. R. Unwin, *J. Phys. Chem. B*, **101**, 10851, 1997.

40. C. J. Slevin, S. Ryley, D. J. Walton and P. R. Unwin, *Langmuir*, **14**, 5331, 1998.

41. P. R. Unwin, *J. Chem. Soc.*; *Faraday Trans.*, **94**, 3183, 1998.

42. A. J. Bard, G. Denuault, C. Lee, D. Mandler and D. O. Wipf, *Acc. Chem. Res.*, **23**, 357, 1990.

43. M. E. Abdelsalam, *Development of Microelectrode Techniques for Analytical and Environmental Applications*, A thesis submitted for the degree of Doctor of Philosophy, 2000.

44. C. J. Slevin and P.R. Unwin, *Langmuir*, **13**, 4799, 1997.

45. C. J. Slevin and P.R. Unwin, *Langmuir*, **15**, 7361, 1999.

46. J. Zhang, C. J. Slevin and P. R. Unwin, *Chem. Commun.*, 1501, 1999.

47. R. C. Engstrom, M. Webber, D. J. Wunder, R. Burgess and S. Winquist, *Anal. Chem.*, **58**, 844, 1986.

48. A. L. Barker, M. Gonsalves, J. V. Macpherson, C. J. Slevin and P. R. Unwin, *Analytica Chimica Acta*, **385**, 223, 1999.

49. J. L. Amphlett and G. Denuault, *J. Phys. Chem. B*, **102(49)**, 9946, 1998.

50. P. W. Atkins, *Physical Chemistry*, Oxford University Press 7th addition, 2002.

51. A. Franscescutto and R. Nabergoj, *Acustica*, **41**, 215, 1978.

52. G. Ducom, H. Matamoros and C. Cabassud, *J. Memb. Sci.*, **204**, 221, 2002.

53. B. C. Kirtland, C. M. Aelion and M. A. Widdowson, *J. Environ. Eng. Asce.*, **127**, 134, 2001.

54. S. Mas and C. Ghommidh, *Biotechnol. Bioeng.*, **76**, 91, 2001.

55. C. Cabassud, C. Burgaud and J. M. Espenan, *Desalination*, **137**, 123, 2001.

56. N. Ibl and J. Venczel, *Metalloberflache*, **24**, 366, 1970.

57. L. J. J. Janssen and J. G. Hoogland, *Electrochim. Acta*, **15**, 1013, 1970.

58. L. J. J. Janssen and J. G. Hoogland, *Electrochim. Acta*, **18**, 543, 1973.

59. L. J. J. Janssen and E. Barendrecht, *Electrochim. Acta*, **24**, 693, 1979.

60. K. Stephan and H. Vogt, *Electrochim. Acta*, **24**, 11, 1979.

61. R. Higbie, *Trans. Am. Inst. Chem. Eng.*, **31**, 365, 1935.

62. G. Palasantzas, D. T. L. van Agterveld and J. T. M. De Hosson, *Appl. Surf. Sci.*, **191**, 266, 2002.

63. J. T. Dawley, R. J. Ong and P.G. Clem, *J. Mater. Res.*, **17(7)**, 1678, 2002.

64. M. Minnaert, *Philosophical Magazine*, **16**, 235, 1933.

65. C. Devin, *J. Acoust. Soc. Am.*, **31**, 1654, 1959.

66. A. I. Eller, *J. Acoust. Soc. Am.*, **47**, 1469, 1970.

67. A. J. Walton and G. T. Reynolds, *Ad. Phys.*, **33**, 595, 1984.

68. E. A. Neppiras, *Acoustic Cavitation. Physics Reports 3.*, 159, 1980.

69. A. I. Eller and H. G. Flynn, *J. Acoust. Soc. Am.*, **46**, 722, 1969.

70. W. Lauterborn, *J. Acoust. Soc. Am.*, **59**, 283, 1976.

71. M. Faraday, *Phil. Trans. Roy. Soc.*, **121**, 319, 1831.

72. C. Hullin, *Acustica*, **37**, 64, 1977.

73. A. D. Phelps and T. G. Leighton, *J. Acoust. Soc. Am.*, **99**, 1985, 1996.

74. D. G. Ramble, A. D. Phelps and T. G. Leighton, *Acustica*, **84**, 986, 1998.

75. P. R. Birkin, Y. E. Watson, T. G. Leighton and K. L. Smith, *Langmuir*, **18,** 2135, 2002.

76. K. L. Smith, *Third Year Chemistry Project*, 1999.

77. A. D. Phelps, D. G. Ramble and T. G. Leighton, *J. Acoust. Soc. Am.*, **101(4)**, 1981, 1997.

78. T. G. Leighton, S. D. Meers, M. D. Simpson, J. W. L. Clarke, G. T. Yim, P. R. B. Birkin, Y. E. Watson, P. R. White, G. J. Heald, H. A. Dumbrell, R. L. Culver and S. D.

Richards, *Acoustical Oceanography*, Proceedings of the Institute of Acoustics, **23(2)**, 227, 2001, T. G. Leighton, G. J. Heald, H. Griffiths and G. Griffiths (eds.), Institute of Acoustics.

79. A. O. Maksimov, and T. G. Leighton, *Acustica*, **87(3)**, 322, 2001.

80. C. C. Church, *J. Acoust. Soc. Am.*, **84(5)**, 1758, 1988.

81. R. K. Gould, *J. Acoust. Soc. Am.*, **56(6)**, 1740, 1974.

82. A. I. Eller, *J. Acoust. Soc. Am.*, **46(5)**, 1246, 1969.

83. L. A. Crum, *J. Acoust. Soc. Am.*, **72(5)**, 1586, 1982.

84. L. E. Steiner, *Introduction to Chemical Thermodynamics*, Mc Graw-Hill, New York, 1941.

85. J. V. Macpherson, *Electroanalysis*, **12(13)**, 1001, 2000.

86. K.W. Pratt and D. C. Johnson, *Electrochim. Acta*, **27**, 115, 1982.

87. H. D. Dewald and B. A. Peterson, *Anal. Chem.*, **62(7)**, 779, 1990.

88. E. L. Cooper and L. A. Coury, *J. Electrochem. Soc.*, **145(6)**, 1994, 1998.

89. J. Kwak and A. J. Bard, *Anal. Chem*, **61**, 1221, 1989.

90. D. G. Ramble, *Characterisation of bubbles in liquids using acoustic techniques*, A thesis submitted for the degree of Doctor of Philosophy,1997.

91. G. T. Yim, P. R. White and T. G. Leighton, '*Acoustical Oceanography', Proceedings of the Institute of Acoustics*, **23 (2)**, 250, 2001, T. G. Leighton, G. J. Heald, H. Griffiths and G. Griffths, (eds.), Institute of Acoustics.

92. C. Beriet and D. Pletcher, *J. Electroanal. Chem.*, **361**, 93, 1993.

93. H. S. Wroblawa, Y. C. Pan and G. Rauzumney, *J. Electroanal. Chem.*, **69**, 195, 1976.

94. R. W. Zurilla, R. K. Sen and E. Yeager, *J. Electrochem. Soc.*, **125**, 1103, 1978.

95. A. Damjanovic, M. A. Greenshaw and J. O' M. Bockris, *J. Electrochem. Soc.*, **114**, 1107, 1967.

96. D. Pletcher and S. Sotiropoulos, *J. Electroanal. Chem.*, **356**, 109, 1993.

97. P. R. Birkin, J. M. Elliot and Y. E. Watson, *Chem. Commun.*, 1693, 2000.

98. A. L. Barker, J. V. Macpherson, C. J. Slevin and P. R. Unwin, *J. Phys. Chem. B*, **102**, 1586, 1998.

99. J. Heyrovsky and P. Zuman, *Practical Polarography*, Academic Press, New York, 1968.

100. Z. Yoshida and S. Kihara, *J. Electronal. Chem.*, **227**, 171, 1987.

101. J. Zhang, C. J. Slevin, L. Murtomaki, K. Kontturi, D. E. Williams and P. R. Unwin, *Langmuir*, **17**, 821, 2001.

102. J. Zhang and P. R. Unwin, *J. Electroanal. Chem.*, **494**, 47, 2000.

103. H. H. J. Girault, D. J. Schriffrin and B. D. V. Smith, *J. Electroanal. Chem.*, **137**, 207, 1982.

104. G. Peng, M. Ishizuka, S. Cao and S. Hayama, *Japenese Journal of Applied Physics*, **40**, L1250, 2001.

105. P. R. Birkin and S. S. Martinez, *J. Electroanal. Chem.*, **416**, 127, 1996.

106. P. R. Birkin and S. S. Martinez, *J. Chem. Soc., Chem. Commun.*, 1807,1995.

107. S. S. Martinez, *Applications of Ultrasound in Electrochemistry*, A thesis submitted for the degree of Doctor of Philosophy, 1997.

108. C. R. S. Hagan and L. A. Coury, *Anal. Chem.*, **66**, 399, 1994.

109. H. Zhang and L. A. Coury, *Anal. Chem.*, **65**, 1552, 1993.

110. R. G. Compton, J. C. Eklund and S. D. Page, *J. App. Electrochem.*, **26(8)**, 775, 1996.

111. R. G. Compton, J. C. Eklund, S. D. Page and T. O. Rebbitt, *J. Chem. Soc., Dalton Trans.*, 389, 1995.

112. D. Y. Heish and M. S. Plesset, *J. Acoust. Soc. Amer.*, **33**, 206, 1961.

113. D. Y. Heish, *J. Acoust. Soc. Amer.*, **56**, 392, 1974.

114. L.E. Kinsler, A. R. Frey, A. B. Coppens and J. V. Sanders, *Fundamentals of Acoustics*, John Wiley and Sons, 1982.

115. A. Harkin, A. Nadim and T. J. Kaper, *Physics of fluids*, **11(2)**, 274, 1999.

116. J. K. Ferri and K. J. Stebe, *Adv. Colloid Interfac.*, **85(1)**, 61, 2000.

117. V. L. Newhouse and P. M. Shankar, *J. Acoust. Soc. Am.*, **75**, 1473, 1984.

118. T. G. Leighton, R. J. Lingard, A. J. Walton and J. E. Field, *Ultrasonics*, **29**, 319, 1991.

119. V. G. Levich, *Physicochemical Hydrodynamics*, Prentice-Hall, London, 1962.

120. W. Ryczynski, *Bull. Int. Acad. Pol. Sci. Lett. C1 Sci., Mat. Nat. Ser. A*, 40, 1911.

121. J. Hadamard, *Comput. Rend.*, **152**, 1735, 1911.

122. G. H. Kelsall, S. Tang, A. L. Smith, S. Yurdakul, *J. Chem. Soc., Faraday Trans.*, **92**, 3879, 1996.

123. T. G. Leighton, D. G. Ramble and A. D. Phelps, *J. Acoust. Soc. Am.*, **101**, 2626, 1997.

124. R. S. Gupta and D. Kumar, *Computers and Fluids*, **11**, 341, 1983.

125. C. C. Church, *J. Acoust. Soc. Am.*, **83**, 2210, 1988.

126. A. Eller and H. G. Flynn, *J. Acoust. Soc. Am.*, **37**, 493, 1965.

127. L. A. Skinner, *J. Acoust. Soc. Am.*, **47**, 327, 1970.

128. A. I. Eller, *J. Acoust. Soc. Am.*, **52**, 1447, 1972.

129. R. K. Gould, *J. Acoust. Soc. Am.*, **56**, 1740, 1974.

130. A. I. Eller, *J. Acoust. Soc. Am.*, **57**, 1374, 1975.

131. Yu. G. Statnikov, *Akust. Zh.*, **13**, 464, 1967 [*Sov. Phys. Acoust.*, **13**, 398, 1968].

132. E.O Brigham, *The Fast Fourier Transform and its Applications*, Mc Graw-Hill/Kogakusha, New York/Tokyo, 1978.

133. C. M. Pharr and P. R. Griffiths, *Anal. Chem.*, **69(22)**, 4665, 1997.

134. C. M. Pharr and P. R. Griffiths, *Anal. Chem.*, **69(22)**, 4673, 1997.

135. P. R. Birkin, Y. E. Watson and T. G. Leighton, *Chem. Commun.*, 2650, 2001.

136. P. R. Birkin, R. O'Connor, C. Rapple and S. S. Martinez, *J. Chem. Soc. Faraday Trans.*, **94**, 3365, 1998.

137. S. A. Perusich and R. C. Alkire, *J. Electrochem. Soc.*, **138**, 700, 1991.

138. S. A. Perusich and R. C. Alkire, *J. Electrochem. Soc.*, **138**, 708, 1991.